DYNAMICS OF UNFOLDED AND α-HELICAL POLYPEPTIDE CHAINS

INAUGURALDISSERTATION

zur

Erlangung der Würde eines Doktors der Philosophie

vorgelegt der

Philosophisch-Naturwissenschaftlichen Fakultät

der Universität Basel

von

Beat Fierz

aus Zürich, ZH

Basel, 2006

Genehmigt von der Philosophisch-Naturwissenschaftlichen Fakultät
auf Antrag von

Prof. Dr. Thomas Kiefhaber
Prof. Dr. Wolfgang Zinth

Basel, den 6. Juni 2006

Prof. Dr. Hans-Jakob Wirz
(Dekan)

Für meine Eltern

Table of Contents

1. Introduction

1.1 Proteins and Protein Folding

1.1.1 Proteins in Biology

Proteins are the major class of biomolecules and play a crucial role in most biological processes. Their functions are diverse and include catalysis, transport and storage of nutrients and metabolites, mechanical support and signaling. In higher organisms proteins take on complex processes like immune protection, transport and processing of information and coordinated motion. Proteins are macromolecules consisting of amino acid subunits, which are connected by amide linkages, the peptide bonds. In most organisms proteins are constructed of 20 different amino acids, which allows almost unlimited variability in sequence. *In vivo* the synthesis of a protein chain (translation) is performed at the ribosome. In higher organisms, proteins are often posttranslationally modified at different defined positions by attachment of sugars, lipids or other chemical groups.

To fulfil their various functions, proteins have to adopt a defined three dimensional structure. The transition from an unstructured chain molecule in solution to an highly ordered molecule with a defined three dimensional structure is called protein folding. Protein structure is determined by a huge number of non-covalent interactions like hydrogen-bonds, hydrophobic interactions, van der Waals interactions and electrostatics. These weak forces that stabilise proteins allow spontaneous unfolding due to thermal fluctuations. The folded and unfolded states of a protein are in equilibrium thus folding and unfolding reactions occur constantly in a protein population.

If protein folding fails the protein is usually taken up by cellular machinery and the folding process is either repeated or the protein is degraded. Systematical misfolding of proteins however can lead to diseases like Altzheimer and Parkinson disease or prion diseases (1) as Creutzfeldt-Jacob disease (CJD), Scrapie or Bovine Spongiforme Encephalopathy (BSE). On the other hand protein based drugs are becoming increasingly important and can be applied as cancer therapeutics, anti-microbial agents or for vaccination. Thus it is essential to understand the process of protein folding in a quantitative manner.

1.1.2 Protein Folding

Enzymes that are subjected to conditions as high temperature, high pressure, extreme pH values or solvents containing urea or guanidinium hydrochloride (GdmCl) loose their catalytic function. Their structure is destroyed and they are denatured. It has been recognised in the first half of the 20st century that protein denaturation is a reversible process (2-4) and that proteins can be folded *in vitro* in the absence of the cellular machinery.

Using ribonuclease A (RNase A) as a model system, Anfinsen showed that the information to fold to the native structure is contained in the amino acid sequence of a protein. It was observed that by refolding denatured and reduced RNase A, which contains four disulfide bridges in the native state, only one of 105 possible disulfide arrangements is formed in the test tube (5). These findings lead to the "thermodynamic hypothesis" which states that the adopted three dimensional structure at a given set of conditions is the conformation which minimises the Gibbs free energy of the whole system (6; 7).

Protein folding is a cooperative process. In small proteins mainly fully folded and fully unfolded molecules are present in equilibrium (number of amino acids $n \sim 100$), the number of partially folded proteins is low and those species are transient (8). The folding reaction can then be described as a two state transition from the folded or native state N to the denatured or unfolded state U

$$U \rightleftarrows N \qquad [1]$$

The native state corresponds to a narrow ensemble of molecules that exhibit defined structure and are functionally active. The denatured state on the other hand includes the whole ensemble of unfolded molecules. Because they interchange on a fast timescale, this very broad ensemble can be viewed as a thermodynamic state. The equilibrium constant for a folding reaction K_f is then defined as

$$K_f = \frac{[U]}{[N]} \qquad [2]$$

where the square brackets denote the concentrations of unfolded and folded proteins and the thermodynamic stability of the folded state is thus given by

$$\Delta G^0 = -RT \ln K_f . \qquad [3]$$

Medium to large proteins often fold through intermediates (9). Because of their transient nature these intermediates are difficult to observe in equilibrium. However, under certain conditions where the native state is selectively destabilised partially folded states can be populated as in the Ca^{2+} binding protein α-lactalbumin in the absence of its ligand (10) or in apo-myoglobin at low pH (11).

Population of folding intermediates in the cell may lead to problems like misfolding or aggregation of partially unfolded proteins due to their extreme concentration in the cell (e.g. 200 mg/ml in the ER lumen). Folding helper enzymes minimise these side reactions by speeding up the slow steps of protein folding as peptidyl prolyl bond isomerisation (12; 13) and disulfide bond shuffling (14). On the other hand, partially folded or misfolded states are recognised by certain proteins (called "Chaperones") which prevent aggregation and allow the proteins to refold (15).

Protein stability is affected by different perturbations. From the Gibbs fundamental equation where ΔV^0, ΔS^0 and $\Delta \mu_i^0$ denote the changes in volume, entropy and chemical potential upon folding

$$d\Delta G^0 = \Delta V^0 dp - \Delta S^0 dT + \sum_i \Delta \mu_i^0 dn_i \qquad [4]$$

it is shown that folding equilibria can be perturbed by pressure, temperature or changes in chemical potential e.g. upon the addition of chemical denaturants like urea or guanidinium hydrochloride (GdmCl). This enables the study of protein denaturation in equilibrium and to obtain stability information from the unfolding transition.

1.1.3 Protein Folding Kinetics

The time a protein would need to find the native conformation by randomly sampling all possible conformations is astronomic. Nevertheless, folding times for small proteins range from microseconds to seconds (16), a contradiction that is known as the Levinthal paradox (17). Theoreticians and experimenters searched for explanations of this phenomenon.

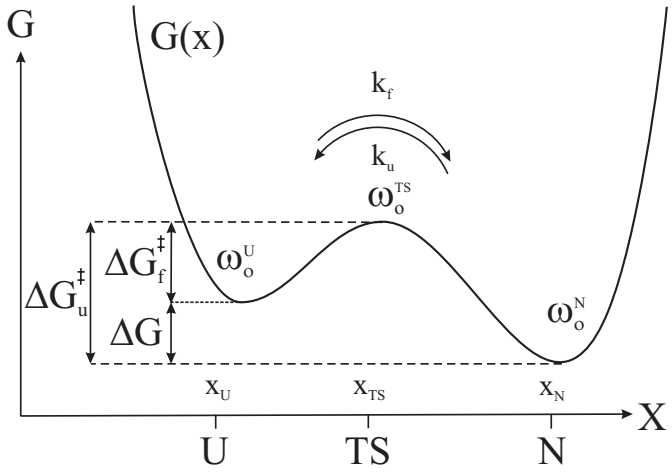

Figure 1: *The free energy landscape of a two state folding reaction. The transition state (TS) on top of a free energy barrier separates native (N) and denatured state (U). The motion of the system in the wells and on top of the barriers is given by the frequencies ω.*

As a random search is apparently not feasible it was suggested that there must be pathways for folding. Although small proteins often show two-state equilibrium denaturation (18), kinetic unfolding (19) and refolding intermediates were detected in many examples (20; 21). This was interpreted as evidence toward obligatory intermediates in many proteins that drive the folding reaction over defined reaction pathways (9; 22). Further attempts to explain folding in biological time include nucleation events followed by further condensation of structure around the formed nucleus (23) or hierarchical models where local interactions guide folding by formation of secondary structure and subsequent stabilisation by long range interactions (24-27).

On the other hand, the existence of kinetic two state folding (16; 28; 29) in small single domain proteins, where neither equilibrium nor kinetic intermediates are observed, was puzzling. The concept of a funnel like energy landscape was introduced (30) based on the analogy of proteins and glasses as suggested by Frauenfelder (31). In this model a small energy bias towards the native state is assumed which reduces the time needed to search for the native state to seconds (32). Intermediates or metastable states are viewed as non-productive kinetic traps.

These concepts are disputed and new results point toward a picture of a complex free energy surface containing defined saddle points and minima which guide the folding process. It has been shown that in apparent kinetic two state folders high energy intermediates can exist, which are states higher in energy than the native and the unfolded state (33; 34). These intermediates are not populated but speed up folding (35).

Because of the existence of major free energy barriers, transition state theory (36) has been applied to analyse folding kinetics. The thermodynamic states (U and N) which are separated by a free energy barrier are in equilibrium with a postulated state, the activated complex or transition state, which is situated on the saddle-point of the barrier separating folding products and educts (see Figure 1). The folding rate constant is related to the barrier height as follows

$$k = k_0 \exp\left(-\Delta G^{0\ddagger} / RT\right) \qquad [5]$$

where $\Delta G^{0\ddagger}$ denotes the free energy barrier for folding and the pre-exponential factor k_0 is the maximal folding rate in absence of a barrier.

Folding transition states are usually structurally well defined and their position along several different reaction coordinates can be determined experimentally, showing that classical concepts can be used to analyse folding kinetics (37; 38). Using perturbations by changing solvent conditions (37; 39), temperature (40), pressure (41) or modifying the structure of the protein by single mutations (42-44) properties of the transition state can be studied relative to the ground states (for further information see (38)). Studying folding kinetics at different denaturant concentrations can yield information on the solvent accessible surface area of the transition state relative to the native and the denatured state (45). It has been found that transition states are usually compact and have native-like topology (46-48).

In the original transition state theory describing reactions in small organic molecules in the gas phase, the pre-exponential factor is related to bond vibration as the elementary reaction of the breakage or formation of a covalent bond (36). This is not an appropriate description for folding reactions because interactions are weak and noncovalent. Alternatively, Kramers theory (49; 50) is more appropriate for describing reactions in solution. Barrier crossing is diffusional and strongly coupled to solvent motion through a friction coefficient γ that is related to viscosity. The friction γ enters the pre-exponential factor together with the frequency of motion ω_o^{U} of the system in the starting well (U for a folding reaction) and on top of the barrier ω_o^{TS} (see Figure 1)

$$k = \frac{\omega_0^{U}\omega^{TS}}{2\pi\gamma} \exp\left(-E / kT\right). \qquad [6]$$

This equation can be expressed in terms of thermodynamic parameters by including entropic contributions from the frequency parameters into a free energy barrier and by applying Stokes law to express the friction parameter as solvent viscosity

$$k = C/\eta \cdot \exp\left(-\Delta G^{0\ddagger}/RT\right) = k_0 \cdot \exp\left(-\Delta G^{0\ddagger}/RT\right). \qquad [7]$$

The reaction rate is inversely coupled to solvent viscosity η and the pre-exponential factor is related to $\omega_0{}^U$ and $\omega_0{}^{TS}$ (for more information, see (51)).
However, in some cases the dependence of the reaction rate on solvent viscosity is more complex and a fractional viscosity dependence is observed

$$k = k_0 \left(\frac{\eta_0}{\eta}\right)^{\beta} \qquad [8]$$

with $\beta < 1$. Such behaviour has been observed for polymer motions in organic solvents (52-54), for intramolecular contact formation in peptides (55) or protein dynamics (56-58). Possible explanations for this phenomenon include preferential hydration effects (59), position dependent (60) or frequency dependent (61; 62) friction coefficients leading to a breakdown of the Stokes law or the existence of steep and narrow barriers (63).
Dynamics of the polypeptide chain in the unfolded protein determine the motion of the protein system on the free energy landscape thereby contributing to the pre-exponential factor of protein folding (see (51) for further discussion).

1.2 The Free Energy Surface of Proteins

The free energy surface is a concept of physics which can be used to describe dynamics in a complex system. It is constructed from the full phase space of a protein, i.e. the multidimensional space where every possible state of the system is represented as one point, which does not only include position and momentum of every atom in the protein structure but also of the surrounding solvent. A reduced description of this extremely complex system is achieved by choosing suitable reaction coordinates and thus projecting the full phase space onto a surface of lower dimensionality. As a result, the concepts of entropy and friction are introduced. Entropy ac-

counts for the reduction of all coupled degrees of freedom to a potential of mean force, while friction concerns the reduced action of the degrees of freedom that are lost in the projection. An effective potential of mean force is generated that governs the reduced dynamics of the reaction coordinate (50). Any conformational transition of a protein can be viewed as motion on this free energy surface.

Proteins are not static systems but have many degrees of freedom also in the folded state. Through conformational transitions structural excited states of higher energy are accessible and are populated according to the Boltzmann distribution. Proteins are immersed in solvent that acts as a heat bath supplying the energy for fluctuations. Such fluctuations have been recognised as being important for protein function (64; 65). Fluctuations in proteins occur on very different time scales, from bond vibrations (femtoseconds) over small scale backbone and side chain motions (picoseconds) (66) and loop dynamics (nanoseconds) (67) to domain motion or partial unfolding (microseconds to milliseconds) as revealed by fluorescence spectroscopy (68), NMR (69; 70), Raman scattering (71) or FTIR (72). From this distribution of time scales a hierarchical organisation of the free energy landscape was inferred (73) which determines protein motions. Because of the ruggedness of the free energy landscape, glasses are often used as a simple model for protein dynamics (31). A model reaction to study protein dynamics is CO rebinding after photodissociation in myoglobin (Mb) (74). The observed kinetics were non-exponential and were interpreted using a power law function

$$y(t) = \left(1 + kt\right)^{-\eta} \qquad [9]$$

with the dimensionless exponent η. Alternatively, a stretched exponential function, or Kohlrausch-William-Watts (KWW) function can be used to describe the data.

$$y(t) = \mathrm{e}^{-\left(k_{KWW} \cdot t\right)^{\beta_{KWW}}} \qquad [10]$$

where β_{KWW} denotes the stretch factor. In most cases it is not possible to discriminate between those two equations.

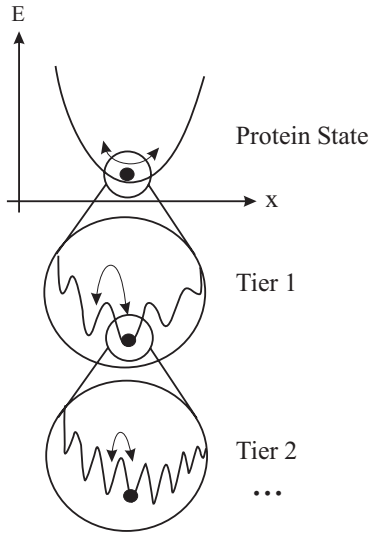

Figure 2: *The energy landscape of a protein state shows a hierarchy of conformational substates. The number of states increases at lower tiers and the motions of the system, shown as a black dot, are governed by barriers of decreasing size. Only two tiers of substates are shown, however there are further tiers below. (Figure adapted from ref. (73))*

There are two possibilities to interpret non-exponential reactions. Either the process is intrinsically non-exponential in time (homogenous non-exponential behaviour) or it is a superposition of a distribution of exponential decays with different rate constants (inhomogeneous non-exponential behaviour). The interplay between homogenous and inhomogeneous relaxation has been experimentally observed and discussed (75; 76). In the inhomogeneous case, the KWW function can be resolved into a distribution of exponential decays as

$$e^{-(k_{KWW}\cdot t)^{\beta_{KWW}}} = \int_0^\infty e^{-\kappa\cdot t}\rho_{KWW}(\kappa)\,d\kappa \qquad [11]$$

with $\rho_{KWW}(\kappa)$ being the distribution function of exponential decays. From this distribution the first moment can be calculated as

$$\langle k\rangle = \beta_{KWW}\, k_{KWW}\,\Gamma\left(\frac{1}{\beta}\right)^{-1} \qquad [12]$$

where Γ is the gamma function. Equation [12] defines the average rate constant $\langle k\rangle$ of the distribution of rate constants. For a reaction which requires the protein or peptide to acquire a certain structure (occupy a certain conformational substate) inhomogeneous non-exponential kinetics are observed if parallel paths from different starting wells lead to the reactive substate and equilibration between the states is slow (see chapter 3.4).

The complex kinetic behaviour of protein dynamics leads to the conclusion that a protein in its native state exists in a number of conformational substates, i.e. local minima on the free energy surface, that are organised in a hierarchical manner in different tiers (31; 77) (see Figure 2). This view is also supported by recent single molecule measurements (78). On the highest tier, structurally different substates can be characterised that are important for function, so called “taxonomic substates”. Within each taxonomic substate, a large number of statistical substates is found which govern smaller scale motions. For proteins, the estimated number of tiers is more than four. In this picture, protein motions are viewed as a random walk on the free energy surface, while the energy is supplied and at the same time dissipated by the solvent.

1.3 The Unfolded state

Protein domains can unfold transiently via spontaneous fluctuations. However, such states are difficult to study because they are unstable and their population is low. Thus, denatured proteins at conditions like low pH, high temperature, pressure or at high concentrations of denaturant are used to obtain information about the unfolded state. These denatured states are however not necessarily equivalent to an unfolded protein in water.

It was shown early that at conditions where the unfolding transition is complete, a defined equilibrium population of unfolded molecules is reached which interconvert rapidly (79; 80). Denatured proteins have long been viewed as random coils (18; 80; 81), applying the theory by Flory (82). The three dimensional conformations of random coils follow Gaussian probability distributions. In addition, no long range interactions exist and the conformation of a chain segment is only influenced by its direct neighbours (the Flory isolated pair hypothesis (82)). Experiments where the dimensions of unfolded proteins were determined and compared to theory supported the concept of the random coil (18). Additionally, in recent experiments it was shown directly by small angle X-ray scattering (SAXS) that unfolded proteins obey random coil statistics (83). The view of the unfolded state as complete random coil however poses some questions (84). Folding from a random coil is very improbable (Levinthal paradox (17)) and energetically very unfavourable because of the high entropy cost. On the other hand it is questionable if denatured states at highly non-native conditions are good models for the unfolded state.

Using various methods including NMR and X-ray scattering techniques, unfolded proteins (85-89) and peptide fragments derived from proteins (90) have been studied in detail. Surprisingly, in many proteins significant amounts of residual structure have been found thus revealing a conformational bias in the unfolded state in contrast to a random coil. The observed residual structure ranges from local secondary structure propensities to persisting hydrophobic clusters or nativelike topology. Additionally, it was observed that CD spectra of homo-polypeptides that adopt poly-proline II conformation (P_{II}) have similarities to CD spectra of unfolded proteins (91; 92). Thus, it was proposed that denatured proteins possess a significant amount of P_{II} structure (93). Recent work on peptides (94-97) strengthened the hypothesis that fluctuating P_{II} conformation might contribute substantially to the unfolded population in proteins.

However, the existence of residual structure in the unfolded state does not necessarily conflict with the global random coil behaviour for unfolded protein. Calculations showed that random coil statistics can be obtained even for locally structured proteins (98). On the other hand, calculations on peptides showed that the Flory isolated pair hypothesis is not valid and significant steric clashes occur between non-neighbouring residues (99). This leads to a restriction of conformational space. Interactions between chain segments, i.e. hydrogen bonds, result in a further compaction of the chain, which can produce an effective collapse of the polypeptide when transferred from a good to a bad solvent (99).

As a conclusion, it is now believed that the unfolded state structure is less heterogeneous than previously thought because of steric restrictions, intrachain interactions and conformational bias. This, in turn, reduces the entropic cost of folding significantly because the relative reduction of conformational space upon folding is smaller than assumed on the basis of a random coil. Structure and dynamics in the unfolded state are directly related to the mechanism and speed of folding (37). Thus the study of the unfolded state using model peptides, protein fragments and unfolded proteins under native conditions is important to understand the mechanism of protein folding.

1.4 Local Structure and Early Events of Folding

Starting from an unfolded ensemble which may contain residual structure, interactions are formed which drive the protein towards the folded state. Long range interactions stabilise secondary structure and global order is established. At the transition state, a native-like topology and a critical amount of structure is established. Subsequently, during the last steps the structure is refined, water is expelled from the interior and the native state is reached.

Loops are required in the nucleation of secondary structure but also to connect structural elements. Contacts between amino acid residues stabilise loop structures through hydrogen bonds, hydrophobic or electrostatic interactions. Loop formation is a prerequisite for the establishment of local and global structure and thus considered as an elementary step of protein folding. Thus, loop closure sets the speed limit for protein folding and determines the rate with which a protein can explore its free energy surface (see chapter 1.2).

To elucidate the thermodynamics and kinetics of secondary structure formation, isolated elements are often studied in model peptides. Kinetics of β-hairpin formation

have been studied by laser temperature-jump experiments (100) and a folding time of 6 μs has been observed. The kinetics have been interpreted with a nucleation mechanism, where an initial turn is elongated to form a hairpin. The α-helix is very well characterised, both experimentally and theoretically (see chapter 1.6). Theoretical models have been developed to understand the energetics of helix formation (101; 102) and to predict the helix content for a given sequence. Like in the case of the hairpin the formation of helical structures is initiated by a contact of peptide units close in sequence. Using relaxation experiments, time scales from 10ns to 1μs were estimated for helix formation (103-106). However, the mechanism of helix formation and the exact time scales are still disputed. In the following chapters, loop closure and α-helix formation are discussed as the elementary steps of protein folding.

1.5 Loop Formation and Chain Dynamics

Motions of an unfolded polypeptide chain eventually lead to loop closure and nucleation of local structure. To understand the principles of chain dynamics, it is convenient to use simplified models of the unfolded state based on the properties of polypeptide chains. Some of these models will be discussed in short terms (for more details see (51)).

1.5.1 Chain Models

The simplest description of an unstructured polymer is the freely jointed chain. The chain is described as a random walk of n steps in three dimensional space where all directions are equally probable and all steps are of equal length l (107). The distribution of end-to-end distances is Gaussian, if the chain is sufficiently long and unperturbed by long-range self interactions or by external constraints. The mean square end-to-end distance $\langle r^2 \rangle$ for a freely jointed chain can be calculated as

$$\langle r^2 \rangle = nl^2 \qquad [13]$$

where the angle brackets denote the statistical mechanical average. An alternative and even more abstract model is the Gaussian chain where the segment length follows a Gaussian distribution, while in a freely jointed chain the segment size is fixed. Gaussian chain segments can be thought of Gaussian chains themselves, thus concepts as contour length or number of segments are meaningless.

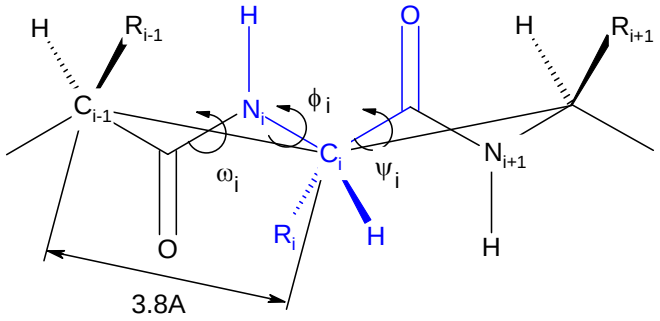

Figure 3: *The chemical structure of the peptide backbone. The side chains are represented by R_i. One peptide unit is shown in blue. The dotted lines denote virtual bonds that connect the C_α centers.*

In real chains however end-to-end distances are generally longer compared to the prediction for freely jointed chains because of fixed bond angles, steric hindrances or electrostatics. Thus, the characteristic ratio C_n was introduced to account for these effects (82)

$$C_n = \frac{\langle r^2 \rangle}{nl^2}. \qquad [14]$$

The individual segments of polypeptide chains are rather complex (see Figure 3) and possess several properties that are special compared to other polymers. (i) They are composed of chemically different subunits, the amino acids, (ii) they are directional because of different end groups (an amine at the N-terminus, a carboxylic acid at the C-terminus), (iii) an asymmetric C atom is present at the -C_αHR- positions of α-amino acids (iv) the peptide bond connecting different subunits is planar and most of the time in trans ($\omega = 180^o$) and (v) the amide bonds have a large dipole moment of 3.7 D resulting in dipole-dipole interactions which can affect chain dimensions significantly (108).

Because of the planarity of the peptide bond and the low probability of cis-peptide bonds the conformation of a polypeptide backbone is given by specifying the dihedral angles ϕ and ψ of all residues. Between two neighbouring residues different settings of ϕ and ψ lead to steric clashes of side chains and backbone atoms. Many of these steric clashes can be avoided by changing bond angles at the cost of energy. A map of conformational energy for a pair of amino acids dependent on the torsional angles ϕ and ψ is the Ramachandran map (109). It was suggested by Flory (82) in his

isolated pair hypothesis that interactions between non-neighbouring residues can be neglected and that the short range interactions are well covered in Ramachandran diagrams. This view has recently been challenged by calculations (99) where it has been shown that for peptides longer than seven residues non-local steric clashes can occur with increasing probability thus leading to generally more extended chains.

However, calculations based on the Ramachandran maps give good estimates for the dimensions of unstructured chains and peptides. For polypeptides, the real bonds are replaced by a virtual bond of length of 3.8 Å connecting the C_α atoms (see Figure 3). Using averaged transformation matrices, characteristic ratios for polypeptides of various composition can be calculated (ref. (82), equation I-43). These matrices are specific for alanine, proline and glycine and contain the steric information from Ramachandran type maps including dipole dipole interactions (108; 110; 111). C_n is a function of n and increases to an asymptotic value of 2.16 for *poly-Glycine*, 9.27 for *poly-Alanine* and $Cn \approx 100$ for *poly-Proline* chains. From the obtained C_n values average end-to-end distances can be calculated for unperturbed polypeptides. Experiments were performed in various solvents (112) and characteristic ratios around 8.8-9.0 were found, in good agreement with theory.

A real chain molecule is composed of atoms that occupy space and cannot overlap. This leads to excluded volume (107) resulting in a self avoiding chain that shows non ideal behaviour and different scaling laws.

$$\sqrt{\langle r^2 \rangle} = l \cdot n^{\nu}. \qquad [15]$$

The scaling exponent for the end-to-end distance changes from $\nu = 0.5$ for a freely jointed chain to $\nu = 3/5$ based on relatively simple calculations by Flory (113) and refined to values of $\nu = 0.588$ by renormalisation group theory (114). In recent experiments on unfolded proteins, scaling exponents of $\nu = 0.598 \pm 0.028$ have been found (89), which shows that the global properties of unfolded proteins are compatible with an excluded volume random coil model (compare to chapter 1.3). For such an excluded volume chain, the end-to-end distance distribution can be approximated by a skewed Gaussian function (115)

$$p(r) = 4\pi r^2 e^{-((r-r0)/\sigma)^2}. \qquad [16]$$

Additionally, the solvent plays a critical role. In principle the calculations assume θ conditions, where peptide self-interactions are exactly balanced with peptide-solvent interactions. If peptide self-interactions (e.g. hydrogen bonds) are stronger, as in the case for peptides dissolved in water, the solvent is considered "bad". On the other hand, if peptide-solvent interactions are stronger, the solvent is considered "good", e.g. for solutions containing denaturants. The former case leads to a shrinking, the latter to a swelling of the chain. This has recently been observed by fluorescence resonance energy transfer (FRET) in peptides (116). One reason why experimental results of peptides in aqueous solution are consistent with calculations that imply θ conditions is that excluded volume effects partially compensate for the effect of a bad solvent.

1.5.2 Dynamics of Random Coils

A random coil chain immersed in solvent is a highly dynamic system that is subjected to a multitude of forces exerted from the solvent molecules. To obtain an idea how a chain molecule moves under such conditions several theoretical approaches have been developed. In this chapter a selection of concepts is presented.

The motion of a polymer system in solution on a complex free energy surface (see chapter 1.2) is diffusional in character. Solvent molecules transfer momentum upon collision or by dipolar interactions and thus supply the energy for chain movement. At the same time energy is dissipated through interactions of solvent with the polymer. If solvent rearrangement is fast compared to polymer motion (the Markovian approximation) then the system can be described by a stochastic differential equation, the Langevin equation (117)

$$M\ddot{x} = -\partial U(x)/\partial x - \gamma\dot{x} + F_{fluc}(t) \qquad [17]$$

where x is the reaction coordinate, a stochastic variable, M is the particle mass, $U(x)$ denotes the energy landscape, γ is a friction coefficient (50) that provides the coupling of system to solvent and $F_{fluc}(t)$ is the random force which models the thermal motion of the environment which is modelled by *Gaussian white noise* of zero mean and a δ correlation function

$$\left\langle F_{fluc}(t)\right\rangle = 0$$
$$\left\langle F_{fluc}(t)\cdot F_{fluc}(t')\right\rangle = 2k_B T\gamma\delta(t-t'). \qquad [18]$$

By classical polymer theory the dynamical behaviour of Gaussian chains under the influence of a random force can be described analytically. Two models based on Gaussian chains are mentioned in the following: the Rouse model (118) and the Zimm model (119) for a polymer chain in dilute solution.

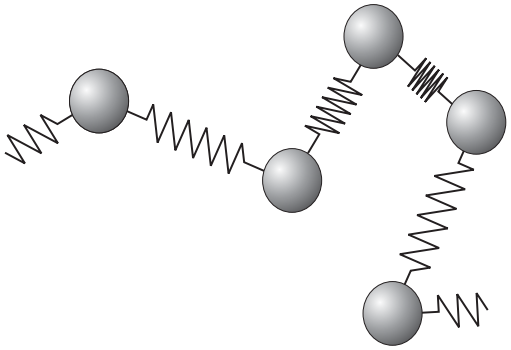

Figure 4: *Schematic depiction of a Rouse Chain. Spring connected beads forming a Gaussian Chain move in a stochastic force field. The bond length is Gaussian distributed with mean square length b^2. No excluded volume effects are included.*

In the Rouse chain the polymer is modelled as a set of N beads with the coordinates ($\mathbf{R}_1$, $\mathbf{R}_2$, $\mathbf{R}_3$, … $\mathbf{R}_N$) connected by bonds modelled as harmonic springs with mean square length b^2 and spring constant k, leading to a mean square end-to-end distance Nb^2. The springs represent Gaussian chains so that the whole chain exhibits Gaussian behaviour. The Langevin equation [17] is used to describe the Brownian motion of the connected beads. In a system of high viscosity and high damping the term containing the acceleration term is dropped in equation [17]. This leads to a set of uncoupled linear equations for $\mathbf{R}_n$. For internal beads (n = 2,3,…,N-1) if the frictional and activating force from the solvent $F_{fluc}(t)$ is modelled to act on all the beads independently

$$\gamma\frac{d\mathbf{R}_n}{dt} = -k(2\mathbf{R}_n - \mathbf{R}_{n+1} - \mathbf{R}_{n-1}) + F_{fluc}(t) \qquad [19]$$

and for the end beads (n=1, N)

$$\gamma\frac{d\mathbf{R}_1}{dt} = -k(\mathbf{R}_1 - \mathbf{R}_2) + F_{fluc}(t)$$
$$\gamma\frac{d\mathbf{R}_N}{dt} = -k(\mathbf{R}_N - \mathbf{R}_{N-1}) + F_{fluc}(t). \qquad [20]$$

These equations can be used to numerically calculate chain behaviour or solutions can be extracted by transformation into chain-internal normal coordinates. While the solution in normal coordinates yields equations for *n* modes of motion that correspond to internal dynamics comparable with vibrational modes of a string, numerical calculations yield chain bead position at every time and the chain behaviour can be evaluated directly. However, a moving particle in a liquid creates a flow field that influences other particles in its vicinity. Neglecting these interactions leads to incorrect scaling laws, as seen from comparing results for Rouse chains to experiment (120). In first approximation, hydrodynamic interactions can be modelled by introducing a diffusion tensor $\mathbf{D}_{nm}$ that replaces the simple diffusion coefficient for the single beads. The Oseen Tensor is commonly used to describe the hydrodynamic interaction

$$\mathbf{D}_{nm} = \frac{1}{8\pi\eta|\mathbf{r}_{nm}|}\left[\frac{\mathbf{r}_{nm}\cdot\mathbf{r}_{nm}}{|\mathbf{r}_{nm}|^2} + \mathbf{I}\right] \qquad [21]$$

where $\mathbf{r_{nm}} = \mathbf{R}_n - \mathbf{R}_m$ and $\mathbf{I}$ is the unity matrix. Upon introduction into the Langevin equation the equation of motion becomes

$$\frac{\partial}{\partial t}\mathbf{R}_n = \sum_m \mathbf{D}_{nm}\cdot\left(k\frac{\partial^2}{\partial m^2}\mathbf{R}_m + F_{fluc}(t)\right). \qquad [22]$$

The equations are however no longer linear of $\mathbf{R}_n$ and can thus only be solved numerically. However, solutions in normal coordinates can be obtained if approximations to the diffusion tensor are used (121). This is known as the Zimm model (119). Chain properties obtained from calculations using the Zimm model produce results that are in better agreement with experiment as the Rouse model. The theory was extended to include polymers of finite length and significant degree of stiffness (122), the optimised Rouse-Zimm (ORZ) approach. This allowed calculating the relaxation behaviour of stiff rings, rods or wormlike chains, which is drastically different from flexible chains and included properties of the freely rotating chain to overcome the use of the Gaussian chain as a basic model.

1.5.3 Theories describing Intramolecular Reactions in Polymers

Based on these models for chain dynamics intramolecular reactions can be analysed and related to experimental results. As such loop formation reactions are not only important for protein folding but occur as side reactions in polymerisation reactions several theoretical approaches were developed to deduct scaling laws and cyclisation probabilities depending on the properties of the polymer.

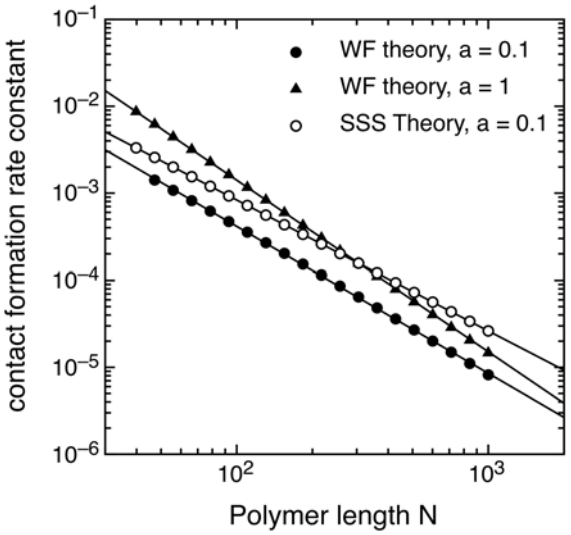

Figure 5: *Contact formation in a Rouse Chain, calculated using either WF or SSS theory in the Smoluchovski limit (diffusion control). Parameters: N, b = 1, D_0 = 1 and a = 0.1 or 1, with N being the number of beads, b the segment length, D_0 the diffusion coefficient of the beads and a the reactive radius. k_{WF} scales with an exponent of 1.69 for a = 0.1 and 1.97 for a = 1, k_{SSS} scales with an exponent of 1.5. The calculations were performed following ref. (127).*

Early studies of Jacobsen and Stockmayer considered the cyclisation probability in polymers and obtained a scaling law of $p \sim N^{-1.5}$ (123). Considering dynamics, Wilemski and Fixman (WF) developed a general theory of diffusion controlled reactions (DCR) that was extended to account for intramolecular reactions in polymers (124-126). An exponential decay is assumed and the reaction rate constant of contact formation is evaluated by solving the Smoluchovski diffusion equation for a Rouse chain. The reaction is introduced by a sink function that removes polymers from the system which have the reactive groups closer than the reactive boundary. The reactive boundary denotes the distance over which the reaction takes place (for an overview of the method see (127)). It is shown that the loop formation rate constant is related to the slowest relaxation time of the polymer. The theory is very general, thus not only the sink functions but also the polymer model that determines the underlying dynamics can be extended from a Rouse chain to a more realistic model. Perico (128-130) introduced the ORZ approach into the WF theory of diffusion controlled reactions (ORZ-DCR). This allowed studying contact formation dynamics in a chain of variable stiffness with different position of the reactive groups.

A different approach was followed by Szabo, Schulten and Schulten (SSS) to evaluate contact formation reactions in polymers (131). They solved the diffusion equation for the time dependent probability distribution of end-to-end distances of a chain. The chain properties are included as the initial end-to-end distribution and by a choice of a suitable diffusion coefficient, but chain dynamics based on a chain model are not included. It is shown that the process can be approximated as single-exponential for small reaction radii thus contact formation rate constants can be obtained.

For Rouse chains, scaling laws can be deduced in both cases. The dependence of the end-to-end contact formation rate constant on chain length is $k = k_0 \cdot N^{-\nu}$ with an exponent of $\nu = 1.5$ for the SSS theory while in the WF case the exponent depends on the chosen capture radius (see

Figure 5) adopting values of 1.7 for small capture radii to 2 for capture radii in the range of a bond length. Calculations of Wilemski and Fixman using a chain model that includes hydrodynamic interactions (see eq. [22]) give faster cyclisation rate constants and a scaling law of $k_c \sim N^{-1.5}$ is again received (132; 133).

1.5.4 Experimental Results on Loop Formation

To compare the scaling laws to experimental results several experimental systems have been developed. Early studies involved fluorescence quenching (134) in polyethylene oxide and pyrene excimer formation (135) in polystyrene chains (for a review see (136)). In the latter system, loop formation time constants in the microsecond timescale and scaling coefficients of $k_c \sim N^{-1.6}$ were obtained, in good agreement with theoretical values. However, the polymerisation procedure produced distribution of polymer lengths, thus the measured rate constants are averages over the ensemble of different chains.

Another approach was the use of time resolved Förster resonance energy transfer between two probes attached to peptides to determine intrachain diffusion constants (137; 138) in glycerol solutions. The data could be interpreted assuming a skewed Gaussian end-to-end distribution function for the chain (see equation [16]) and yielded loop closure time constants in the nanosecond regime.

In a work on GdmCl - unfolded cytochrome c (139; 140) heme rebinding to a methionine residue after photodissociation of CO was measured as a model for contact

formation between regions of the unfolded protein around 50-60 amino acids apart in sequence. From these measurements the rates constants were extrapolated to short peptides using SSS theory (see chapter 1.5.3) and a maximal rate constant of $(1\ \mu s)^{-1}$ for contact formation and thus for protein folding was postulated. However, this method suffered from the reaction controlled mechanism that slowed down the observable rate and thus made a quantitative evaluation impossible.

More recently, fast photochemical methods were developed such as triplet-triplet energy transfer (TTET) (141), triplet quenching (142) or fluorescence quenching (143) in short peptides. The application of diffusion controlled TTET allows direct and model free observation of loop formation processes in peptides (67; 141) thus yielding information on the chain motions underlying protein folding and dynamics. In *poly-(Gly-Ser)* and *poly-Ser* chains time constants for loop formation from 10 to 100 nanoseconds were measured. For sufficiently long chains scaling laws with an exponent of $\nu = 1.72 \pm 0.08$ for the *poly-(Gly-Ser)* and $\nu = 2.1 \pm 0.3$ for the *poly-Ser* chains respectively were observed. Thus a pre-exponential factor for protein folding on the order of $k_0 = 10^8\ s^{-1}$ was proposed (see equation [7]). These results are part of current work and are discussed in more detail in ref. (51; 67).

1.6 Formation of α-Helices

Around 30% of all amino acid residues from protein structures are found in α-helices making the α-helix the most abundant secondary structure (144) and one of the most fundamental structural motives in proteins. In protein folding, the formation of local secondary structure is an elementary step. In many proteins helix formation has been shown to occur independently and before establishment of tertiary structure (25; 26). Since the helix propensity is strongly dependent on local sequence helices can be formed in the unfolded state of proteins (145; 146). Thus, knowledge of the thermodynamics and kinetics of α-helix formation is needed for a deeper understanding of protein folding.

The α-helix is stabilised by hydrogen bonds between the carbonyl group of the ith and the amide hydrogen of the $(i + 4)$th amino acid residue. Consequently the formation of the first helical hydrogen bond requires the fixing of the φ and ψ angles of three intervening residues (or the spatial fixing of four consecutive peptide units).

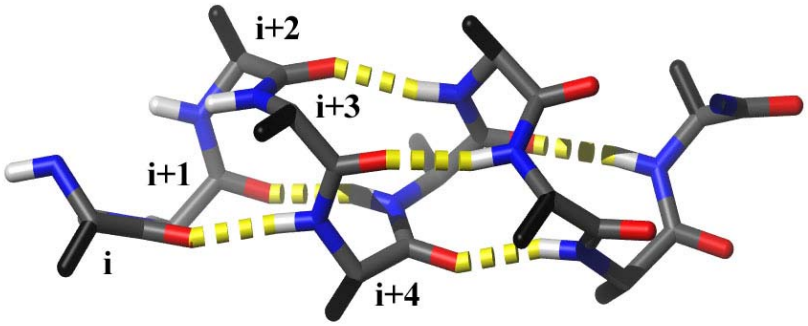

***Figure 6**: The hydrogen bond pattern of the α-helix. The hydrogen bonds from the CO of residue i to NH of residue i+4 are shown in yellow.*

In helix-coil theory, two processes can be distinguished in helix formation. To form the first hydrogen bond the dihedral angles of three consecutive amino acid residues have to be fixed. The formation of at least one first turn is called the nucleation step. Then, starting from this nucleation site, further residues are added to the ends of the growing helix. The elongation steps require the fixing of only two angles per added residue.

$$\ldots ccccc \ldots \underset{}{\overset{\sigma s}{\rightleftharpoons}} \ldots cchcc \ldots \quad \textit{Nucleation}$$

$$\ldots cchcc \ldots \underset{}{\overset{s}{\rightleftharpoons}} \ldots chhcc \ldots \quad \textit{Elongation}$$

An equilibrium constant *s*, which depends on the nature of the residue that is added to the helix, is assigned to the elongation steps. The formation of a hydrogen bond in elongation involves a change in free energy $\Delta G^0_s = -RT \ln s$ which is composed of the free energy of hydrogen-bond formation, of the negative change in entropy for fixing the main-chain conformation and of the change in free energy of the side chains. Nucleation occurs at a high cost of entropy because fixing three residues in helical geometry is only partially compensated by the enthalpy of the formed hydrogen bond. Thus, nucleation has a low probability and a parameter $\sigma < 1$ is introduced to account for entropy barrier of nucleation.

The nucleation parameter has a huge impact on the cooperativity of the transition. The smaller the probability of nucleation the sharper is the transition. Because nucleation of helices is an unlikely event, it is usually assumed that a short peptide contains only one helical stretch. The so called “single sequence approximation” reduces the conformational space significantly.

The helical content of peptides can be estimated using statistical mechanics. By counting peptide hydrogen-bonds (101) in Zimm-Bragg (ZB) or residue conformations (102) in Lifson-Roig (LR) theory the partition function of the peptide can be formulated. A statistical weight is given to any conformation of the molecule and from the partition function their relative probability can be determined.

Since helices lack a hydrophobic core it was assumed that stable helices can only be found in proteins or in very long peptides because hydrogen bonds are too weak to stabilise the structure. Nevertheless, short alanine based helices have been found to form stable helices in water (147-149). This allowed to measure helix propagation constants *s* in host guest systems which can now be included into the calculation of helix content based on ZB or LR theory. Additionally, further helix stabilisation effects were identified like side chain to backbone hydrogen bonds, (i, i+3) and (i, i+4) salt bridges and aromatic interactions (147-149). AGADIR, an helix prediction program that was developed by Muñoz and Serrano (150-152) includes in addition to the 20 single residue helix propensities the pairwise side-chain interactions at i, i+3 and i, i+4 positions, values for peptide hydrogen bonds and values for helix propensities of all amino acids at N and C-cap positions (the N- and C-terminal ends of an helix). This allows reasonable prediction of helical contents of small peptides.

Based on equilibrium models, a theory of helix formation kinetics was developed by Schwarz (153) and further refined by Poland and Scheraga (154). Rate constants are assigned to the elementary steps of helix formation which are the nucleation step and the transformation of a single unit in the peptide chain from coil to helix state c → h or *vice versa*. For an helix with *N* residues a coupled system of 2^N differential equations is obtained with 2^N*-1* observable rate constants. In relaxation experiments, where the helical content of a peptide is perturbed by a fast change in conditions, a mean relaxation time can be assumed under certain conditions which contains contributions from the nucleation and elongation reactions.

The helix-coil transition is not a two state transition but a whole ensemble of helices of different lengths exists in equilibrium. The ends of an α-helix are significantly less stable than the center. This phenomenon is called end-fraying and follows from helix theory (101; 102) and has been experimentally observed by amide hydrogen exchange (155), by alanine to glycine substitutions (156), in NMR studies (157-161) or by electron spin resonance (ESR) (162; 163). Thus, in most cases, a peptide is never

fully helical but is in a very dynamic equilibrium, constantly folding and unfolding from the ends.

In early experiments, helix-coil transition kinetics were measured in long polypeptide chains (like poly(γ-benzyl L-glutamate)) in organic solvents using dielectric relaxation (103) and ultrasonic absorption techniques (104). Relaxation time constants in the 100's of nanoseconds time range have been obtained.

With the development of nanosecond temperature jump techniques helix-coil relaxation in alanine based peptides were measured using infrared (105; 106; 164) or UV Raman spectroscopy (165). Relaxation time constants of 10-600 ns were observed. However, due to the fact that helix-coil transition is not a two state reaction it is difficult to extract microscopic folding rate constants from relaxation data and to discriminate elongation from nucleation processes. A picture of the dynamic heterogeneity in helices comes from site specific observation of relaxation rates in C_{13} labelled peptides (166-168). The position dependent dynamics in helical peptides are the topic of current work and are discussed in more detail in chapter 3.5.

1.7 Triplet-Triplet Energy Transfer

The method of choice to monitor contact formation processes in polypeptides is triplet-triplet energy transfer. An electronically excited donor molecule in the triplet state produces upon contact an excited acceptor molecule while relaxing to the ground state.

$$D^*(T_1) + A(S_0) \xrightarrow{k_{TTET}} D(S_0) + A^*(T_1) \qquad [23]$$

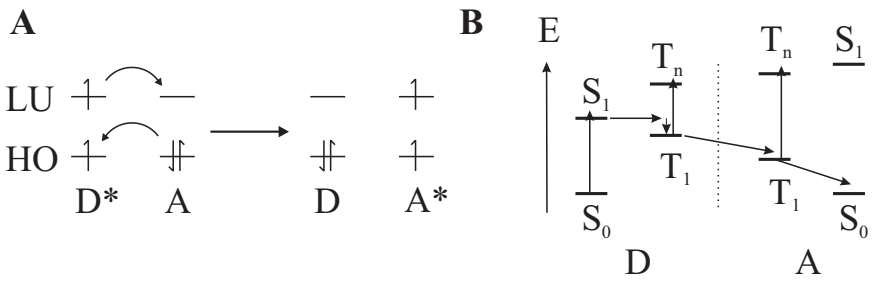

Figure 7: A) *Schematic description of triplet-triplet energy transfer by an exchange mechanism. Two electrons are simultaneously exchanged by HO-HO and LU-LU interactions requiring orbital overlap. Figure adapted from (169).* ***B)*** *Jablonski diagram for TTET from the donor D to acceptor A involving excitation of D followed by ISC to the triplet state T_1 that can be detected by a triplet absorption band. The triplet is transferred upon orbital overlap to the acceptor A that relaxes back to the ground state.*

Transfer over a dipole-dipole mechanism is “forbidden”, however it is “spin-allowed” in an exchange mechanism (169), where two electrons are simultaneously exchanged to transfer the triplet from the donor to the acceptor.

The process occurs by overlap of the highest occupied molecular orbital (HO) of the excited donor D* with the HO of the acceptor and an overlap of the lowest unoccupied molecular orbital (LU) of the donor with the LU of the acceptor. If those overlaps are favourable then an electron jumps from the LU of the donor to the LU of the acceptor while at the same time an electron from the HO of the acceptor jumps to the HO of the donor, thus producing an excited acceptor A* (see Figure 7). A formulation for the rate constant of such a process was worked out by Dexter (170) who proposed

$$k_{ET}(exchange) = C \cdot e^{-2R_{DA}/L} \qquad [24]$$

where C denotes a factor dependent on photophysical properties of the donor and acceptor molecules and R_{DA} is the donor-acceptor separation relative to their VdW-radii L. The exponential dependence of the exchange rate on donor-acceptor distance originates from the decay of the orbitals and leads to a vanishing rate at around one to two molecular diameters (5-10Å), in contrast to the through space mechanism of dipole - dipole energy transfer. Triplets are usually long lived excited states because the relaxation to the ground state is spin-forbidden. This allows measurements over a large time window. If the triplet energy of the acceptor lies several kJ below the triplet energy of the donor TTET is very efficient and no back transfer is observed. Donor-acceptor pairs which can be used for TTET have to meet several requirements.

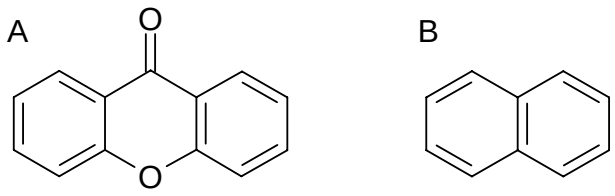

Figure 8: *Labels used for TTET. A) Xanthone is used as triplet donor. It undergoes very fast intersystem crossing (~2ps, see ref. (171)) with high quantum yield (~99%) to a long lived triplet state (τ ~30μs in water) with energy of 310 kJ/mol (172) . Xanthone has a strong triplet absorbance band at 590nm B) Naphthalene is used as a triplet acceptor moiety with a triplet energy of 253 kJ/mol (172) and a triplet absorbance band at 420nm.*

The donor is chosen to have very fast intersystem crossing with high quantum yield, a long triplet lifetime and high triplet energy. The acceptor on the other hand is required to have lower triplet energy than the donor. A system that meets these requirements is xanthone as the triplet donor and naphthalene as the triplet acceptor. In peptides, TTET serves to measure contact formation processes between the labels. The system allows direct observation of the loop closure rate constant k_c because the excitation and transfer process are several orders of magnitude faster than contact formation (k_{ex}, $k_{TTET} >> k_c$) and because the cyclic state is not stable ($k_c << k_{-c}$). Thus the directly observable rate constant is k_c. The exact time scales involved in excitation and transfer of xanthone are the topic of current work and discussed in more details in references (51; 171; 173).

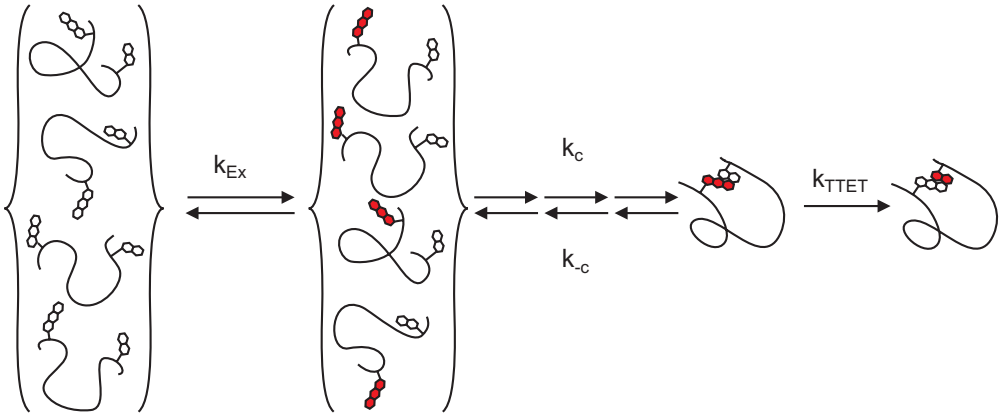

Figure 9: *Simplified scheme of triplet-triplet transfer experiments in peptides. The xanthone moiety is excited to the triplet state with a rate constant k_{ex}, ($1/k_{ex}$, ~ 2ps). Chain diffusion leads to contact with a rate constant k_c that depends on chain properties. Subsequently, the triplet is transferred to the acceptor moiety naphthalene with a rate constant k_{TTET} ($1/k_{TTET}$~ 1ps). If kex >> k_c and k_{-c} >> k_c the observed rate constant of the decay of xanthone triplets corresponds to*

$$k_{obs} = \frac{k_c k_{TTET}}{k_{-c} + k_{TTET}}$$

If the transfer is diffusion controlled ($k_{TTET} >> k_{-c}$) transfer occurs at every encounter of the two labels and therefore $k_{obs} = k_c$. The time constants are taken from ref. (171) .

2. Aims of Research

The Kinetics of Loop Formation of Unstructured Polypeptide Chains

The initial steps of protein folding involve formation of local interactions and secondary structure elements. The fundamental process of contact formation between two parts on a polypeptide chain determines how fast interactions can be formed. We wanted to use triplet-triplet energy transfer to study the kinetics of loop formation in model peptides. In earlier experiments rate constants for end-to-end loop formation have been determined in poly-*Ser* and poly-*(Gly-Ser)* peptides of different length. For both homopolymers the rate constants were found to asymptotically approach a limiting value for short chains and scale with a power law for longer chains. To gain information on the effect of the amino acid sequence on local chain dynamics we wanted to measure loop formation kinetics in short host-guest model peptides containing different amino acids at the guest position.

In contrast to our model peptides, protein chains have a higher complexity as they consist of 20 different amino acids. To compare results from model peptides to chain dynamics in biological sequences we wanted to study contact formation reactions in fragments derived from proteins.

During protein folding, most interactions are established between interior residues. Up to date, only end-to-end contact formation reactions have been studied experimentally. Thus, we wanted to use TTET to measure loop formation involving interior positions in a polypeptide chain. We therefore extended one or both ends of a loop to systematically probe the effect of additional tails on the kinetics of loop formation. These results can be used to estimate loop closure kinetics between two points at any position of the protein chain.

Testing for Sub-Nanosecond Loop Formation Reactions

Exponential kinetics on the nanosecond time scale have been observed for loop formation in unstructured polypeptides. However, faster reactions on the sub-nanosecond time scale could not be ruled out. To test whether TTET can be used to monitor ultrafast processes we wanted to investigate the limits set by the photochemistry of the TTET process. Our aim was to use femtosecond-laserflash spectroscopy to determine the time scales of triplet formation in xanthone and to measure the rate constant of triplet transfer to naphthalene.

By combining femtosecond and nanosecond spectroscopy we wanted to study loop formation from picoseconds to microseconds to see if additional loop formation reactions occur on a sub-nanosecond time scale which should yield insight into the conformational distribution of polypeptides.

The Properties of the Free Energy Surface of Peptide Dynamics

The formation of a loop requires the unstructured peptide to explore its free energy surface, driven by the thermal motions of the solvent molecules. At room temperature, transitions between local minima (conformational substates) are fast compared to the loop formation reaction. This results in exponential kinetics for loop closure as predicted by the theory of Szabo, Schulten and Schulten (131). We wanted to test for complex kinetics under conditions where the interconversion of conformations is slow. This can be achieved by decreasing the temperature or increasing the friction. We wanted to characterise the kinetics of loop formation under these conditions, which should give information about the properties of the free energy surface of peptide dynamics.

The Dynamics of α-Helix Formation

α-helices are the most abundant secondary structure elements. During folding they form fast and often before establishment of long range contacts. The coil to helix transition is complex, non two-state and its kinetics are not well understood. By introducing TTET labels at different position into α-helical peptides we wanted to gain information about local and global helix stability and dynamics.

To directly observe α-helix nucleation folding has to start from the ensemble of unfolded states. We tried to achieve this by cyclisation of a short peptide using a photocleavable linker. The peptide should form an α-helix in the linear form but it should not adopt structure in the crosslinked state. Upon photorelease by laser irradiation, the peptides are expected to rapidly relax to the ensemble of unfolded states. Subsequently, they adopt an α-helical conformation. This reaction can be monitored by spectroscopic techniques. We wanted to develop a strategy to synthesise such caged peptides which should allow us to determine rate constants α-helix nucleation.

3. Summary of Published Work and Manuscripts Ready for Submission

3.1 Dynamics of Unfolded Polypeptide Chains studied by triplet-triplet energy transfer

To measure contact formation dynamics in peptides and proteins, our group has applied triplet-triplet energy transfer from xanthone to naphthalene. This two electron exchange process requires van der Waals contact between the triplet donor and triplet acceptor labels and exhibits diffusion controlled kinetics with a bimolecular rate constant of $4 \cdot 10^9\ M^{-1}s^{-1}$. Single exponential kinetics with time constants in the nanosecond time regime were observed. Using polypeptide chains of different length and amino acid sequence allowed to derive scaling laws. The rate constants for loop closure in flexible *(Gly-Ser)$_n$* (n = 1 to 28) copolymers scaled with $k_c \sim N^{-1.7\pm0.1}$ for long chains ($N > 20$, N denotes the number of amino acids). This is in agreement with the value expected from polymer theory for an excluded volume chain (see chapter 1.5.3). For shorter chains, the rate constants asymptotically approached a limiting value of $1.8(\pm0.2)\cdot10^8\ s^{-1}$. In stiffer poly-*Ser* chains, similar behaviour has been found with a limiting value of $8.7(\pm0.8)\cdot10^7\ s^{-1}$ and a scaling law of $k_c \sim N^{-2.1\pm0.3}$ for longer chains. The different behaviour for short and long chains results from a different mechanism for loop formation within these regimes. In long chains the dynamics are dominated by diffusion, while over short distances the chain properties are strongly influenced by chain stiffness and the dynamics are dominated by barriers.

To study the influence of the polypeptide-sequence, contact formation rate constants were measured in a series of host-guest peptides. In peptides of the canonical sequence *Xan-Ser-Xaa-Ser-NalA-Ser-Gly-OH* (*Xan*: xanthone, *NalA*: naphthylalanine) the guest amino acids *Xaa = Ser, Gly, Pro, Ala, Ile, Glu, Arg, His* were included and contact formation kinetics were measured. The influence of different amino acids on local contact formation was shown to be small. The rate constants differed by a factor of six from the most flexible (*Gly,* $k_c = 1.2(\pm0.1)\cdot10^8\ s^{-1}$) to the most rigid amino acid (*trans-Pro,* $k_c = 2.0(\pm0.3)\cdot10^7\ s^{-1}$). The other amino acids could be divided into two groups. Amino acids containing a C_β-atom led to contact formation rate constants from $4.4 - 5.4\cdot10^7\ s^{-1}$ (*Glu, Arg, Ile*), while peptides containing the shorter amino acids *Ala* and *Ser* gave faster rate constants of $8.0(\pm0.7)\cdot10^7 s^{-1}$ and

$6.7(\pm0.7)\cdot10^7\ s^{-1}$. In the *Pro* containing peptide, however, double exponential kinetics were monitored. An additional fast phase with a rate constant of $2.5(\pm0.5)\cdot10^8\ s^{-1}$ corresponds to the molecules with a *cis-Pro* peptide bond. This leads to a kink in the peptide structure and thus to a closer end-to-end distance (174) resulting in the fastest loop formation rate constants of all peptides. Loop formation thus sets a speed limit for protein folding at around 10-20 ns.

The rate constants for intrachain contact formation measured in poly-(*Gly-Ser*) and poly-*Ser* were compared to the dynamics of natural loops. There are however amino acids that interfere with TTET by quenching xanthone triplets. To test for such reactions, the bimolecular quenching rate constant of several amino acids was measured under pseudo-first-order conditions. Near diffusion controlled quenching reactions were observed for *Trp*, *Tyr* and *Met*. *His* was an effective quencher when deprotonated at high pH. All the other amino acids or functional groups were either only very weakly quenching (*His^+, Cys*, N-terminus) or not interfering at all (*Ala, Arg, Asn, Asp, Gly, Lys, Ser, Phe*). Quenching xanthone triplets with *Trp* and *Tyr* produces complex kinetics due to radical formation, making them not suitable for the use in quenching experiments. These results show that contact formation experiments are feasible in proteins, however, only if the sequences are free of *Trp, Tyr* and *Met*.

To measure intrachain contact formation kinetics in a natural occurring protein loop, we used an unstructured 18-residue fragment from carp muscle β-parvalbumin (residues 85-102). Single exponential kinetics with a rate constant of $1.9(\pm0.1)\cdot10^7 s^{-1}$ were measured, which is comparable to the expected value from results on poly-*Ser* chains.

This work is published in the following articles:

Krieger, F., Fierz, B., Bieri, O., Drewello, M. & Kiefhaber, T. *Dynamics of Unfolded Polypeptide Chains as a Model for the Earliest Steps in Protein Folding*. J. Mol. Biol., 2003, **332**: p. 265-274.

Krieger, F., Fierz, B., Axthelm, F., Joder, K., Meyer, D. & Kiefhaber, T., *Intrachain diffusion in a protein loop fragment from carp parvalbumin*. Chem. Phys., 2004, **307**: p. 209-215.

3.2 End-to-End vs. Interior Loop Formation

In all experiments described up to now end-to-end contact formation (type I-loop) has been studied. However, in proteins most interactions take place in the interior of the polypeptide chain, thus end-to-interior (type II-loop) and interior-to-interior (type III-loop) contact formation reactions are more common in folding.

To study the influence of an additional tail on the contact formation kinetics of a loop segment (type II), TTET experiments were performed in several series of peptides containing C-terminal extensions consisting of either *(Ser-Gly)$_n$* or *(Thr-Gly-Gln-Ala)$_n$-Gln-Ala-Ser-Gly* sequences. In all peptides single exponential kinetics for contact formation were observed, with k_c decreasing with increasing length of the extension. The logarithms of the observed rate constants correlate with the average end-to-end distance of the complete chain $\sqrt{\langle r^2 \rangle}$ which can be estimated using calculated characteristic ratios for the different sequences (see chapter 1.5.1).

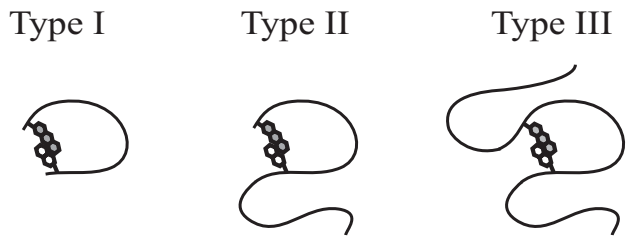

Figure 10: *Different loops in polymer chains. Type I-loops are formed by end-to-end, type II-loops by end-to-interior and Type III-loops by interior-to-interior contacts. Type III-loops are most common in proteins.*

Polymer theory predicts a limiting value for the effect of additional tails on the kinetics of loop closure. This limit was explored for a *(Gly-Ser)$_4$* loop sequence by coupling one end of the peptide to an avidin molecule. In the limit of type II loop formation, k_c is decreased by a factor of 2.3 for a *(Gly-Ser)$_4$* loop. Measuring type II loop formation rate constants in several different loop sequences, we observed that the influence of additional tails was stronger for shorter and stiffer loops compared to long and flexible loops.

Thus, to compare the kinetics in different loops we defined a reduced rate constant $k_{red} = k_c / k_{c,\,reference}$, where k_c denotes the loop formation rate constant of a type II-loop and $k_{c,reference}$ is the loop formation rate constant of the corresponding type I-

loop without extension. On the other hand to compare chain dimensions, we defined a reduced loop size

$$\sqrt{\langle r^2 \rangle}_{red} = \sqrt{\langle r^2 \rangle}_{loop} \Big/ \sqrt{\langle r^2 \rangle}_{total} \qquad [25]$$

where $\sqrt{\langle r^2 \rangle}_{loop}$ denotes the average end-to-end distance of the loop and $\sqrt{\langle r^2 \rangle}_{total}$ is the end-to-end distance of the total chain. The logarithm of the reduced rate constant $\ln k_{red}$ correlates with $1/\sqrt{\langle r^2 \rangle}_{red}$ for all type II peptides (r = 0.99). This shows that the relative effects are similar in all systems. From this dependence, it can further be concluded that the limiting value for type II loop formation is reached when the total chain size is about three times the average end-to-end distance of the loop.

During protein folding, type III loop formation events are most frequent. We studied these reactions using a *(Gly-Ser)*$_4$ loop with N- and C-terminal extensions which allowed us to compare the results to type I & II contact formation. In these peptides tail sequences consisted of *(Gly-Ser)*$_n$ or *(Thr-Gly-Gln-Ala)*$_n$. We observed that extension of both ends leads to a 1.6 fold stronger effect on the rate constant for type III loop formation compared to type II loops of identical length.

However, a limiting value was not reached in our model peptides. For the longest peptide (34 amino acids) which corresponds to the size of the smallest protein domains known k_c was reduced by a factor of 2.1. If the limiting value of type III contact formation is assumed to be reached at the same reduced loop size as in type II loops, then the maximal slowdown would be about a factor of 4.

It is thus shown that additional tails have an effect on loop formation dynamics. This effect is small and reaches a limit in long chains. However, when using loop formation rate constants measured in type I-loops to estimate kinetics of such processes in proteins, tail effects have to be considered and the rate constants have to be scaled accordingly.

These findings are described in detail in the following article:

Fierz, B. & Kiefhaber, T., End-to-End vs. Interior Loop Formation Kinetics in Unfolded Polypeptide Chains, J. Am. Chem. Soc. 2007, **129** (3): p. 672 -679

3.3 Photodynamics of the Xanthone / Naphthalene System

To gain more information on the photochemistry of TTET and to determine rate constants of triplet formation in xanthone and of the transfer reaction to naphthalene, we performed femtosecond fluorescence and absorption spectroscopy on xanthone dissolved in ethanol. The kinetics observed in the xanthone triplet absorption band from 550 nm to 650 nm were described by four processes with time constants of 0.63 ps, 1.3 ps, 12 ps and 62 ps.

The 0.63 ps, 1.3 ps and 12 ps processes correspond to a buildup of triplet absorption while the 62 ps process describes a blueshift of the triplet band. These processes are compatible with a sequential model for xanthone photodynamics where after excitation the $^1\pi\pi^*$ state is reached (0.63 ps process), intersystem crossing (ISC) to the $^3n\pi^*$ occurs according to the El-Sayed rules (1.3 ps process), and finally, by a slower internal conversion process (IC) the lower lying $^3\pi\pi^*$ triplet state is reached, which has a shifted absorption maximum (62 ps process).

Using 1-methylnaphthalene (1-MN) as triplet acceptor, pseudo-first-order kinetics of triplet-triplet energy transfer were measured with varying 1-MN concentrations, ranging from millimolar to molar concentrations up to measurements in neat 1-MN. Two limits of TTET could be discriminated. In a dynamic limit, diffusion is the rate limiting step and pseudo-first-order with a bimolecular rate constant of $7.2 \cdot 10^9\ M^{-1}s^{-1}$ kinetics are observed. In the static limit the xanthone is surrounded by 1-MN molecules and the photophysical processes are limiting leading to complete TTET within 1.8 ps in neat 1-MN. Under these conditions, no xanthone absorption is built up. It can be concluded that (i) the xanthone molecule undergoes ISC within 2 ps, (ii) the process of TTET is faster than ISC in xanthone and (iii) the $^3n\pi^*$ triplet state that is reached within these 1.8 ps allows TTET to naphthalene.

In ethanol, xanthone fluorescence is very weak with a quantum yield of $\phi_{fl} = 4.9 \cdot 10^{-4}$ and emission decays with a time constant of 60 ps. In water however, the quantum yield of fluorescence is higher by two orders of magnitude and the fluorescence decay is much slower with τ_{fl} = 700 ps for xanthone. Up to now, fluorescence and absorption spectroscopy on xanthone was difficult to perform in water due to the low solubility of the compound. We therefore attached a xanthone moiety to a peptide which increased the solubility and enabled us to obtain reference data for TTET experiments. In the xanthone-peptide the fluorescence decayed with τ_{fl} = 316 ps and

femtosecond absorption spectroscopy in water showed that the blueshift of the triplet band proceeds with a time constant of 316 ps compared to 62 ps in ethanol.

These findings are explained by a delayed fluorescence mechanism. Due to solvent polarity, the energy gap between the $^1\pi\pi^*$ and $^3n\pi^*$ states is decreased leading to an equilibrium between these two states. This equilibrium is depleted by a temperature dependent IC process to the $^3\pi\pi^*$ state with τ_{IC} = 316 ps (62 ps in ethanol). This process leads to the observed spectral shift in the time resolved xanthone triplet absorption.

Concluding, it was shown that xanthone ISC occurs on the 2 ps timescale and TTET to naphthalene is even faster. Thus, the time window for the observation of contact formation processes using TTET reaches over six orders of magnitude in time from around 5 ps to 20 μs. However, the photodynamics of xanthone are complex in water, thus photochemistry has to be considered in the analysis of sub-nanosecond events.

This work is described in detail in the following articles:

Satzger, H., Schmidt, B., Root, C., Zinth, W., Fierz, B., Krieger, F., Kiefhaber, T. & Gilch, P., *Ultrafast Quenching of the Xanthone Triplet by Energy Transfer: New Insight into the Intersystem Crossing Kinetics*. J. Phys. Chem. A, 2004, **108(46)**: p. 10072-10079.

Heinz, B., Schmidt, B., Root, C., Satzger, H., Milota, F., Fierz, B., Kiefhaber, T., Zinth, W. & Gilch, P., *On the Unusual Fluorescence Properties of Xanthone in Water*, Phys. Chem. Chem. Phys., 2006, **8(29)**, 3432-3439

3.4 Dynamics in Conformational Substates of Unfolded Polypeptide Chains Revealed by TTET on the ps to μs timescale

Nanosecond laserflash TTET experiments on loop formation in different peptides show an initial loss of xanthone absorption within the dead time of the experiment. The effect is more pronounced for shorter loops. As shown in chapter 3.3, the TTET reaction allows monitoring contact formation kinetics with a picosecond time resolution. The combination of femtosecond and nanosecond laserflash spectroscopy en-

abled us to monitor TTET processes on the timescale from picoseconds to microseconds.

To resolve the dead-time events observed in nanosecond experiments, loop formation in a small peptide containing two *Ser* residues between the xanthone donor and naphthalene acceptor labels (Ser_2) was studied by a combination of femtosecond and nanosecond laserflash experiments. As discussed in chapter 3.3, the kinetics of xanthone ISC and IC are complex. In both peptides sub-nanosecond processes were detected. To separate xanthone photophysics from actual TTET reactions, the TTET kinetics were compared to the kinetic traces in a donor-only peptide. The difference traces revealed two sub-nanosecond processes in the Ser_2 peptide. A fast 3-4 ps process with 15% amplitude was followed by a slower TTET process on the 100's of picoseconds. These processes are responsible for a 50% loss of xanthone absorption within the first nanoseconds of the experiment, in agreement with the results from nanosecond spectroscopy. The kinetics and amplitude of the fast processes depend on peptide length and sequence. In a longer Ser_8 peptide the 100's of picoseconds process was found to be slower but exhibited a larger amplitude while in a stiff Pro_5 peptide the amplitude of all fast processes was found to be small.

These results indicate that peptide motions occur on a complex free energy surface that contains local minima (conformational substates) separated by barriers. For peptides which have the labels in contact during the laser flash, TTET is limited only by xanthone photophysics leading to the 3-4 ps process. The processes on the 100's of ps timescale can be interpreted as the fast depletion of species within the same local minimum on the free energy surface. Within these local minima, contact can be established without the crossing of any major barriers. On the other hand, the remaining peptide population has to cross several small barriers to establish contact. The exchange between different wells however is fast at room temperature and exponential kinetics in the nanosecond time scale are observed.

To learn more about the organisation of the free energy landscape governing polypeptide dynamics we tested for conditions where transitions between substates are slow. We performed measurements on both a short *(Ser-Gly)* and a long loop $(Gly\text{-}Ser)_{12}$ at low temperature (298 – 208 K) in 60% glycerol/water solutions. Below 240 K complex kinetics were observed in both peptides. The kinetic traces can be described by a combination of a fast initial exponential decay and a slower stretched process (see chapter 1.2, equation [10]). The faster process most likely corresponds

to the process on the picosecond timescale observed at room temperature, which results from motion within a conformational substate on the free energy surface that allows contact without major barrier crossing. The slower non-exponential process is attributed to the dynamics of those molecules that reside in different conformational substates and have to cross several barriers to establish contact. These barriers arise from peptide-peptide and peptide-solvent interactions, from steric hindrances and from rotational potentials of the mobile torsional angles within the polypeptide chains. Due to low thermal energy, equilibration between the substates is slow and different kinetics are observed for the different conformational substates, resulting in stretched exponential relaxation. Increasing the viscosity instead of lowering the temperature leads to a similar effect due to high friction of the peptide on the energy landscape, which slows down barrier crossing.

Peptide motions are coupled to solvent dynamics, thus the contact formation rate constants should follow the dielectric relaxation rate constant of the solvent, which is a measure for the tumbling time of water molecules. This is observed for the long *(Gly-Ser)*$_{12}$ peptide over the whole range of temperatures, whereas loop formation dynamics of the short *(Ser-Gly)* peptide are increasingly decoupled from solvent motion below a certain temperature, due to barrier limited dynamics or temperature induced solvent inhomogeneities.

The ratio between the dielectric relaxation and contact formation rate constant can be interpreted as the average number of steps needed to form a loop. Our results suggest that a long peptide needs around 10^4 solvent rearrangements to establish end-to-end contact. This gives a picture of the conformational search an unfolded protein has to perform in order to establish short and long range interactions upon folding.

These findings are described in detail in the following articles:

Fierz, B., Satzger, H., Root, C., Gilch. P., Zinth, W., Kiefhaber, T., *Loop formation in unfolded polypeptide chains on the picoseconds to microseconds time scale*, Proc. Natl. Acad. Sci. U S A, 2007, **104** (7): p. 2163-2168

Fierz, B. & Kiefhaber, T., (2007) *Non-exponential Kinetics of Intrachain Contact Formation in Unstructured Peptides at Low Temperature, to be submitted*

3.5 Global and Local α-Helix Dynamics and Stability Measured by Triplet-Triplet Energy Transfer

α-helices are the most abundant secondary structure element in proteins. They often form fast during refolding and independent of long range interactions. The properties of α-helices have been studied for more than 40 years. While thermodynamics of helix stability are quite well understood, less is known about the kinetics of the helix coil transition. Applying relaxation techniques e.g. ultrasonic absorption, dielectric relaxation or temperature jump, the unfolding of helices has been studied. However, the interpretation of relaxation rate constants is difficult and only global parameters were monitored, thus no site specific information about dynamics in α-helices could be obtained.

We applied TTET from xanthone to naphthalene introduced at different positions in helical peptides to study global and local dynamics and stability in α-helices. As a model system we used small helical peptides of the general design *Ac-(Ala)$_5$-(Ala-Ala-Ala-Arg-Ala)$_3$-Ala-NH$_2$*. This peptide is reported to exhibit high helicity (> 80%) in solution at 0^o C (175; 176).

To monitor global helix dynamics the triplet labels were introduced at the N- and at the C-terminus in one peptide. Positioning the labels with a (i, i+6) spacing allowed to observe local motions. The labels were introduced at the N-terminus, at central positions of the helix and at the C-terminus. The positioning of the labels at both ends or with a (i, i+6) spacing does not allow contact in the helical conformation. Thus, the helix has to unfold at least partially to allow contact so TTET can occur. The kinetics for contact formation can then be interpreted with a three state model

$$H^* \underset{k_{cl}}{\overset{k_{op}}{\rightleftharpoons}} C^* \xrightarrow{k_c} C \qquad [26]$$

where H^* denotes the peptide population with local structure formed (the asterisk denotes excited donor labels), C^* denotes peptides where the local structure is partially opened to allow contact and C are peptides that have undergone TTET. k_{op}, k_{cl} and k_c are transition rate constants between these states.

Helix content was determined in all peptides using CD spectroscopy and it was found that by positioning the labels into the interior of an helix the stability is reduced

while label positions at the termini have a small effect compared to the unperturbed peptide. TTET experiments were performed at 5° C. In all peptides contact formation showed double exponential kinetics. The two phases arise from two populations of peptides. Peptides that are locally disordered can establish contact leading to a fast exponential phase with a rate constant comparable to expected values in unstructured poly-*Ser* chains. Local helical structure between the labels prevents contact formation. The population of peptides with an helix formed has to open in order to establish contact, thus the observed rate constants correspond to the local unfolding reaction if $k_{op} << k_c$. This is reflected in a slow phase in the kinetics. The amplitudes of the two kinetic phases report on the corresponding populations. From the amplitude information it could be concluded that the center has higher helical content than the ends. In addition, the stability of an helix was found to be much lower at the C-terminus than at N-terminus. The amplitude ratio does however not correlate with global helix content observed by CD spectroscopy which shows that local structure is probed by TTET.

Using a three state model to analyse the data, information on helix unfolding and refolding can be obtained at the same time. All microscopic rate constants contribute to the observed kinetics if they are in the same range. This can be achieved by applying a perturbation on the helix formation reaction. We used urea to vary helix content, whereas the urea dependence of the microscopic rate constants was assumed to be linear according to the findings on protein folding (45) and peptide dynamics (55). All obtained observable rate constants and amplitudes were fitted globally to the analytical solution of the three state model (eq. [26]). The rate constant for helix opening k_{op} was found to be in the range of 10^6 s^{-1} in the interior while at the ends opening is three times faster with rate constants of $3 \cdot 10^6$ s^{-1}. Structure formation on the other hand was found to be similar throughout the peptide with rate constants k_c in the 2-$3 \cdot 10^6$ s^{-1} range. This shows that the lower stability of the helical structure at end position results from faster unfolding. On the other hand, the rate constants for global helix unfolding and refolding from the peptide with the labels at both ends were found to be much slower than local kinetics ($k_{op} = 3.4 \cdot 10^5$ s^{-1}, $k_{cl} = 8.4 \cdot 10^5$ s^{-1}).

For the positions at the end of the helix, the rate constant which monitors contact formation k_c is in good agreement with values expected from unstructured poly-*Ser* peptides. In the center contact formation is slower. When the microscopic rate constants are compared in 8 M urea, k_c is equal for all peptides and corresponds well to

Serine peptides, which shows that in the absence of helical structure the peptides have similar properties.

The urea dependence of k_{op} shows that with increasing denaturant concentration structure formation is strongly slowed down. This effect is similar at all positions, indicating that the same process is probed in the center and at the ends. As urea competes for hydrogen bonds, intrachain interactions are less favourable compared to peptide solvent interactions and it is more difficult to form an helix. Helix unfolding on the other hand shows different behaviour at the ends than in the centre. While unfolding gets faster with increasing urea concentration for the central positions and the global dynamics, indicating a free energy barrier for unfolding, the reversed effect is observed at terminal positions. These results show that TTET can be used to report on local dynamics in α-helices. Unfolding time constants in the range of 100's of nanoseconds range for local processes have been found, depending on the position. These time constants correspond well to observed relaxation time constants found in ultrasonic absorption or temperature jump experiments. Thus, our results show that global and local helix unfolding occurs with 3-9 fold difference in rate constant, depending if global unfolding is compared to the dynamics at the center or at the helix termini. While at the helix termini local fluctuations dominate and significant end-fraying is detected the dynamics are much slower in the interior due to free energy barriers.

These findings are described in detail in the following manuscript:

Fierz, B., Reiner, A. & Kiefhaber, T., (2007) *Global and Local α-Helix Dynamics and Stability Measured by Triplet-Triplet Energy Transfer*, *to be submitted*

3.6 Dynamics of Unfolded Polypeptide Chains, Review Articles

Intrachain loop formation is an elementary step in protein folding. The rate constants for loop formation contribute to the pre-exponential factor for a folding reaction and set an upper speed limit for folding. A realistic estimate of the pre-exponential factor for folding is necessary to calculate the heights of the free energy barrier for folding.

In the contributions to the "Protein Folding Handbook" and to "Methods in Molecular Biology vol. 350: Protein Folding Protocols" we present an overview of the field of polypeptide chain dynamics. Concepts from polymer theory are applied to give a theoretical background on the dimensions and dynamics of polypeptide chains. These predictions from theory are compared to experimental results. We discuss experimental systems that have been used to measure intramolecular dynamics in polypeptide chains. In particular, results obtained in our lab on contact formation processes in polypeptides using triplet-triplet energy transfer are summarised. Scaling laws for the effect of chain length on the end-to-end contact formation rate constants are discussed and compared to several theoretical models. The role of amino acid sequence, position of the labels and the influence of the solvent on chain dynamics are covered. In addition, the results obtained in model peptides are compared to rate constants of loop formation in fragments derived from natural proteins.
In the methodical part of the reviews, the prerequisites for a system that can be used to accurately measure chain dynamics and contact formation processes are discussed. To study contact formation processes using spectroscopic techniques, it is of importance that the photochemistry of the system is fast enough and that transfer or quenching processes are diffusion controlled, i.e. every encounter of donor/acceptor or excited molecule/quencher is productive.

This work is published in the following articles:

Fierz, B. & Kiefhaber, T., Dynamics of Unfolded Polypeptide Chains, in *Protein Folding Handbook*, J. Buchner and T. Kiefhaber, Editors. 2005, WILEY-VCH: Weinheim. p. 809-855.

Fierz, B., Joder, K., Krieger, F. & Kiefhaber, T., Using Triplet-Triplet Energy Transfer to Measure Conformational Dynamics in Polypeptide Chains, in *Methods in Molecular Biology vol. 350: Protein Folding Protocols*, Y. Bai, R. Nussinov, Editors, 2006 Humana Press.

4. Unpublished Results: Helix Formation Studied by Photorelease of a Caged Peptide

4.1 Introduction

The kinetics of α-helix formation are still not well understood. Models predict a nucleation growth mechanism where the elementary steps occur on different timescales and peptides with varying degree of helical structure interconvert rapidly. Most kinetic data were obtained by relaxation techniques where helix unfolding is monitored as a result of a fast change in conditions, e.g. a nanosecond jump to a higher temperature. To analyse the data usually a two state assumption is made which is generally invalid because α-helices fold through a succession of many small conformational transitions. The process of nucleation itself is difficult to study because the experiment has to start from the unfolded state to assure that no propagation steps from partially helical peptides contribute to the experimental signal. Conventional methods as stopped flow or continuous flow techniques, where a chemical denaturant is rapidly diluted out of a peptide solution, thus allowing the peptide to fold, are not feasible because the time resolution of these techniques is too low to observe a submicrosecond process as helix formation.

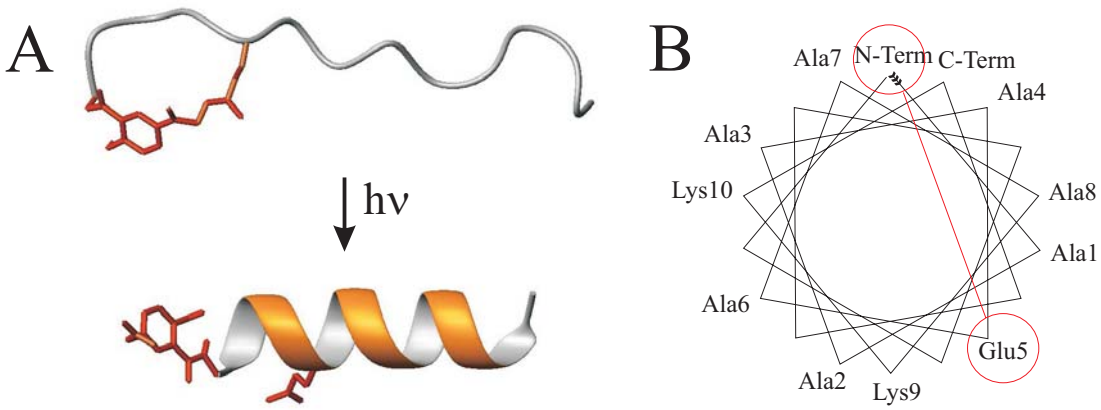

Figure 11: A) *The helical peptide is caged by a (i, i+5) crosslink that does not allow helix formation. By laser irradiation, the crosslink, a PHP derivate, is opened and the peptide is free to relax. Subsequently, helical structure is formed. This process can be monitored spectroscopically.* ***B)*** *Helical wheel representation of crosslinked peptide showing the position of the crosslink.*

The application of photocleavable crosslinkers however enables to observe α-helix formation directly. A cyclic peptide which forms an α-helix in solution is cyclised using a suitable photocleavable crosslinker. This cyclisation prevents secondary structure formation. Upon cleavage of the crosslinker by irradiating the sample with a short laser flash the peptides are allowed to relax to an extended conformation. In the following, the peptides are able to adopt their specific secondary structure. The relaxation of the peptide and the subsequent secondary structure formation can then be monitored by spectroscopic means (UV, IR or fluorescence spectroscopy). In an earlier experiment photoinitiated disulfide cleavage (177) was used to generate an unfolded ensemble of an helix forming peptide, however due to recombination of the generated thiyl radicals no clear results have been obtained. Thus, the opening reaction has to be irreversible.

Recently, the use of the p-hydroxyphenacyl group (pHP) was proposed as a water soluble, photoremovable protecting group for peptides (178) and phosphates (179; 180). The mechanism of photorelease involves a short lived triplet state as the reactive excited state (179-181) which forms within a few picoseconds and has a lifetime of 0.4 ns. Subsequently, rearrangements take place that involve a tautomerisation of the system to the quinoid enol tautomer and produce a phenylacetic acid residue at the trigger moiety and the free carboxylic acid function of the caged molecule (181).

It was shown that the derivates of pHP can be used as intramolecular crosslinking reagents (R. Givens*, unpublished*). For different derivates of pHP irradiation at 300-350 nm releases the product in an irreversible rearrangement reaction at high yield (ϕ~0.5) and with fast kinetics in the nanosecond time scale (ref. (181) and J. Wirz, *personal communication*). Thus, we used pHP derivates to cage helical peptides, which allows measuring α-helix folding kinetics.

4.2 Peptide Design

In a good model system, helix formation should be prevented in the pHP-crosslinked state but a large amount of helix should be formed in the linear form. Short peptide based on *Ala*-containing sequences (149) were tested for helical content using the helix prediction program *AGADIR* by Muñoz and Serrano (150-152). The general sequence *Ala-Ala-Ala-Ala-Glu-Ala-Ala-Ala-Lys-Lys-*NH_2 was predicted to form ~36% helix (at 5° C). Introducing an intramolecular crosslink between the N-terminus and Glu_5 should disrupt any helical structure (see Figure 11).

To test helical content in the linear form we synthesised reference peptides with either glutamate or oxocarbonylbenzoic acid (OCBA) as N-terminal groups to model the pHP protecting group after photocleavage (see Figure 12). The Glu- and OCBA-peptides are predicted to have a high helical content (~35%) due to the high helical propensity of alanine residues and to charge/helix dipole interactions. On the other hand, the *Lys*-peptide shows very weak helix propensity in *AGADIR*.

To determine the helical content of the peptides we recorded circular dicroism spectra (see Figure 13). The CD-data shows that the *Lys*-peptide forms almost no helix even at 4° C. The OCBA-peptide exhibits some helical structure and the *Glu*-peptide is 30% helical, in agreement with prediction.

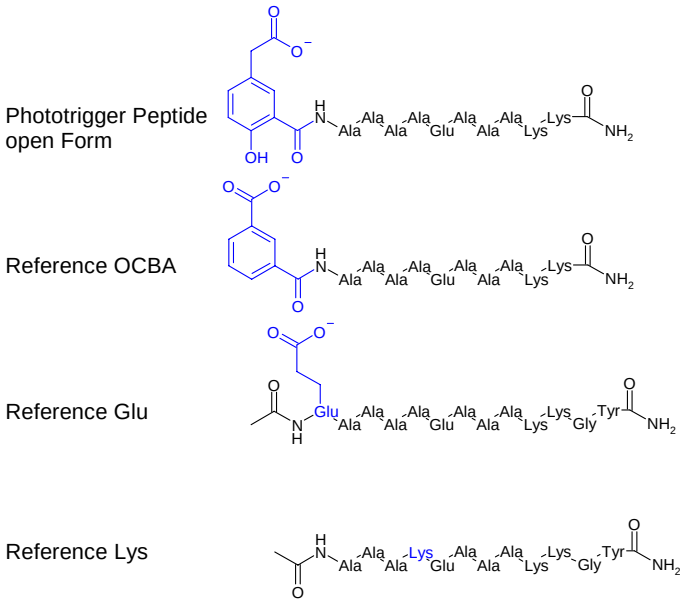

***Figure 12**: Structure of open form of the pHP-peptide after photocleavage of the crosslinker compared to structures of reference peptides. The reference peptides were used to select a sequence and study properties of the open form of the phototrigger peptide.*

Based on the results of the *Glu*-peptide, the sequence pHP-*Ala-Ala-Ala-Ala-Glu-Ala-Ala-Ala-Lys-Lys-*NH_2 was initially chosen for cyclisation. However, due to the low helix content of the *OCBA*-peptide, which is a better model for the open form of the pHP-crosslinker, the sequence has to be varied in further studies.

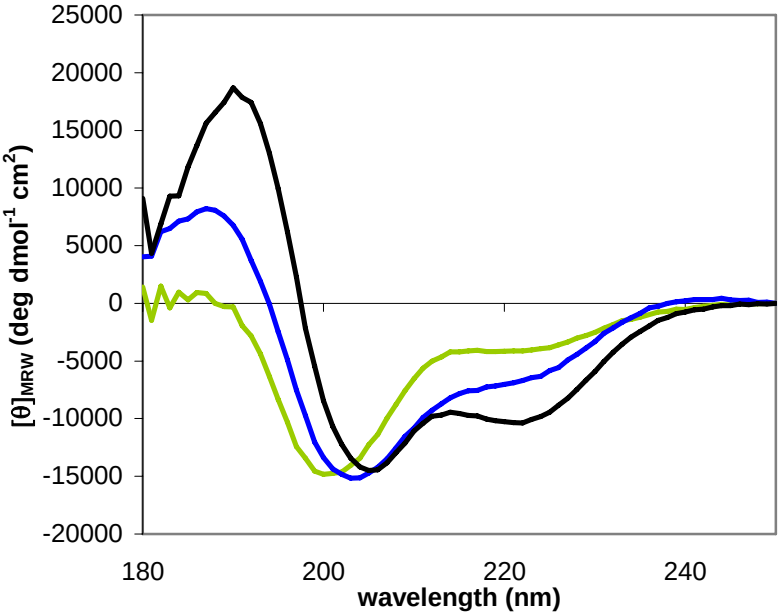

Figure 13: *CD spectra of reference peptides at 4^{O} C. (—) Glu- peptide, (—) Lys -peptide and (—) OCBA - peptide. The CD spectrum of peptide 3 was scaled to match the other two spectra because of lacking information about the absorption coefficient of OCBA. All spectra were measured in 10 mM phosphate buffer at pH 7 in 1 mm cuvettes.*

4.3 Synthesis of the Caged Helical Peptide

The synthesis of the cyclic peptide is described in the following. The synthetic route chosen is outlined in Figure 14. The pHP derivative 5-acetylsalicylic acid has to be protected at the hydroxyl and carboxyl position and is activated by transformation into a bromoketone that reacts with nucleophiles. It is then coupled to a selectively deprotected glutamate residue of the peptide on resin. After deprotection of the acid function of the pHP derivative and the N-terminus, the peptide is cyclised and cleaved. A final deprotection step yields the product.

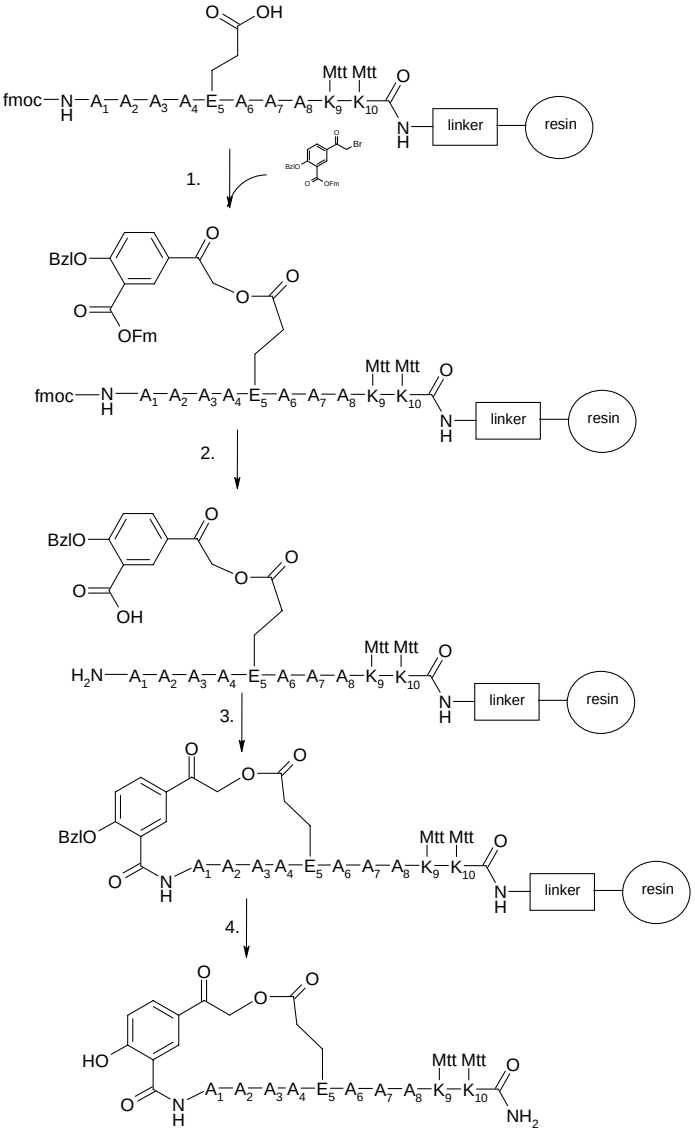

Figure 14: *Route chosen for the synthesis of the cyclic peptide: Four different orthogonal protecting group systems have been used. Reaction conditions: 1) Compound* ***5****, DIPEA, DMF; 2) 2% DBU, 2% piperidine in DMF; 3) HATU, DIPEA, DMF; 4) TFA, TIS in DCM; Pd/C, H_2 in methanol*

Protection and Activation of photocleavable crosslinker (see Figure 15)

The p-hydroxyphenacyl derivative compound **5** was synthesised in four steps starting from the commercially available methyl-5-acetylsalicylicate (**1**). Two orthogonal protecting groups were introduced to enable attachment to the peptide and subse-

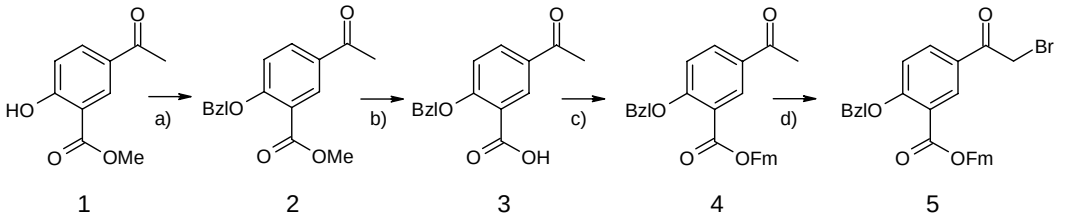

Figure 15: *Synthesis of the p-hydroxyphenacyl derivate used in caging of helical peptides. Reaction conditions: a) BzlBr, K_2CO_3, DMF, b) LiOH, THF/H_2O, c) Fmoc-Cl, DMAP, DIPEA, DCM, d) $TBABr_3$, THF*

quent cyclisation. A benzyl protection group was used to protect the phenolic hydroxyl moiety that is cleaved by hydrogenolysis using H_2, Pd/C, while the carboxylic acid was protected by an base labile 9-fluorenyl methyl ester (OFm) (182). This allows deprotection of the carboxylic group together with the Fmoc-protected N-terminus in one step followed by cyclisation (see Figure 14).

Synthesis of O-benzyl-5-acetylsalicylic acid (3)

Methyl-5-acetylsalicylicate (**1**) was converted via a nucleophilic substitution reaction with benzylbromide in dimethylformamide (DMF) followed by cleavage of the methyl ester under mild conditions using LiOH in tetrahydrofurane (THF) and water.

Synthesis of fluorenylmethyl O-benzyl-5-acetylsalicate (4)

Fluorenylmethyl esters can be synthesised using 9-fluorenylmethanol in the presence of dicyclohexylcarbodiimide/dimethylaminopyridine (DMAP) (182), with diazofluorene (183) or in the presence of imidazole (184). However, satisfying results were only obtained using fluorenylmethyl chloroformate (FmocCl) in the presence of N,N-diisopropyl ethylamine (DIPEA) and DMAP (185). The reaction proceeds via the formation of a mixed carboxylic-carbonic anhydride which produces the ester by decarboxylation. The reaction is performed in dichloromethane (DCM) and proceeds rapidly as monitored by CO_2 evolution.

Synthesis of fluorenylmethyl O-benzyl-5α-bromoacetylsalicate (5)

To couple the crosslinker to the peptide, **4** is activated by conversion of the acetyl group to a bromoketone. This can be achieved by using molecular Br_2, using Cu(II)Br (186) or tetrabutylammonium tribromide ($TBABr_3$) as a selective bromination agent (187). This approach was successful as compound **4** was readily converted to the bromoketone in the presence of $TBABr_3$. The fully protected and brominated compound **5** was used for cyclisation after recristallisation.

Peptide Synthesis

The synthesis of cyclic peptides requires that the protection groups of several groups can be selectively removed. To introduce the photocleavable crosslinker, a glutamate residue has to be deprotected, leaving all other protecting groups intact. Subsequently, the N-terminal 9-fluorenylmethyloxycarbonyl (Fmoc) has to be removed to allow cyclisation. For the protection of the glutamate, an allylic ester (OAll) was chosen which could be cleaved under mild conditions by Pd(0) catalysed allyl transfer (188). The N-terminus was protected by base labile Fmoc, while the lysine side chains protecting groups (4-methyltrityl group, Mtt (189)) and resin linker were acid labile thus providing full orthogonality and allowing cleavage of the peptide at low concentration of trifluoroacetic acid (TFA) without hydrolysis of the cyclic ester.

The peptide Fmoc-*$(Ala)_4$-Glu-$(Ala)_3$-Lys-Lys-NH_2* was assembled on an acid sensitive resin (Sieber amide, Novagel). Peptide synthesis was performed according to

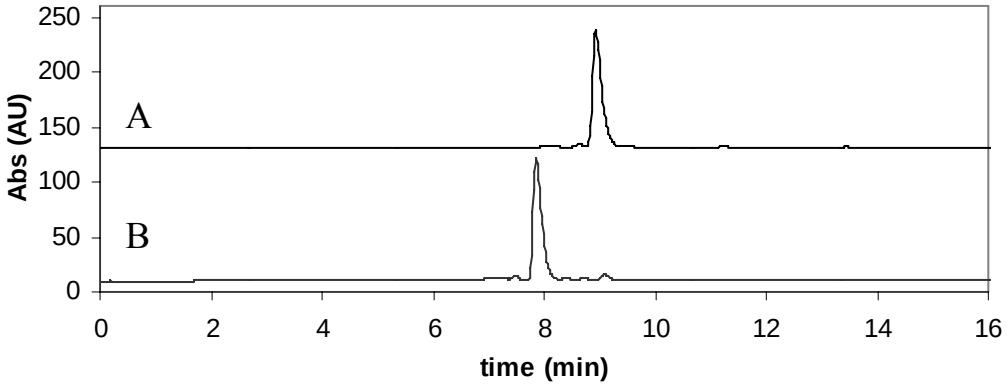

Figure 16: *HPLC profiles of peptide synthesis and Glu(OAll) deprotection.* ***A)*** *HPLC of crude peptide,* ***B)*** *HPLC of peptide after glu deprotection, 5-35% acetonitrile gradient in 16 min on a RP-8 analytical column, detection at 280 nm.*

standard Fmoc- chemistry protocols (190) involving O-Benzotriazole-N,N,N',N'-tetramethyluronium-hexafluorophosphate (HBTU) activation and deprotection of the N-terminal Fmoc with piperidine in DMF. However, the last three amino acids (Ala 1-3) had to be coupled using 2-(7-aza-1H-benzotriazole-1-yl)-1,1,3,3-tetramethyluronium hexafluorophosphate (HATU) as coupling reagent (191; 192) and a double coupling protocol, where the coupling cycle is repeated two times without Fmoc-deprotection in between. Only this procedure gave acceptable synthesis results as shown by HPLC and matrix assisted laser desorption ionisation mass spectrometry (MALDI-MS). The last synthesis cycle was run without final Fmoc cleavage to leave the N-terminus protected.

Selective glutamate deprotection was subsequently achieved on resin applying the method of Kates *et al.* (193) utilising a mixture $Pd(Ph_3)_4/CHCl_3$/acetic acid/N-methyl morpholine (NMM) under inert atmosphere. The reaction was checked by taking resin aliquots and analysis by HPLC. Within 4h the glutamate side chain was completely deprotected as indicated by a shift in retention time on HPLC of *tr = 8.9* min for the protected and t_r = 7.9 min for the free glutamate and by mass spectrometry ($M + H^+$ = 1162.6 protected and $M + H^+$ = 1122.6).

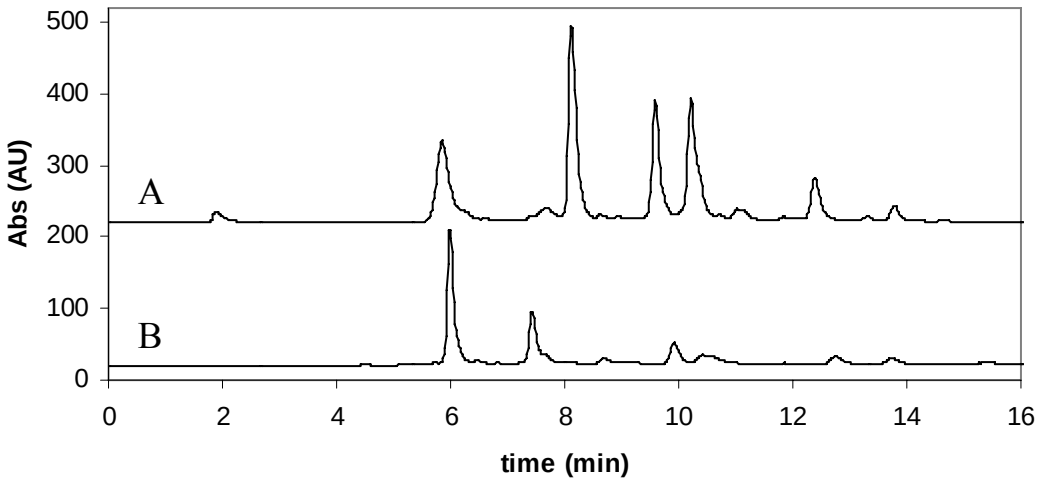

Figure 17: *HPLC profiles of modification reaction.* ***A)*** *after modification, several peaks are observed due to instability of Fm-ester.* ***B)*** *after deprotection of the N-terminal Fmoc group and the Fm-ester, a main peak corresponding to the main product is followed by a side product peak corresponding to a piperidine adduct that points to transient ring formation in some peptides. HPLC conditions: 5-35% acetonitrile gradient in 16 min on a RP-8 analytical column, detection at 280 nm.*

Modification of peptide with fluorenylmethyl O-benzyl-5α-bromoacetylsalicate

Compound **5** was coupled in 3-fold excess to the deprotected glutamate sidechain of the peptide in DMF for 30 min (see Figure 14, step 1). To ensure deprotonation of the glutamate sidechain, DIPEA was used as base. It has been observed that prolonged coupling times can lead to side products due to slow cleavage of the Fm-ester in basic conditions. Coupling was monitored by taking resin samples at different times and analysing the peptide on HPLC and MALDI-MS. On the HPLC several peaks are detected (see Figure 17) due to instability of the Fm-ester group to the cleavage conditions from the resin (see 4.4.6, cleavage conditions). Subsequent deprotection of the N-terminus and the carboxylic acid of the coupled compound was achieved using 20% piperidine or a mixture of DBU and piperidine in DMF (see Figure 14, step 2). After removal of Fmoc two major peaks were detected on HPLC. The first (t_r = 6.0 min, see Figure 17) was identified by MALDI-MS as the desired coupling product ($M + H^+ = 1168.6$), while the second (t_r = 7.6 min) with a mass of $M + H^+ = 1234.2$ could be explained by a piperidine adduct to the carboxylic acid function of the crosslinker moiety. Such piperidides have been observed as a result of cyclic aspartimide formation in peptides where an aspartate is followed by a glycine residue (194). It has been found that shorter coupling times of compound **5** reduce the amount of this side product.

Cyclisation reaction

Peptide cyclisation was achieved on resin using HATU / DIPEA as reagents (step 3 in Figure 14). HATU was added incrementally to reduce capping of the amino terminus by guanidine formation (195). The reaction was monitored by taking resin aliquots, cleavage, HPLC and mass spectrometry. As seen in Figure 18 the peak corresponding to the linear peptide moves to longer retention times (from t_r = 6 min for the linear peptide to t_r = 7.8 min in the cyclic state) upon cyclisation of the peptide. At the same time, some side product peaks appear that correspond to the guanidine modification of the amino terminus as determined by mass spectrometry. The major side product peak at t_r = 7.7 min does however overlap with the desired product thus making purification difficult. This problem was solved by treating the resin with 10% acetic anhydride, 10% DIPEA in DMF to acetylate free N-termini. The result of this procedure is seen in Figure 18, trace C. While as the cyclic product is unaffected by acetylation, the side product containing a free N-terminus is modified and shifted to

higher retention times (t_r = 9.5 min). Subsequently the peptide was cleaved from the resin at mild conditions (1% TFA, 5% TIS in DCM) and purified over semipreparative HPLC.

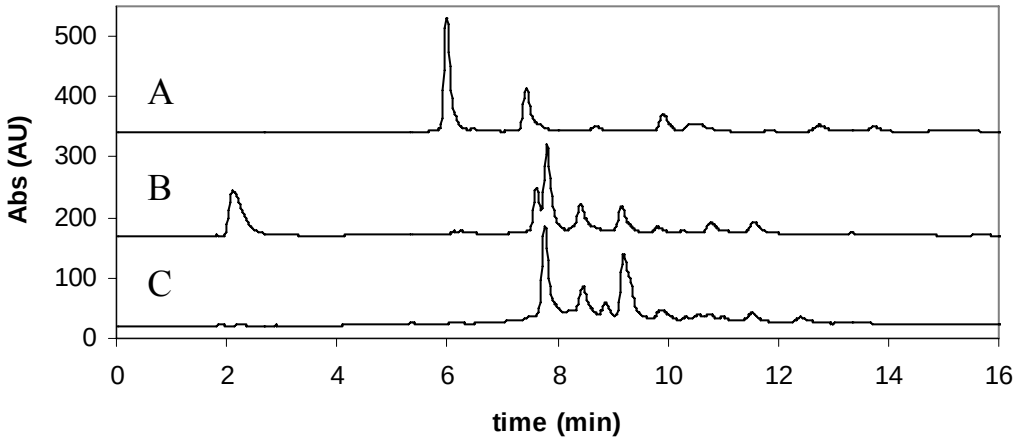

Figure 18: *HPLC profiles of peptide cyclisation.* ***A)*** *modified peptide before cyclisation.* ***B)*** *after 7h of cyclisation cyclic product is detected at tr = 8.1 min* ***C)*** *to separate the products, unreacted or hindered peptides are acetylated. HPLC conditions: 5-35% acetonitrile gradient in 16 min on a RP-8 analytical column, detection at 280 nm.*

Hydrogenolytic cleavage of Benzyl Protecting Group

To enable photocleavage of the crosslinker moiety, the remaining benzyl protecting group had to be removed (see Figure 14, step 4). It was observed that TFA could cleave a number of aromatic benzyl ethers when the aromatic ring contained either meta-directing or ortho-para-directing groups (196). In tests using the free crosslinker (compound 3, see Figure 15) treatment with TFA removed the benzyl group readily. However, in the cyclic peptide compound, TFA was not able to cleave the benzyl ether. Even prolonged exposure to neat TFA did not yield deprotected peptide. Thus another method has been applied. Generally benzyl groups are removed by catalytic hydrogenolysis using H_2 and palladium on activated charcoal.

The choice of solvent is important because polar solvents promote keto-enol isomerisation of the crosslinker moiety which leads to reduction of the aryl ketone thus inactivating the phototrigger. The peptide proved to be soluble in an 1:5 mixture of water:methanol. Addition of an equivalent amount of Pd/C and subsequent violent stirring under H_2 resulted in cleavage of the benzyl ether. The reaction was monitored by analytical HPLC (see Figure 19) where a shift of the peak at t_r = 9.1 min corre-

sponding to the protected peptide to a retention time of t_r = 6.9 min for the deprotected product was observed. Based on the HPLC data the reaction was completed after 80 min. The solution was filtered by a cellulose filter and lyophilised. The crude product was purified by HPLC over a semipreparative RP-18 column using an acetonitrile gradient and eluted at approximately 27% acetonitrile. The product obtained was analysed by MALDI-MS and ESI-LC MS and a mass of 1060.54 was detected (calculated for $C_{47}H_{73}N_{13}O_{15} + H^+ = 1060.54$). The total yield of lyphilised product was ~2 mg (2%).

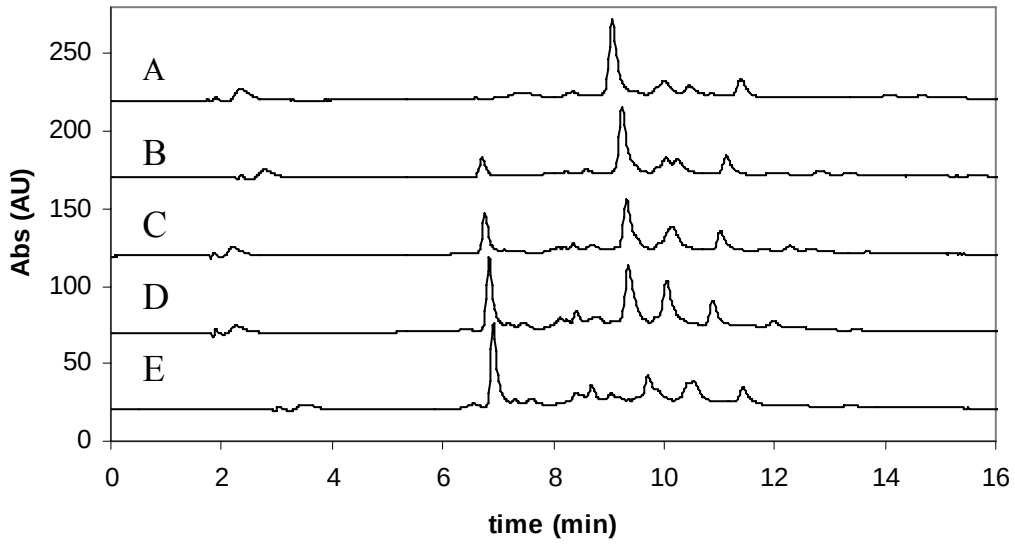

Figure 19: *HPLC traces of the benzyl deprotection reaction. 5-35% acetonitrile gradient in 16 min on a RP-8 analytical column, detection at 280 nm.* ***A)*** *before deprotection,* ***B)*** *20 min reaction time,* ***C)*** *40 min reaction time,* ***D)*** *60 min reaction time,* ***E)*** *reaction is complete after approx. 80 min.*

4.4 Characterisation of Cyclic Peptide

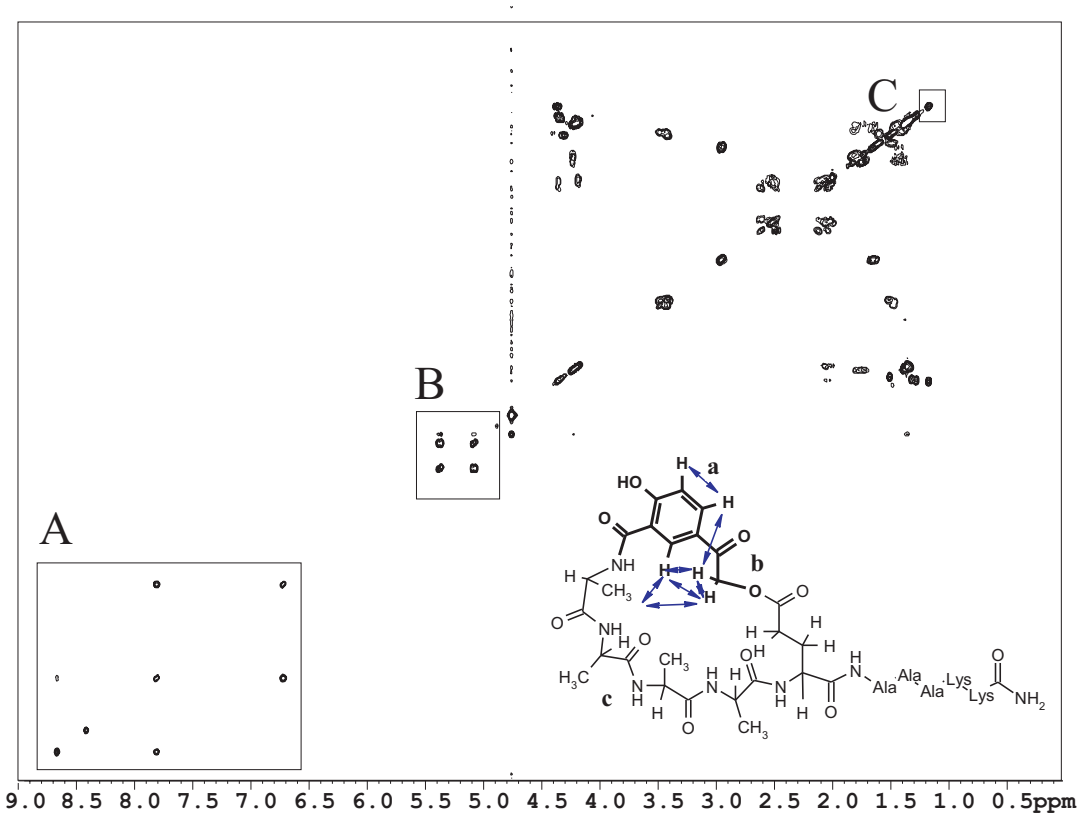

Figure 20: *^{1}H-^{1}H COSY spectrum of the deuterated cyclic peptide in D_2O, 1 mM phosphate buffer, pH 7. The structure of the cyclic peptide is shown in the inset, the observed ROE's are shown as blue arrows.* ***A:*** *The resonances corresponding to the aromatic system of the pHP moiety (**a**),* ***B:*** *A doublet of doublets arising from the methylene group (**b**) of the ester indicating a cyclic structure,* ***C:*** *An alanine methyl group from within the cycle (**c**) shifted upfield to 1.18 ppm due to ring current effects.*

To verify the correct cyclic structure the peptide was analysed by NMR spectroscopy. After completely exchanging all labile protons to deuterons, COSY (see Figure 20), ROESY, HMBC and HMQC spectra were recorded in D_2O. Using the HMBC and HMQC ^{13}C shifts the COSY and ROESY peaks could be assigned to amino acids or the pHP-moiety. At chemical shifts of 8.65 ppm (1H), 7.8 ppm (1H) and 6.7 ppm (1H) the resonances of the pHP aromatic ring system are observed (region A in Figure 20). The resonances at 5.36 ppm (1H) and 5.07 ppm (1H) arising from the methylene group connecting the pHP moiety attached to the N-terminus and the glutamate residue in the interior of the peptide serve as clear evidence for the correct cyclic structure of the peptide (Figure 20, B). Additionally, one alanine methyl side chain is shifted upfield (Figure 20, C), indicating vicinity to the pHP aromatic system.

From the ROESY spectrum, several ROE's can be extracted showing interactions between the methylene group and two aromatic hydrogens, the one at 8.65 ppm, the other at 7.8 ppm. Another ROE is detected between the shifted alanine at 1.18 ppm and the aromatic hydrogen 8.65 ppm. The NMR data thus point to a defined cyclic connectivity lacking a defined three dimensional structure.

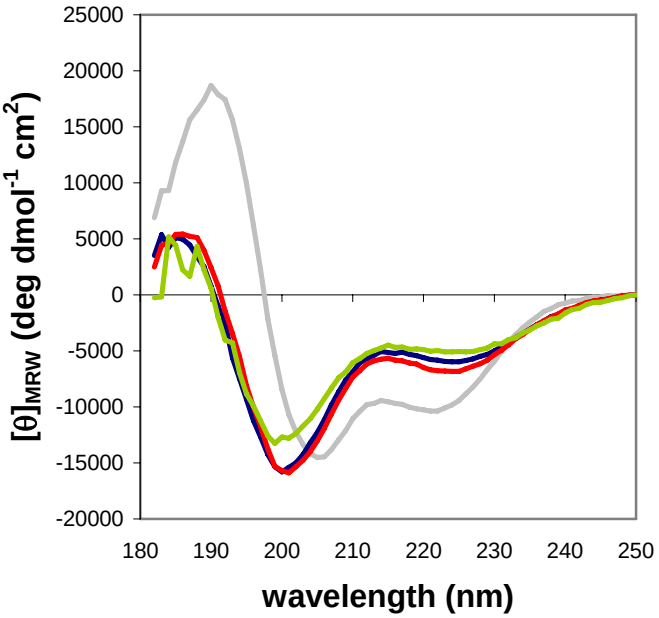

Figure 21: *CD spectra of cyclic peptide in 10 mM phosphate buffer pH 7 at 22.5° C (—) at (—) 4° C and (—) 80° C. The temperature dependence of the CD spectrum is weak indicating no stable secondary structure in the peptide. As a comparison the helical spectrum of the Glu containing reference peptide (—) is shown.*

To further characterise the conformation of the cyclic peptide, CD spectra were recorded (see Figure 21). The data do not show the features expected for a clear helical spectrum. The identical CD spectra recorded at 4° C, 22.5° C and 80° C serves as further evidence against persistent secondary structure of the cyclic peptide.

However, the observed CD-data are also not compatible with random coil spectra. This is expected because the cyclic structure of the peptide restricts conformation and the aromatic system in an asymmetric surrounding which contributes to the CD signal.

UV spectroscopy shows a strong pH dependence of the pHP moiety due to deprotonation of the phenolic hydroxyl group. At pH 7 the phenol is completely dissociated resulting in an strong absorbance band centered at 328 nm. Upon acidification, the phenolic hydroxyl group is protonated and the absorbance band of pHP shifts to a

maximum at 278 nm. As the mechanism for photocleavage requires the protonated hydroxyl group, experiments have to be performed below pH 4.5 to enable photorelease of peptide. Thus, for further studies, peptide systems have to be tailored for maximal helix formation at low pH.

These results show that the desired peptide has been synthesised, it is free of defined secondary structure and can be used for kinetic studies of helix formation. However, the peptide design has to be improved, as the current sequence shows a too low helix content in the linear state.

4.5 Conclusions and Outlook

A synthetic access to photoreleasable cyclic peptides has been developed based on the photocleavable crosslinker p-hydroxy phenacyl (pHP). Upon laser irradiation the pHP crosslinker can be cleaved leading to linearisation of the peptide, which is allowed to relax and to adopt structure. Due to the high rate constant and efficiency of photorelease kinetics, processes in the nanosecond time scale can be observed which should make the system suitable for studying formation of secondary structure elements in model peptides or even folding of small proteins.

In the current project, a peptide with helix propensity has been synthesised and cyclised by the pHP moiety to prevent helix formation in the closed state. The synthesis product has been characterised by NMR and CD spectroscopy and has been found to be free of defined secondary structure. This allows studying helix nucleation after photorelease because the reaction starts from a state where no preformed helical structure is present.

In the next step, the photorelease of the linear peptide by laser irradiation has to be studied and a detection method has to be worked out. As the UV absorption band of the peptide bond is sensitive to secondary structure (197) monitoring absorbance below 210 nm gives information on helix content and can be used as a fast detection method for nanosecond spectroscopy. Fourier transformed infrared spectroscopy FTIR on the other hand has the advantage of high sensitivity and by incorporation of ^{13}C carbonyls, site specific information can be obtained.

If correctly implemented, this system may provide nucleation rate constants for helix formation. For a deeper understanding of the molecular processes computer simulations on the same peptide are performed in collaboration with P. Tavan. This allows direct comparison of experimental and simulated data on a small system.

4.6 Materials and Methods

Synthesis of O-benzyl-methyl-5-acetylsalicylicate (2)

1.884 g (9.7 mmol) methyl-5-acetylsalicylicate (ACROS) were dissolved in 20 ml DMF. 4 g anhydrous K_2CO_3 (29 mmol) were added. Under argon, 1.38 ml benzyl-bromide (11.64 mmol, 1.2 eq) were added dropwise and the suspension was stirred overnight at room temperature. Subsequently, the reaction mixture was then poured into 10 ml of ice water and extracted with diethyl ether twice. The organic phase was thoroughly washed with water, dried with Na_2SO_4 and evaporated. The off-white oily product was used without further purification. ^{1}H NMR ($CDCl_3$) δ 8.43 (d, 1H), 8.07 (dd, 1H), 7.5-7.3 (m, 5H), 7.06 (d, 1H), 5.27 (s, 2H), 3.93 (s, 3H), 2.58 (s, 3H)

Synthesis of O-benzyl-5-acetylsalicylic acid (3)

2 g of **2** is dissolved in 13.1 ml THF, 0.90 g LiOH in 13 ml water was added, the mixture was stirred overnight at room temperature, acidified with 10% HCl at 0^o C and extracted with ethyl acetate. The organic phase was dried with Na_2SO_4 and evaporated. The product was recristallised from 25% ethanol in water (120 ml / gram product) and obtained as white crystals. ^{1}H NMR ($CDCl_3$) δ 10.45 (s, 1H), 8.76 (d, 1H), 8.22 (dd, 1H), 7.5-7.3 (m, 5H), 7.22 (d, 1H), 5.38 (s, 2H), 2.63 (s, 3H)

Synthesis of fluorenylmethyl O-benzyl-5-acetylsalicate (4)

0.68 g of **3** (2.5 mmol) were dissolved in 10 ml DCM containing 0.323 g (2.5 mmol, 0.425 ml) DIPEA (Aldrich). At 0^o C 0.71 g (2.75 mmol) Fmoc-Cl (Patras) dissolved in 5 ml DCM were added portion wise under argon. After 5 min, 30.5 mg (0.25 mmol) DMAP (FLUKA) were added. Subsequently the mixture was allowed to equilibrate to room temperature. CO_2 evolution was observed as the reaction proceeded. After 2 h 100 ml ethyl acetate were added and the solution was washed three times with 2% citric acid, once with 30 ml water, three times with 30 ml 0.5N $NaHCO_3$ (4.2%) and 3x30 ml water. The organic phase was dried and evaporated and **4** was recristallised from ethanol. MP 122.75^o C, ^{1}H NMR ($CDCl_3$) δ 8.56 (d, 1H), 8.19 (dd, 1H), 7.77 (d, 2H), 7.62 (d, 2H), 7.50 (d, 2H), 7.46-7.2 (m, 7H), 7.14 (d, 1H), 5.3 (s, 2H), 4.51 (d, 2H), 4.29 (t, 1H), 2.62 (s, 3H)

Synthesis of fluorenylmethyl O-benzyl-5α-bromoacetylsalicate (5)

0.448 g (1 mmol) **4** was dissolved in 6 ml THF. To this solution, 0.530 g (1.1 mmol) $TBABr_3$ (FLUKA) were added. The dark orange solution was stirred overnight while the colour faded to slight yellow. The solvent was evaporated and the residue was taken up in 200 ml diethyl ether (**5** has only low solubility in water, thus a precipitate forms). The organic phase was washed with water several times and evaporated. The residue was dissolved in DCM, dried with Na_2SO_4, the solvents were evaporated and the product could be recristallised from ethanol producing white powder. MP 123.8^o C (phase transition at 115^o C), ^{1}H NMR ($CDCl_3$) δ 8.60 (d, 1H), 8.22 (q, 1H), 7.77 (d, 2H), 7.62 (d, 2H), 7.5-7.3 (m, 7H), 7.17 (d, 2H), 5.32 (s, 2H), 4.52 (d, 2H), 4.42 (s, 2H), 4.30 (t, 1H), ^{13}C NMR ($CDCl_3$) δ 189.5, 163.6, 159.3, 149.7, 143.3, 141.7, 136.7, 135.5, 135.0, 129.2, 128.8, 128.5, 127.7, 127.4, 127.0, 125.6, 120.6, 118.0, 114.2, 71.8, 71.5 ,46.8, 30.6

Peptide modification

The resin (corresponding to 0.05 mmol peptide) was placed in a dry synthesis column connected to an argon cylinder over a three way valve. The resin was preincubated in 1eq. DIPEA (8.7 µl) in 500 µl DMF. 3 eq. **5** (79 mg) was dissolved in 1 ml anhydrous DMF and added to the solution. The mixture was agitated for 30 min by bubbling argon through the solvent. After coupling, the resin was washed 3x5 min with DMF, 3x5 min with DCM and dried under reduced pressure.

FMOC-Deprotection

The resin was washed and preswollen in DMF. Subsequently, 4 ml of a solution of 2% DBU (FLUKA) and 2% piperidine (Aldrich) in DMF were added and the mixture was agitated for 2 minutes. The resin was washed by 5 ml DMF and the treatment with deprotection solution was repeated 2x2 min and 3x10 min. The resin was washed 3x2 min with DMF, 3x2 min with DCM and dried under reduced pressure.

Peptide cyclisation

The resin (corresponding to 0.05 mmol peptide) was placed in a dry synthesis column connected to an argon cylinder over a three way valve, washed and preswollen in 1 ml anhydrous DMF. A solution of 1 eq. (19 mg) HATU (AnaSpec) in 1 ml DMF was prepared, from which 100 µl were added to the resin. After the addition of 2 eq

DIPEA (17.4 µl) the resin was agitated with argon for 30 min. Another 100 µl of HATU solution was added and the procedure repeated ten times in total. Subsequently, the resin was washed with DMF and DCM.

Peptide cleavage

The resin was transferred to a synthesis column and washed with DCM. 5 ml of a mixture of 3:5:94 TFA:TES:DCM were added and the resin was agitated for two minutes. The solvent was removed and replaced by fresh cleavage mixture. This was repeated three times and another three times with 10 min cleavage time. All the fractions were pooled and evaporated to 10 ml under reduced pressure. The organic phase was extracted with water which was subsequently lyophilised. The lyophilisate was dissolved in 20% acetonitrile, purified over semi-preparative HPLC and lyophilised.

Hydrogenolysis

The lyophilised peptide was transferred to a clean flask containing a magnetic stirrer bar, dissolved in methanol (10 mg in ~3 ml) and an equal amount of palladium on charcoal (weight) was added. The flask was closed with a rubber septum and flushed with H_2. The flask was subsequently pressurised with H_2 and the solution was stirred vigorously. The reaction was monitored by taking aliquots and subsequent HPLC analysis. After completion, water was added, the solution was purified over semi-preparative HPLC and lyophilised.

Test cleavages

Cleavage of resin samples was achieved by shaking the sample for 10 min in 3% trifluoroacetic acid (FLUKA) and 5% triisopropylsilane (ACROS) in DCM. Subsequently DCM and TFA were removed under reduced pressure and 1 ml of water was added. The sample was centrifuged before injection onto the analytical HPLC to spin down precipitated material.

5. Summary

The aim of this thesis was the investigation of the dynamics of elementary steps in protein folding. During folding, the polypeptide chain explores the free energy surface and first interactions are established. These interactions lead to formation of secondary structure elements which then can assemble to form protein structure. Contact formation between different residues in the polypeptide chain limits the rate with which a protein can explore its conformational space and sets an upper limit for the speed of folding.

We studied loop closure reactions in polypeptides and dynamics of α-helices applying the method of triplet-triplet energy transfer (TTET). Triplet excitation is transferred by a two electron exchange mechanism from a xanthone (*Xan*) donor moiety to a naphthalene (*Nal*) acceptor upon van der Waals contact. The transfer reaction is diffusion controlled allowing direct determination of rate constants for loop formation by observing the decay of xanthone triplet absorption or the concomitant increase in naphthalene triplets.

By introducing the triplet labels into unfolded model peptides we wanted to test the effect of polypeptide chain length, amino acid sequence and solvent conditions.

In a short host-guest loop *Xan-Ser-Xaa-Ser-Nal-Ser-Gly-OH* the local effect of different amino acids on loop formation was probed by introducing the guest amino acids *Xaa = Ser, Gly, Pro, Ala, Ile, Glu, Arg* and *His*. We observed similar kinetics for all amino acids except glycine and proline, although amino acids with a C_β-atom showed slightly slower loop closure rate constants. In glycine containing peptides the contact formation rate constant was found to be faster because of the increased flexibility of the glycine residue. The introduction of proline however led to double exponential kinetics. A slow phase corresponding to *trans-Pro* showed the slowest kinetics of all peptides due to the rigid structure of the proline residue, whereas *cis-Pro* showed the fastest kinetics due to the introduction of a kink and thus smaller end-to-end distances.

To probe chain dynamics in a natural loop derived from a protein we introduced the TTET labels into an unstructured 18-residue loop from carp muscle β-parvalbumin. This allowed us to compare loop formation rate constants obtained in a natural sequence to values obtained in model peptides. The kinetics in the parvalbumin loop corresponded well to values obtained for poly-*Ser* chains. This showed that a small

amount of glycine in the sequence can compensate for the slowing down of chain dynamics induced by large amino acids.

During protein folding, interactions are mostly established between amino acids in the interior of the chain. Thus, the effect of additional tails on the loop closure rate constants has to be taken into account. Three types of loops can be distinguished. Type I loops denote end-to-end loops, type II-loops are end-to-interior loops, while type III-loops denote interior-to-interior loops.

We measured loop formation rate constants in type II and type III-loops depending on the size of the additional tails. It was observed that the loop formation rate constant is decreased with increasing size of the tail. For different type II-loops this effect was found to reach a limit when the tail dimensions are about three times larger than the loop size. In this limit, loop closure rates are decreased by a factor of 2.3. For type III-loops the effect of additional tails was found to be stronger than in the type II case. However, the limiting value could not be determined. Assuming that the limit for type III-loop formation is reached at the same tail size as in the type II case this would result in a decrease in loop closure rates by a factor of four.

All observed rate constants in TTET experiments were found to be on the nanosecond time scale. However, faster reaction could not be ruled out. To study reactions on a shorter time scale using TTET it is necessary to understand the photophysics of xanthone triplet formation and energy transfer to naphthalene in detail. Thus, femtosecond timescale experiments were performed to determine the timescale of xanthone intersystem crossing and triplet-triplet energy transfer. It was found that xanthone triplet formation proceeds on the 2 ps timescale and TTET to naphthalene occurs below 2 ps. This allows to observe contact formation processes with time constants of 5-10 ps.

As analysis of initial amplitudes in TTET experiments suggested fast reactions that cannot be observed in nanosecond time resolution experiments, we studied contact formation in small peptides applying femtosecond laserflash spectroscopy. Two fast processes were detected. A faster decay with a time constant of 3-4 ps and 15% amplitude was followed by a slower process on the 100's of picosecond time scale which accounted for 30-40% of the xanthone triplet absorption decay. These fast reactions result from motions of a subpopulation of peptides within a conformational substate on the free energy surface that allows contact without major barrier crossing.

The remaining population of molecules has to sample the free energy surface which leads to exponential kinetics in the nanosecond time range at room temperature.
To gain more insight into the properties of the free energy surface we tested conditions where barrier crossing between the local minima on the free energy surface is slow. At low temperature or high viscosity the kinetics for loop formation were found to deviate from exponential behaviour and could be described by a stretched exponential decay. These results show that the concept of conformational substates which was initially developed to describe protein motions is valid for unstructured polypeptides.

During protein folding, initial contacts lead to formation of local structure. α-helices represent the most abundant and most local secondary structure element. We studied global and local stability and dynamics in α-helices applying TTET to alanine based helical peptides. We introduced TTET labels at different positions and could thus obtain information about local and global helix unfolding and refolding kinetics. We observed that α-helices exhibit higher stability and slower kinetics at central positions, whereas the termini were frayed and showed fluctuations on a faster timescale. These results show that α-helix formation is a complex process and its kinetics are position dependent.
To observe elementary reactions of α-helix formation as nucleation steps or propagation reactions, kinetic experiments have to start with an unfolded ensemble. We developed a synthetic access to a peptide system where an α-helical peptide is cyclised by a photocleavable crosslinker moiety based on a p-hydroxyphenacyl moiety which prevents helix formation. This system can now be used to monitor helix formation upon a fast release of the peptide by nanosecond laser irradiation.

6. Acknowledgements

This work was carried out from November 2002 until April 2006 in the laboratory of Prof. Dr. Thomas Kiefhaber in the Department of Biophysical Chemistry at the Biozentrum of the University of Basel.

At first I want to thank Prof. Thomas Kiefhaber for his excellent supervision, for his motivating support and his endless supply of interesting projects and ideas. I am very grateful for the trust and independency I experienced during my thesis.

Many thanks to Prof. Wolfgang Zinth for the excellent collaboration and fruitful discussions, and special thanks to Helmut Satzger and Christopher Root for performing the femtosecond measurements.

I want to thank my current and former colleagues of the TK lab, in particular Annett, Andi, Andreas, Christophe, Florian, Judith, Joseph, Karin, Manuela, Marilo, Rita, Sarah, Stefan and Therese for the support, discussions, practical help, the good atmosphere and the great time in and outside of the lab.

Thanks to Joseph Wey for synthesis of the xanthonic acid. Further thanks go to Peter Ganz for his support in the organic lab. Thanks to Ignacio Sánchez for his introduction into the synthesis of cyclic helices. Many thanks to Hans-Peter Märki and Hans Fierz for their expert advice on organic synthesis. For proofreading I want to acknowledge Andreas Reiner, Therese Schulthess, Hans Fierz, Hans Peter Märki and Yvonne Märki.

I want to thank the technical workshop, in particular Gernot Hänisch, Hans Vogt, Leo Faletti and Simon Saner for keeping everything up and running.

Finally, I want to thank my parents, family and friends for their support not only during this thesis but through my whole life.

7. References

1. Prusiner, S. B. (1998). Prions. *Proc. Natl. Acad. Sci. USA* 95, 13363-13383.
2. Wu, H. (1931). Studies on denaturation of proteins. *Chin. J. Physiol.* V, 321-344.
3. Anson, M. L. & Mirsky, A. E. (1934). The Equilibrium Between Active Native Trypsin and Inactive Denatured Trypsin. *J. Gen. Physiol.* 17, 393-408.
4. Lumry, R. & Eyring, H. (1954). Conformational Changes of Proteins. *J. Phys. Chem.* 58, 110.
5. Anfinsen, C. B., Haber, E., Sela, M. & White Jr., F. H. (1961). The kinetics of formation of native ribonuclease, during oxidation of the reduced polypeptide chain. *Proc. Natl. Acad. Sci. USA* 47, 1309-1314.
6. Epstein, C. J., Goldberger, R. F. & Anfinsen, C. B. (1963). The genetic control of tertiary protein structure: studies with model systems. *Cold Spring Harbor Symp. Quant. Biol.* 28.
7. Anfinsen, C. B. (1973). Principles that govern the folding of protein chains. *Science* 181, 223-230.
8. Brandts, J. F. (1965). The Nature of the Complexities in the Ribonuclease Conformational Transition and the Implications Regarding Clathrating. *J Am Chem Soc* 87, 2759-60.
9. Kim, P. S. & Baldwin, R. L. (1990). Intermediates in the folding reactions of small proteins. *Annu. Rev. Biochem.* 59, 631-660.
10. Kuwajima, K., Nitta, K., Yoneyama, M. & Sugai, S. (1976). Three-state denaturation of alpha-lactalbumin by guanidine hydrochloride. *J Mol Biol* 106, 359-73.
11. Hughson, F. M., Wright, P. E. & Baldwin, R. L. (1990). Structural characterization of a partly folded apomyoglobin intermediate. *Science* 249, 1544-1548.
12. Lang, K., Schmid, F. X. & Fischer, G. (1987). Catalysis of protein folding by prolyl isomerase. *Nature* 329, 268-270.
13. Fischer, G. (2005). Catalysis of Peptidyl-prolyl cis/trans Isomerization by Enzymes. In *Protein Folding Handbook* (Buchner, J. & Kiefhaber, T., eds.), Vol. 2, pp. 377-414. 2 vols. WILEY-VCH, Weinheim.

14. Collet, J.-F. & Bardwell, J. C. (2005). The Catalysis of Disulfide Bond Formation in Prokaryotes. In *Protein Folding Handbook* (Buchner, J. & Kiefhaber, T., eds.), Vol. 2, pp. 358-376. 2 vols. WILEY-VCH, Weinheim.
15. Buchner, J. & Walter, S. (2005). Analysis of Chaperone Function in Vitro. In *Protein Folding Handbook* (Buchner, J. & Kiefhaber, T., eds.), Vol. 2, pp. 162-196. 2 vols. WILEY-VCH, Weinheim.
16. Jackson, S. E. (1998). How do small single-domain proteins fold? *Folding & Design* 3, R81-R91.
17. Levinthal, C. (1969). *Mössbauer Spectroscopy in Biological Systems, Allerton House, Monticello, Ill.*
18. Tanford, C. (1968). Protein denaturation. *Advan. Prot. Chem.* 23, 121-282.
19. Kiefhaber, T., Labhardt, A. M. & Baldwin, R. L. (1995). Direct NMR evidence for an intermediate preceeding the rate-limiting step in the unfolding of ribonuclease A. *Nature* 375, 513-515.
20. Ikai, A. & Tanford, C. (1971). Kinetic evidence for incorrectly folded intermediate states in the refolding of denatured proteins. *Nature* 230, 100-102.
21. Tsong, T. Y., Baldwin, R. L. & Elson, E. L. (1971). The sequential unfolding of ribonuclease A: detection of a fast initial phase in the kinetics of unfolding. *Proc. Natl. Acad. Sci. USA* 68, 2712-2715.
22. Kim, P. S. & Baldwin, R. L. (1982). Specific intermediates in the folding reactions of small proteins and the mechanism of protein folding. *Annu. Rev. Biochem.* 51, 459-489.
23. Wetlaufer, D. B. (1973). Nucleation, rapid folding, and globular intrachain regions in proteins. *Proc. Natl. Acad. Sci. USA* 70, 697-701.
24. Karplus, M. & Weaver, D. L. (1976). Protein Folding Dynamics. *Nature* 260, 404-406.
25. Karplus, M. & Weaver, D. L. (1994). Protein folding dynamics: The diffusion-collision model and experimental data. *Protein Sci.* 3, 650-668.
26. Baldwin, R. L. & Rose, G. D. (1999). Is protein folding hierarchic? I. Local structure and peptide folding. *Trends Biochem. Sci.* 24, 26-33.
27. Baldwin, R. L. & Rose, G. D. (1999). Is protein folding hierarchic? II. Folding intermediates and transition states. *Trends Biochem. Sci.* 24, 77-83.

28. Jackson, S. E. & Fersht, A. R. (1991). Folding of chymotrypsin inhibitor 2. 1. Evidence for a two-state transition. *Biochemistry* 30, 10428-10435.

29. Jackson, S. E. & Fersht, A. R. (1991). Folding of chymotrypsin inhibitor 2. 2. Influence of proline isomerization on the folding kinetics and thermodynamic characterization of the transition state of folding. *Biochemistry* 30, 10436-10443.

30. Bryngelson, J. D., Onuchic, J. N., Socci, N. D. & Wolynes, P. G. (1995). Funnels, pathways, and the energy landscape of protein folding: A synthesis. *Proteins: Struct. Funct. Genet.* 21, 167-195.

31. Ansari, A., Berendzen, J., Bowne, S. F., Frauenfelder, H., Iben, I. E., Sauke, T. B., Shyamsunder, E. & Young, R. D. (1985). Protein states and proteinquakes. *Proc Natl Acad Sci U S A* 82, 5000-4.

32. Zwanzig, R., Szabo, A. & Bagchi, B. (1992). Levinthal's paradox. *Proc. Natl. Acad. Sci. USA* 89, 20-22.

33. Bachmann, A. & Kiefhaber, T. (2001). Apparent two-state tendamistat folding is a sequential process along a defined route. *J. Mol. Biol.* 306, 375-386.

34. Sanchez, I. E. & Kiefhaber, T. (2003). Evidence for sequential barriers and obligatory intermediates in apparent two-state protein folding. *J Mol Biol* 325, 367-76.

35. Wagner, C. & Kiefhaber, T. (1999). Intermediates can accelerate protein folding. *Proc. Natl. Acad. Sci. USA* 96, 6716-6721.

36. Eyring, H. (1935). The activated complex in chemical reactions. *J. Chem. Phys.* 3, 107-115.

37. Sanchez, I. E. & Kiefhaber, T. (2003). Hammond behavior versus ground state effects in protein folding: evidence for narrow free energy barriers and residual structure in unfolded states. *J Mol Biol* 327, 867-84.

38. Kiefhaber, T., Sanchez, I. E. & Bachmann, A. (2005). Characterization of Protein Folding Barriers with Rate Equilibrium Free Energy Relationships. In *Protein Folding Handbook* (Buchner, J. & Kiefhaber, T., eds.), Vol. 1, pp. 411-444. 2 vols. WILEY-VCH, Weinheim.

39. Sanchez, I. E. & Kiefhaber, T. (2003). Non-linear rate-equilibrium free energy relationships and Hammond behavior in protein folding. *Biophys Chem* 100, 397-407.

40. Chen, B. L. & Schellman, J. A. (1989). Low-temperature unfolding of a mutant of phage T4 lysozyme. 1. Equilibrium studies. *Biochemistry* 28, 685-691.

41. Pappenberger, G., Saudan, C., Becker, M., Merbach, A. E. & Kiefhaber, T. (2000). Denaturant-induced movement of the transition state of protein folding revealed by high pressure stopped-flow measurements. *Proc. Natl. Acad. Sci. USA* 97, 17-22.

42. Matthews, C. R. (1987). Effect of point mutations on the folding of globular proteins. *Meth. Enzymol.* 154, 498-511.

43. Goldenberg, D. P., Frieden, R. W., Haack, J. A. & Morrison, T. B. (1989). Mutational analysis of a protein-folding pathway. *Nature* 338, 127-32.

44. Fersht, A. R., Matouschek, A. & Serrano, L. (1992). The folding of an enzyme. I. Theory of protein engineering analysis of stability and pathway of protein folding. *J. Mol. Biol.* 224, 771-782.

45. Myers, J. K., Pace, C. N. & Scholtz, J. M. (1995). Denaturant m values and heat capacity changes: relation to changes in accessible surface areas of protein unfolding. *Protein Sci.* 4, 2138-2148.

46. Sanchez, I. E. & Kiefhaber, T. (2003). Origin of Unusual phi-Values in Protein Folding: Evidence Against Specific Nucleation Sites. *J. Mol. Biol.* 334, 1077-1085.

47. Makarov, D. E., Keller, C. A., Plaxco, K. W. & Metiu, H. (2002). How the folding rate constant of simple, single-domain proteins depends on the number of native contacts. *Proc Natl Acad Sci U S A* 99, 3535-9.

48. Vendruscolo, M., Paci, E., Dobson, C. M. & Karplus, M. (2001). Three key residues form a critical contact network in a protein folding transition state. *Nature* 409, 641-645.

49. Kramers, H. A. (1940). Brownian motion in a field of force and the diffusion model of chemical reactions. *Physica* 4, 284-304.

50. Hänggi, P., Talkner, P. & Borkovec, M. (1990). Reaction-rate theory: fifty years after Kramers. *Rev. Mod. Phys.* 62, 251-341.

51. Fierz, B. & Kiefhaber, T. (2005). Dynamics of Unfolded Polypeptide Chains. In *Protein Folding Handbook* (Buchner, J. & Kiefhaber, T., eds.), Vol. 1, pp. 809-855. 2 vols. WILEY-VCH, Weinheim.

52. Zhu, W., Gisser, D. J. & Ediger, M. D. (1994). C-13 Nmr Measurements of Polybutadiene Local Dynamics in Dilute-Solution - Further Evidence for

Non-Kramers Behavior. *Journal of Polymer Science Part B-Polymer Physics* 32, 2251-2262.

53. Zhu, W. & Ediger, M. D. (1997). Viscosity Dependence of Polystyrene Local Dynamics in Dilute Solutions. *Macromolecules* 30, 1205-1210.
54. Tylianakis, E. I., Dais, P. & Heatley, F. (1997). Non-Kramers' Behavior of the Chain Local Dynamics of PVC in Dilute Solution. Carbon-13 NMR Relaxation Study. *J Polym Sci: Part B* 35, 317-329.
55. Moglich, A., Krieger, F. & Kiefhaber, T. (2005). Molecular basis for the effect of urea and guanidinium chloride on the dynamics of unfolded polypeptide chains. *J Mol Biol* 345, 153-62.
56. Beece, D., Eisenstein, L., Frauenfelder, H., Good, D., Marden, M. C., Reinisch, L., Reynolds, A. H., Sorensen, L. B. & Yue, K. T. (1980). Solvent Viscosity and Protein Dynamics. *Biochemistry* 19, 5147-5157.
57. Yedgar, S., Tetreau, C., Gavish, B. & Lavalette, D. (1995). Viscosity dependence of O2 escape from respiratory proteins as a function of cosolvent molecular weight. *Biophys J* 68, 665-70.
58. Kleinert, T., Doster, W., Leyser, H., Petry, W., Schwarz, V. & Settles, M. (1998). Solvent Composition and Viscosity Effects on the Kinetics of CO Binding to Horse Myoglobin. *Biochemistry* 37, 717-733.
59. Timasheff, S. N. (2002). Protein hydration, thermodynamic binding and prefential hydration. *Biochemistry* 41, 13473-13482.
60. Gavish, B. (1980). Position-Dependent Viscosity Effects on Rate Coefficients. *Physical Review Letters* 44, 1160-1163.
61. Doster, W. (1983). Viscosity Scaling and Protein Dynamics. *Biophysical Chemistry* 17, 97-103.
62. Schlitter, J. (1988). Viscosity Dependence of Intramolecular Activated Processes. *Chemical Physics* 120, 187-197.
63. Grote, R. F. & Hynes, J. T. (1980). The stable states picture of chemical reactions. II. Rate constants for condensed and gas phase reaction models. *J. Chem. Phys.* 73, 2715-2732.
64. Careri, G., Fasella, P. & Gratton, E. (1979). Enzyme dynamics: the statistical physics approach. *Annu Rev Biophys Bioeng* 8, 69-97.

65. Wagner, G. (1983). Characterization of the distribution of internal motions in the basic pancreatic trypsin inhibitor using a large number of internal NMR probes. *Q Rev Biophys* 16, 1-57.

66. Sporlein, S., Carstens, H., Satzger, H., Renner, C., Behrendt, R., Moroder, L., Tavan, P., Zinth, W. & Wachtveitl, J. (2002). Ultrafast spectroscopy reveals subnanosecond peptide conformational dynamics and validates molecular dynamics simulation. *Proc Natl Acad Sci U S A* 99, 7998-8002.

67. Krieger, F., Fierz, B., Bieri, O., Drewello, M. & Kiefhaber, T. (2003). Dynamics of Unfolded Polypeptide Chains as a Model for the Earliest Steps in Protein Folding. *J Mol Biol* 332, 265-274.

68. Sinev, M. A., Sineva, E. V., Ittah, V. & Haas, E. (1996). Domain closure in adenylate kinase. *Biochemistry* 35, 6425-37.

69. Kay, L. E. (1998). Protein dynamics from NMR. *Nat. Struct. Biol.* 5, 513-517.

70. Ishima, R. & Torchia, D. A. (2000). Protein dynamics from NMR. *Nat. Struc. Biol.* 7, 740-743.

71. Ames, J. B., Ros, M., Raap, J., Lugtenburg, J. & Mathies, R. A. (1992). Time-resolved ultraviolet resonance Raman studies of protein structure: application to bacteriorhodopsin. *Biochemistry* 31, 5328-34.

72. Gilmanshin, R., Williams, S., Callender, R. H., Woodruff, W. H. & Dyer, R. B. (1997). Fast events in protein folding: relaxation dynamics and structure of the I form of apomyoglobin. *Biochemistry* 36, 15006-12.

73. Frauenfelder, H., Sligar, S. G. & Wolynes, P. G. (1991). The energy landscapes and motions of proteins. *Science* 254, 1598-603.

74. Austin, R. H., Beeson, K. W., Eisenstein, L., Frauenfelder, H. & Gunsalus, I. C. (1975). Dynamics of ligand binding to myoglobin. *Biochemistry* 14, 5355-5373.

75. Post, F., Doster, W., Karvounis, G. & Settles, M. (1993). Structural relaxation and nonexponential kinetics of CO-binding to horse myoglobin. Multiple flash photolysis experiments. *Biophys J* 64, 1833-42.

76. Tian, W. D., Sage, J. T., Champion, P. M., Chien, E. & Sligar, S. G. (1996). Probing heme protein conformational equilibration rates with kinetic selection. *Biochemistry* 35, 3487-502.

77. Frauenfelder, H., Petsko, G. A. & Tsernoglou, D. (1979). Temperature-dependent X-ray diffraction as a probe of protein structural dynamics. *Nature* 280, 558-63.

78. Hofmann, C., Aartsma, T. J., Michel, H. & Köhler, G. (2003). Direct observation of tiers in the energy landscape of a chromoprotein: A single molecule study. *Proc. Natl. Acad. Sci. USA* 100, 15534-15538.

79. Ginsburg, A. & Carrol, W. R. (1965). Some specific ion effects on the conformation and thermal stability of ribonuclease. *Biochemistry* 4, 2159-2174.

80. Tanford, C., Pain, R. H. & Otchin, N. S. (1966). Equilibrium and kinetics of the unfoldign of lysozyme (muramidase) by guanidinium hydrochloride. *J. Mol. Biol.* 15, 489-504.

81. Tanford, C. (1970). Protein Denaturation. Part C. Theoretical models for the mechanism of denaturation. *Adv. Prot. Chem.* 24, 1-95.

82. Flory, P. J. (1969). *Statistical Mechanics of Chain Molecules*, Hanser Publishers, Munich.

83. Millet, I. S., Doniach, S. & Plaxco, K. W. (2002). Toward a taxonomy of the denatured state: small angle scattering studies of unfolded proteins. *Adv. Protein Chem.* 62, 241-262.

84. Fleming, P. J. & Rose, G. D. (2005). *Conformational Properties of Unfolded Proteins*. Protein Folding Handbook (Buchner, J. & Kiefhaber, T., Eds.), WILEY-VCH, Weinheim.

85. Damaschun, G., Damaschun, H., Gast, K. & Zirwer, D. (1998). Denatures states of yeast phosphoglycerate kinase. *Biochemistry (Moscow)* 63, 259-275.

86. Neri, D., Billeter, M., Wider, G. & Wüthrich, K. (1992). NMR determination of residual structure in a urea-denatured protein, the 434-repressor. *Science* 257, 1559-1563.

87. Klein-Seetharaman, J., Oikawa, M., Grimshaw, S. B., Wirmer, J., Duchardt, E., Ueda, T., Imoto, T., Smith, L. J., Dobson, C. M. & Schwalbe, H. (2002). Long-range interactions within a nonnative protein. *Science* 295, 1719-1722.

88. Shortle, D. & Ackerman, M. (2001). Persistence of native-like topology in a denatured protein in 8M Urea. *Science* 293, 487-489.

89. Kohn, J. E., Millett, I. S., Jacob, J., Zagrovic, B., Dillon, T. M., Cingel, N., Dothager, R. S., Seifert, S., Thiyagarajan, P., Sosnick, T. R., Hasan, M. Z.,

Pande, V. S., Ruczinski, I., Doniach, S. & Plaxco, K. W. (2004). Random-coil behavior and the dimensions of chemically unfolded proteins. *Proc Natl Acad Sci U S A* 101, 12491-6.

90. Dyson, H. J., Merutka, G., Waltho, J. P., Lerner, R. A. & Wright, P. E. (1992). Folding of peptide fragments comprising the complete sequence of proteins. Models for initiation of protein folding. I. Myohemerythrin. *J Mol Biol* 226, 795-817.
91. Tiffany, M. L. & Krimm, S. (1968). New chain conformations of poly(glutamic acid) and polylysine. *Biopolymers* 6, 1379-82.
92. Tiffany, M. L. & Krimm, S. (1973). Extended conformations of polypeptides and proteins in urea and guanidine hydrochloride. *Biopolymers* 1, 575-587.
93. Shi, Z., Woody, R. W. & Kallenbach, N. R. (2002). Is polyproline II a major backbone conformation in unfolded proteins? *Adv Protein Chem* 62, 163-240.
94. Stapley, B. J. & Creamer, T. P. (1999). A survey of left-handed polyproline II helices. *Protein Sci* 9, 587-595.
95. Creamer, T. P. (1998). Left-handed polyproline II helix formation is (very) locally driven. *Proteins* 33, 218-226.
96. Rucker, A. L., Pager, C. T., Campbell, M. N., Qualls, J. E. & Creamer, T. P. (2003). Host-guest scale of left-handed polyproline II helix formation. *Proteins* 53, 68-75.
97. Shi, Z., Olson, C. A., Rose, G. D., Baldwin, R. L. & Kallenbach, N. R. (2002). Polyproline II structure in a sequence of seven alanine residues. *Proc Natl Acad Sci U S A* 99, 9190-5.
98. Fitzkee, N. C. & Rose, G. D. (2004). Reassessing random-coil statistics in unfolded proteins. *Proc Natl Acad Sci U S A* 101, 12497-502.
99. Pappu, R. V., Srinivasan, R. & Rose, G. D. (2000). The Flory isolated-pair hypthesis is not valid for polypeptide chains: Implications for protein folding. *Proc. Natl. Acad. Sci. USA* 97, 12565-12570.
100. Munoz, V., Thompson, P., Hofrichter, J. & Eaton, W. (1997). Folding dynamics and mechanism of β-hairpin formation. *Nature* 390, 196-199.
101. Zimm, B. H. & Bragg, J. K. (1959). Theory of phase transition between helix and random coil in polypeptide chains. *Journ. Chem. Phys.* 31, 526-535.
102. Lifson, S. & Roig, A. (1961). On the theory of helix-coil transitions in polypeptides. *J. Chem. Phys.* 34, 1963-1974.

103. Schwarz, G. & Seelig, J. (1968). Kinetic Properties and the Electric Field Effect of the Helix-Coil Transition of Poly(g-benzyl L-Glutamate) Determined from Dielectric Relaxation Measurements. *Biopolymers* 6.

104. Gruenewald, B., Nicola, C. U., Lustig, A. & Schwarz, G. (1979). Kinetics of the helix-coil transition of a polypeptide with non-ionic side chain groups, derived from ultrasonic relaxation measurements. *Biopys. Chem.* 9, 137-147.

105. Williams, S., Causgrove, T. P., Gilmanshin, R., Fang, K. S., Callender, R. H., Woodruff, W. H. & Dyer, R. B. (1996). Fast events in protein folding: helix melting and formation in a small peptide. *Biochemistry* 35, 691-697.

106. Thompson, P., Eaton, W. & Hofrichter, J. (1997). Laser temperature jump study of the helix-coil kinetics of an alanine peptide interpreted with a "kinetic zipper" model. *Biochemistry* 36, 9200-9210.

107. Kuhn, W. (1934). Über die Gestalt fadenförmiger Moleküle in Lösungen. *Kolloid-Z* 52, 269.

108. Brant, D. A. & Flory, P. J. (1965). The configuration of random polypeptide chains. II. Theory. *J. Am. Chem. Soc.* 87, 2791-2800.

109. Ramachandran, G. N. & Sasisekharan, V. (1968). Conformation of polypeptides and proteins. *Advan. Protein Chem.* 23, 283-437.

110. Brant, D. A., Miller, W. G. & Flory, P. J. (1967). Conformational energy estimates for statistically coiling polypeptide chains. *J Mol Biol* 23, 47.

111. Schimmel, P. R. & Flory, P. J. (1967). Conformational energy and configurational statistics of poly-L-proline. *Proc. Natl. Acad. Sci. USA* 58, 52-59.

112. Brant, D. A. & Flory, P. J. (1965). The Configuration of Random Polypeptide Chains. I. Experimental Results. *J Am Chem Soc* 87, 2788-2791.

113. Flory, P. J. (1953). *Principles of polymer chemistry*, Cornell University Press, Ithaca.

114. de Gennes, P. G. (1979). *Scaling Concepts in Polymer Physics*, Cornell University Press, Ithaca, New York.

115. Edwards, S. F. (1965). The statistical mechanics of polymers with excluded volume. *Proc. Phys. Soc.* 85, 613-624.

116. Möglich, A. & Kiefhaber, T. (2006). Effect of Guanidinium Chloride on Dimensions and Dynamics of Unfolded Polypeptide Chains. *To be submitted*.

117. Gardiner, C. W. (1985). *Handbook of Stochastic Methods*, Springer Verlag, Berlin, Heidelberg, New York.

118. Rouse, P. E. (1953). A theory of the linear viscoelastic properties of dilute solutions of coiling polymers. *J. Chem. Phys.* 21, 1272-1280.

119. Zimm, B. (1956). Dynamics of polymer molecules in dilute solutions: viscoelasticity, flow bifringence and dielectric loss. *J. Chem. Phys.* 24, 269-278.

120. Doi, M. & Edwards, S. F. (1986). *The Theory of Polymer Dynamics*, Oxford University Press, Oxford, UK.

121. Kirkwood, J. G. & Riseman, J. (1948). The Intrinsic Viscosities and Diffusion Constants of Flexible Macromolecules in Solution. *J Chem Phys* 21, 565-573.

122. Bixon, M. & Zwanzig, R. (1978). Optimized Rouse-Zimm theory for stiff polymers. *J Chem Phys* 68, 1896-1902.

123. Jacobsen, H. & Stockmayer, W. H. (1950). Intramolecular reaction in polycondensations. I. The theory of linear systems. *J. Phys. Chem.* 18, 1600-1606.

124. Wilemski, G. & Fixman, M. (1974). Diffusion-controlled intrachain reactions of polymers. II Results for a pair of terminal reactive groups. *J Chem Phys* 878-890.

125. Wilemski, G. & Fixman, M. (1973). General Theory of diffusion-controlled reactions. *J Chem Phys* 58, 4009-4019.

126. Wilemski, G. & Fixman, M. (1974). Diffusion-controlled intrachain reactions of polymers. I Theory. *J Chem Phys* 60, 866-877.

127. Pastor, R. W., Zwanzig, R. & Szabo, A. (1996). Diffusion limited first contact of the ends of a polymer: Comparison of theory with simulation. *J Chem Phys* 105, 3878-3882.

128. Perico, A. & Cuniberti, C. (1977). Dynamics of chain molecules. Intramolecular diffusion controlled reactions for a pair of terminal reactive groups. *J. Polym. Sci., Polym. Phys. Ed.* 15, 1435.

129. Perico, A., Piaggio, P. & Cuniberti, C. (1975). Dynamics of chain molecules. I. Solutions to the hydrodynamic equation and intrinsic viscosity. *J Chem Phys* 62, 4911.

130. Perico, A. & Beggiato, M. (1990). Intramolecular Diffusion-Controlled Reactions in Polymers in the Optimized Rouse Zimm Approach .1. The Effects of Chain Stiffness, Reactive Site Positions, and Site Numbers. *Macromolecules* 23, 797-803.

131. Szabo, A., Schulten, K. & Schulten, Z. (1980). First passage time approach to diffusion controlled reactions. *J. Chem. Phys.* 72, 4350-4357.

132. Fixman, M. (1978). Simulation of polymer dynamics. II. Relaxation rates and dynamic viscosity. *J Chem Phys* 69, 1538-1545.

133. Fixman, M. (1978). Simulation of polymer dynamics. I. General theory. *J Chem Phys* 69, 1527-1537.

134. Perico, A. & Cuniberti, C. (1977). Intramolecular excimers and microbrownian motion of flexible polymer molecules in solution. *Eur. Polym. J.* 13, 369.

135. Winnik, M. A., Redpath, T. & Richards, D. H. (1980). The Dynamics of End-to-End Cyclization in Polystyrene Probed by Pyrene Excimer Formation. *Macromolecules* 13, 328-335.

136. Winnik, M. A. (1981). Cyclization and the Conformation of Hydrocarbon Chains. *Chem. Rev.* 81, 491-524.

137. Haas, E., Wilchek, M., Katchalskikatzir, E. & Steinberg, I. Z. (1975). Distribution of End-to-End Distances of Oligopeptides in Solution as Estimated by Energy-Transfer. *Proceedings of the National Academy of Sciences of the United States of America* 72, 1807-1811.

138. Haas, E., Katchalski-Katzir, E. & Steinberg, I. Z. (1978). Brownian motion at the ends of oligopeptid chains as estimated by energy transfer between chain ends. *Biopolymers* 17, 11-31.

139. Jones, C. M., Henry, E. R., Hu, Y., Chan, C.-K., Luck, S. D., Byuhan, A., Roder, H., Hofrichter, J. & Eaton, W. A. (1993). Fast events in protein folding initiated by nanosecond laser photolysis. *Proc. Natl. Acad. Sci. USA* 90, 11860-11864.

140. Hagen, S. J., Hofrichter, J., Szabo, A. & Eaton, W. A. (1996). Diffusion-limited contact formation in unfolded cytochrome c: Estimating the maximum rate of protein folding. *Proc. Natl. Acad. Sci. USA* 93, 11615-11617.

141. Bieri, O., Wirz, J., Hellrung, B., Schutkowski, M., Drewello, M. & Kiefhaber, T. (1999). The speed limit for protein folding measured by triplet-triplet energy transfer. *Proc. Natl. Acad. Sci. USA* 96, 9597-9601.

142. Lapidus, L. J., Eaton, W. A. & Hofrichter, J. (2000). Measuring the rate of intramolecular contact formation in polypeptides. *Proc. Natl. Acad. Sci. USA* 97, 7220-7225.

143. Hudgins, R. R., Huang, F., Gramlich, G. & Nau, W. M. (2002). A fluorescence-based method for direct measurements of submicroscond intramolecular contact formation in biopolymers: an exploratory study with polypeptides. *J. Am. Chem. Soc.* 124, 556-564.

144. Barlow, D. J. & Thornton, J. M. (1988). Helix geometry in proteins. *J Mol Biol* 201, 601-19.

145. Waltho, J. P., Feher, V. A., Merutka, G., Dyson, H. J. & Wright, P. E. (1993). Peptide models of protein folding initiation sites. 1. Secondary structure formation by peptides corresponding to the G- and H- helices of myoglobin. *Biochemistry* 32, 6337-6347.

146. Yao, J., Chung, J., Eliezer, D., Wright, P. E. & Dyson, H. J. (2001). NMR structural and dynamic characterization of the acid-unfolded state of apomyoglobin provides insights into the early events in protein folding. *Biochemistry* 40, 3561-71.

147. Shoemaker, K. R., Kim, Brems, Marqusee, York, Chaiken, Stewart & Baldwin, R. L. (1985). Nature of the charged group effect on the stability of the C-peptide helix. *Proc. Natl. Acad. Sci. USA* 82, 2349-2353.

148. Marqusee, S. & Baldwin, R. L. (1987). Helix stabilization by Glu-…Lys+ salt bridges in short peptides of de novo design. *Proc. Natl. Acad. Sci. USA* 84, 8898-8902.

149. Marqusee, S., Robbins, V. H. & Baldwin, R. L. (1989). Unusually stable helix formation in short alanine-based peptides. *Proc Natl Acad Sci U S A* 86, 5286-5290.

150. Munoz, V. & Serrano, L. (1994). Elucidating the folding problem of helical peptides using empirical parameters. *Nature Struct. Biol.* 1, 399-409.

151. Munoz, V. & Serrano, L. (1995). Elucidating the folding problem of helical peptides using empirical parameters. III. Temperature and pH dependence. *J. Mol. Biol.* 3, 297-308.

152. Munoz, V. & Serrano, L. (1995). Elucidating the folding problem of helical peptides using empirical paramters. II. Helix macrodipole effects and rational modification of the helical content of natural peptides. *J. Mol. Biol.* 3, 275-296.

153. Schwarz, G. (1965). On the kinetics of the helix-coil transition of polypeptides in solution. *J. Mol. Biol.* 11, 64-77.

154. Poland, D. & Scheraga, H. (1966). Kinetics of the Helix—Coil Transition in Polyamino Acids. *J Chem Phys* 45, 2071-2091.

155. Rohl, C. A. & Baldwin, R. L. (1994). Exchange kinetics of individual amide protons in 15N-labeled helical peptides measured by isotope-edited NMR. *Biochemistry* 33, 7760-7.

156. Chakrabartty, A., Schellman, J. A. & Baldwin, R. L. (1991). Large differences in the helix propensities of alanine and glycine. *Nature* 351, 586-588.

157. Jimenez, M. A., Blanco, F. J., Rico, M., Santoro, J., Herranz, J. & Nieto, J. L. (1992). Periodic properties of proton conformational shifts in isolated protein helices. An experimental study. *Eur J Biochem* 207, 39-49.

158. Liff, M. I., Lyu, P. C. & Kallenbach, N. R. (1991). Local effect of glycine substitution in a model helical peptide. *J Am Chem Soc* 113, 1014-1019.

159. Bradley, E. K., Thomason, J. F., Cohen, F. E., Kosen, P. A. & Kuntz, I. D. (1990). Studies of synthetic helical peptides using circular dichroism and nuclear magnetic resonance. *J Mol Biol* 215, 607-22.

160. Pease, J. H., Storrs, R. W. & Wemmer, D. E. (1990). Folding and activity of hybrid sequence, disulfide-stabilized peptides. *Proc Natl Acad Sci U S A* 87, 5643-7.

161. Osterhout, J. J., Baldwin, R. L., York, E. J., Stewart, J. M., Dyson, H. J. & Wright, P. E. (1989). 1H NMR studies of the solution conformations of an analogue of the C-peptide of ribonuclease A. *Biochemistry* 28, 7059-7064.

162. Miick, S. M., Casteel, K. M. & Millhauser, G. L. (1993). Experimental molecular dynamics of an alanine-based helical peptide determined by spin label electron spin resonance. *Biochemistry* 32, 8014-21.

163. Miick, S. M., Todd, A. P. & Millhauser, G. L. (1991). Position-dependent local motions in spin-labeled analogues of a short alpha-helical peptide determined by electron spin resonance. *Biochemistry* 30, 9498-503.

164. Thompson, P. A., Munoz, V., Gouri, S. J., Henry, E., Eaton, W. A. & Hofrichter, J. (2000). The Helix-Coil Kinetics of a Heteropeptide. *J. Phys. Chem. B* 104, 378-389.

165. Lednev, I. K., Karnoup, A. S., Sparrow, M. C. & Asher, S. A. (1999). Alpha-Helix Peptide Folding and Unfolding Activation Barriers: A Nanosecond UV Resonance Raman Study. *J Am Chem Soc* 121, 8074-8086.

166. Huang, C. Y., Getahun, Z., Wang, T., DeGrado, W. F. & Gai, F. (2001). Time-resolved infrared study of the helix-coil transition using (13)C-labeled helical peptides. *J Am Chem Soc* 123, 12111-2.

167. Venyaminov, S. Y., Hedstrom, J. F. & Prendergast, F. G. (2001). Analysis of the segmental stability of helical peptides by isotope-edited infrared spectroscopy. *Proteins* 45, 81-9.

168. Wernder, J. H., Dyer, R. B., Fesinmeyer, R. M. & Andersen, N. H. (2002). Dynamics of the Primary Processes of Protein Foldign: Helix Nucleation. *J. Phys. Chem. B* 106, 487-494.

169. Turro, N. (1991). *Modern Molecular Photochemistry*, University Science Books, Sausalito, California.

170. Dexter, D. L. (1953). A Theory of Sensitized Luminescence in Solids. *J Chem Phys* 21, 836-850.

171. Satzger, H., Schmidt, B., Root, C., Zinth, W., Fierz, B., Krieger, F., Kiefhaber, T. & Gilch, P. (2004). Ultrafast Quenching of the Xanthone Triplet by Energy Transfer: New Insight into the Intersystem Crossing Kinetics. *J. Phys. Chem. A* 108, 10072-10079.

172. Murov, S. L., I. Carmichael, I. & Hug, G. L. (1993). *Handbook of Photochemistry*. 2nd edit, Dekker, New York.

173. Fierz, B., Satzger, H., Root, C., Gilch, P., Zinth, W. & Kiefhaber, T. (2007). Loop formation in unfolded polypeptide chains on the picoseconds to microseconds time scale. *Proc. Natl. Acad. Sci. U S A,* 107, 2163-2168

174. Krieger, F., Moeglich, A. & Kiefhaber, T. (2005). Effect of Proline and Glycine Residues on Dynamics and Barriers of Loop Formation in Polypeptide Chains. *J. Am. Chem. Soc.* 127, 3346-3352.

175. Lockhart, D. J. & Kim, P. S. (1992). Internal stark effect measurement of the electric field at the amino terminus of an α-helix. *Science* 257, 947-951.

176. Lockhart, D. J. & Kim, P. S. (1993). Electrostatic screening of charge and dipole interactions with the helix backbone. *Science* 260, 198-202.

177. Volk, M., Kholodenko, Y., Lu, H. S. M., Gooding, E. A., DeGrado, W. F. & Hochstrasser, R. M. (1997). Peptide conformational dynamics and vibrational stark effects following photoinitiated disulfide cleavage. *J. Phys. Chem.* 101, 8607-8616.

178. Givens, R. S., Jung, A., Park, C.-H., Weber, J. & Bartlett, W. J. (1997). New Photoactivated Protecting Groups. 7. p-Hydroxyphenacyl: A Phototrigger for Excitatory Amino Acids and Peptides. *J. Am. Chem. Soc.* 119, 8369.

179. Givens, R. S. & Chan-Ho, P. (1996). p-hydroxyphenacyl ATP: a new phototrigger. *Tetrahedron Lett.* 37, 6259-6262.

180. Park, C.-H. & Givens, R. S. (1997). New Photoactivated Protecting Groups. 6. p-Hydroxyphenacyl: A Phototrigger for Chemical and Biochemical Probes. *J. Am. Chem. Soc.* 119, 2453-2463.

181. Conrad II, P. G., Givens, R. S., Hellrung, B., Rajesh, C. S., Ramseier, M. & Wirz, J. (2000). p-Hydroxyphenacyl Phototriggers: The Reactive Excited State of Phosphate Photorelease. *J. Am. Chem. Soc.* 122, 9346-9347.

182. Kessler, H. & Siegmeier, R. (1983). 9-fluorenylmethyl esters as carboxyl protection group. *Tetrahedron Lett.* 24, 281-282.

183. Froussios, C. & Kolovos, M. (1989). Nouvelle methode de protection du carboxyle des acides a-amines: esters 9-fluorenyliques. *Tetrahedron Lett.* 30, 3413-3414.

184. Bednarek, M. & Bodanszky, M. (1983). 9-Fluorenylmethyl esters. *Int J Pept Protein Res* 21, 196-201.

185. Merette, S. A. M., Burd, A. P. & Deadman, J. J. (1999). Synthesis of 9-Fluorenylmethyl Esters Using 9-Fluorenylmethylchloroformate. *Tetrahedron Lett.* 40, 753-754.

186. King, L. C. & Ostrum, G. K. (1964). Selective Bromination with Copper(II) Bromide. *J. Org. Chem.* 29, 3459-3461.

187. Kajigaeshi, S., Kakinami, T., Okamoto, T. & Fujisaki, S. (1987). Synthesis of Bromoacetyl Derivates by Use of Tetrabutylammonium Tribromide. *Bull. Chem. Soc. Jpn.* 60, 1159-1160.

188. Kates, S. A., Solé, N. A., Johnson, C. R., Hudson, D., Barany, G. & Albericio, F. (1993). A novel, convenient, three-dimensional orthogonal strategy for solid-phase synthesis of cyclic peptides. *Tetrahedron Lett.* 34, 1549-1552.

189. Aletras, A., Barlos, K., Gatos, D., Koutsogianni, S. & Mamos, P. (1995). Preparation of the very acid-sensitive Fmoc-Lys(Mtt)-OH. Application in the synthesis of side-chain to side-chain cyclic peptides and oligolysine cores suitable for the solid-phase assembly of MAPs and TASPs. *Int J Pept Protein Res* 45, 488-96.

190. Chan, W. C. & White, P. D. (2000). *Peptide Synthesis: A practical Approach*. The Practial Approach Series (Hames, B. D., Ed.), Oxford University Press, Oxford.

191. Carpino, L. A. (1993). 1-Hydroxy-7-azabenzotriazole. An efficient peptide coupling additive. *J. Am. Chem. Soc.* 115, 4397.

192. Bofill, J. M. & Albericio, F. (1999). Understanding the structure/reactivity of aminium/uronium salts as coupling reagents in peptide synthesis. *Tetrahedron Lett.* 40, 2641.

193. Kates, S. A., Daniels, S. B., Solé, N. A., Barany, G. & Albericio, F. (1994). Automated allyl chemistry for solid-phase peptide synthesis: applications to cyclic and branched peptides. In *Peptides: Chemistry, Structure and Biology, Proc. 13th American Peptide Symposium* (Hodges, R. S. & Smith, J. A., eds.), pp. 113. ESCOM, Leiden.

194. Lauer, J. L., Fields, C. G. & Fields, G. B. (1994). Sequence dependence of aspartimide formation during 9-fluorenylmethoxycarbonyl solid-phase peptide synthesis. *Lett. Peptide Sci.* 1, 197-205.

195. Gausepohl, H. (1992). Schiff base analog formation during in situ activation by HBTU and TBTU. In *Peptides, Chemistry and Biology. Proceedings of the 12th American Peptide Symposium* (Smith, J. A. & Rivier, J. E., eds.), pp. 523. ESCOM, Leiden.

196. Marsh Jr., J. P. & Goodman, L. (1965). Removal of O-Benzyl Blocking Groups with Trifluoroacetic acid. *J. Org. Chem.* 30, 2491.

197. Rosenheck, K. & Doty, P. (1961). The far ultraviolet absorption spectra of polypeptide and protein solutions and their dependence on conformation. *Proc. Natl. Acad. Sci. U.S.A.* 47, 1775-1785.

8. Published Work and Manuscripts Ready for Submission

doi:10.1016/S0022-2836(03)00892-1 *J. Mol. Biol.* (2003) **332**, 265–274

JMB

Available online at www.sciencedirect.com

SCIENCE DIRECT®

ELSEVIER

Dynamics of Unfolded Polypeptide Chains as Model for the Earliest Steps in Protein Folding

Florian Krieger[1], Beat Fierz[1], Oliver Bieri[1], Mario Drewello[2] and Thomas Kiefhaber[1]*

[1]*Department of Biophysical Chemistry, Biozentrum der Universität Basel Klingelbergstr. 70, CH-4056 Basel, Switzerland*

[2]*Max-Planck Arbeitsgruppe "Enzymologie der Proteinfaltung", Weinbergweg 22a, D-06120 Halle, Germany*

**Corresponding author*

The rate of formation of intramolecular interactions in unfolded proteins determines how fast conformational space can be explored during folding. Characterization of the dynamics of unfolded proteins is therefore essential for the understanding of the earliest steps in protein folding. We used triplet–triplet energy transfer to measure formation of intrachain contacts in different unfolded polypeptide chains. The time constants $(1/k)$ for contact formation over short distances are almost independent of chain length, with a maximum value of about 5 ns for flexible glycine-rich chains and of 12 ns for stiffer chains. The rates of contact formation over longer distances decrease with increasing chain length, indicating different rate-limiting steps for motions over short and long chain segments. The effect of the amino acid sequence on local chain dynamics was probed by using a series of host-guest peptides. Formation of local contacts is only sixfold slower around the stiffest amino acid (proline) compared to the most flexible amino acid (glycine). Good solvents for polypeptide chains like EtOH, GdmCl and urea were found to slow intrachain diffusion and to decrease chain stiffness. These data allow us to determine the time constants for formation of the earliest intrachain contacts during protein folding.

Keywords: protein folding; chain dynamics; intrachain diffusion; triplet–triplet transfer; unfolded proteins

Introduction

Many biological polymers have to form specific intramolecular interactions to be able to fulfil their biological functions. The rate at which unstructured polymer chains can explore conformational space is limited by intrachain diffusion, i.e. by the rate at which two points on a polymer chain can make contact. Intrachain diffusion is particularly important during protein folding, which requires formation of a large number of specific long-range and short-range interactions. The knowledge of the rates of intrachain contact formation in polypeptide chains and their dependence on amino acid sequence and chain length is therefore essential for the understanding of the dynamics of the earliest steps in protein folding and for the characterization of the free energy barriers for protein folding reactions. We have recently applied the method of triplet–triplet energy transfer (TTET) between thioxanthone and 1-naphthyl alanine (NAla) to measure intrachain contact formation in short unstructured polypeptide chains.[1] TTET is a diffusion-controlled process that allows direct measurements of the rates of intrachain diffusion. Flexible peptide chains with alternating glycine and serine residues showed exponential kinetics for end-to-end diffusion with time constants on the 15–20 ns time-scale for formation of an $i, i+3$ contact.[1] Due to sensitivity of the triplet energy of the donor to solvent polarity, these experiments were carried out in ethanol. Later, similar experiments were reported for quenching of tryptophan triplet states by cysteine in water, which gave significantly slower rates for chain diffusion compared to TTET.[2] This reaction is, however, not diffusion-controlled and is accompanied by the formation of S· radicals, which does not allow direct model-free measurements of intrachain diffusion kinetics.[2,3] Another experimental approach used

Abbreviations used: TTET, triplet–triplet energy transfer; NAla, 1-naphthyl alanine; DBO, 2,3 diazabicyclo[2.2.2]oct-2-ene.

E-mail address of the corresponding author: t.kiefhaber@unibas.ch

short poly(glycine-serine) peptides and measured intrachain diffusion by the quenching of 2,3 diazabicyclo[2.2.2]oct-2-ene (DBO) fluorescence by tryptophan in water.[4] This system is close to the diffusion limit and gave similar contact rates in water as TTET from thioxanthone to naphthalene in ethanol.

All available data on polypeptide dynamics were obtained from short, glycine-rich polypeptide chains, which gave an estimate of the maximum rate of local contact formation in flexible chains. However, these experiments did not allow a reliable scaling of the contact rates to longer distances and they did not give information on the dynamics of stiffer chains. In addition, no direct measurements of intrachain diffusion have been reported for a completely diffusion-controlled system in water. Here, we present direct model-free TTET measurements of intrachain diffusion in longer poly(glycine-serine) chains with up to 56 amino acid residues between the points of contact formation. We further measured intrachain diffusion in stiffer glycine-free chains and tested the effect of various amino acids on local chain dynamics. Changing the triplet donor from thioxanthone to xanthone (9-oxoxanthen) enabled us to perform all measurements in water and to additionally test the influence of various solvents on chain dynamics.

Results

Intrachain triplet–triplet energy transfer (TTET)

TTET from a triplet donor to a triplet acceptor group involves transfer of two electrons (Dexter mechanism) and requires van der Waals contact between donor and acceptor.[5] Efficient electron transfer occurs if the triplet donor has a high extinction coefficient, a high intersystem crossing efficiency and a higher triplet energy than the acceptor. In suitable donor/acceptor pairs, the transfer process is diffusion-controlled and can be followed easily by changes in the absorbance of the triplet states. This makes TTET a perfect tool to measure rates of contact formation between two reporter groups directly. When triplet donor and acceptor groups are attached to a polypeptide chain, the TTET kinetics are determined by the dynamics and by the conformational properties of the chain. In unfolded polypeptides, a large number of different conformations are present in equilibrium, which gives a wide distribution of donor–acceptor distances. Some polypeptide chains statistically have contact between donor and acceptor at the time of the laser flash. This will lead to instantaneous TTET in these molecules. The remaining molecules have to sample conformational space by intrachain diffusion, which will also lead to collisional TTET (Figure 1). The observed transfer kinetics in these molecules reflects the rate at which chain dynamics allows

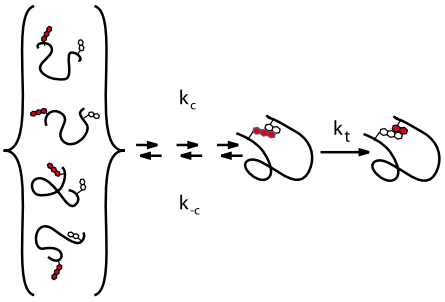

Figure 1. A representation of the triplet–triplet energy transfer (TTET) experiments. Triplet donor and acceptor groups are attached at specific positions on an unstructured polypeptide chain. Triplet states are produced in the donor group by a short laser flash and transferred to the acceptor upon encounter at van der Waals distance in a diffusion-controlled process. The experiments allow determination of the absolute rate constant for contact formation (k_c) in the ensemble of unfolded conformation, if the transfer process is much faster than chain dynamics ($k_t \gg k_c, k_{-c}$).

the two labeled points on the polypeptide chain to meet. This assumes that electron transfer is faster than chain diffusion ($k_t \gg k_c$ and k_{-c}; Figure 1). We used naphthalene as a triplet acceptor and xanthone as a triplet donor. Xanthone has a significantly higher triplet energy than the previously used thioxanthone,[6] which allows TTET to naphthalene in all solvents. The triplet states of xanthone are produced by a 4 ns laser flash at 355 nm. Formation of xanthone triplets from the excited singlet state is a rapid process with a time constant of about 8 ps and a high quantum yield for intersystem crossing (~99%).[7] Xanthone triplets are long-lived ($t_{1/2} \approx 30$ μs in water), which allows measurements of TTET processes from several nanoseconds (limited by the length of the laser pulse) up to about 10 μs. TTET from xanthone to naphthylacetic acid has a bimolecular rate constant of $k_t = 4 \times 10^9\ M^{-1}\ s^{-1}$ in water for donor and acceptor free in solution (data not shown), which is the value expected for a diffusion-controlled bimolecular reaction. This shows that electron transfer is significantly faster than formation of the encounter complex. In TTET measurements of xanthone dissolved in liquid 2-methyl naphthalene ($c = 7M$) transfer was complete within the dead-time of the 4 ns laser flash, which shows that transfer occurs in the subnanosecond time region ($k_t \gg 10^9\ s^{-1}$). This is consistent with data for similar TTET pairs, which showed time constants for transfer ($1/k_t$) in the 10–20 ps time region.[8]

We attached the xanthone group to the N terminus of various model peptides and used the non-natural amino acid NAla to introduce the naphthalene acceptor group near the C terminus. The length and the sequence of the polypeptide chain between donor and acceptor were varied, which gave peptides (A) of the general form:

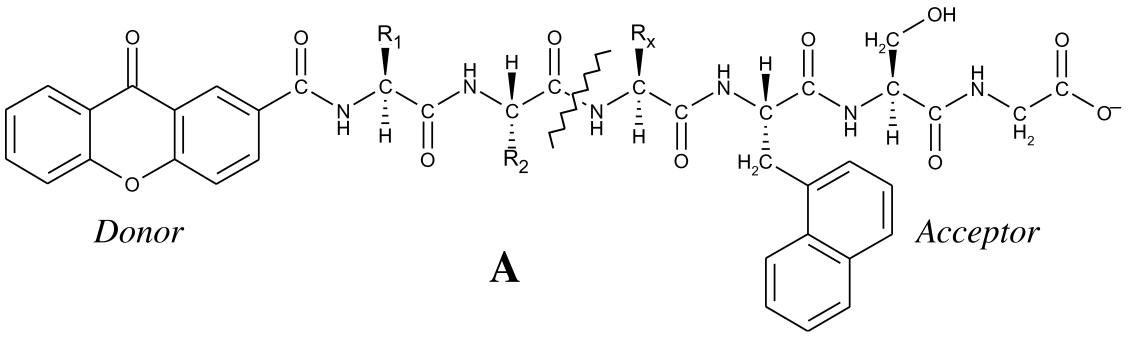

A

where R_1 and R_2 represent any amino acid side-chain, and x indicates the number of amino acid residues between donor an acceptor. All peptides used in this study were unstructured, as judged by CD and NMR spectroscopy.

Intrachain contact formation in glycine-rich polypeptides in water

To compare the results obtained from the xanthone/naphthyl TTET pair in water with previous experimental results on short flexible peptides,[1,4,9] we measured intrachain contact formation in poly(glycine-serine) peptides in water. In contrast to the earlier studies that were limited to chains of two to 15 amino acid residues, we were able to extend the distance between donor and acceptor to 57 amino acid residues. Figure 2 shows the kinetics of TTET from xanthone to naphthalene in a Xan-(Gly-Ser)$_{14}$-NAla-Gly-Ser peptide as a representative example. The formation of xanthone triplets is reflected by the laser-induced appearance of an absorbance band at 590 nm. Decay of the xanthone triplets is accompanied by the appearance of a new absorbance band at 420 nm, indicating formation of naphthalene triplets through intramolecular TTET. Both triplet states show a fine structure in their absorbance spectra in water, in accordance with previous reports.[10,11] The absence of any absorbance bands between 450 nm and 500 nm indicates the absence of xanthone radicals throughout the experiment.[12] Monitoring the time-dependent decrease in the xanthone triplet absorbance band at 590 nm (Figure 3) clearly shows that intrachain contact formation can be described by single-exponential kinetics, in agreement with predictions from theoretical studies.[13] A fit of the data gives a time constant for contact formation ($\tau = 1/k_c$) of 57($\pm$3) ns for formation of an $i, i+29$ contact (Figures 2 and 3). The observation of single-exponential kinetics indicates that: (i) the rates of interconversion between the different conformations in the ensemble of random coil states is fast and thus allows the chain to maintain the equilibrium distribution of the ensemble of conformations that has not made contact; and (ii) the number of equilibrium conformations that have donor and acceptor in van der Waals contact is small compared to the total number of states.[13] Rapid interconversion between the different conformations in the ensemble of unfolded states is in agreement with sub-nanosecond relaxation kinetics in a cyclic azo-peptide after a photo-induced switch from the *cis* to the *trans* conformation.[14] The TTET kinetics observed in our experiments cannot be due to intermolecular exchange processes. The peptide concentrations used in the experiments are typically in the 50–100 μM range, which should not allow bimolecular processes with half-times faster than 50 μs, even for the shortest peptides. This was confirmed in experiments using a mixture of peptides containing either xanthone or naphthalene both present at the same concentration as in the intramolecular transfer experiments. In these experiments, no TTET

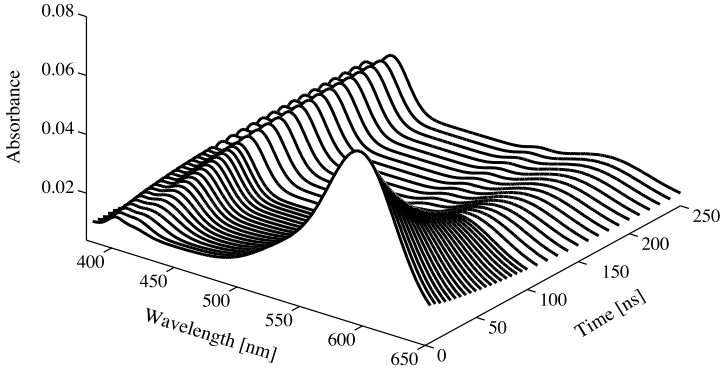

Figure 2. Time-dependent change in the absorbance spectrum of a Xan-(Gly-Ser)$_{14}$-NAla-Ser-Gly peptide after a 4 ns laser flash at 355 nm. The decay in the intensity of the xanthone triplet absorbance band around 590 nm is accompanied by a corresponding increase in the naphthalene triplet absorbance band around 420 nm.

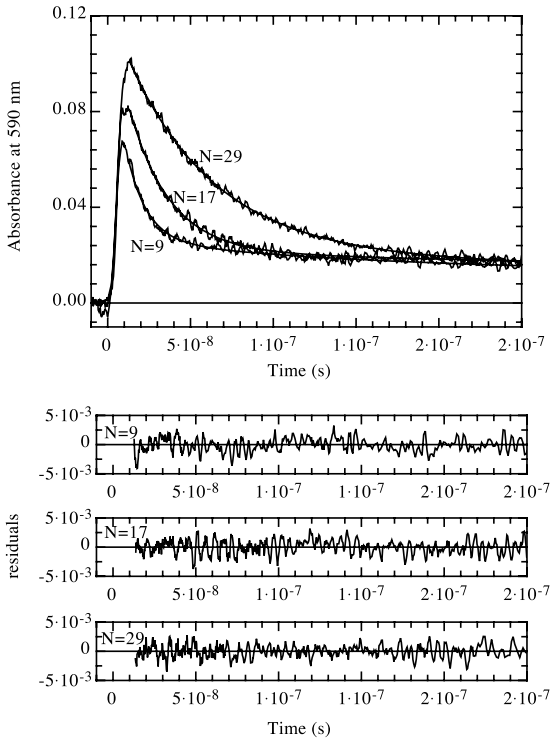

Figure 3. Time-course of formation and decay of xanthone triplets in peptides of the form Xan-(Gly-Ser)$_n$-NAla-Ser-Gly after a 4 ns laser flash at $t = 0$ and measured by the change in absorbance of the xanthone triplets at 590 nm. Data for different numbers of peptide bonds (N) between donor and acceptor are displayed. Additionally, single-exponential fits of the data (continuous line) and the corresponding residuals are displayed. The fits gave time constants of 11.6($\pm$0.4) ns, 25.0($\pm$1.3) ns and 57.1($\pm$3.3) ns for $N = 9$, 17, and 29, respectively. At the end of the exponential decay a small amount of xanthone groups remain in the triplet state. These triplets decay on a much slower time-scale with a rate corresponding to the intrinsic lifetime of xanthone triplets ($t_{1/2} \approx 30$ µs). For comparison, all curves were normalized to identical amplitudes from the fit of the fast decay, i.e. all curves meet at $t = 0$, corresponding to the start of the laserflash. Chain conformations that have donor and acceptor in close contact at the time-point of the laserflash should lead to fast TTET during the 4 ns laser flash. Comparison with the kinetics of triplet decay of free xanthone shows that this fraction is less than 2% for longer peptides. In short peptides this fraction is more difficult to determine due to an uncertainty in $t = 0$ compared to the fast time-scale of diffusional TTET in these peptides. We can, however, estimate that the fraction of rapid transfer does not exceed 10% even in the shortest peptides used in our studies.

from xanthone to naphthalene was observed (data not shown). We can further neglect contributions from through-bond transfer processes, since this cannot occur over distances beyond eight bonds.[15,16] Even in our shortest peptides, donor and acceptor are separated by 11 bonds.

At the end of the fast exponential decay, a small amount of xanthone remains in the triplet state (Figure 3). These triplets decay on a much slower time-scale with a rate corresponding to the intrinsic lifetime of xanthone triplets ($t_{1/2} \approx 30$ µs). In contrast to the fast triplet decay, which is limited by chain dynamics, the slow reaction is sensitive to oxygen concentration and is not accompanied by a corresponding increase in naphthalene triplets at 420 nm. This reaction might be due to a second triplet state of xanthone that cannot transfer its electrons to naphthalene. However, the slow reaction is more likely caused by a population of peptides that cannot form contact between donor and acceptor on the time-scale of our experiments, e.g. due to a small population of multimeric peptide associates. These triplets will decay with the intrinsic lifetime of the xanthone triplet state. This idea is supported by a decrease of the amplitude of the slow reaction observed in good solvents like urea and GdmCl solutions (data not shown).

To test the effect of donor–acceptor distance on the rates of intrachain diffusion, we measured TTET kinetics in peptides containing between one and 28 Gly-Ser units between donor and acceptor. This allows measurements of contact formation kinetics for distances ranging from $i, i+3$ to $i, i+57$, which covers the range of side-chain contacts in small proteins. Figure 3 displays three representative TTET kinetics for peptides of different

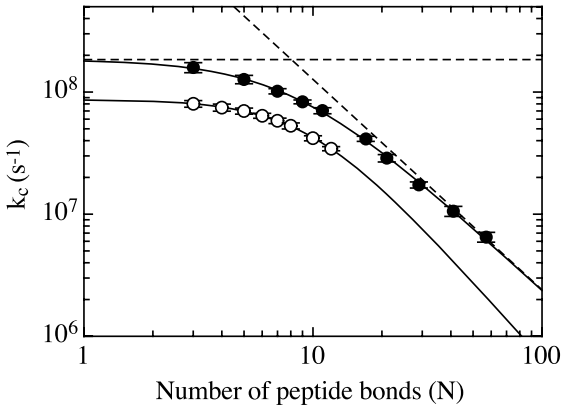

Figure 4. Effect of increasing chain length (N) on the rate constant of contact formation in a series of peptides with alternating glycine-serine (●) and with polyserine (○) between donor and acceptor. The continuous lines represent fits to the equation:

$$k_c = \frac{1}{1/k_0 + 1/(k_i N^m)}$$

The fits give values of $k_0 = 1.8(\pm 0.2) \times 10^8\ s^{-1}$, $k_i = 6.7(\pm 1.6) \times 10^9\ s^{-1}$ and $m = -1.72 \pm 0.08$ for the poly-(glycine-serine) series, and values of $k_0 = 8.7(\pm 0.8) \times 10^7\ s^{-1}$, $k_i = 1.0(\pm 0.8) \times 10^{10}\ s^{-1}$ and $m = -2.1 \pm 0.3$ for polyserine. The broken lines represent the limiting regimes for contact formation in the poly(glycine-serine) peptides with a length-independent upper limit for contact formation of $k_0 = 1.8(\pm 0.2) \times 10^8\ s^{-1}$ and length-dependent parameters of $k_i = 6.7 \times 10^9\ s^{-1}$ and $m = -1.72$.

length. For all polypeptide chains, single-exponential kinetics for contact formation are observed. Figure 4 shows that for long donor–acceptor distances ($x > 30$) the rate of contact formation decreases with $N^{-1.7\pm0.1}$ ($N = x + 1$ is the number of peptide bonds between donor and acceptor). This indicates a stronger distance-dependence than expected for purely entropy-controlled intrachain diffusion in ideal, freely-jointed Gaussian chains, which should scale with $k \sim N^{-1.5}$.[13,17] However, Flory already pointed out that excluded volume effects should significantly influence the chain dimensions.[18] Accounting for excluded volume effects in the end-to-end diffusion model presented by Szabo *et al.*[13] leads to $k \sim N^{-1.8}$, which is nearly identical with the value found for the long poly(glycine-serine) chains. This indicates that the dimensions and the dynamics of unfolded polypeptide chains in water are influenced significantly by excluded volume effects, which is in agreement with recent results on conformational properties of polypeptides derived from simplified Ramachandran maps.[19] Another source for the stronger distance dependence observed in our experiments might be an additional small enthalpic barrier, which was observed in the temperature dependence of intrachain diffusion (F.K. & T.K., unpublished results). For shorter chains ($i < 20$) the observed simple scaling law breaks down and contact formation becomes virtually independent of chain length, with a limiting value of $k_0 = 1.9 \times 10^8\ s^{-1}$. As pointed out above, the limiting rate for contact formation in short chains is not due to limits of triplet–triplet transfer (k_t in Figure 1), since this process occurs on the subnanosecond time-scale. Obviously, the intrinsic dynamics of polypeptide chains are limited by different processes for motions over short and over long segments. This is in agreement with polymer theory, which suggests that the properties of short chains are influenced strongly by chain stiffness, which leads to a breakdown of theoretically derived scaling laws for ideal chains.[20]

To characterize the dimensions and the stiffness of polymer chains, Flory introduced the characteristic ratio (C_n) :[20]

$$C_n = \frac{\langle r^2 \rangle_0}{nl^2}$$

for a chain with n segments of length l. The characteristic ratio relates the increase in the mean square end-to-end distance $\langle r^2 \rangle_0$ of an unperturbed polymer chain, i.e. of a real chain without intramolecular interactions, to the change in $\langle r^2 \rangle_0$ of an ideal random walk or freely jointed chain, which grows with $\langle r^2 \rangle_0 = nl^2$. For short chains, C_n increases with chain length due to preferential chain propagation into one direction. For long chains, C_n reaches a constant limiting value (C_∞). In this limit, $\sqrt{\langle r^2 \rangle_0}$ grows proportional to $n^{1/2}$, like an ideal random-walk chain. However, in a real chain, $\sqrt{\langle r^2 \rangle_0}$ increases by a factor of C_∞ more per segment compared to an ideal random-walk chain. The value of C_∞ gives the average number of consecutive chain segments that propagate in the same direction ("statistical segment"). Larger values of C_∞ therefore indicate stiffer chains. For polypeptide chains, polyglycine represents the most flexible chain with $C_\infty = 2$.[21,22] The 1:1 mixture of glycine and serine used in our experiments is expected to have a C_∞ value of about 3 and C_∞ should be reached for $N > 10$.[23] Figure 4 shows, however, that the poly(glycine-serine) chains behave like random chains only over distances longer than 20–30 amino acid residues when the contact rates scale with $k_c \sim N^{-1.7}$. This indicates increased chain stiffness compared to the predicted value, which could be due to specific intrachain hydrogen bonds or van der Waals interactions and to excluded volume effects that restrict the number of chain conformations (see below).

Effect of amino acid sequence on intrachain diffusion

Both theoretical considerations[21–23] and experimental results[24] show that polypeptide chains are especially flexible around glycyl residues. All amino acids except proline ($C_\infty > 100$) and glycine ($C_\infty = 2$) are predicted to have C_∞ values around 9, and C_∞ should be reached for intrachain distances longer than about 40–50 amino acid residues.[21–23] This indicates increased chain stiffness and longer mean end-to-end distances ($\sqrt{\langle r^2 \rangle_0}$) compared to the poly(glycine-serine) chains. To test the effect of chain stiffness on peptide dynamics, we measured the rates of contact formation in polyserine peptides. Figure 4 shows the distance dependence of intrachain diffusion in a series of Xan-$(Ser)_x$-NAla-Ser-Gly peptides with $x = 2–11$ ($N = 3–12$). We observed single exponential kinetics for contact formation in all polyserine peptides. For short chains ($N < 5$), contact formation is virtually independent of chain length, with a limiting value of $k_0 = 8.7 \times 10^7\ s^{-1}$. This shows that the local dynamics in polyserine are about twofold slower than in the poly(glycine-serine) peptides, which seems to be small compared to the largely different properties expected for the stiffer polyserine chains. A possible origin of this rather small effect is that the decreased flexibility and the longer end-to-end distances in the polyserine chains are compensated by the decreased conformational space available for polyserine compared to poly(glycine-serine) peptides. For longer polyserine chains, contact formation slows with increasing chain length. The effect of increasing chain length on the rates of contact formation seems to be slightly larger in polyserine compared to the poly(glycine-serine) series ($k \sim N^{-2.1\pm0.2}$). However, due to limitations in peptide synthesis, we were not able to obtain longer peptides, which will be required to get a reliable scaling law for the polyserine peptides.

The kinetics of contact formation over short

Table 1. Effect of different amino acids on local peptide dynamics

Xaa	k_c (10^7 s^{-1})
Gly	12 ± 1
Ala	8.0 ± 0.7
Ser	6.7 ± 0.7
Glu	5.4 ± 0.2
Arg	5.5 ± 0.7
His	4.9 ± 0.4
Ile	4.4 ± 0.3
trans Pro	2.0 ± 0.3
cis Pro	25 ± 5

The rate constants for end-to-end contact formation (k_c) were measured by TTET from xanthone (Xan) to 1-naphthyl alanine (NAla) in host guest peptides of the sequence Xan-Ser-Xaa-Ser-NAla-Ser-Gly with varying guest amino acid (Xaa). Conditions were 22.5 °C, pH 7 in water.

distances differ only by a factor of 2 for polyserine compared to poly(glycine-serine) (Figure 4). To investigate the effect of other amino acids on local chain dynamics, we measured TTET in short host-guest peptides of the canonical sequence Xan-Ser-Xaa-Ser-NAla-Ser-Gly using the guest amino acid residues Xaa = Gly, Ser, Ala, Ile, His, Glu, Arg and Pro. Table 1 shows that the amino acid side-chain indeed has only little effect on the rates of contact formation. All amino acids except proline and glycine show very similar dynamics. Interestingly, there is a small but significant difference in rate between short side-chains (Ala, Ser) and amino acids with longer side-chains (Ile, Glu, Arg, His). Obviously, chains that extend beyond the C^{β} atom slightly decrease the rates of local chain dynamics, whereas charges do not influence the dynamics. Glycyl and prolyl residues show significantly different dynamics compared to all other amino acids, as expected from their largely different conformational properties.[22] As seen before (Figure 4), glycine accelerates contact formation about twofold compared to serine. Proline shows slower and more complex kinetics of contact formation with two relaxation times of $1/k_1 = 2.5 \times 10^8$ s^{-1} and $1/k_2 = 2 \times 10^7$ s^{-1} and respective amplitudes of $A_1 = 80(\pm 5)\%$ and $A_2 = 20(\pm 5)\%$. This essentially reflects the *cis–trans* ratio at the Ser-Pro peptide bond in our host-guest peptide, which has a *cis* content of 16(±2)% as determined by 1D ^{1}H NMR spectroscopy using the method described by Reimer *et al.*[25] Since the rate of *cis–trans* isomerization is slow ($1/k \sim 20$ seconds at 22 °C) there is no equilibration between the two isomers on the time-scale of the TTET experiments. This allows the measurement of the dynamics of both the *trans* and the *cis* form. Our results show that the two isomers differ significantly in their dynamic properties of $i, i+4$ contact formation.

Effect of solvent on chain dynamics

The dynamics of short poly(glycine-serine) peptides measured with the xanthone–naphthalene TTET pair in water are about three times faster than the previously measured rates in the same peptides using the thioxanthone–naphthalene pair in EtOH,[1] although both systems were shown to be diffusion-controlled. To test whether this difference originates in the influence of the solvent on chain dynamics we measured the EtOH-dependence of intrachain diffusion using the xanthone–naphthalene pair. Figure 5(A) shows that the logarithm of k_c decreases linearly with increasing concentration of EtOH in a Xan-(Gly-Ser)$_4$-NAla-Ser-Gly peptide. A possible origin of this effect is an influence of the solvent on the chain properties. EtOH is a better solvent for polypeptide chains than water and should thus lead to a more extended ensemble of unfolded states. To test whether good solvents generally slow intrachain diffusion, we measured the effect of GdmCl and urea on the contact rates in aqueous solutions. Both denaturants show similar effects on intrachain diffusion as EtOH. They lead to a linear decrease in $\ln k_c$ with increasing concentration of

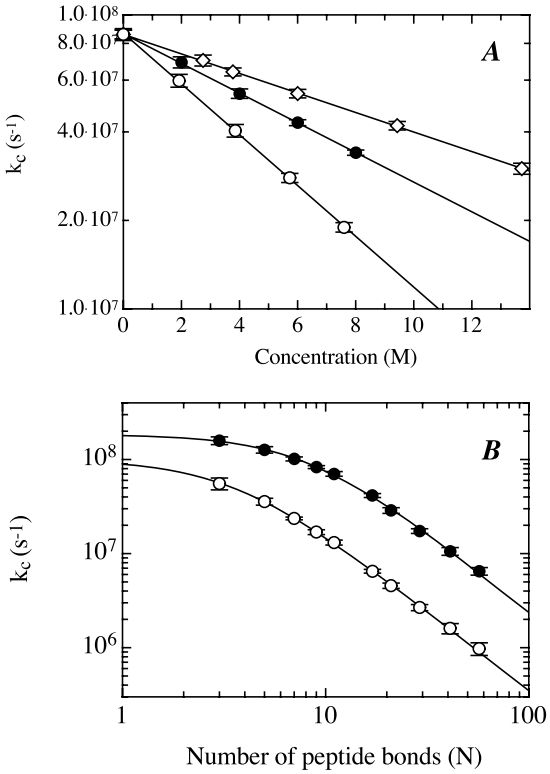

Figure 5. (A) Effect of various co-solvents on the dynamics of intrachain contact formation in a Xan-(Gly-Ser)$_4$-NAla-Ser-Gly peptide. TTET was measured in aqueous solutions in the presence of ethanol (◇), urea (●) and GdmCl (○). (B) Effect of donor–acceptor distance (N) on the rate constant of contact formation in a series of peptides with alternating glycine-serine between donor and acceptor. The rate constants for contact formation in water (●) are compared to the values in 8 M GdmCl (○).

denaturant. Interestingly, the change in $\ln k_c$ with concentration of denaturant ($m_c = \mathrm{d} \ln k_c / \mathrm{d}[\mathrm{Den}]$) is twofold higher for GdmCl compared to urea, which essentially corresponds to their relative strength in unfolding proteins.[26] Similar m_c-values for EtOH, urea and GdmCl are observed in a Xan-$(Ser)_9$-NAla-Ser-Gly peptide (data not shown). The observed effect is significantly stronger than expected from the increased solvent viscosity in concentrated GdmCl and urea solutions (F.K. & T.K., unpublished results).

Since the effect of GdmCl and urea on the chain dynamics suggests that these co-solvents change the chain properties significantly, we measured the effect of GdmCl on the distance-dependence of intrachain diffusion. Figure 5(B) shows that the distance-dependence of contact formation in the Xan-$(Gly\text{-}Ser)_n$-NAla-Ser-Gly series is changed at high concentrations of denaturant compared to water. In 8 M GdmCl, the switch from the distance-independent dynamics over short contact distances to the distance-dependent regime for longer peptides occurs at shorter distances. This indicates decreased chain stiffness in 8 M GdmCl compared to water, although the dynamics are slowed significantly in the presence of GdmCl both for short and for long donor–acceptor distances. For long peptides, the effect of donor–acceptor distance on the rates of contact formation is similar in 8 M GdmCl and water with $k_c \sim N^{-1.8 \pm 0.1}$.

Structure and dynamics of unfolded polypeptide chains

Our results show that both in the poly(glycine-serine) peptides and in polyserine, the rate-limiting steps for motions over short and over long distances are different. For long poly(glycine-serine) chains ($N > 30$) contact formation scales with $N^{-1.7 \pm 0.1}$ as expected for an ideal chain with contributions from excluded volume effects. For shorter chains the dynamics reach a limiting value due to limited chain stiffness. The less flexible polyserine chains show about twofold slower local dynamics. These results are in contrast to theoretical considerations based on the contributions of chain entropy to the process of loop formation, which predicted that intrachain contact formation should show a maximum rate for an $i, i+10$ interaction[27] and should decrease for longer and shorter chains. Our experiments rather show that the process of intrachain contacts continues to become faster for interactions shorter than $i, i+10$ in all peptides and asymptotically approaches a limiting value for short chains (Figure 4).

Denaturants like GdmCl and urea slow local chain dynamics but lead to more flexible chains that behave like ideal polymers already at shorter end-to-end distances (Figure 5(B)). These seemingly contradicting findings can be rationalized by considering the effect of denaturants on the conformational properties of polypeptide chains. Unlike water, solutions with high concentrations of denaturants represent good solvents for polypeptide chains. This reduces the strength of intramolecular interactions like hydrogen bonds and van der Waals interactions relative to peptide–solvent interactions, which makes unstructured polypeptide chains more flexible and leads to a behavior expected for an unperturbed chain. In agreement with this interpretation, the distance-dependence of the rates of contact formation in 8 M GdmCl is close to the behavior of an unperturbed polypeptide chain predicted by Flory and co-workers.[23] The decreased rate of contact formation at high concentrations of denaturant can be explained, in part, by an increased solvent viscosity and by an increased end-to-end distance that is expected in good solvents compared to water. Additional effects like denaturant binding might also slow chain dynamics.

Another interesting feature of the dynamics of contact formation are single exponential kinetics seen in all peptides. This is in agreement with our earlier results from the thioxanthone–naphthalene pair in EtOH. Due to the additional barriers that limit Trp-triplet quenching by Cys and DBO quenching by Trp, no direct information on the dynamics of contact formation systems is available from these systems.[2–4] For protein folding without significant energy barriers ("downhill protein folding")[28] complex kinetics with "stretched exponential" behavior ($A = A_0 \exp - (kt)^{\beta}$) were predicted.[29] Our results from the kinetics of contact formation show that even the elementary steps of protein folding show simple exponential behavior. The dynamics of intrachain contact formation are kinetically similar to the proposed downhill scenario for protein folding: many states with similar free energy are in rapid equilibrium and many different routes to the formation of productive contacts exist. This suggests that protein folding in the absence of barriers should show exponential kinetics after a rapid equilibration process in the ensemble of unfolded conformations. Experimentally observed stretched exponential kinetics for protein folding on the milliseconds time-scale[29] might have a different origin. They could be caused by the presence of local energy minima and/or parallel folding pathways, e.g. due to prolyl and non-prolyl peptide isomerization in addition to the direct folding process. The observation of single-exponential folding kinetics in the absence of energy barriers is in agreement with theoretical considerations by Zwanzig.[30,31]

The earliest steps in protein folding

Our results show that the amino acid sequence has only little effect on the local dynamics of polypeptide chains. All amino acids show very similar rates of end-to-end diffusion with time constants between 12 ns and 20 ns for the formation of $i, i+4$ contacts. Polypeptide chains are significantly more flexible around glycine ($\tau = 8$ ns) and stiffer around prolyl residues ($\tau = 50$ ns for the *trans*

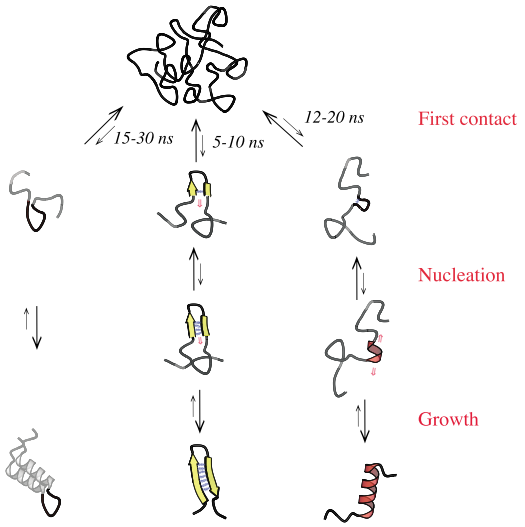

Figure 6. A representation of the time constants for the first steps in formation of loops, β-hairpins and α-helices during protein folding derived from the data measured by TTET in water.

isomer). Presumably due to the shorter distances resulting from a *cis* peptide bond the rates of $i, i+4$ contact formation are fastest around the *cis* Ser-Pro bond ($\tau = 4$ ns). These results allow us to set an upper limit to the rates of formation of the first productive local contacts during protein folding (Figure 6). β-Hairpins, which are the most local structures in proteins, are often glycine and proline-rich.[32] Gly-Ser is actually one of the most frequent sequences found in hairpin loops. Our results indicate that the time constants for the first steps in the formation of the tightest turns with $i, i+3$ contacts are around 5 ns for Gly and *cis* Xaa-Pro (Table 1). In glycine and proline-free turns, these rates are slowed to about 10–20 ns, depending on the amino acid sequence. Formation of α-helices is most likely initiated by formation of a helical turn, which involves formation of an $i, i+4$ interaction.[33,34] Since helices are usually free of glycyl and prolyl residues, the initiation cannot occur faster than about 12–20 ns (Figure 4 and Table 1). It should be noted that these rates do not represent the time constants for nucleation of helices and hairpins, which requires formation of more than one specific interaction and most likely encounters additional entropic and enthalpic barriers (Figure 6). Our results rather represent an upper limit for the kinetics of secondary structure formation and can thus be used to calculate the height of the free energy barriers once rates for helix and hairpin nucleation can be measured directly. The measured time constants for intrachain contact formation can, however, be used directly to predict the kinetics of loop formation, which are typically of the size of six to ten amino acid residues.[35] Contacts at the end of loops form with time constants of about 15 ns for glycine-rich loops and 30–40 ns for stiffer loops.

These considerations show that proteins will not be able to fold faster than on the 10–20 ns timescale due to the limitations set by chain dynamics. A value of $10^8\ s^{-1}$ therefore seems a reasonable pre-exponential factor (k_0) for determining the free energy barriers ($\Delta G^{0\ddagger}$) for folding reactions starting from the ensemble of unfolded states with:

$$k = k_0\ e - (\Delta G^{0\ddagger}/RT)$$

It is likely, however, that the pre-exponential factor changes along the reaction coordinate when intramolecular interactions are formed.

It may be argued that intrachain contacts in a polypeptide chain with a stronger bias towards folded structures can form faster than the observed dynamics in our unstructured model peptides. However, weak interactions like van der Waals contacts between side-chains and hydrogen bonds should dominate the early interactions during the folding process and our data will provide a good model for theses earliest events in folding. A stronger energy bias towards the native state will mainly increase the strength or the number of these interactions but not their dynamics of formation.

The rates of intrachain diffusion measured by TTET in water are significantly faster than the values from the tryptophan–cysteine quenching pair[2] and for the DBO quenching by tryptophan.[4] This is expected, since both systems are not completely diffusion-controlled. Especially, tryptophan triplet quenching by cysteine is limited by large additional barriers. It is further accompanied by radical formation and gives only minor absorbance changes, which introduces additional uncertainties in the data analysis.[2,36] Thus, the rates for contact formation from this system had to be estimated using various assumptions. Even after correction, the rate constants obtained from these experiments are significantly smaller than the values we obtained using TTET from xanthone to naphthalene.[9] These results show that it is essential to use diffusion-controlled systems in order to obtain accurate model-free rates on intrachain diffusion processes.

Materials and Methods

Peptide synthesis

All peptides were synthesized using standard fluorenylmethoxycarbonyl (F-moc) chemistry on preloaded TentaGel S Trityl-resins (Rapp Polymer). 9-Oxoxanthen-2-carboxylic acid was synthesized as described[37] and attached to the N terminus of the peptides using F-moc chemistry. Peptides were purified by reversed-phase HPLC (RP-8-column). Purity of all peptides, which was checked by mass spectroscopy and HPLC, exceeded 98% for short peptides and 95% for long peptides. The mass was confirmed by electrospray ionization mass spectroscopy.

Laser flash experiments

Transient triplet absorption decay data were collected using a Laser Flash Photolysis Reaction Analyzer (LKS.60) from Applied Photophysics. Xanthone as triplet donor was excited selectively by using a Quantel Nd:YAG-Laser (354.6 nm, 4 ns pulse of 50 mJ). All solutions were degassed before the measurements to minimize triplet quenching by oxygen. Peptide concentrations were determined by UV absorbance at 343 nm using a molar absorption coefficient of 3900 M^{-1} cm^{-1} for xanthone in water and were typically in the 50–100 μM range. All measurements were performed at 22.5 °C and pH 7 in water. The data for contact formation for the Xan-Ser-Pro-Ser-NAla-Ser-Gly peptide (Table 1) were obtained by measuring kinetics at different concentrations of GdmCl between 0 M and 8 M, and extrapolating the data to zero denaturant. This improved the accuracy of the data for the faster kinetic phase corresponding to the dynamics of the *cis* Ser-Pro conformation. The concentrations of all guanidine hydrochloride and urea solutions were calculated from the refractive index.[26] The concentration of ethanol was adjusted by net weight. Transient triplet absorption of xanthone and of naphthalene was measured at 590 nm and 420 nm, respectively. Individual kinetics were typically measured five times, averaged and analyzed using ProFit (Quansoft, Zürich, Switzerland). All given rate constants were obtained by fitting the decay of xanthone triplets at 590 nm, which is more accurate than fitting the increase of naphthalene triplets at 420 nm due to small contributions of xanthone fluorescence in the early timescales at this wavelength.

Acknowledgements

We thank Annett Bachmann and Andreas Möglich for discussion and comments on the manuscript. This work was supported by a grant from the Schweizerischen Nationalfonds (SNF).

References

1. Bieri, O., Wirz, J., Hellrung, B., Schutkowski, M., Drewello, M. & Kiefhaber, T. (1999). The speed limit for protein folding measured by triplet–triplet energy transfer. *Proc. Natl Acad. Sci. USA*, **96**, 9597–9601.
2. Lapidus, L. J., Eaton, W. A. & Hofrichter, J. (2000). Measuring the rate of intramolecular contact formation in polypeptides. *Proc. Natl Acad. Sci. USA*, **97**, 7220–7225.
3. Yeh, I.-C. & Hummer, G. (2002). Peptide loop-closure kinetics from microsecond molecular dynamics simulations. *J. Am. Chem. Soc.* **124**, 6563–6568.
4. Hudgins, R. R., Huang, F., Gramlich, G. & Nau, W. M. (2002). A fluorescence-based method for direct measurements of submicroscond intramolecular contact formation in biopolymers: an exploratory study with polypeptides. *J. Am. Chem. Soc.* **124**, 556–564.
5. Klessinger, M. & Michl, J. (1995). *Excited States and Photochemistry Of Organic Molecules*, VCH, Weinheim.
6. Murov, S. L., Carmichael, I. & Hug, G. L. (1993). *Handbook of Photochemistry*, Marcel Dekker, New York.
7. Damschen, D. E., Merritt, C. D., Perry, D. L., Scott, G. W. & Talley, L. D. (1978). Intersystem crossing kinetics of aromatic ketones in the condensed phase. *J. Phys. Chem.* **82**, 2268–2272.
8. Anderson, R. W., Jr, Hochstrasser, R. M., Lutz, H. & Scott, G. W. (1974). Direct measurements of energy transfer between triplet states of molecules in liquids using picosecond pulses. *J. Chem. Phys.* **61**, 2500–2506.
9. Lapidus, L. J., Steinbach, P. J., Eaton, W. A., Szabo, A. & Hofrichter, J. (2002). Effects of chain stiffness on the dynamics of loop formation in polypeptides. Appendix: testing a 1-diensional diffusion model for peptide dynamics. *J. Phys. Chem. B*, **106**, 11628–11640.
10. Ley, C., Morlet-Savary, F., Fouassier, J. P. & Jacques, P. (2000). The spectral shape dependence of xanthone triplet–triplet absorption on solvent polarity. *J. Photochem. Photobiol. A*, **137**, 87–92.
11. Grabner, G., Rechthaler, K., Mayer, B., Köhler, G. & Rotkiewicz, K. (2000). Solvent influence on the photophysics of naphthalene: fluorescence and triplet state properties in aqueous solutions and in cyclodextrin complexes. *J. Phys. Chem. A*, **104**, 1365–1376.
12. Garner, A. & Wilkinson, F. (1976). Laser photolysis of the triplet state of xanthone and its ketyl radical in fluid solution. *J. Chem. Soc. Faraday Trans. 2* **72**, 1010–1020.
13. Szabo, A., Schulten, K. & Schulten, Z. (1985). First passage time approach to diffusion controlled reactions. *J. Chem. Phys.* **72**, 4350–4357.
14. Spörlein, S., Carsten, H., Satzger, H., Renner, C., Behrendt, R. & Moroder, L. (2002). Ultrafast spectroscopy reveals subnanosecond peptide conformational dynamics and validates molecular dynamics simulation. *Proc. Natl Acad. Sci. USA*, **99**, 7998–8002.
15. Closs, G. L., Johnson, M. D., Miller, J. R. & Piotrowiak, P. (1989). A connection between intramolecular long-range electron, hole and triplet energy transfer. *J. Am. Chem. Soc.* **111**, 3751–3753.
16. Wagner, P. J. & Klán, P. (1999). Intramolecular triplet energy transfer in flexible molecules: electronic, dynamic, and structural aspects. *J. Am. Chem. Soc.* **121**, 9626–9635.
17. Jacobsen, H. & Stockmayer, W. H. (1950). Intramolecular reaction in polycondensations. I. The theory of linear systems. *J. Phys. Chem.* **18**, 1600–1606.
18. Flory, P. J. (1953). *Principles of Polymer Chemistry*, Cornell University Press, Ithaca.
19. Pappu, R. V., Srinavasan, R. & Rose, G. D. (2000). The Flory isolated-pair hypothesis is not valid for polypeptide chains: implications for protein folding. *Proc. Natl Acad. Sci. USA*, **97**, 12565–12570.
20. Flory, P. J. (1969). *Statistical Mechanics of Chain Molecules*, Hanser Publishers, Munich.
21. Brant, D. A. & Flory, P. J. (1965). The configuration of random polypeptide chains. II. Theory. *J. Am. Chem. Soc.* **87**, 2791–2800.
22. Schimmel, P. R. & Flory, P. J. (1967). Conformational energy and configurational statistics of poly-L-proline. *Proc. Natl Acad. Sci. USA*, **58**, 52–59.
23. Miller, W. G., Brant, D. A. & Flory, P. J. (1967). Random coil configurations of polypeptide chains. *J. Mol. Biol.* **23**, 67–80.
24. Schwalbe, H., Fiebig, K. M., Buck, M., Jones, J. A., Grimshaw, S. B. & Spencer, A. (1997). Structural and

dynamical properties of a denatured protein. Heteronuclear 3D NMR experiments and theoretical simulations of lysozyme in 8 M urea. *Biochemistry*, **36**, 8977–8991.
25. Reimer, U., Scherer, G., Drewello, M., Kruber, S., Schutkowski, M. & Fischer, G. (1998). Side-chain effects on peptidyl-prolyl *cis/trans* isomerization. *J. Mol. Biol.* **279**, 449–460.
26. Pace, C. N. (1986). Determination and analysis of urea and guanidine hydrochloride denaturation curves. *Methods Enzymol.* **131**, 266–280.
27. Camacho, C. J. & Thirumalai, D. (1995). Theoretical predictions of folding pathways by using the proximity rule, with applications to bovine pancreatic inhibitor. *Proc. Natl Acad. Sci. USA*, **92**, 1277–1281.
28. Eaton, W. A., Thompson, P. A., Chan, C. K., Hagen, S. J. & Hofrichter, J. (1996). Fast events in protein folding. *Structure*, **4**, 1133–1139.
29. Sabelko, J., Ervin, J. & Gruebele, M. (1999). Observation of strange kinetics in protein folding. *Proc. Natl Acad. Sci. USA*, **96**, 6031–6036.
30. Zhou, H.-X. & Zwanzig, R. (1991). A rate process with an entropic barrier. *J. Chem. Phys.* **94**, 6147–6152.
31. Zwanzig, R. (1997). Two-state models for protein folding. *Proc. Natl Acad. Sci. USA*, **94**, 148–150.
32. Wilmot, C. M. & Thornton, J. M. (1988). Analysis and prediction of the different types of β-turns in proteins. *J. Mol. Biol.* **203**, 221–232.
33. Zimm, B. H. & Bragg, J. K. (1959). Theory of phase transition between helix and random coil in polypeptide chains. *J. Chem. Phys.* **31**, 526–535.
34. Lifson, S. & Roig, A. (1961). On the theory of helix-coil transitions in polypeptides. *J. Chem. Phys.* **34**, 1963–1974.
35. Leszcynski, J. F. & Rose, G. D. (1986). Loops in globular proteins: a novel category of secondary structure. *Science*, **234**, 849–855.
36. Lapidus, L. J., Eaton, W. A. & Hofrichter, J. (2001). Dynamics of intramolecular contact fromation in polypeptides: distance dependence of quenching rates in a room-temperature glass. *Phys. Rev. Letters*, 258101-1–258101-4..
37. Graham, R. & Lewis, J. R. (1978). Synthesis of 9-Oxoxanthen-2-carboxylic acids. *J. Chem. Soc., Perkin Trans. 1*, 876–881.

Edited by R. Huber

(Received 30 April 2003; received in revised form 7 July 2003; accepted 7 July 2003)

Available online at www.sciencedirect.com
SCIENCE DIRECT®
Chemical Physics 307 (2004) 209–215
Chemical Physics
www.elsevier.com/locate/chemphys

Intrachain diffusion in a protein loop fragment from carp parvalbumin

Florian Krieger, Beat Fierz, Fabian Axthelm, Karin Joder, Dominique Meyer, Thomas Kiefhaber *

Department of Biophysical Chemistry, Biozentrum der Universität Basel, Klingelbergstr. 70, CH-4056 Basel, Switzerland

Received 17 May 2004; accepted 27 May 2004
Available online 28 July 2004

Abstract

During protein folding a polypeptide chain has to form specific intrachain interactions starting from an ensemble of unfolded conformation. Thus, intrachain diffusion in unfolded polypeptide chains can be regarded as an elementary step in protein folding, which should determine the dynamics of the early stages in the folding process. We have previously applied exothermic triplet–triplet energy transfer from xanthone to naphthalene to determine rate constants for intrachain end-to-end contact formation in unstructured homo-polypeptide chains. Here we show that the method can be applied to determine absolute rate constants for intrachain diffusion in natural loop sequences, if they are free of methionine, tryptophan and tyrosine. We measured the rate of loop formation in an 18 amino acid polypeptide chain corresponding to a natural loop sequence from carp muscle β-parvalbumin (residues 85–102). Contact formation shows single exponential kinetics with a time constant ($\tau=1/k$) of 53 ± 3 ns at 22.5 °C in water. Comparison with the results on homo-polypeptide chains shows that this value agrees well with rates obtained earlier for a polyserine chain of the same length.

Keywords: Protein folding; Chain dynamics; Intrachain diffusion; Triplet–triplet energy transfer; Carp-parvalbumin; Calcium-binding

1. Introduction

During protein folding a polypeptide chain has to form specific intramolecular interactions to finally reach its biologically active native state. Starting from the ensemble of unfolded conformations a polypeptide chain has to sample a vast conformational space in search for energetically favourable conformations. To understand the dynamics of the folding process it is essential to characterize the structure, the dimensions and the dynamics of unfolded and partially folded states. A large amount of structural information on unfolded proteins and folding intermediates has been obtained from nuclear magnetic resonance spectroscopy [1–3] and small-angle X-ray scattering [3–5]. Much less is known about the dynamics of conformational sampling in these states and about the rates of interconversion between different local minima on the free energy landscape. The rate at which an unstructured polypeptide chain can explore conformational space during the earliest steps in protein folding is limited by intrachain diffusion, i.e. by the maximum rate at which two specific points on the chain can make contact. We have recently applied the method of exothermic triplet–triplet energy transfer (TTET) from xanthone to naphthalene to directly measure end-to-end diffusion rates in unstructured polypeptide chains [6,7]. TTET is a two-electron transfer process (Dexter

* Corresponding author. Tel.: +41-61-267-2194; fax: +41-61-267-2189.
E-mail address: t.kiefhaber@unibas.ch (T. Kiefhaber).

0301-0104/$ - see front matter © 2004 Elsevier B.V. All rights reserved.
doi:10.1016/j.chemphys.2004.05.036

mechanism) and requires van-der-Waals contact between donor and acceptor [8]. Formation of xanthone triplet states (k_T) and electron transfer from xanthone to naphthalene (k_{TTET}) both occur on the 1–5 ps time scale (H. Satzger, W. Zinth, B.F. and T.K., in preparation) and the bimolecular transfer process is diffusion-controlled ($k_T = 4\times10^9$ $M^{-1}s^{-1}$) [6,7]. Thus, this system allows us to determine absolute rate constants for intrachain diffusion processes slower than about 20 ps (Fig. 1). In earlier experiments the spectroscopic labels were placed at the ends of poly(glycine–serine) and polyserine chains [6,7]. The length-dependence of end-to-end diffusion in these homopolymers showed that diffusion over long and over short distances is limited by different processes (Fig. 2). For contact formation over short distances we observed that the dynamics of intrachain diffusion are virtually independent of chain length with limiting time constants ($1/k_0$) of 5 ns for poly(glycine–serine) chains and of 12 ns for polyserine [7]. Contact formation over longer distances decreases with increasing chain length and scales with $k \sim N^{-1.7}$ for poly(glycine–serine) and $k \sim N^{-2.1}$ for polyserine with N being the number of peptide bonds between donor and acceptor. The complete length-dependence of intrachain diffusion could thus be described by the following equation (Fig. 2)

$$k_c = \frac{1}{1/k_0 + 1/(k_i \cdot N^m)}. \quad (1)$$

This suggests that chain stiffness governs local chain dynamics whereas entropy-limited conformational search sets the limit for contact formation over longer distances. These results contradicted theoretical considerations, which postulated a maximum rate constant in the distance-dependence of end-to-end diffusion for formation of an i, $i+9$ contact and predicted slower contact rates for shorter distances [9]. The effect of the amino acid sequence on local chain dynamics was probed with a series of host–guest peptides and showed that formation of local contacts is only eightfold slower around the stiffest amino acid (proline) compared to the most flexible amino acid (glycine) [7]. Experiments carried out in different solvents further revealed that good solvents for polypeptide chains like ethanol and concentrated solutions of denaturants like urea and GdmCl significantly slow down chain dynamics compared to the dynamics in water [7]. This explained the faster dynamics observed in water [7] compared to our earlier studies, which were carried out in ethanol [6].

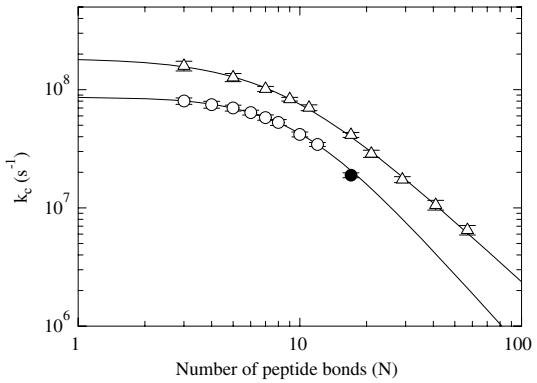

Fig. 2. Comparison of the end-to-end diffusion kinetics of the parvalbumin loop fragment 85–102 (●) with results on poly(glycine–serine) (Δ) and polyserine (○) homo-polypeptides. The experimentally measured rate constants for contact formation between xanthone and naphthalene (k_c) are plotted against the number of peptide bonds (N) between xanthone and naphthalene. The data were fitted to Eq. (1) and gave values of $k_0 = (1.8\pm0.2)\times10^8$ s^{-1}, $k_i = (6.7\pm1.6)\times10^9$ s^{-1} and $m = -1.72\pm0.08$ for the poly(glycine–serine) series and of $k_0 = (8.7\pm0.8)\times10^7$ s^{-1}, $k_i = (1.0\pm0.8)\times10^{10}$ s^{-1} and $m = -2.1\pm0.3$ for polyserine. The data for the parvalbumin loop were not included in the fit. Data for poly(glycine–serine) and for polyserine as well as the fit of the data were taken from [7].

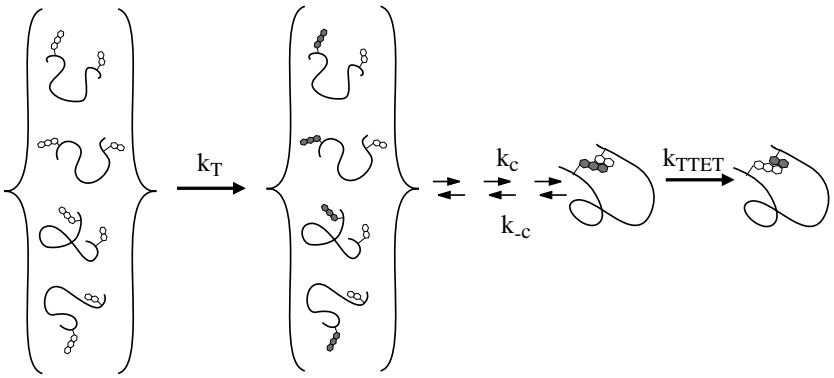

Fig. 1. Schematic of the triplet–triplet energy transfer (TTET) measurements applied to measure intrachain diffusion in polypeptide chains. The time constants for triplet formation ($1/k_T$) and electron transfer ($1/k_{TTET}$) are around 1–5 ps (H. Satzger, W. Zinth, B.F. and T.K., in preparation) and TTET is diffusion-controlled [7]. This allows measurements of absolute rate constants for intrachain diffusion (k_c) for processes slower than about 20 ps.

Our previous studies were mainly aimed at the scaling laws for intrachain diffusion in homo-polypeptide chains and at the effect of the amino sequence on local chain dynamics. However, polypeptide sequences from natural proteins are usually more complex and consist of different amino acids with a variety of side chains of different size and chemical properties. Here we test, whether the results from homo-polypeptides can be applied to dynamics of natural sequences. We measured intrachain contact formation between the ends of a loop region derived from a natural protein structure. Since triplet states may be quenched by a variety of chemical groups and triplet energy of xanthone may be transferred to aromatic amino acids we first determined the effect of various amino acids on the xanthone triplet lifetime. The results show that methionine, tryptophan, tyrosine and deprotonated histidine efficiently interact with xanthone triplets. We then choose a loop sequence of β-carp parvalbumin (residues 85–102) as a model to study kinetics of intrachain diffusion. This loop sequence is perfectly suited to measure intrachain diffusion using the xanthone/naphthalene pair since none of its amino acids interferes with the TTET experiments and the loop brings together two phenylalanine residues in native carp parvalbumin, which have similar properties as our donor and acceptor group (Fig. 3). In addition, this loop binds Ca^{2+} in the native state, which allows us to test the influence of Ca^{2+} on the dynamics of the

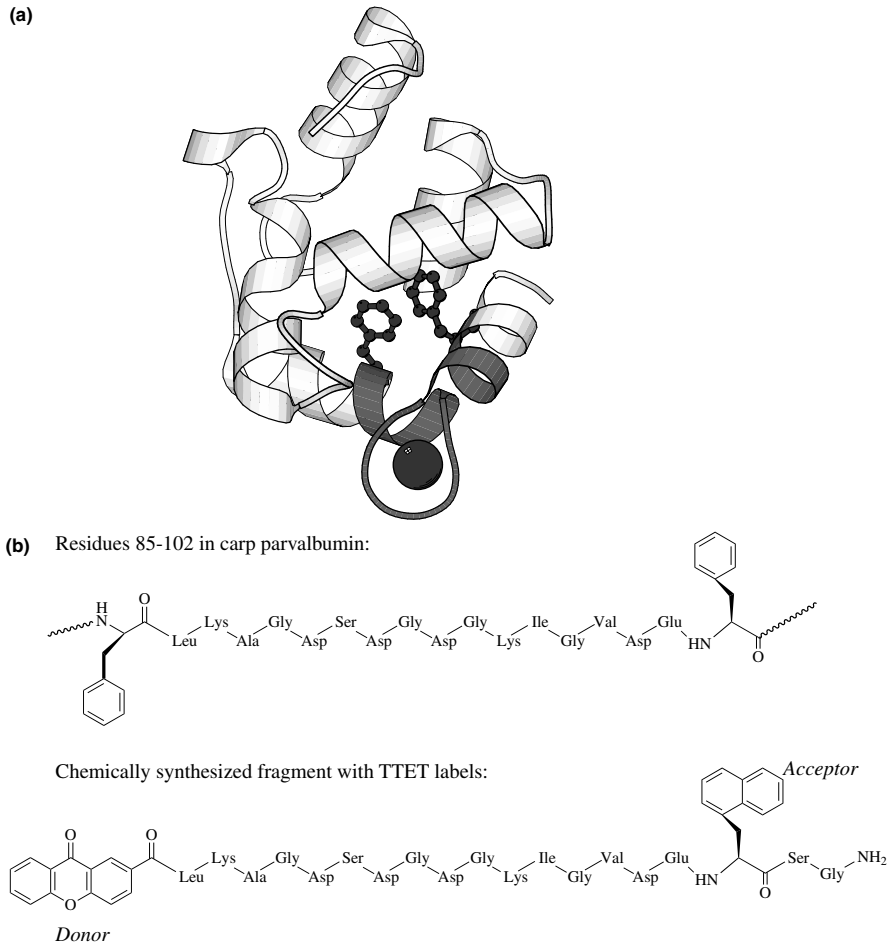

Fig. 3. (a) Ribbon diagram of the structure of carp muscle β-parvalbumin [13] with the loop region residues 85–102 shown in dark. Phe85 and Phe102 are shown as ball-and-stick models and the Ca^{2+} ion bound to the EF-loop is displayed as space-fill model. The phenylalanine residues have been replaced by the triplet donor and acceptor labels, xanthone acid and naphthylalanine, respectively. The figure was prepared using the program MolScript [20] and the pdb file 4CPV [13]. (b) Sequence of the β-carp muscle parvalbumin EF loop region (residues 85–102) and the synthesized fragment labeled with the two phenylalanine residues at positions 85 and 102 replaced by donor (xanthone) and acceptor (naphthylalanine) groups for triplet–triplet energy transfer.

isolated loop fragment. The results show that the rate constant of formation of this 18 amino acid loop corresponds well to the rate constant expected for a polyserine peptide of the same length. Ca^{2+} has no effect on the structure and chain dynamics, indicating that the binding constant for Ca^{2+} is significantly reduced compared to native parvalbumin.

2. Experimental

9-Oxoxanthen-2-carboxylic acid (xanthone acid) synthesis and synthesis of the sequence Xan–Leu–Lys–Ala–Gly–Asp–Ser–Asp–Gly–Asp–Gly–Lys–Ile–Gly–Val–Asp–Glu–NAla–Ser–Gly–NH_2 (NAla = 1-naphthylalanine) were performed as described previously [7]. Transient triplet absorption decay data were collected using a Laser Flash Photolysis Reaction Analyzer (LKS.60) from Applied Photophysics. Xanthone as triplet donor was excited selectively by using a Continuum Surelite Nd:YAG-Laser operating at 354.6 nm (~4 ns pulse width, ~100 mJ pulse energy). Peptide concentrations were determined by UV absorbance at 343 nm using a molar absorption coefficient of 3900 $M^{-1}cm^{-1}$ for xanthone in water and were typically in the 30–50 μM range. At these concentrations no intermolecular triplet–triplet energy transfer between two peptides occurs on the time scale of the experiments (5 ns to 50 μs) [6,7]. Transient triplet absorption of xanthone and of naphthalene was measured at 590 and 420 nm, respectively. All measurements were performed in 10 mM sodium cacodylate, pH 7.0 at 22.5 °C. 1 mM EDTA was added to remove traces of Ca^{2+} ions from the solutions, since this loop region binds Ca^{2+} with high affinity in native carp parvalbumin [10]. The effect of calcium on structure and dynamics of the loop was tested by adding various amounts of Ca^{2+} (1–100 mM) in the absence of EDTA. Sodium cacodylate, EDTA and Ca^{2+} have no influence on the xanthone triplet lifetime. Individual kinetics were measured five times, averaged and analyzed using ProFit software program. The kinetics were described by a double exponential fit. The faster reaction corresponds to TTET limited by intrachain diffusion and the slower reaction ($\tau = 1.2$ μs) represents spontaneous triplet decay of xanthone under the given conditions. The solutions were not degassed for the measurements described in this work, since the kinetics of contact formation occur on a much faster time scale than spontaneous triplet decay. Degassing the solution leads to an increase in the triplet lifetime of xanthone triplets from $\tau = 1.3$ to 10 μs, indicating that the triplet lifetime of xanthone in water is determined by oxygen quenching. The rate of intrachain diffusion is not affected by degassing the solutions [7]. The bimolecular rate constants for quenching and TTET for the different amino acids were determined by measuring xanthone acid triplet lifetimes in the presence of the various amino acids under pseudo-first-order conditions with xanthone acid concentration was 35 μM and amino acid concentrations between 1 and 50 mM. For all amino acids which interacted with xanthone acid a linear dependence of the pseudo-first-order rate constant on the quencher concentration was observed. The slope of this dependence was used for calculating the bimolecular quenching constant (k_q). Circular dichroism (CD) measurements of the peptide fragment were performed at 22.5 °C using an Aviv 62DS spectropolarimeter equipped with a temperature-control unit.

3. Results and discussion

3.1. Effect of various amino acids on xanthone triplet lifetimes

To test how experimental results on intrachain contact formation obtained on poly(glycine–serine) and polyserine chains compare to the dynamics of natural sequences we measured the rates of intrachain contact formation between the ends of a natural loop sequence. We first tested for possible interference from amino acid side chains with the TTET reaction from xanthone to naphthalene by determining the effect of various amino acids on the xanthone triplet lifetimes. Table 1 shows bimolecular triplet quenching and TTET rate constants measured under pseudo-first-order conditions. The thioether group of methionine ($k_q = (2.0 \pm 0.1) \times 10^9$ $M^{-1}s^{-1}$) and the deprotonated imidazole ring of histidine ($k_q = (1.8 \pm 0.1) \times 10^9$ $M^{-1}s^{-1}$) quench xanthone triplets very efficiently with a rate constant close to the diffusion limit. The other amino acid side chains quench xanthone triplets either very inefficiently (Cys, His^+, N-terminus)

Table 1
Interaction of different amino acids with the triplet state of xanthone[a]

Amino acid	k_q ($M^{-1}s^{-1}$)[b]	Conditions
Naphthyl acetic acid[c]	$(4.0 \pm 0.1) \times 10^9$	Water, pH 7
Trp[c]	$(3.0 \pm 0.1) \times 10^{9e}$	Water, pH 7
NAla[c]	$(2.8 \pm 0.1) \times 10^9$	Water, pH 7
Tyr[c]	$(2.5 \pm 0.1) \times 10^{9e}$	Water, pH 7
Met[d]	$(2.0 \pm 0.1) \times 10^9$	Water, pH 7
His[d]	$(1.8 \pm 0.1) \times 10^{9e}$	0.1 M KPP, pH 8
His^{+d}	$(2.8 \pm 0.2) \times 10^7$	0.1 M NaOAc, pH 4
Cys[d]	$(5.1 \pm 0.2) \times 10^7$	Water, pH 7
N-terminal NH^{3+d}	$(2.0 \pm 0.5) \times 10^6$	Water, pH 7

[a] No effect on the xanthone triplet lifetime was observed for Ala, Arg^+, Asn, Gly, Lys^+, Phe, Ser, Asp, Asp^-.
[b] Bimolecular quenching constants were measured under pseudo-first-order conditions as described in Section 2.
[c] Triplet–triplet energy transfer (TTET).
[d] Triplet quenching.
[e] Radical formation as side reaction.

or not at all (Ala, Arg, Asn, Asp, Gly, Lys, Ser, Phe). The aromatic amino acids tryptophan, tyrosine and phenylalanine are possible acceptors for xanthone triplets in TTET reactions. Table 1 shows that TTET between xanthone and tryptophan ($k_{TTET} = (3.0 \pm 0.1) \times 10^9$ $M^{-1}s^{-1}$) and tyrosine ($k_{TTET} = (2.5 \pm 0.1) \times 10^9$ $M^{-1}s^{-1}$) occur in diffusion-controlled reactions with virtually the same bimolecular rate constants as observed for TTET from xanthone to naphthylalanine ($k_{TTET} = (2.8 \pm 0.1) \times 10^9$ $M^{-1}s^{-1}$). However, TTET from xanthone to tryptophan and tyrosine are complex reactions with at least two observable rate constants. For both amino acids TTET is accompanied by radical formation [11,12], which explains the complex kinetics and makes them not suitable for the use as TTET acceptors in polypeptide chains. These results show that mainly methionine, tryptophan and tyrosine interfere with TTET from xanthone to naphthalene in intrachain diffusion experiments. Histidine containing sequences can be measured with this donor/acceptor pair if the pH of the solution is below 5.5.

3.2. Contact formation in an 18-residue loop fragment from β-parvalbumin

To measure intrachain contact formation in a naturally occurring protein loop we chemically synthesized a polypeptide fragment corresponding to residues 85–102 in β-carp parvalbumin (EF-loop; Fig. 3) as model system. None of the amino acids in this loop region influences the triplet states of xanthone (see Table 1). In the native state of parvalbumin the two phenylalanine residues at positions 85 and 102 are located near the C-terminus of the E-helix and near the N-terminus of the F-helix, respectively, and are in close contact with each other (Fig. 3(a)) [13]. We replaced Phe85 by xanthone and Phe102 by naphthylalanine (Fig. 3(b)) to measure intrachain diffusion between the ends of the EF-loop. The CD spectrum of the labelled peptide resembles a random coil spectrum (Fig. 4) and addition of 8 M urea has no influence on the CD signal, suggesting that the fragment is completely unfolded in water. This makes the parvalbumin EF-loop a suitable model to investigate the dynamics of intrachain contact formation in an unfolded polypeptide chain. In native carp parvalbumin the EF-loop binds calcium with a binding constant of $k_D = 10^{-8}$ M^{-1} [10]. Addition of 1–100 mM $CaCl_2$ to the synthesized fragment did not induce structure formation (data not shown) indicating that the peptide fragment has a significantly reduced binding affinity for calcium compared to native parvalbumin.

Fig. 5 shows the time-course of TTET from xanthone to naphthalene in the synthetic parvalbumin EF-loop in the absence of Ca^{2+}. The kinetics of contact formation can be described by a single-exponential, as previously observed for all poly(glycine–serine) and polyserine peptides. A fit of the data gives a time constant ($\tau = 1/k$) of 53 ± 3 ns for end-to-end contact formation. This value is in good agreement with the value expected from

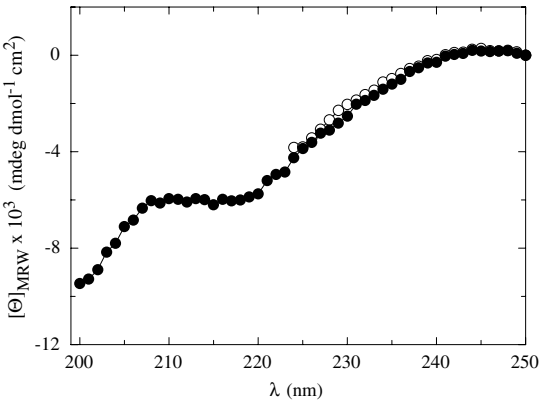

Fig. 4. Circular dichroism spectrum of chemically synthesized parvalbumin fragment 85–102 labeled with xanthone and naphthylalanine (see Fig. 3(b)). Spectra were recorded in 10 mM sodium cacodylate, 1 mM EDTA, pH 7.0 (●) and in 10 mM sodium cacodylate, 8 M urea, pH 7.0 (○).

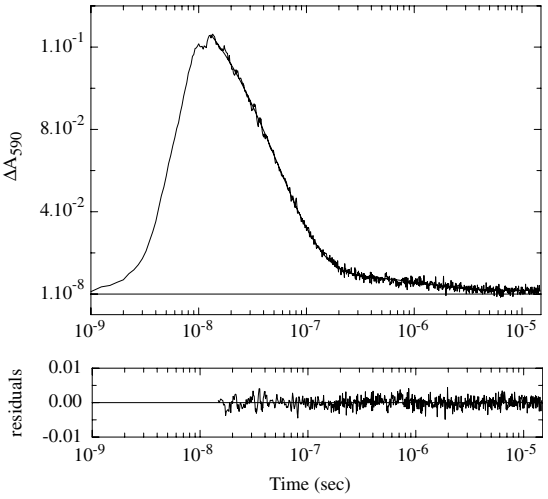

Fig. 5. Time-course of formation and decay of xanthone triplets in parvalbumin loop fragment 85–102 after a 4 ns laser flash at $t = 0$. The change of xanthone triplet absorbance is measured at 590 nm. The kinetic data can be described by a double-exponential fit. The residuals of the double exponential fit are displayed. The fast main phase has a rate constant $\tau = 1/k$ of 54 ± 3 ns (95% amplitude) and corresponds to end-to-end contact formation. The second phase (5% amplitude) has the same rate constant as spontaneous triplet decay of xanthone in water ($\tau = 1.3 \pm 0.1$ μs). This reaction presumably corresponds to xanthone triplet decay in peptides, which are not able to form end-to-end contacts, e.g. due to intermolecular association reactions [7]. It is not observed in the presence of 8 M urea, which dissolves associates (data not shown). The experiments were carried out in 10 mM sodium cacodylate, 1 mM EDTA, pH 7.0 at 25 °C. EDTA was added to remove traces of Ca^{2+}.

TTET measurements on polyserine peptides (Fig. 2). For contact formation in a peptide with sixteen serine residues between xanthone and naphthalene the polyserine series predicts a time constant of 49 ± 4 ns for end-to-end contact formation [7]. Unfortunately, we cannot directly measure the rate to a Xan–$(Ser)_{16}$–NAla peptide due to limitations in peptide synthesis. The presence of four glycine residues in the EF-loop sequence should lead to faster chain dynamics in the parvalbumin loop compared to polyserine. However, residues with branched C_β-positions like valine and leucine show slightly slower local dynamics than alanine and serine [7,14], which might explain the good agreement with the polyserine data. In addition, electrostatic repulsion between the five negatively charged aspartate/glutamate residues might increase the chain dimensions and thus compensate for the effect of the flexible glycines. The presence of 10 mM $CaCl_2$ does not effect the kinetics of end-to-end diffusion in the parvalbumin loop ($\tau = 54 \pm 3$ ns; data not shown). This shows that the fragment is not able to bind calcium ions with high affinity in the absence of the native tertiary structure and confirms the results from the CD measurements. These results indicate that the specific conformation of this loop in the native state rather than merely its amino acid sequence is responsible for strong Ca^{2+}-binding.

3.3. Comparison with dynamics of other natural and non-natural peptide sequences

Recently several other experimental systems have been used to measure the dynamics of intrachain diffusion in polypeptide chains. Quenching of tryptophan triplet states by cysteine in various peptide sequences gave significantly slower rates for chain diffusion compared to TTET from xanthone to naphthylalanine [15]. This reaction is, however, accompanied by the formation of $S^{\cdot}$ radicals and it is far from the diffusion limit. Thus, is can not be used to measure absolute model-free rate constants for intrachain diffusion [15,16]. Significantly slower rate constants compared to a diffusion-controlled TTET are thus expected in this system. Another experimental approach used short poly(glycine–serine) peptides and measured intrachain diffusion by the quenching of 2,3 diazabicyclo[2.2.2]oct-2-ene (DBO) fluorescence by tryptophan in water [17]. This quenching reaction is close to the diffusion limit but due to the short fluorescence lifetime of DBO it is restricted to fast contact kinetics, i.e. to short fluorophor-quencher distances. The results from these experiments gave slightly slower contact rates compared to TTET from xanthone to naphthylalanine in the same peptides. Again, this is in agreement with the observation that DBO quenching by tryptophan is not completely diffusion-controlled. A third experimental approach investigated intrachain contact formation in unfolded cytochrome *c* using electron transfer from a triplet excited Zn–porphyrine group to Ru bound to a specific histidine residue (His 33). This resulted in a loop size of 15 residues and yielded a time constant for electron transfer of 250 ns [18], which is significantly slower than our results on the 18 amino acid carp parvalbumin loop ($\tau = 54$ ns). However, the experiments on unfolded cytochrome *c* were performed in the presence of 5.4 M GdmCl, in order to completely unfold the protein. Our earlier experiments have shown that chemical denaturants like urea and GdmCl significantly decrease the rates of intrachain diffusion [7]. Both in poly(glycine–serine) and in polyserine peptides the presence of 5.4 M GdmCl slows down contact formation about threefold, which would result in a contact time constant of 80 ns in water for chain diffusion-limited electron transfer the 15 residues cytochrome *c* loop. The remaining small discrepancy between the dynamics in unfolded cytochrome *c* and the carp parvalbumin loop in water is probably due to the effect of end extensions on intrachain diffusion. We observed both in the poly(glycine–serine) and in the polyserine peptides that extensions of the polypeptide chains beyond the points of contact formation decreases the rates of intrachain diffusion (B.F. and T.K., manuscript in preparation). This effect will slow down contact formation in the 15 amino acid loop in unfolded cytochrome *c*, which comprises a total of 104 amino acids, compared to the synthesized parvalbumin loop, which just extends for just two additional amino acids beyond naphthylalanine (Fig. 3(b)). The rate constants for intrachain diffusion measured in unfolded cytochrome *c* using the Zn–porphyrine/Ru system are significantly faster than the dynamics estimated from intrachain diffusion in unfolded cytochrome *c* using methionine binding to heme as reporter reaction [19]. This can be explained by the reaction-controlled heme to methionine binding process, which does not allow the measurement of absolute rate constants for intrachain diffusion.

4. Conclusions

We showed that triplet–triplet energy transfer from xanthone to naphthylalanine can be used to measure absolute rate constants for end-to-end diffusion in natural loop sequences. This method will also be applicable to measure chain dynamics in unfolded and partially folded proteins provided the proteins are free of methionine, tryptophan and tyrosine. The results on the end-to-end contact formation in the EF-loop from carp parvalbumin revealed that our earlier measurements on polyserine peptides provide a good estimate for dynamics of natural protein loops. This is probably due to the compensating effect of flexible glycine residues, which leads

to faster dynamics and of C_β-branched side chains, which slow down chain dynamics.

References

[1] D. Neri, M. Billeter, G. Wider, K. Wüthrich, Science 257 (1992) 1559.
[2] J. Klein-Seetharaman, M. Oikawa, S.B. Grimshaw, J. Wirmer, E. Duchardt, T. Ueda, T. Imoto, L.J. Smith, C.M. Dobson, H. Schwalbe, Science 295 (2002) 1719.
[3] W.Y. Choy, F.A. Mulder, K.A. Crowhurst, D.R. Muhandiram, I.S. Millet, S. Doniach, J.D. Forman-Kay, L.E. Kay, J. Mol. Biol. 316 (2002) 101.
[4] G. Damaschun, H. Damaschun, K. Gast, D. Zirwer, Biochemistry (Moscow) 63 (1998) 259.
[5] D. Segel, A. Bachmann, J. Hofrichter, K. Hodgson, S. Doniach, T. Kiefhaber, J. Mol. Biol. 288 (1999) 489.
[6] O. Bieri, J. Wirz, B. Hellrung, M. Schutkowski, M. Drewello, T. Kiefhaber, Proc. Natl. Acad. Sci. USA 96 (1999) 9597.
[7] F. Krieger, B. Fierz, O. Bieri, M. Drewello, T. Kiefhaber, J. Mol. Biol. 332 (2003) 265.
[8] M. Klessinger, J. Michl, Excited States and Photochemistry of Organic Molecules, Weinheim/D, VCH, 1995.
[9] C.J. Camacho, D. Thirumalai, Proteins 22 (1995) 27.
[10] R.H. Kretsinger, CRC Crit. Rev. Biochem. 8 (1980) 119.
[11] D.V. Bent, E. Hayon, J. Am. Chem. Soc. 97 (1975) 2612.
[12] D.V. Bent, T. Hayano, J. Am. Chem. Soc. 97 (1975) 2599.
[13] V.D. Kumar, L. Lee, B.F. Edwards, Biochemistry (1990) 1404.
[14] F. Huang, W.M. Nau, Angew. Chem. Int. Ed. Engl. 42 (2003) 2269.
[15] L.J. Lapidus, W.A. Eaton, J. Hofrichter, Proc. Natl. Acad. Sci. USA 97 (2000) 7220.
[16] I.-C. Yeh, G. Hummer, J. Am. Chem. Soc. 124 (2002) 6563.
[17] R.R. Hudgins, F. Huang, G. Gramlich, W.M. Nau, J. Am. Chem. Soc. 124 (2002) 556.
[18] I.-J. Chang, J.C. Lee, J.R. Winkler, H.B. Gray, Proc. Natl. Acad. Sci. USA 100 (2003) 3838.
[19] S.J. Hagen, J. Hofrichter, A. Szabo, W.A. Eaton, Proc. Natl. Acad. Sci. USA 93 (1996) 11615.
[20] P. Kraulis, J. Appl. Cryst. 24 (1991) 946.

J|A|C|S
ARTICLES
Published on Web 12/23/2006

End-to-End vs Interior Loop Formation Kinetics in Unfolded Polypeptide Chains

Beat Fierz and Thomas Kiefhaber*

Contribution from the Division of Biophysical Chemistry, Biozentrum der Universität Basel, Klingelbergstrasse 70, CH-4056 Basel, Switzerland

Received September 14, 2006; E-mail: t.kiefhaber@unibas.ch

Abstract: The conformational search for favorable intramolecular interactions during protein folding is limited by intrachain diffusion processes. Recent studies on the dynamics of loop formation in unfolded polypeptide chains have focused on loops involving residues near the chain ends. During protein folding, however, most contacts are formed between residues in the interior of the chain. We compared the kinetics of end-to-end loop formation (type I loops) to the formation of end-to-interior (type II loops) and interior-to-interior loops (type III loops) using triplet−triplet energy transfer from xanthone to naphthylalanine. The results show that formation of type II and type III loops is slower compared to type I loops of the same size and amino acid sequence. The rate constant for type II loop formation decreases with increasing overall chain dimensions up to a limiting value, at which loop formation is about 2.5-fold slower for type II loops compared to type I loops. Comparing type II loops of different loop size and amino acid sequence shows that the ratio of loop dimension over total chain dimension determines the rate constant for loop formation. Formation of type III loops is 1.7-fold slower than formation of type II loops, indicating that local chain motions are strongly coupled to motions of other chain segments which leads to faster dynamics toward the chain ends. Our results show that differences in the kinetics of formation of type I, type II, and type III loops are mainly caused by differences in internal flexibility at the different positions in the polypeptide chain. Interactions of the polypeptide chain with the solvent contribute to the kinetics of loop formation, which are strongly viscosity-dependent. However, the observed differences in the kinetics of formation of type I, type II, and type III loops are not due to the increased number of peptide−solvent interactions in type II and type III loops compared to type I loops as indicated by identical viscosity dependencies for the kinetics of formation of the different types of loops.

Introduction

During protein folding many short-range and long-range intrachain interactions have to be established. Intrachain diffusion allows the chain to bring interacting groups together and to probe for favorable intramolecular interactions. Intrachain loop formation can thus be viewed as a fundamental step of protein folding and sets an upper limit for the rate at which the free energy surface can be explored. It was shown that inserting long loops into protein sequences reduces the stability of the native state[1,2] and slows down the folding kinetics,[3,4] which indicates that the size of loops is an important determinant of protein folding and stability. Three categories of intramolecular loops can be distinguished (Figure 1A). Type I loops are formed between the chain ends. The kinetics of formation of these loops has been studied in different polypeptide chains and with different experimental systems[5−10] (for a review see ref 11). However, during protein folding loop formation between an end and the interior of the chain (type II loops) or between two internal residues (type III loops) is much more common. In both cases, loop formation involves motions of additional chain segments (tails) beyond the region of contact formation. Polymer theory predicts that loop closure reactions become slower with increasing tail length until a limiting value is reached.[12−15] The effects of additional tails were predicted to depend on the size and on the stiffness of both the loop and the tails.[12] Experimental data on loop formation in long organic homopolymers showed slower dynamics for formation of type III loops compared to type I loops, but no clear dependency on the tail length was

(1) Nagi, A. D.; Regan, L. *Folding Des.* **1997**, *2*, 67−75.
(2) Wang, L.; Rivera, E. V.; Benavides-Garcia, M. G.; Nall, B. T. *J. Mol. Biol.* **2005**, *353*, 719−729.
(3) Viguera, A. R.; Serrano, L. *Nat. Struct. Biol.* **1997**, *4*, 939−946.
(4) Ladurner, A. G.; Fersht, A. R. *J. Mol. Biol.* **1997**, *273*, 330−337.
(5) Bieri, O.; Wirz, J.; Hellrung, B.; Schutkowski, M.; Drewello, M.; Kiefhaber, T. *Proc. Natl. Acad. Sci. U.S.A.* **1999**, *96*, 9597−9601.
(6) Krieger, F.; Fierz, B.; Bieri, O.; Drewello, M.; Kiefhaber, T. *J. Mol. Biol.* **2003**, *332*, 265−274.
(7) Krieger, F.; Fierz, B.; Axthelm, F.; Joder, K.; Meyer, D.; Kiefhaber, T. *Chem. Phys.* **2004**, *307*, 209−215.
(8) Chang, I.-J.; Lee, J. C.; Winkler, J. R.; Gray, H. B. *Proc. Natl. Acad. Sci. U.S.A.* **2003**, *100*, 3838−3840.
(9) Hudgins, R. R.; Huang, F.; Gramlich, G.; Nau, W. M. *J. Am. Chem. Soc.* **2002**, *124*, 556−564.
(10) Lapidus, L. J.; Eaton, W. A.; Hofrichter, J. *Proc. Natl. Acad. Sci. U.S.A.* **2000**, *97*, 7220−7225.
(11) Fierz, B.; Kiefhaber, T. Dynamics of unfolded polypeptide chains. In *Protein Folding Handbook*; Buchner, J., Kiefhaber, T., Eds.; WILEY-VCH: Weinheim, 2005; pp 805−851.
(12) Perico, A.; Beggiato, M. *Macromolecules* **1990**, *23*, 797−803.
(13) Friedman, B.; O'Shaughnessy, B. *Macromolecules* **1993**, *26*, 4888−4898.
(14) Ortiz-Repiso, M.; Rey, A. *Macromolecules* **1998**, *31*, 8356−8362.
(15) Ortiz-Repiso, M.; Rey, A. *Macromolecules* **1998**, *31*, 8363−8369.

10.1021/ja0666396 CCC: $37.00 © xxxx American Chemical Society

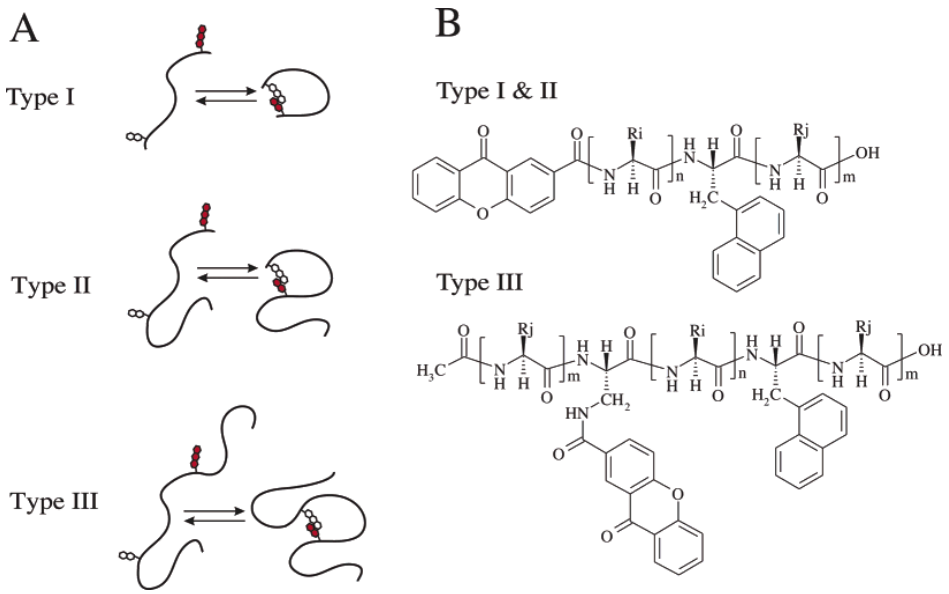

Figure 1. (A) Schematic representation of type I, and type II and type II loop formation reactions. (B) General structures of peptides used in TTET experiments. In type I and type II loops the xanthone label is attached to the N-terminus and naphthylalanine (NAla) defines the C-terminus of the loop region. For type III loop peptides xanthone is attached to an α,β-diaminopropionic acid side chain at the N-terminal end of the loop region.

observed.[16] Measurements of loop formation between two internal residues in unfolded cytochrome c yielded slower kinetics[8] than expected from results on type I loop formation in model peptides.[6,11] However, to date it has not been systematically investigated whether end extensions affect the kinetics of loop formation in polypeptide chains.

We have studied the kinetics of end-to-end loop formation in unfolded polypeptide chains using triplet−triplet energy transfer (TTET) between a xanthone (Xan) moiety and a naphthylalanine (NAla) group.[6,7,11,17−19] TTET between Xan and NAla requires van der Waals contact between donor and acceptor, and all photophysical processes involved in this process occur on the picoseconds time scale.[6,20,21] This allows measurements of diffusion controlled intrachain loop formation reactions on an absolute time scale. In previous studies triplet donor and acceptor groups were attached at the ends of poly-serine and poly-(glycine-serine) chains of different lengths[6] and fragments from natural proteins.[7] In all investigated chains single-exponential kinetics for loop formation were observed with rate constants, k_c, around 10^7-10^8 s^{-1}. These studies allowed us to elucidate the effect of amino acid sequence on loop formation and to derive scaling laws. In flexible glycine-serine copolymers it was found that for sufficiently long chains (number of loop residues $N > 20$) k_c decreases with $N^{-1.7\pm0.1}$, which is the expected behavior for an excluded volume chain.[6,11] For shorter loops, the dynamics reached an upper limit of $k_c = 1.9 \times 10^8$ s^{-1}. Stiffer chains devoid of glycine residues showed similar scaling laws with only slightly slower kinetics compared to poly(glycine-serine).[6] Here we test whether additional tails beyond the loop region influence the kinetics of loop formation. We used TTET between xanthone and naphthylalanine to measure formation of type II and type III loops in several model polypeptide chains and compared the results to kinetics of type I loops with the same loop region. In addition, we studied the effect of length and amino acid sequence of the additional tails on the dynamics of loop formation.

Results

Type II vs Type I Loop Formation. To investigate the effect of an additional tail at one end of a loop on the kinetics of contact formation we measured TTET between Xan and NAla attached to the ends of a loop consisting of four Gly-Ser pairs (see Figure 1B). This represents a model for an average size protein loop with high flexibility.[22] We used two different series of C-terminal extensions (see Table 1). In series 1, the extension is composed of $(Ser\text{-}Gly)_n$ units ($n = 1, 4, 7, 12$). In series 2 the tail consists of the sequence Ser-Gly-$(Thr\text{-}Gly\text{-}Gln\text{-}Ala)_n$-Gln-Ala-Ser-Gly ($n = 2, 4$). All peptides from both series are free of charged side-chains and unstructured as judged from circular dichroism spectra (data not shown). Figure 2 compares kinetics of contact formation in the *Xan*-$(Gly\text{-}Ser)_4$-*NAla*-Ser-Gly peptide and in a peptide with the same loop sequence but with the amino acids Ser-Gly-$(Thr\text{-}Gly\text{-}Gln\text{-}Ala)_4$-Gln-Ala-Ser-Gly attached C-terminal from the NAla moiety. The reaction was initiated by a 4 ns laserflash at 355 nm, which produces xanthone triplet states within the duration of the laserflash.[6,20,21] Loop formation between xanthone and naphthylalanine was monitored by the decrease in xanthone triplet absorbance at 590 nm.[6] Loop formation is slowed down 1.6-fold in the presence of the additional 20 C-terminal tail residues in the longer peptide. Varying the length of the C-terminal extension reveals that $\log(k_c)$ decreases linearly with increasing tail length (Figure 3A). However, the effect of increasing tail length on k_c is not identical

(16) Lee, S.; Winnik, M. A. *Macromolecules* **1997**, *30*, 2633−2641.
(17) Bieri, O.; Kiefhaber, T. *Biol. Chem.* **1999**, *380*, 923−929.
(18) Krieger, F.; Möglich, A.; Kiefhaber, T. *J. Am. Chem. Soc.* **2005**, *127*, 3346−3352.
(19) Möglich, A.; Krieger, F.; Kiefhaber, T. *J. Mol. Biol.* **2005**, *345*, 153−162.
(20) Satzger, H.; Schmidt, B.; Root, C.; Zinth, W.; Fierz, B.; Krieger, F.; Kiefhaber, T.; Gilch, P. *J. Phys. Chem. A* **2004**, *108*, 10072−10079.
(21) Heinz, B.; B., S.; Root, C.; Satzger, H.; Milota, F.; Fierz, B.; Kiefhaber, T.; Zinth, W.; Gilch, P. *Phys. Chem. Chem. Phys.* **2006**, *8*, 3432−3439.
(22) Leszcynski, J. F.; Rose, G. D. *Science* **1986**, *234*, 849−855.

Table 1. Sequences of Peptides Used for TTET Experiments[a]

peptides	sequence	*n*
series 1	**Xan-(Gly-Ser)$_4$-NAla-**(Ser-Gly)$_n$-OH	1, 4, 7, 12
series 2	**Xan-(Gly-Ser)$_4$-NAla-**Ser-Gly-(Thr-Gly-Gln-Ala)$_n$-Gln-Ala-Ser-Gly-OH	2, 4
series 3	**Xan-Gly-Ser-NAla-**(Ser-Gly)$_n$-OH	1, 6
series 4	**Xan-Gly-Ser-NAla-**(Thr-Gly-Gln-Ala)$_n$-Gln-Ala-Ser-Gly-OH	2, 4
series 5	**Xan-Ser-Ser-Ser-NAla-**(Ser-Gly)$_n$-OH	1, 6
series 6	**Xan-Ser-Ser-Ser-NAla-**(Thr-Gly-Gln-Ala)$_n$-Gln-Ala-Ser-Gly-OH	2, 4
series 7	**Xan-(Gly-Ser)$_{10}$-NAla-**(Ser-Gly)$_n$-OH	1, 6
series 8	**Xan-(Gly-Ser)$_{10}$-NAla-**(Thr-Gly-Gln-Ala)$_n$-Gln-Ala-Ser-Gly-OH	2
series 9	Ac-(Gly-Ser)$_n$-**Dpr(Xan)-(Gly-Ser)$_4$-NAla-**(Ser-Gly)$_n$-OH	2, 4, 6
series 10	Ac-Gly-Ser-Ala-Gln-(Ala-Gln-Gly-Thr)$_n$-**Dpr(Xan)-(Gly-Ser)$_4$-NAla-**(Thr-Gly-Gln-Ala)$_n$-Gln-Ala-Ser-Gly-OH	2
biotin	**Xan-(Gly-Ser)$_4$-NAla-**(Ser-Gly)$_8$-Lys(Biotin)-Ser-Gly-OH	

[a] Ac: acetylated N-terminus. Xan: xanthonic acid. NAla: naphthylalanine. Dpr: α,β-diaminopropionic acid. Loop regions are printed in boldface.

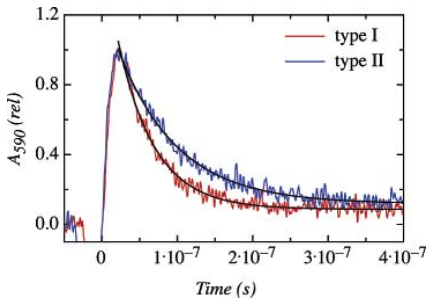

Figure 2. Comparison of the kinetics of formation of a type I loop (Xan-(Gly-Ser)$_4$-NAla-Ser-Gly) and a type II loop (Xan-(Gly-Ser)$_4$-NAla-Ser-Gly-(Thr-Gly-Gln-Ala)$_4$-Gln-Ala-Ser-Gly-OH) with identical loop regions monitored by the decay in xanthone triplet absorbance at 590 nm. Single-exponential fits to the data yield rate constants of $(2.1 \pm 0.1) \times 10^7$ s^{-1} and $(1.3 \pm 0.1) \times 10^7$ s^{-1} for the type I and type II loop, respectively. The experiments were carried out in a 44% (v/v) glycerol/water mixture corresponding to $\eta = 3$ cP. Data for the type I loop were taken from ref 6.

for the two series of extensions when the number of amino acids in the tail, *N*, is compared. The rate constants are less affected by the (Ser-Gly)$_n$ extension compared to the (Thr-Gly-Gln-Ala)$_n$ series of equal length (Figure 3A) indicating that the effect on k_c does not correlate with the number of chain segments in the tail.

To elucidate the origin of the observed effect of end extensions on the kinetics of type II loop formation we tested the correlation of k_c with various parameters. Peptide motions in water are overdamped, and thus inertial forces should not contribute to the dynamics. The kinetics of loop formation should thus not correlate with the mass of the tail. Intrachain motions are rather coupled to solvent motion[23,24] as indicated by the observed strong viscosity-dependence of the kinetics of end-to-end loop formation.[5,19] The increased number of interactions of the polypeptide chain with the solvent in type II loops compared to type I loops may slow down chain dynamics. In this case the effect of the additional tail on k_c should correlate with the solvent accessible surface area (ASA) of the tail. The exact ASA of an unfolded polypeptide chain is typically approximated by calculating the ASA of a fully extended chain.[25] Figure 3B shows log(k_c) as a function of the ASA of the tail (ASA$_{tail}$) for both series of extension. The effect of ASA$_{tail}$ on k_c is similar for both series, but there is still a slight deviation between the two series of extensions for long tails. The data can be fitted according to

$$k_c = k_0 \exp(\alpha \mathrm{ASA}_{tail}) \quad (1)$$

where k_0 represents the rate constants for type I loop formation. A fit to the data from both series of extensions gave values of $k_0 = (8.5 \pm 0.1) \times 10^7$ s^{-1} and $\alpha = (-1.5 \pm 0.1) \times 10^{-4}$ Å^{-2}.

Theoretical considerations based on polymer theory suggested that the effect of additional tails on the dynamics of loop formation is a function of tail length and chain stiffness, i.e., of the dimensions of the tail.[12] Flory introduced the characteristic ratio, C_N, to calculate dimensions of polymer chains[26] which includes contributions from the number of chain segments and from chain stiffness

$$C_N = \frac{\langle r^2 \rangle}{Nl^2} \quad (2)$$

where $\langle r^2 \rangle$ denotes the mean square end-to-end distance, *N* is the number of chain segments, and l^2 is the squared segment length. C_N for real chains is larger than unity; i.e., the dimensions of a real chain grow more strongly with increasing number of chain residues compared to an ideal chain where the end-to-end distance grows with $\langle r^2 \rangle = Nl^2$. C_N is a function of *N* and increases with increasing chain length up to a limiting value, C_∞, which is related to the persistence length of the chain.[26] In polypeptide chains C_∞ is 9.27 for poly-alanine, and a similar value was proposed for all other amino acids except glycine and proline. Introduction of glycine residues leads to more flexible chains and thus to a smaller C_N and decreased chain dimensions. Using the transformation matrices to calculate characteristic ratios for polypeptide chains determined by Flory[26] we calculated mean square end-to-end distances for all investigated polypeptide chains according to eq 2. This allows us to test for the effect of changes in chain dimensions caused by additional tails on the rate constant of loop formation. The absolute values of $\langle r^2 \rangle$ are most likely inaccurate, since only nearest neighbor potentials were considered by Flory. Long-range intrachain interactions[27] and peptide−solvent interactions, which are neglected in these calculations, were also shown to affect the chain dimensions. However, the calculated $\langle r^2 \rangle$-values allow an estimate of the relative dimensions of the different loops. Figure 3C shows log(k_c) as a function of the average

(23) Kramers, H. A. *Physica* **1940**, *4*, 284−304.
(24) Szabo, A.; Schulten, K.; Schulten, Z. *J. Chem. Phys.* **1980**, *72*, 4350−4357.
(25) Myers, J. K.; Pace, C. N.; Scholtz, J. M. *Protein Sci.* **1995**, *4*, 2138−2148.
(26) Flory, P. J. *Statistical Mechanics of Chain Molecules*; Hanser Publishers: Munich, 1969.
(27) Pappu, R. V.; Srinivasan, R.; Rose, G. D. *Proc. Natl. Acad. Sci. U.S.A.* **2000**, *97*, 12565−12570.

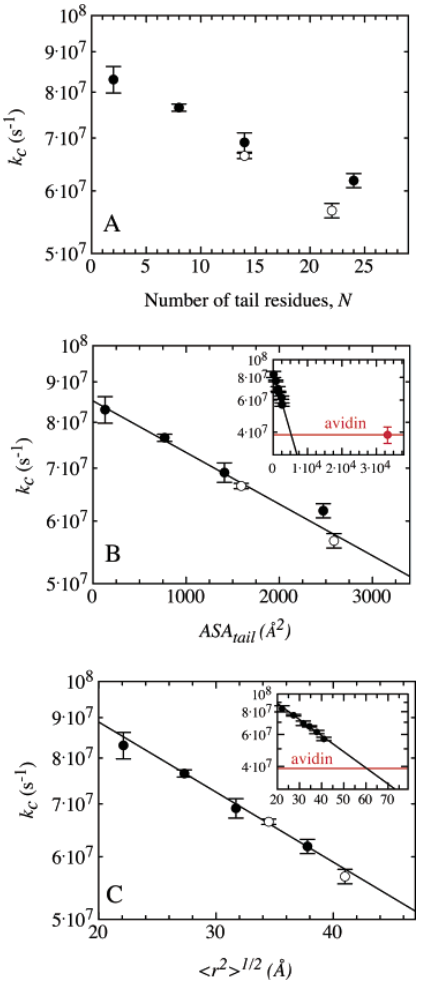

Figure 3. (A) Effect of the number of tail residues, *N*, on the rate constants for type II loop formation, k_c, in a Xan-(Gly-Ser)$_4$-NAla loop with (Ser-Gly)$_n$ (●, series 1 peptides) or with Ser-Gly-(Thr-Gly-Gln-Ala)$_n$-Gln-Ala-Ser-Gly (○, series 2 peptides) C-terminal extensions. (B) Effect of the accessible surface area (ASA) of the C-terminal tail on the rate constants for type II loop formation. Peptides and symbols are the same as those in panel A. The solid line is an exponential fit of eq 1 to the data with $k_0 = (8.5 \pm 0.1) \times 10^7$ s^{-1} and $\alpha = (-1.5 \pm 0.1) \times 10^{-4}$ Å^{-2}. (C) Effect of the calculated average end-to-end distance, $\sqrt{\langle r^2 \rangle}$, on the rate constants for type II loop formation. Peptides and symbols are the same as those in panel A. The solid line is an exponential fit of eq 3 to the data with $k_0 = (8.9 \pm 0.2) \times 10^7$ s^{-1} and $\alpha = (-2.0 \pm 0.1) \times 10^{-2}$ Å^{-1}. The insets in panels B and C show k_c for the biotinylated peptide bound to avidin. Rate constants are given for 22.5° in water.

end-to-end distance of the whole chain ($\sqrt{\langle r^2 \rangle}$) for both series of *Xan*-(Gly-Ser)$_4$-*NAla* type II loops. Changes in $\sqrt{\langle r^2 \rangle}$ have the same effect on k_c in the (Ser-Gly)$_n$ and (Thr-Gly-Gln-Ala)$_n$ extension series, which can be described by

$$k_c = k_0 \exp(\alpha \sqrt{\langle r^2 \rangle}) \qquad (3)$$

where k_0 denotes the rate constant of the type I loop formation at $\sqrt{\langle r^2 \rangle_{loop}}$, which is 20 Å for the *Xan*-(Gly-Ser)$_4$-*NAla* loop. A fit of eq 3 to the data obtained from both series of peptides gives values of $k_0 = (8.9 \pm 0.2) \times 10^7$ s^{-1} and $\alpha = (-2.0 \pm 0.1) \times 10^{-2}$ Å^{-1} (see Table 2). This suggests that the effect of an additional tail on the dynamics of loop formation depends on the overall chain dimensions. This finding supports the results from polymer theory which suggested that both chain length and chain stiffness influence loop formation. The agreement of data obtained from the two series of chain extensions seems to be slightly better when k_c is correlated with $\sqrt{\langle r^2 \rangle}$ (Figure 3C) compared to the correlation between k_c and ASA$_{tail}$ (Figure 3B). However, $\sqrt{\langle r^2 \rangle}$ is correlated with ASA$_{tail}$, which makes it difficult to evaluate the major determinant for the effect of end extensions on chain dynamics.

Table 2. Dimensions and Rate Constants for Loop Formation for the Different Type I Loops and Effect of a C-Terminal Extension on the Kinetics of Loop Formation

loop sequence	$\sqrt{\langle r^2 \rangle_{loop}}$[a] (Å)	k_0[b] (s^{-1})	α[b] (Å^{-1})
Xan-Gly-Ser-NAla	11.3	$(1.9 \pm 0.1) \times 10^8$	$(-4.6 \pm 0.2) \times 10^{-2}$
Xan-(Gly-Ser)$_4$-NAla	20.0	$(8.9 \pm 0.2) \times 10^7$	$(-2.0 \pm 0.1) \times 10^{-2}$
Xan-(Gly-Ser)$_{10}$-NAla	30.3	$(3.0 \pm 0.2) \times 10^6$	$(-2.1 \pm 0.8) \times 10^{-2}$
Xan-Ser-Ser-Ser-NAla	14.8	$(8.1 \pm 0.2) \times 10^6$	$(-3.0 \pm 0.2) \times 10^{-2}$

[a] Calculated using the parameters given by Flory.[26] [b] k_0 and α were determined by a fit of eq 3 to the data shown in Figure 4A.

Polymer theory predicts that the effect of end extensions on the kinetics of loop formation should reach a limiting value for long tails.[12] The effect of a C-terminal extension on the kinetics of formation of the *Xan*-(Gly-Ser)$_4$-*NAla* loop does not reach a limiting value in the range of extensions accessible with standard peptide synthesis. To test whether a very large polypeptide chain attached to the C-terminus has a strong effect on the kinetics of loop formation, we synthesized a type II *Xan*-(Gly-Ser)$_4$-*NAla* loop containing a biotinylated lysine residue near the end of the C-terminal extension (Table 1). This allowed us to bind the peptide to avidin, a tetrameric glycoprotein from hen egg white ($M_r = 62\,400$, ASA = 21 000 Å^2), which strongly binds a biotin group per monomer with a dissociation constant of 1.3×10^{-15} M.[28] Considering the dimensions of an avidin tetramer this leads to a very large increase in chain dimensions and should allow us to answer the question of a limiting value for type II loop dynamics. The rate constant for loop formation in the biotinylated peptide in the absence of avidin is $(6.3 \pm 0.2) \times 10^7$ s^{-1}. Upon addition of avidin, the rate constant decreases to $(3.9 \pm 0.4) \times 10^7$ s^{-1}, which corresponds to a 2.3-fold slower loop formation compared to the corresponding type I loop. The effect of avidin is much smaller than expected from the surface area (Figure 3B, inset) or the size (Figure 3C, inset) of the avidin tetramer with four biotinylated polypeptide chains bound (ASA ≈ 33 000 Å^2). This result shows that the kinetics of loop formation in the type II Xan-(Gly-Ser)$_4$-NAla loop become independent of tail length when the overall chain dimensions are larger than $\sqrt{\langle r^2 \rangle} = 62$ Å (Figure 3C, inset), i.e. when the overall chain dimensions are about three times the dimensions of the loop region. This limiting value can be explained by an increased flexibility of polypeptide chains toward the chain ends, which was directly observed in NMR experiments.[29,30] In type

(28) Green, N. M. *Adv. Protein Chem.* **1975**, *29*, 85−133.
(29) Schwalbe, H.; Fiebig, K. M.; Buck, M.; Jones, J. A.; Grimshaw, S. B.; Spencer, A.; Glaser, S. J.; Smith, L. J.; Dobson, C. M. *Biochemistry* **1997**, *36*, 8977−8991.
(30) Klein-Seetharaman, J.; Oikawa, M.; Grimshaw, S. B.; Wirmer, J.; Duchardt, E.; Ueda, T.; Imoto, T.; Smith, L. J.; Dobson, C. M.; Schwalbe, H. *Science* **2002**, *295*, 1719−1722.

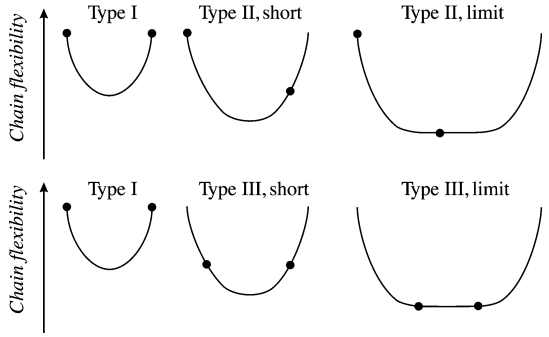

Figure 4. Schematic representation of the position-dependence of chain flexibility and the resulting position of the points of contact formation in type I, type II, and type III loops. The scheme shows that a limiting value for the chain stiffness is reached for long type II and type III loops. The position-dependence of chain stiffness is based on theoretical work[31] and on results from NMR experiments.[29,30]

I loops, both contact points are located in flexible parts of the chain ends, which leads to faster dynamics compared to type II loops, where one of the contact points is located in a stiffer chain segment of the chain (Figure 4). This effect should be saturated for longer type II loops, when chain stiffness at the interior contact point has reached a limiting value. The observation of a limiting value for the effect of an end extension supports the model that the ASA of the tail is not the major determinant for the effect of a type II tail on k_c. In this case, a much larger effect of avidin on k_c would be expected (Figure 3B, inset). In the following, we will therefore correlate the rate constants of loop formation with changes in $\langle r^2 \rangle$. This correlation allows us to compare our results with theoretical results from polymer theory.

Effect of Loop Length and Loop Sequence on the Kinetics of Type II Loop Formation. To test the effect of loop length and loop sequence on the kinetics of type II loop formation we investigated type II loops with different loop regions (see Table 1). A loop consisting of *Xan*-Gly-Ser-*NAla* (series 3, 4) was used as a model for an i, $i + 3$ contact, which is frequently observed in β-turn sequences. A *Xan*-Ser-Ser-Ser-*NAla* loop (series 5, 6) was used as a model for short and stiff loops, and a *Xan*-$(Gly\text{-}Ser)_{10}$-*NAla* loop (series 7, 8) served as a model for long and flexible loops. The effect of the additional tail on the kinetics of loop closure in the different peptides is shown in Figure 5. In agreement with our earlier results,[6] a large variation in k_c is observed for the different type I loops, but also the effect of end extensions is different for the different loops. Contact formation in the short *Xan*-Gly-Ser-*NAla* and *Xan*-Ser-Ser-Ser-*NAla* loops is more strongly influenced by additional tails compared to the *Xan*-$(Gly\text{-}Ser)_4$-*NAla* and the *Xan*-$(Gly\text{-}Ser)_{10}$-*NAla* loops (Figure 5A). In the short *Xan*-Gly-Ser-*NAla* loop the two longest extensions show the same k_c values within experimental error. For these peptides the total peptide dimensions are 2.6 times and 3.3 times larger, respectively, than the dimensions of the loop region and the rate constant for contact formation is 2.3-fold smaller than that in the corresponding type I reference loop. The relative size of the additional tail and the decrease in k_c are comparable to the respective values found for the limiting regime in the longer *Xan*-$(Gly\text{-}Ser)_4$-*NAla* type II loop (Figure 3C, inset). This indicates that the rate constants for loop formation in the two

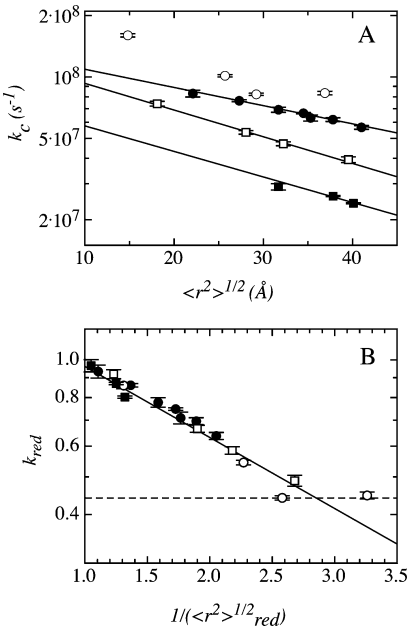

Figure 5. (A) Effect of $\sqrt{\langle r^2 \rangle}$ on the rate constants for type II loop formation in different peptide systems with varying loop sequence: (○) Gly-Ser loop (series 3 and 4 peptides); (●) $(Gly\text{-}Ser)_4$ loop (series 1 and 2 peptides); (□) Ser_3 loop (series 5 and 6 peptides), (■) $(Gly\text{-}Ser)_{10}$ loop (series 7 and 8 peptides). For peptide sequences see Table 1. (B) Effect of the inverse of the reduced loop size, $\sqrt{\langle r^2 \rangle_{red}} = \sqrt{\langle r^2 \rangle_{loop}}/\sqrt{\langle r^2 \rangle}$, on the reduced rate constants, $k_{red} = k_c/k_0$ for type II loop formation. Peptide and symbols are the same as those in panel A. Values for k_0 were obtained from the fit to the data shown in panel A using eq. 3 and are given in Table 2. Values of $\sqrt{\langle r^2 \rangle_{loop}}$ for the different loops are also given in Table 2. A fit of eq 6 to the data gives $\alpha = (-4.5 \pm 0.1) \times 10^{-1}$.

longest peptides of the type II *Xan*-Gly-Ser-*NAla* loops may have already reached the limiting value.

Effect of Relative Loop Size on Kinetics of Type II Loop Formation. To directly compare the results from the different type II loops and to test whether the ratio of total peptide dimensions, $\sqrt{\langle r^2 \rangle}$, over loop dimensions, $\sqrt{\langle r^2 \rangle_{loop}}$, is rate-determining for loop formation, we calculated the reduced loop sizes, $\sqrt{\langle r^2 \rangle_{red}}$, for all type II loops according to

$$\sqrt{\langle r^2 \rangle_{red}} = \sqrt{\langle r^2 \rangle_{loop}}/\sqrt{\langle r^2 \rangle} \qquad (4)$$

The $\sqrt{\langle r^2 \rangle_{red}}$ values were compared to reduced rate constants for loop formation, k_{red}, calculated according to

$$k_{red} = k_c/k_0 \qquad (5)$$

which allows a comparison of the different type II loops by accounting for the differences in k_0. Figure 5B shows that $\log(k_{red})$ is correlated with the inverse of the reduced loop size, $1/\sqrt{\langle r^2 \rangle_{red}}$ and that the k_{red} values of all type II loops show the same dependence on $1/\sqrt{\langle r^2 \rangle_{red}}$ which can be described by

$$k_{red} = \exp(\alpha/\sqrt{\langle r^2 \rangle_{red}}) \qquad (6)$$

with $\alpha = (-4.5 \pm 0.1) \times 10^{-1}$ (eq. 6). Figure 5B further shows that the limiting value for k_{red} and $\sqrt{\langle r^2 \rangle_{red}}$ are very similar for

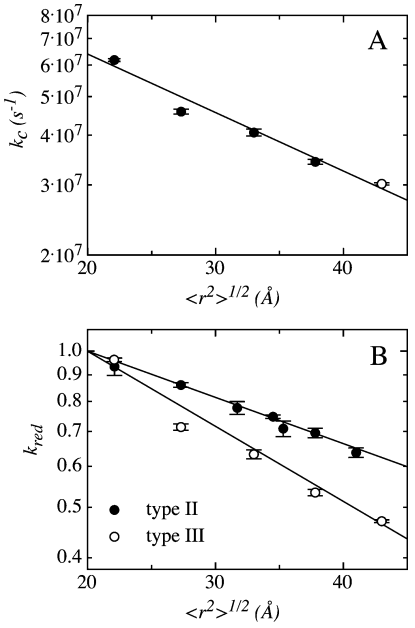

Figure 6. (A) Effect of the calculated average end-to-end distance, $\sqrt{\langle r^2 \rangle}$, on the rate constants for type III loop formation in a *Dpr(Xan)*-(Gly-Ser)$_4$-*NAla* loop with (Ser-Gly)$_n$ (●, series 9 peptides) or with (Thr-Gly-Gln-Ala)$_n$ (○, series 10 peptides) C- and N-terminal extensions. The solid line is an exponential fit of eq 3 to the data with $k_0 = (6.4 \pm 0.1) \times 10^7$ s^{-1} and $\alpha = (-3.3 \pm 0.1) \times 10^{-2}$ Å^{-1}. (B) Comparison of the reduced rate constants, k_{red}, for type II and type III loop formation with the identical loop sequence Xan-(Gly-Ser)$_4$-NAla. A fit of eq 6 to the data gives $\alpha = (-2.0 \pm 0.1) \times 10^{-2}$ for type II loops (see Figure 5B) and $\alpha = (-3.3 \pm 0.2) \times 10^{-2}$ for type III loops.

the type II loop sequences *Xan*-Gly-Ser-*NAla* and *Xan*-(Gly-Ser)$_4$-*NAla*. These results suggest that the reduced loop size $\sqrt{\langle r^2 \rangle}_{red}$ determines the effect of tails on contact formation in type II systems and that the limiting value for short and long loops is reached at similar values of $\sqrt{\langle r^2 \rangle}_{red} = 0.35$ with $k_{red} = 0.43$.

Type III Loop Formation. Interior-to-interior loop formation reactions (type III loops, see Figure 1A) are most relevant during protein folding. To probe the dynamics of type III loop formation we synthesized different series of peptides with extensions at both ends of the loop region (Table 1). To compare the dynamics of type III and type II loops we chose a *Xan*-(Gly-Ser)$_4$-*NAla* loop sequence. The xanthone moiety was attached to a diaminopropionic acid side chain at the N-terminal end of the loop region. This allows the addition of amino acids N-terminal from the loop regions in order to produce type III loops (see Figure 1B). The C-terminal end of the loop was again defined by a NAla residue. The C-terminal chain extensions were composed of (Ser-Gly)$_n$ ($n = 2$, 4, 6) or of (Thr-Gly-Gln-Ala)$_2$ sequences, whereas for the N-terminal extensions the sequences were inverted (series 9, 10 peptides). To compare these peptides to a type I system, a reference peptide with the same loop sequence but without extensions was produced. Due to the attachment of the xanthone moiety to a side chain via an amide bond in this series of peptides the kinetics were slightly slower than those in previously used type I systems with the xanthone attached directly to the N-terminus via an amide bond.

Figure 6A compares the rate constant of contact formation in the *Xan*-(Gly-Ser)$_4$-*NAla* type III loop with different extensions. Contact formation becomes slower when tails are attached to both sides of the loop region. A comparison of k_c in peptides bearing (Ser-Gly)$_n$ or (Thr-Gly-Gln-Ala)$_n$ extensions shows that log(k_c) linearly decreases with increasing overall chain dimensions, $\sqrt{\langle r^2 \rangle}$, as observed for type II loops (see Figure 3). A fit of eq 3 to the data yields $\alpha = (-3.3 \pm 0.1) \times 10^{-2}$ Å^{-1} for the type III loops compared to $\alpha = (-2.0 \pm 0.1) \times 10^{-2}$ Å^{-1} observed for type II loops with the same loop sequence (Figure 3C). To directly compare kinetics of *Xan*-(Gly-Ser)$_4$-*NAla* type II and III loops we calculated reduced rate constants according to eq 5, which eliminates the differences in k_0 caused by the different attachments of the xanthone labels. Figure 6B shows that an increase in the overall chain dimensions has a 1.7-fold stronger effect on the formation of type III loops compared to type II loops, but there is no evidence for a limiting value for the effect of end extensions on the dynamics of type III loops. However, the reduced dimension, $\sqrt{\langle r^2 \rangle}_{red}$, of the longest investigated type III loop is 0.47 whereas saturation in type II loops was not observed above $\sqrt{\langle r^2 \rangle}_{red} = 0.35$. It is expected that the kinetics for type III loop formation also reach a limiting value in longer chains, when both points of contact formation are located in the stiff central part of the chain (Figure 4B). If the limiting value would be reached at the same $\sqrt{\langle r^2 \rangle}_{red}$-value as in type II loops the maximum effect of tails in type III loops would result in a 3.8-fold decrease in k_c.

Discussion

Contact formation between two amino acid side chains on a polypeptide chain is an elementary reaction in protein folding. To gain insight into the mechanism of loop formation we have previously studied end-to-end diffusion in model polypeptide chains and in fragments from natural proteins. In proteins, however, the majority of contacts involve internal residues. Local motions of a chain segment depend on the motions of its nearest neighbors which was predicted to lead to faster motions at the ends of the chain (see Figure 4).[31] This has been directly observed using NMR spin−lattice relaxation measurements in organic polymers[32−34] and in unfolded proteins.[29,30] Increased chain flexibility at the ends implies that formation of intrachain interactions is slower in the interior of a chain compared to the ends of the chain. Our results show that intrachain loop formation is slowed down by extending the chain beyond the loop region on either one side (type II loops) or on both sides (type III loops). Above a certain chain size the kinetics of type II loop formation become independent of chain dimensions. In this limit a 2.3-fold reduction in k_c is observed. The limit is reached when the overall chain dimensions are about 3 times larger than the dimensions of the loop region, independent of loop size and amino acid sequence. The effect of end extensions is independent of the size and the type of the loops. The longest investigated loops were shown to behave like Gaussian chains,[6,11] whereas the shortest loops are similar in length or even shorter

(31) Perico, A. *Biopolymers* **1989**, *28*, 1527−1540.
(32) Allerhand, A.; Hailstone, R. *J. Chem. Phys.* **1972**, *56*, 3718−3720.
(33) Logan, T. M.; Theriault, Y.; Fesik, S. W. *J. Mol. Biol.* **1994**, *236*, 637−648.
(34) Frank, M. K.; Clore, G. M.; Gronenborn, A. M. *Protein Sci.* **1995**, *4*, 2605−2615.

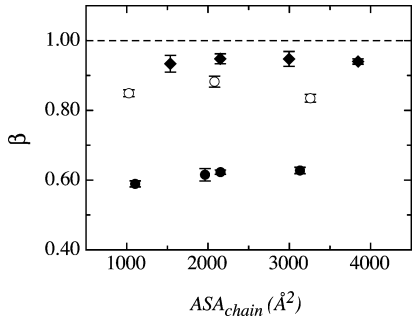

Figure 7. Dependence of viscosity-dependence of the rate constants of loop formation (β) on the ASA_{chain} in type II loops with the loop sequences *Xan*-(Gly-Ser)-*NAla* (●; series 3 and 4 peptides) and *Xan*-Ser-Ser-Ser-*NAla* (○; series 5 and 6 peptides). In addition, the results for the type III loop with the loops sequence *Xan*-(Gly-Ser)$_4$-*NAla* (◆; series 9, 10 peptides) are shown. The β-values are the results of the fits of the original data to eq 7 and reflect the sensitivity of the loop formation reactions toward changes in solvent viscosity.

than the persistence length of the chain. Despite these different chain properties, the same effect of $\sqrt{\langle r^2\rangle_{red}}$ on k_c is observed for all loops (Figure 5B), which shows that only the chain dimensions determine the internal polypeptide chain dynamics. Comparison of type II and type III loops with identical loop regions and with identical overall chain dimensions reveals that extending the chain at both ends has a stronger effect on the kinetics of loop formation than extensions at only one end (Figure 6). The rate constants for type III loop formation also scale with the overall chain dimensions, but the decrease in k_c with increasing $\sqrt{\langle r^2\rangle}$ is about 1.7 times larger for type III loops. This is compatible with an increased flexibility toward the ends of a polypeptide chain,[29,31] which allows faster formation of type II loops, which have one flexible end (Figure 4). These results indicate that local internal chain motions are strongly coupled to motions of other chain segments and imply that the internal flexibility at different positions along a polypeptide chain is the major origin for the differences in contact formation in type I, type II, and type III loops.

If the observed differences in the kinetics of loop formation would contain major contributions from the additional ASA of the tails, a difference in the viscosity-dependence for the different types of loops would be expected. We therefore measured the effect of solvent viscosity, η, on k_c for all peptides. In all cases log(k_c) was linearly dependent on log η and the data could be fitted according to

$$k_c = k_c^0\left(\frac{\eta}{\eta_0}\right)^{-\beta} \qquad (7)$$

where η_0 is the reference solvent viscosity of water at 22.5 °C ($\eta_0 = 0.94$ cP), k_c^0 is the rate constant of end-to-end diffusion at η_0, k_c is the rate constant at a given viscosity η, and the exponent β reflects the sensitivity of the reaction to solvent viscosity. A β-value of 1 indicates that k_c is inversely proportional to solvent viscosity, and a β-value of 0 indicates that k_c is independent of solvent viscosity. For all peptides the β-values are independent of tail length and type of tails (Figure 7). For longer type I loops β-values around 1 are observed[19] and an additional increase due to the addition of the tail is not expected. However, for short loops the β-values are significantly smaller than unity and the increased number of solvent−peptide interactions in type II and type III loops should increase the β-values. Figure 7 shows that the β-values of the different type II and type III loops are independent of tail length and that identical overall ASA results in different β-values for short and long loop regions. This result indicates that the additional peptide−solvent interactions introduced by the tails have only minor contributions to the kinetics of loop formation.

We cannot exclude that the decreased rate constants for loop formation in type II and type III loops contain contributions from steric effects of the additional tails, which decrease the accessibility of the interacting groups. However, the observed difference in the effect of end extensions on the kinetics of formation of different loops (Figure 5A) argues against major contributions from local steric effects. This is supported by the observation that the limiting value for the effect of a type II extension is reached for rather long tails (Figure 3).

Results from theoretical work proposed that the effect of additional tails on the kinetics of loop III formation is a function of chain stiffness and reaches a limiting value when the length of the end extensions is around 0.5 to 2 times the loop length.[12,14] Due to restrictions in chain length given by peptide synthesis we could not investigate whether a limit for the rate constants of formation of type III loops exists. The longest synthesized type III chain consists of 35 amino acids with a calculated $\sqrt{\langle r^2\rangle}$-value of 43.0 Å. This is similar to the size of the smallest known independently folding protein subdomains. We could not attach avidin to both ends of the chain, since this leads to cross-linking of the tetramers and to precipitation.

Our results allow an extrapolation of data obtained from type I loops to kinetics of formation of type III loops in longer chains. The investigated *Xan*-(Gly-Ser)$_4$-*NAla* loop located in the interior of a typical 100 amino acid globular protein would form about 10 times slower compared to end-to-end contact formation in the same type I loop, if the extrapolations hold over the complete range. If a limiting value would be reached at the same reduced loop size, $\sqrt{\langle r^2\rangle_{red}}$, as observed for type II loops, the kinetics would only be slowed down about 4-fold in larger proteins. Type III loop formation was measured in GdmCl-unfolded Zn-cyt c by electron transfer between a $Ru(NH_3)_5^{3+}$ moiety attached to His33 and the Zn-porphyrine-coordinated His-18 residue,[8] which corresponds to an ~15 residue type III loop. Electron transfer occurred with a rate constant of $k_c = 4.0 \times 10^6$ s^{-1} in the presence of 5.4 M GdmCl. Using TTET we measured a rate constant of $(1.9 \pm 0.1) \times 10^7$ s^{-1} for end-to-end contact formation in 18-residue fragments from carp parvalbumin.[7] If this rate constant is rescaled to the type III limit and corrected for the effect of GdmCl on loop formation,[19] a value of 2.0×10^6 s^{-1} is obtained, which is similar to k_c measured in unfolded cytochrome c.

Conclusions

We compared the kinetics of end-to-end contact formation (type I loops) to the formation of end-to-interior (type II loops) and interior-to-interior loops (type III loops) using triplet−triplet energy transfer from xanthone to naphthylalanine. The results show that formation of type II and type III loops compared to type I loops of the same loop size and amino acid sequence is slower until a limiting value is reached. The limiting regime is reached when the overall chain dimensions are about 3 times

larger than the loop dimensions. For these chains loop formation is about 2.5 times slower for type II loops compared to type I loops. Formation of type III loops is about 1.7 times slower than formation of type II loops of the same loop sequence and overall chain dimensions. These results show that local chain motions are strongly coupled to motions of other chain segments and are faster at the chain ends than in the interior of the chain. Our results suggest that differences in the kinetics of formation of type I, II, and II loops are caused by differences in flexibility at the different positions in a polypeptide chain (Figure 4). Interactions of the whole chain with the solvent contribute to the kinetics of loop formation as indicated by their strong viscosity-dependence. However, the increased number of peptide−solvent interactions in type II and type III loops compared to type I loops does not contribute significantly to the observed differences in the kinetics of loop formation for the different types of loops.

Experimental Section

Peptide Synthesis, Modification, and Purification. All peptides were synthesized using standard fluorenylmethoxycarbonyl (Fmoc) chemistry on an Applied Biosystems 433A peptide synthesizer as described before.[6] The naphthalene moiety was included via 1-naphthylalanine (NAla) by peptide synthesis. The xanthone derivative 9-oxoxanthen-2-carboxylic acid was prepared according to Graham and Lewis[35] and introduced on resin by PyBOP mediated coupling in DMF to either the N-terminus or to the free amino group of an α,β-diaminopropionic acid residue. The biotin labeled peptides were prepared with biotinylated Fmoc-lysine (Novabiochem) which was introduced by standard peptide synthesis. All peptides were purified to >95% purity by preparative HPLC on an RP-8 column. The purity of the peptides was checked by analytical HPLC, and the mass was determined by MALDI or ESI mass spectrometry. Avidin (Fluka chemicals) was added to the purified peptide in buffered solution in slight excess.

Triplet−Triplet Energy Transfer Measurements. All measurements were performed on a Laser Flash Photolysis Reaction Analyzer (LKS.60) from Applied Photophysics. A Quantel Nd:YAG Brilliant laser (354.6 nm, 4 ns pulse width, 50 mJ) was used to selectively excite the xanthone moiety. Transient absorbance traces were recorded at 590 nm for the xanthone and at 420 nm for the naphthalene triplet band. All measurements were performed at 22.5 °C. For each experiment at least four traces were recorded, averaged, and fitted to exponential functions. For all peptides loop formation was measured in water and in the presence of different concentrations of glycerol to increase solvent viscosity. Measuring the viscosity-dependence of loop formation allows a more reliable determination of k_c in water when loop formation is fast and allowed the determination of the viscosity-dependence of k_c according to eq. 7. For all peptides $\ln(k_c)$ was linearly dependent on $\ln(\eta)$. Peptide concentrations were 20−100 μM and were determined by UV-absorption at 343 nm using a molar extinction coefficient of 3900 M^{-1} cm^{-1} for xanthone. All solutions were degassed prior to measurements. Viscosities were determined by a falling ball viscosimeter (Haake, Germany).

To test the effect of avidin on the xanthone triplet lifetime a donor-only control was synthesized with NAla replaced by phenylalanine which is not able to quench xanthone triplets.[7] This peptide revealed that binding of avidin does not influence the lifetime of the xanthone triplet state.

Calculation of ASA. Accessible surface areas (ASAs) of the peptides were calculated using the program MOLMOL[36] using a sphere of 1.4 Å diameter to probe the ASA.

Data Analysis. For data evaluation the ProFit and Matlab software packages were used.

Acknowledgment. We thank Annett Bachmann and Andreas Reiner for comments on the manuscript, Florian Krieger for discussion, and Josef Wey for synthesis of 9-oxoxanthen-2-carboxylic acid. This work was funded by a grant from the Schweizerische Nationalfonds and from the Volkswagen Stiftung.

JA0666396

(35) Graham, R.; Lewis, J. R. *J. Chem. Soc., Perkin Trans. I* **1978**, 876−881.
(36) Koradi, R.; Billeter, M.; Wüthrich, K. *J. Mol. Graphics* **1996**, *14*, 51−55.

10072 *J. Phys. Chem. A* **2004,** *108,* 10072−10079

Ultrafast Quenching of the Xanthone Triplet by Energy Transfer: New Insight into the Intersystem Crossing Kinetics

H. Satzger,[†] B. Schmidt,[†] C. Root,[†] W. Zinth,[†] B. Fierz,[‡] F. Krieger,[‡] T. Kiefhaber,[‡] and P. Gilch*,[†]

Department für Physik, Ludwig-Maximilians-Universität, Oettingenstrasse 67, D-80538 München, Germany, and Division of Biophysical Chemistry, Biozentrum, University of Basel, Klingelbergstrasse 50/70, CH-4056 Basel, Switzerland

Received: June 4, 2004; In Final Form: August 11, 2004

The formation and quenching of the triplet state of xanthone are studied by femtosecond techniques. As revealed by femtosecond fluorescence spectroscopy, the primarily excited $^1\pi\pi^*$ state decays within 1.5 ps. In a transient absorption experiment, this time constant is associated with a partial rise of a triplet signature. This rise has a second and slower component with a time constant of 12 ps. In the presence of high concentrations of the quencher 1-methylnaphthalene, the slow 12 ps rise component is absent. This finding gives strong evidence that the biphasic rise of the triplet absorption of xanthone is due to a sequential mechanism, namely, a $^1\pi\pi^* \rightarrow {}^3n\pi^*$ with fast intersystem crossing followed by a $^3n\pi^* \rightarrow {}^3\pi\pi^*$ internal conversion. Furthermore, an analysis of the concentration dependence of the quenching kinetics allows one to pin down the intrinsic transfer time of the triplet energy from xanthone to 1-methylnaphthalene to ~1 ps.

1. Introduction

Many biological polymers have to form specific intramolecular interactions to be able to fulfill their biological function. The rate at which polymers can explore conformational space is limited by intrachain diffusion, that is, by the rate at which two points on a polymer chain can make contact. Experimental methods are therefore needed which allow direct measurement of intrachain diffusion rates. Triplet−triplet energy transfer (TTET) between a triplet donor (D) and a triplet acceptor (A) has recently been applied to measure intrachain contact formation in polypeptide chains to gain information on the dynamics of the earliest steps in the protein folding process.[1−3] In these experiments (see Figure 1), the two positions of interest on the polypeptide chain are labeled with a D/A pair. The donor is photoexcited, which marks the beginning of the detection period. When the donor meets the acceptor, an energy transfer process takes place transferring the triplet state to the acceptor. The transfer is detected by the concomitant absorbance changes. An ideal D/A system for such studies should have the following properties (see Figure 1): (i) The rate constant for formation of the excited donor state should be higher than the rate constant for intrachain diffusion ($k_{ex} \gg k_c$). (ii) The excited donor state should be very long-lived, so that the peptide dynamics can be traced throughout a large time window. (iii) The transfer rate constant between D and A should be higher than the rate constant for breaking of the contact ($k_{TT} \gg k_{-c}$), and (iv) the transfer rate should decay very rapidly with distance. A D/A system that matches these criteria is the couple xanthone (D) and naphthalene (A). Following photoexcitation, xanthone undergoes intersystem crossing (ISC) with a quantum yield close to 1[4] preparing a long-lived triplet state ($\tau = 20$ μs in water[2]). The energy of this state can be transferred to the naphthalene. TTET occurs via a two-electron exchange process (Dexter mechanism); thus the transfer rate decays very rapidly with distance (and the transfer is only efficient for a close contact situation (van der Waals contact)).[5] By incorporation of xanthone and naphthalene moieties in a peptide chain, intramolecular contact time constants on the nanosecond time scale could be determined.[2,3] In these experiments, the donor triplet states were produced by a 4 ns laser flash and dynamics with time constants between 5 ns and several microseconds were observed, depending on the length and the sequence of the polypeptide chains.[2,3] Tests for the presence of faster chain dynamics on the subnanosecond time scale require a characterization of the photodynamics of the xanthone/naphthalene TTET pair in detail. This yields information on the limitations of the method in the early time region set by triplet formation and TTET dynamics.

The first transient absorption experiments on xanthone with picosecond resolution[6,7] yielded time constants for triplet formation in the 10 ps range. Later experiments with higher time resolution[8] revealed a biphasic rise of the triplet absorption $A(t)$; that is, the rise could be described by

$$A(t) = A_1(1 - \exp(-t/\tau_1)) + A_2(1 - \exp(-t/\tau_2)) \quad (1)$$

with time constants $\tau_1 \approx 1$ ps and $\tau_2 \approx 10$ ps and amplitudes A_1 and A_2. This biphasic behavior was attributed to a branched reaction scheme. In the proposed model (Figure 2a), the primarily excited $^1\pi\pi^*$ decays via two channels: internal conversion (IC) to the $^1n\pi^*$ state *and* ISC to the $^3n\pi^*$ state. The time constants of both processes were assumed to be similar. They should lead to the observed value of $\tau_1 \approx 1$ ps. Subsequently the $^1n\pi^*$ state is depleted by a second ISC process to the $^3\pi\pi^*$ state. This model obeys the El-Sayed rules for ISC processes:[9] For an ISC process for which the type of the orbitals occupied is changed (e.g., $n\pi^* \rightarrow \pi\pi^*$) in the course of the spin flip, a high ISC rate is expected. By this simultaneous change of spin and orbital character of the electronic wave

* To whom correspondence should be addressed. Fax: +49-89/2180-9202. E-mail: Peter.Gilch@physik.uni-muenchen.de.
[†] Ludwig-Maximilians-Universität.
[‡] University of Basel.

10.1021/jp047583+ CCC: $27.50
Published on Web 10/16/2004

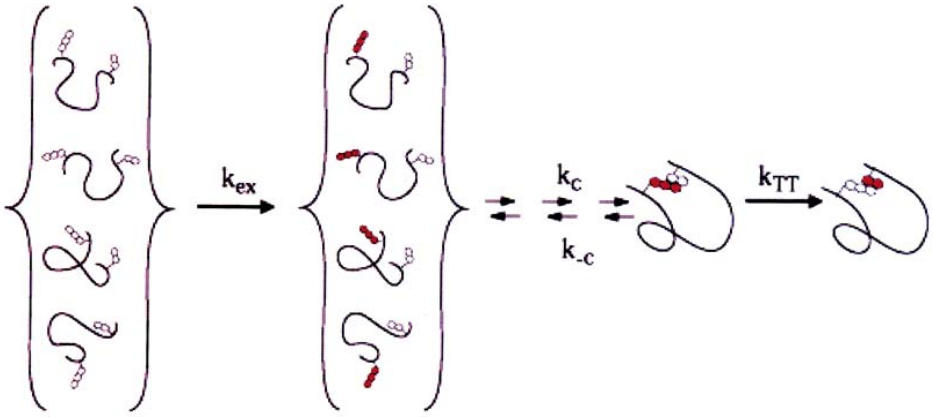

Figure 1. Principle of the experimental determination of contact rates in peptides. Two residues of a peptide chain are marked with an acceptor (A) and a donor (D), respectively. In a thermal ensemble of those marked peptides, the acceptor is photoexcited by a laser pulse. If during their diffusive motion the markers come into close contact, energy will be transferred indicating this contact.

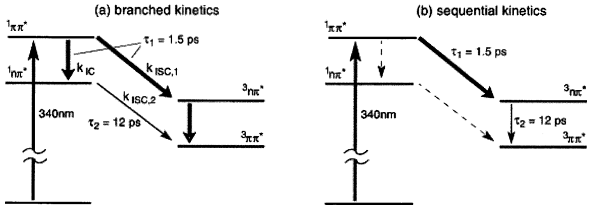

Figure 2. Jablonski diagram depicting the various excited states of xanthone and their potential decay patterns. (a) Branched kinetics. (b) Sequential kinetics. Rate constants for intersystem crossing processes are $k_{ISC,1,2}$, and those for internal conversion are $k_{IC,1,2}$. Only ISC processes allowed by the El-Sayed rules are considered. Thick arrows represent large rate constants.

function, the change of the spin angular momentum in the ISC can be compensated by a corresponding change of the orbital angular momentum. Obviously, the branched kinetic scheme proposed in ref 8 is in agreement with these rules. However, an alternative model with sequential kinetics (Figure 2b), that is, fast ISC from the $^1\pi\pi^*$ to the $^3n\pi^*$ state followed by slower internal conversion in the triplet manifold to the $^3\pi\pi^*$, cannot be ruled out. The authors of ref 8 assumed that only the final product state in the sequential process is spectroscopically visible at the single detection wavelength used in ref 8. Under this assumption, a sequential process would lead to amplitudes A_1 and A_2 with opposite sign. The observation of the same signs of A_1 and A_2 pointed to branched kinetics. However, if the intermediate state contributes to the observed time trace its extinction coefficient has to be taken into consideration and a decision between branched and sequential kinetics with the present information is not possible.

In this paper, we will readdress the ISC of xanthone and we will have a close look at the quenching of the xanthone triplet by naphthalene. We will deal with the problem by combining three experimental approaches. (i) The decay of the fluorescence of xanthone, that is, the depletion of its primarily excited state, is monitored using an ultrafast Kerr shutter. (ii) The formation of the triplet state of xanthone is followed by spectrally resolved transient absorption spectroscopy in a broad spectral range. (iii) Finally, the influence of a quencher, 1-methyl-naphthalene, on the absorption dynamics is investigated. These experiments not only aim at the dynamics of the quenching itself but will yield a deeper insight into the mechanism of the ISC of xanthone, a prerequisite for using this D/A pair as a sensor for the investigation of peptide closure dynamics in the picosecond realm.

2. Experimental Section

The setup for femtosecond fluorescence experiments has been described before in detail in ref 10. Briefly, a Clark CPA 2001 laser/amplifier system (repetition rate of 1 kHz) pumped a two-stage noncollinear optical parametric amplifier (NOPA) tuned to 540 nm. The compressed output of the NOPA was frequency doubled in a 100 μm type I BBO crystal. The resulting 270 nm pulses with an energy of 0.2 μJ are used to excite the xanthone sample. The fluorescence light emitted by the sample is imaged onto a Kerr gate consisting of two wire grid polarizers and a fused silica plate. The Kerr gate is operated by femtosecond NIR (1100 nm) laser pulses obtained from a two-stage optical parametric amplifier (OPA) again pumped by the laser/amplifier system. The fluorescence light that passed the Kerr gate was dispersed by a spectrometer and detected by a liquid nitrogen cooled CCD camera. Parasitic stray light was suppressed by a UG 5 filter (to reject the NOPA fundamental at 540 nm) and KG 5 (to reject the ~1100 nm gate light). The time resolution of the setup in the near UV was ~200 fs (full width at half-maximum (fwhm)). The xanthone fluorescence emission lies in the blue wing of the detection window of the Kerr setup where its spectral sensitivity starts to drop drastically. This circumstance requires prolonged acquisition times which cause an instrumental artifact. The irradiation of the Kerr medium by the gate pulses induces a very weak background gradually rising with time. The rising background signal feigns a long-lived emission of xanthone. Experimental runs with the excitation light blocked, that is, in the absence of the xanthone emission, allow that contribution to be estimated and the intrinsic behavior of xanthone to be extracted.

Femtosecond absorption spectra were recorded with the setup detailed in ref 11. As in the fluorescence experiments, the sample was excited by the frequency doubled output of a NOPA pumped by a conventional 1 kHz Ti:Sa laser/amplifier system. Two wavelengths were used for the excitation process: 266 and 340 nm. The excitation energy was equal to ~400 nJ at the sample location for both wavelengths. Absorption changes induced by these pump pulses were probed by a white light continuum generated by focusing a portion of the amplifier fundamental into a CaF_2 plate. The white light was split into a probe and reference branch. Both probe and reference continua were spectrally dispersed and recorded in single shot fashion

10074 *J. Phys. Chem. A, Vol. 108, No. 46, 2004* Satzger et al.

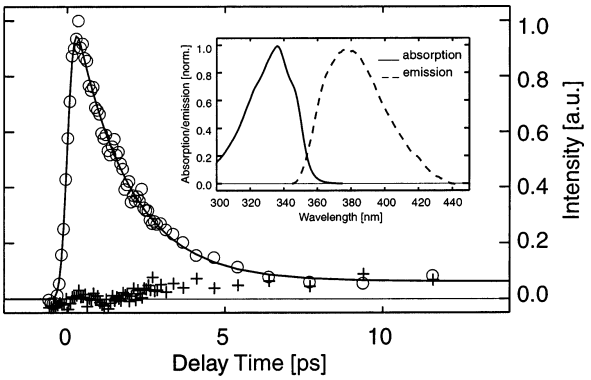

Figure 3. Decay of the fluorescence emission of xanthone at 414 nm (○) following 270 nm excitation recorded with a Kerr setup. The contribution of a slowly rising background emission is included (+). In this blank experiment, all parameters were identical to the experiment on the xanthone except for the blocked excitation light. The insert shows the absorption and fluorescence spectra of xanthone in ethanol.

by diode arrays.[12] The probe continuum overlaps in the sample with the pump light, and the reference continuum passes through a part of the sample not excited by the pump light. The pump−probe spectra were recorded with a magic angle setting.

For the femtosecond experiments, xanthone (Fluka) was dissolved in absolute ethanol (Merck, VLSI Selectipur). The concentrations of the sample solutions were in the range of 2−5 mM. The concentrations of 1-methylnaphthalene (Fluka) were adjusted by adding the respective volumes to the solutions. Xanthonic acid was synthesized and purified as decribed in ref 2. The concentrations of the acid in water and ethanol were about 0.5 mM. The solutions were exchanged between the laser shots by pumping them through fused silica flow cells (optical path length of 0.5 mm in the absorption experiment and 1 mm in the fluorescence experiment).

Transient absorption data in the nano- to microsecond realm were collected using a laser flash photolysis reaction analyzer (LKS.60) from Applied Photophysics. Xanthone was excited selectively by using a Quantel Nd:YAG laser (354.6 nm, 4 ns pulse of 50 mJ). For the pseudo-first-order quenching experiments, xanthone (Fluka, purum) was dissolved in ethanol (Merck, Uvasol) to a concentration of 0.05 mM measured by UV spectroscopy ($\epsilon_{335} = 6700\ M^{-1}\ cm^{-1}$). 1-Methylnaphthalene (Fluka, purum; $\epsilon_{280} = 6000\ M^{-1}\ cm^{-1}$) was added to concentrations ranging from 1 to 10 mM. The temperature was 295.6 K. The kinetics was typically measured five times, averaged, and analyzed using ProFit (Quansoft, Zürich, Switzerland). All rate constants were obtained by fitting the decay of the xanthone triplet at 610 nm.

Steady-state absorption and fluorescence spectra were recorded with a diode array spectrometer (Specord S100) and a Fluorolog 1680 0.22 m double spectrometer from Specs, respectively.

3. Results

3.1. Fluorescence Decay of Xanthone. When excited with UV light, xanthone emits a very weak fluorescence peaking around 380 nm (see the insert in Figure 3). A rough estimate for the lifetime of the excited $^1\pi\pi^*$ state may be obtained from the fluorescence quantum yield and the application of the Strickler−Berg relation[13] yielding a lifetime of the $^1\pi\pi^*$ state of the order of $\tau_1 = 1$ ps. Direct experimental access to τ_1 is obtained by measuring the time dependence of the emission decay with the help of a Kerr shutter setup. A typical time trace

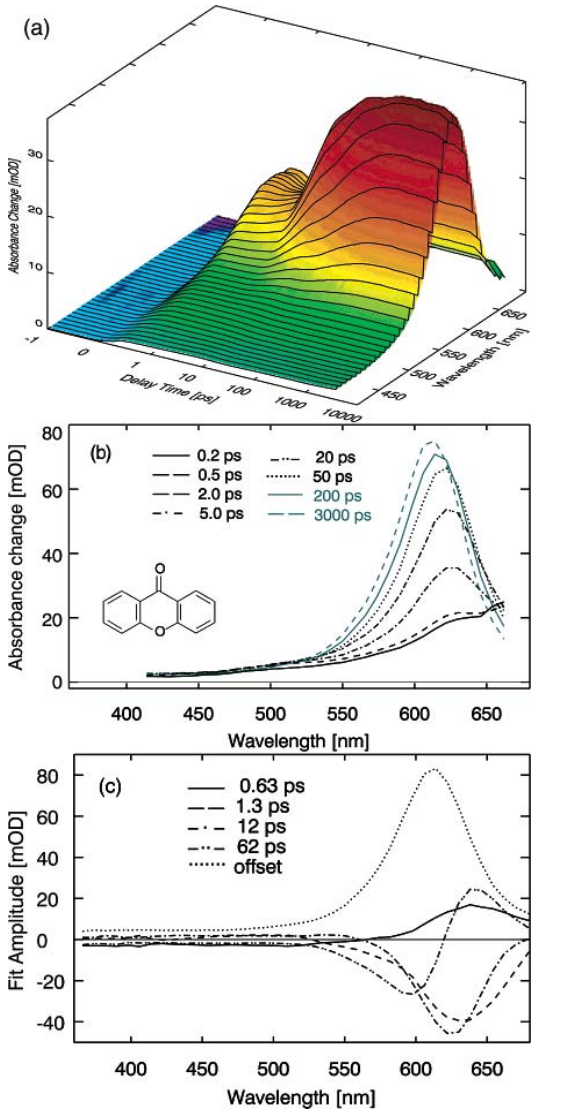

Figure 4. Transient absorption spectra of xanthone following 340 nm excitation. (a) Overview. (b) Transient spectra at distinct delay times. (c) Decay associated spectra.

is depicted in Figure 3. After an instrumentally limited rise, the fluorescence emission decays within ∼1 ps. The weak background observed stems from emission of the Kerr medium induced by the gate pulses. This weak emission gradually rises with time and is responsible for the small offset (see the time trace recorded with the excitation light blocked in Figure 3). Thus, only the initial emission decay originates from the xanthone sample. An exponential fit considering the experimental response function yields a time constant of ∼1.5 ps. Since the emission monitors the population of the excited $^1\pi\pi^*$ state, we can conclude that this state decays with $\tau_1 \sim 1.5$ ps. As this value is in line with the prediction based on fluorescence quantum yield, a contribution of a long-lived component, for which the Kerr setup is not very sensitive, can be ruled out.

3.2. Transient Absorption Spectroscopy. Absorption changes of xanthone with the femtosecond excitation tuned to the maximum of its $\pi\pi^*$ transition (340 nm) were recorded in a spectral region ranging from 370 to 700 nm (Figure 4a gives an overview of the data, and transient spectra at selected delay

times are depicted in Figure 4b). Immediately after photoexcitation, a weak and broad transient absorption peaking around 700 nm is formed (excited-state absorption from the $^1\pi\pi^*$ state). The decay of this signature within ~1 ps gives way to a stronger and sharper feature centered around 620 nm. The 620 nm band continues to rise during ~15 ps. On the time scale of our experiments (up to 3.5 ns), this feature remains constant in amplitude, though the center of the spectrum slightly shifts to the blue on the 50 ps time scale. To obtain quantitative information on the kinetics, the data were subject to a global fitting procedure. As a model function, a sum of exponentials (decaying absorption corresponds to positive amplitudes) convoluted with an instrumental response (Gaussian with a width of 200 fs fwhm) was used. A satisfactory agreement between data and fit was obtained using four exponentials and an offset to account for the triplet absorption persistent in the time range (up to ~3 ns) of the femtosecond experiment. The time constants derived are ~0.5, 1.3, 12, and 62 ps, and the corresponding decay associated spectra are depicted in Figure 4c. The spectra associated with the time constants of 1.3 and 12 ps both have negative sign (indicative for the buildup of an absorption) throughout most of the spectral region covered and are similar though not identical in shape. The 62 ps spectrum is sigmoidal, representing a blue shift of the ~620 nm band with time. The spectrum of the offset peaks at 610 nm and has a width of 50 nm (fwhm). From comparison of this spectrum with the spectrum obtained by nanosecond spectroscopy,[14] it can be safely assigned to the absorption of the relaxed triplet state of xanthone in ethanol. Transient absorption experiments have also been performed with the excitation tuned to 266 nm. The observed transient spectra and derived time constants are virtually identical to those in the experiments presented above (excitation wavelength of 340 nm). Thus, the different excitation wavelengths in the fluorescence and the absorption experiments do not seem to alter the photodynamics and the two may be directly compared. Very similar results were also obtained for xanthonic acid in ethanol (data not shown). Xanthonic acid in water shows similar kinetics in the time domain $\tau < 200$ ps. However, the blue shift of the triplet absorption band occurs here with a 300 ps time constant (data not shown).

3.3. Triplet Quenching by 1-Methyl-naphthalene (1-MN). Naphthalene and derivatives are known to quench the triplet states of aromatic ketones such as benzophenone and xanthone at least partially via intermolecular energy transfer.[15,16] The question of whether electron transfer can compete with energy transfer will be addressed below. In the following, the dependence of the photokinetics of xanthone on the concentration of the naphthalene derivative 1-MN is investigated. These experiments not only allow us to draw conclusions on the quenching dynamics but also help to elucidate the ISC mechanism of xanthone. Addition of 1-MN to a solution of xanthone reduces the lifetime of the triplet spectrum centered around 610 nm (see Figure 5). For low quencher concentrations of ≤0.01 M, the lifetime reduction can be traced by nanosecond laser flash photolysis. Here, the rate constant k_{TT} of the decay of the xanthone triplet absorption scales linearly with the quencher concentrations (Figure 7). Higher quencher concentrations require femtosecond techniques to time resolve the energy transfer dynamics. This is illustrated by a measurement performed on xanthone in the presence of 0.6 M (10 vol %) 1-MN (Figure 5). The 610 nm absorption with an "infinite" lifetime in pure ethanol now decays in ~100 ps. Synchronized with this decay, a spectrum centered around 420 nm rises. This spectrum can be safely assigned to the triplet state of 1-MN;[17,18] that is,

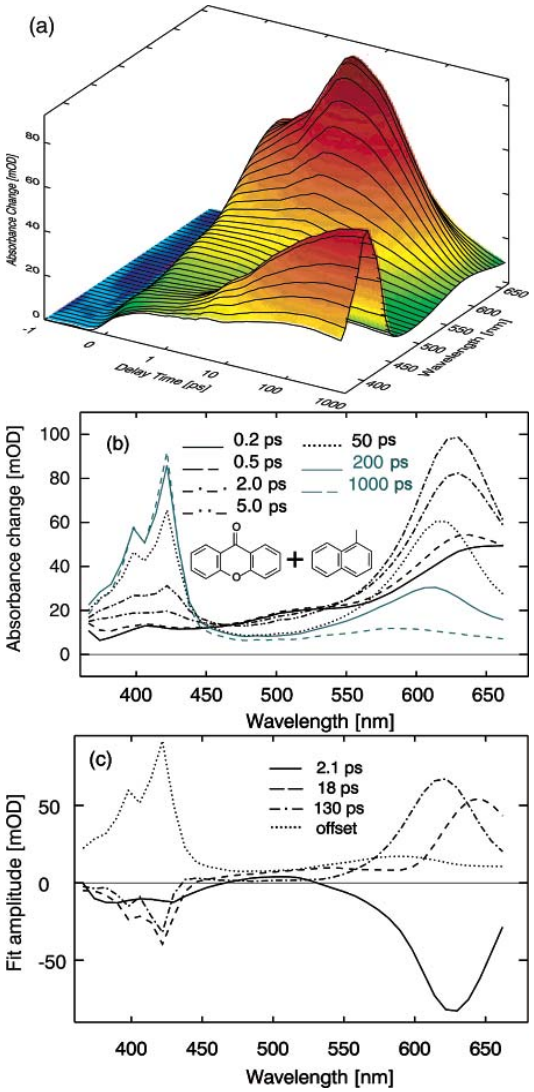

Figure 5. Transient absorption spectra of xanthone in the presence of 0.6 M 1-MN following 340 nm excitation. (a) Overview. (b) Transient spectra at distinct delay times. (c) Decay associated spectra.

as expected for an energy transfer process the decay of the xanthone triplet goes along with the population of the 1-MN triplet.

The temporal behavior of this transfer for various quencher concentrations can be nicely represented by two spectral integrals (Figure 6). The first integral (550−650 nm) covers the triplet absorption of xanthone (lower part of Figure 6), and the second integral (414−438 nm) that of the 1-MN. In the absence of a quencher, the biphasic rise of the xanthone triplet absorption is clearly represented by the "610 nm" integral. The "420 nm" integral is virtually "silent". In the presence of 0.06 M 1-MN, the kinetics of the rise is not altered but now the 610 nm integral decays with a time constant of ~1.5 ns. In parallel, the 420 nm integral rises with the same time constant. Increasing the 1-MN concentration by a factor of 10 has the expected effect of accelerating the decay of the 610 nm integral and the rise of the 410 nm integral by roughly the same factor. A closer inspection of that rise shows that it is multiphasic and its description with exponentials requires at least three terms with

10076 *J. Phys. Chem. A, Vol. 108, No. 46, 2004* Satzger et al.

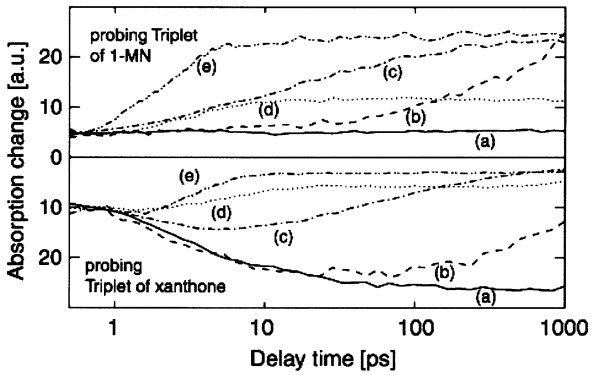

Figure 6. Time dependences of the spectral integrals covering the absorption of the 1-MN triplet (upper part) and that of the xanthone triplet absorption (lower part) for different 1-MN concentrations. For a better representation, the time traces in the lower part have been turned upside down. The 1-MN concentrations were (a) 0 M, (b) 0.06 M, (c) 0.6 M, (d) 3.0 M, and (e) neat 1-MN.

time constants of 2, 15, and 120 ps. The amplitudes of these terms are comparable. Note that the 2 ps time constant is shorter than the slow component observed for the rise of the xanthone triplet in the absence of a quencher. For the highest quencher concentration, that is, when performing the experiment in neat 1-MN, one obtains very fast and very simple quenching kinetics. The 420 nm integral rises in 2 ps, and the integral representing the xanthone triplet absorption decays in 2 ps to a small offset. Inspection of the spectrally resolved data (not shown) clearly demonstrates that this offset stems from a tail of the 1-MN triplet absorption and not from a residual xanthone triplet population.

Surprisingly, for a concentration of 3.0 M kinetics is found that deviates from the overall trend. In addition to the ultrafast kinetics which is comparable to the behavior in neat 1-MN, a longer lived component with a time constant of 1 ns appears that is absent even in the 0.6 M experiment. A possible origin for this anomaly will be addressed in the discussion.

4. Discussion

4.1. Intersystem Crossing in Xanthone. *Ultrafast Spectroscopy of Xanthone.* The time-resolved fluorescence data presented here allow us to exactly pin down the decay time of the primarily excited $^1\pi\pi^*$ state of xanthone. In previous time-resolved absorption experiments,[8] this time could only be inferred indirectly from the rise of the triplet spectrum. Among the four excited states ($^1\pi\pi^*$, $^3\pi\pi^*$, $^1n\pi^*$, and $^3n\pi^*$) within energetic reach of the photoexcitation, only the $^1\pi\pi^*$ state shares an appreciable transition moment with the ground state. Transitions from the singlet ground state to the two triplet state are spin forbidden, and the transition to the $^1n\pi^*$ state is forbidden by symmetry. The extinction coefficient for that transition is 6 M^{-1} cm^{-1} as compared to 12 000 M^{-1} cm^{-1} for the allowed transition to the $^1\pi\pi^*$ state.[19] Thus, the only emissive state is the $^1\pi\pi^*$ state and the decay of the fluorescence with a time constant of $\tau \sim 1.5$ ps[32] can be safely assigned to the depletion of this state. If the 1.5 ps time constant characterizes the depletion of the $^1\pi\pi^*$ state, the additional 0.5 ps component present in the transient absorption experiment has to be associated with relaxation processes within the $^1\pi\pi^*$ state and not with its decay.

From the three states that might be populated in the course of the $^1\pi\pi^*$ decay, the $^3\pi\pi^*$ state can be excluded since such a transition would violate El-Sayed's rules. Thus, only the $^1\pi\pi^* \rightarrow {}^1n\pi^*$ IC process (rate constant $k_{IC,1}$) and the $^1\pi\pi^* \rightarrow {}^3n\pi^*$ ISC process (rate constant $k_{ISC,1}$) have to be taken into consideration. The sum of the rate constants $k_{IC,1} + k_{ISC,1}$ is equal to the observed rate constant for the decay of the emissive state ($k_{IC,1} + k_{ISC,1} = 1/\tau_1 = (1.5\ \text{ps})^{-1}$). Partioning that decay into the two channels requires additional information on the involved states. The global analysis of the transient absorption spectra associates the rise of a strong absorption band around 610 nm with the $\tau_1 = 1.5$ ps kinetic component. The shape and position of that spectrum are very close to those of the triplet spectrum of xanthone reported in the literature.[4] Thus, it seems likely that the 1.5 ps process populates at least partially a triplet state. On the other hand, the singlet $^1n\pi^*$ state could have a very similar spectral signature to the $^3n\pi^*$ state and therefore a contribution or even a domination of the $^1\pi\pi^* \rightarrow {}^1n\pi^*$ IC process cannot be excluded on the basis of these results.

The next process (time constant of 12 ps) in the biphasic rise of the triplet absorption is characterized by a spectrum which is slightly blue shifted and has a somewhat smaller width than the 1.5 ps spectrum. This spectrum represents the changes associated with the population of the finally reached triplet state. The sigmoidal feature with a characteristic time of 62 ps observed thereafter describes a blue shift of the triplet absorption. A similar effect has been found for the thio-analogue of xanthone (thioxanthone).[20] By examination of this shift for thioxanthone in several solvents, it was demonstrated that the characteristic times of this shift correlate with the dielectric responses of the solvents.[20] For ethanol, a value of 72 ps was derived which nicely matches the value reported here. Thus, the 62 ps time constant is not associated with a buildup of the triplet absorption and the 12 ps kinetic component thus describes the slowest part of this rise. Special care has to be taken for the assignment of this ~12 ps kinetic component. The assignment of the observed absorption changes depends on the reaction model. They may result either from an increase of the population in the triplet manifold, that is, from the $^1n\pi^* \rightarrow {}^3\pi\pi^*$ transition (branched kinetics, Figure 2a), or from a $^3n\pi^* \rightarrow {}^3\pi\pi^*$ transition (sequential kinetics, Figure 2b). In the latter case, the absorption spectra of the two triplet states have to be similar in shape but the extinction coefficient of the $^3\pi\pi$ state has to be approximately twice that of the $^3n\pi^*$ state. Since no independent access to these extinction coefficients is available, a final decision between branched and sequential kinetics on the spectroscopic results alone is still not possible. Here, the quenching experiments come into play.

Quenching Kinetics: Dynamic and Static Limit. For bimolecular quenching experiments, two limiting cases are known: the dynamic and static regimes. For low concentrations of the quencher (dynamic regime), the kinetics is pseudo-first-order (even the lowest quencher concentration applied in this paper is much higher than the xanthone concentration) with the rate constant k_{TT} given[5] by

$$k_{TT} = k_q[\text{1-MN}] \qquad (2)$$

The plot of the quenching rate constant versus the 1-MN concentration (Figure 7) confirms this simple law for concentrations lower than 0.06 M. Note that this plot includes results obtained by nanosecond and femtosecond experiments. The bimolecular rate constant k_q obtained by a linear fit of the data in Figure 7 is 7.2×10^9 M^{-1} s^{-1} and is close to the value of 5.4×10^9 M^{-1} s^{-1} predicted by a simple Smoluchowski−Stokes−Einstein treatment.[21] This indicates that in this concentration regime the quenching is controlled by diffusion.

Simple single-exponential kinetics is also observed in neat 1-MN; here the formation of the 1-MN triplet can be described with one time constant of $\tau \sim 1.8$ ps (see the behavior of the

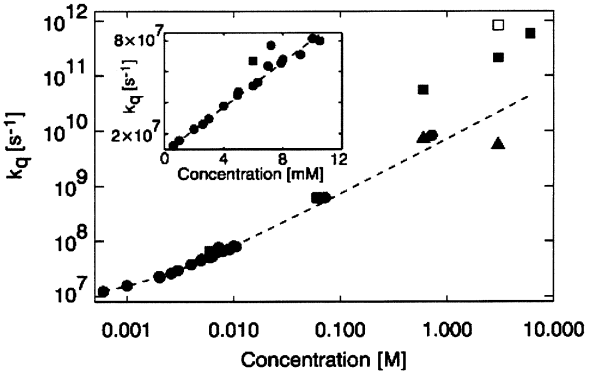

Figure 7. Dynamic quenching rate constant in dependence on the 1-MN concentration. The large (log−log) plot includes nanosecond (●) and femtosecond data (▲ for the slowest component, ■ and □ for the faster components). The insert focuses on the nanosecond experiments.

rise of the 1-MN triplet absorption in the upper part of Figure 6, curve e). In this static limit, the xanthone molecule is surrounded by quenchers at the instant of photoexcitation and no diffusional motion is required to induce the quenching process. The triplet quenching in this limit is faster than the slower component (12 ps) in the formation of the triplet absorption of xanthone in neat ethanol.

Quenching Kinetics: Intermediate Concentration Range and the 3.0 M Anomaly. Of course there is a smooth transition between the dynamic and the static regimes. A concentration of 0.6 M 1-MN nicely marks this interim domain where both regimes leave their kinetic imprint. The slow component of 120 ps obeys the prediction of eq 2, but faster components of 15 ps and even 2 ps for the rise of the 1-MN triplet absorption represent a static contribution to the quenching. Such complex kinetics is frequently observed for bimolecular photoprocesses provided that one of the reaction partners is present in high concentrations. Often these studies addressed the quenching of excited singlet states (for a review which includes theoretical description see ref 22), but an identical behavior should prevail in triplet quenching.

The 3.0 M experiment deviates from the smooth trend from a dynamic to a static behavior. On short time scales, the 2 ps component dominates the quenching kinetics. Thus, static quenching is the exclusive mechanism in that time domain. Quite surprisingly, in addition to this picosecond process the decay kinetics of the xanthone triplet contains a component with a time constant of ∼3 ns. This time is longer than the 120 ps observed for the dynamic quenching in the 0.6 M experiment. At present, a final explanation of this anomaly cannot be given. It might have its origin in the mixing thermodynamics of 1-MN and ethanol in combination with preferential solvation. Aromatic hydrocarbons (like 1-MN) and alcohols are known to have positive mixing enthalpies ΔH_m,[23] and this endothermicity usually peaks for a molar fraction of 0.5 of one of the constituents.[24] A concentration of 3.0 M 1-MN in ethanol corresponds to a molar fraction of 0.3. Typical peak values for ΔH_m are 1 kJ/mol,[24] which is close to the term of the entropy gain $T\Delta S_m$ which equals ∼1.6 kJ/mol[25] for ideal solutions. Therefore, the free energy change of mixing ΔG_m will be close to zero and these solutions are at the edge of separation. It is to be expected that such a solution microscopically consists of clusters where 1-MN is enriched and others where ethanol is enriched. The xanthone molecules could then be partitioned between these clusters. The rather polar xanthone molecule might dominately be solvated by ethanol. Examples for such a preferential solvation are abundant in the literature (see e.g. ref 26 and references therein). With these findings, one could derive a model for the 3.0 M anomaly. A fraction of the xanthone molecules are situated in ethanol clusters. Their triplet states are quenched slowly as the 1-MN molecules have to diffuse into these clusters. The other fraction is surrounded by 1-MN molecules, and rapid static quenching is possible. This is of course only a hypothesis, and its validation requires further experiments. For the purpose of this paper, it can be set aside since on the time scale of interest here (piocoseconds) the 3.0 M experiment is in line with those at other concentrations, particularly with that in neat 1-MN.

Quenching Mechanism: Energy Transfer versus Electron Transfer. In neat 1-MN, the formation of a 1-MN triplet with a time constant of 1.8 ps is faster than the slower component of the rise of the triplet absorption of xanthone in ethanol (12 ps). An interpretation of this surprising finding requires a discussion of the quenching mechanism. Two processes may contribute to the ultrafast quenching: triplet energy transfer and electron transfer generating a radical pair consisting of a 1-MN cation and a xanthone anion. Based on photocurrent measurements, Högemann and Vauthey excluded an electron-transfer quenching of triplet xanthone by 1-MN.[16] For naphthalenes with a less positive oxidation potential, an electron transfer is found to occur. This behavior is explained by the energetics of the process. While the gain of free energy ΔG is essentially zero for the electron transfer between triplet xanthone and 1-MN, it is negative for naphthalenes with a less positive oxidation potential, and electron transfer is feasible. However, for an electron transfer starting from an excited singlet state of xanthone the free energy released during electron transfer is higher than for the triplet electron transfer. The energy of a radical pair is virtually independent of its spin state,[27] and the energy of the initial states is larger by the singlet triplet splitting of xanthone (∼0.3 eV[19]). Therefore, starting from singlet excited xanthone electron transfer is exergonic by ∼0.3 eV and fast electron transfer cannot be excluded. In the experiments presented in ref 16, due to the low (0.1 M) quencher concentrations such a singlet electron transfer could not occur since the intersystem crossing is finished before donor and acceptor meet. For the experiments in neat 1-MN presented here, one could imagine that electron transfer offers an additional decay channel for the excited singlet state.

Several observations allow quenching by electron transfer to be excluded. First, within the accuracy of transient absorption experiments the absorbance of triplet 1-MN after termination of the quenching is identical for different 1-MN concentrations. In other words, the yield of triplet 1-MN shows no dependence on the quencher concentration. Since electron transfer would constitute a competing quenching mechanism, one would expect a reduction of the triplet yield for high quencher concentrations. Second, in the experiments on xanthone in neat 1-MN no spectral signature of the xanthone anion nor of the 1-MN cation is detected. The respective signatures should be observed in a spectral range of 550−720 nm.[16] After the ultrafast decay of the xanthone triplet spectrum within 1 ps, no longer lived signatures can be seen in this region. Thus the radical pair, if formed, has to be generated and has to recombine within less than 1 ps. Considering the highly different free energies which are released in both processes (−0.3 eV for the formation of the singlet radical pair and −3.18 eV[16] for its recombination), simple calculations based on the Marcus theory exclude ultrafast kinetics for both processes. Therefore, for the following it seems justified to take only energy transfer mechanisms into account.

10078 *J. Phys. Chem. A, Vol. 108, No. 46, 2004* Satzger et al.

Quenching Mechanism: Branched versus Sequential Kinetics. The absence of the 12 ps time constant in neat 1-MN can only be understood if all xanthone molecules undergo ISC with a time constant of 1.5 ps. Thus, the data are not compatible with a branched mechanism as described by Figure 2a. In that mechanism, the slow component would originate from the ISC between the $^1n\pi^*$ and the $^3\pi\pi^*$ state. A quenching of the $^1n\pi^*$ state by singlet−singlet energy transfer between excited xanthone and 1-MN is not feasible since the excited singlet state of 1-MN lies energetically well above that of xanthone.[21] A singlet triplet energy transfer though energetically possible is spin-forbidden and will not occur between different molecules with such a short time constant. Therefore, the slow component of the triplet formation cannot be assigned to the depletion of the $^1n\pi^*$ and the branched mechanism must be excluded. In the sequential mechanism, the only deactivation channel of the primarily excited $^1\pi\pi^*$ state is the fast ISC process to the $^3n\pi^*$ state. That state then decays via slower (12 ps) IC to the $^3\pi\pi^*$ state. Already after the first transition the complete population resides in a state of triplet multiplicity. This state *can* be quenched via triplet−triplet energy transfer, and the disappearance of the longer lived component of the xanthone triplet rise in the quenching experiments is naturally explained.

What seems in conflict with this mechanism is the finding reported in ref 8 by Cavaleri et al. that a biphasic rise of the triplet absorption is found irrespective of the solvent polarity. With changing polarity, the energy gap between the $^3n\pi^*$ state and the $^3\pi\pi^*$ state is known to vary.[19] Cavaleri et al. assume, in line with ref 19, that even an inversion occurs; that is, in polar solvents the $^3\pi\pi^*$ state is lowest in energy whereas it is the $^3n\pi^*$ state in nonpolar surroundings. Since El-Sayed's rules require that an ISC process starting in the $^1\pi\pi^*$ state will end up in a $^3n\pi^*$ state, in a nonpolar solvent the *lowest* triplet state would be directly populated. In our model which claims that the $^1\pi\pi^* \rightarrow {}^1n\pi^*$ IC is slow, this would imply a single-exponential ISC behavior in nonpolar solvents, in contradiction to the findings of Cavaleri et al. However, the inversion of the triplet states has been questioned by Connors et al.[28,29] They performed temperature-dependent phosphorescence experiments indicating that the energy gap between the triplet states is very small in nonpolar solvents but that the $^3\pi\pi^*$ state remains the state of lowest energy. The energy gap is smaller than kT at room temperature, and the $^3\pi\pi^*$ state can "behave" like a $^3n\pi^*$ state via thermal activation. Thus, the energetic ordering $^1\pi\pi^*$, $^3n\pi^*$, and $^3\pi\pi^*$ on which our sequential model depends seems to hold irrespective of the solvent polarity.

In the sequential mechanism proposed here, the ISC process from the $^1\pi\pi^*$ state to the $^3n\pi^*$ state is faster than the following IC process within the triplet manifold. This might be somewhat surprising. Yet, for El-Sayed allowed ISC processes the electronic couplings mediating the ISC transitions can be of the same order of magnitude as those of IC processes. For xanthone, this is supported by recent high-resolution spectra.[30] Still, one might argue that the IC process should be faster because of the energy gap law.[5] The energy gap between the triplet states is smaller than the pertinent separation of the $^1\pi\pi^*$ state and the triplet states. As the energetic separations are rather small, a few 1000 cm^{-1} for the ISC and a few 100 cm^{-1} for the IC process, a breakdown of the energy gap law is at least not unlikely, since the energies released in the transitions approach the value of typical vibrational quanta. A thorough analysis would require a quantum chemical treatment not only of the Franck−Condon factors (replacing the energy gap term) but also of the respective coupling elements. Here, we just stress that our experimental kinetic data point to an ISC process that is faster than IC.

4.2. Ultrafast Quenching Dynamics. The experiments on the triplet quenching at different 1-MN concentrations can also be used to obtain information on the quenching process itself. At low 1-MN concentrations, see Figures 5 and 6, exponential kinetics with a linear concentration dependence of the quenching rates is obtained. This is expected from the Smoluchowski−Stokes−Einstein treatment (see eq 2). At higher quencher concentrations, deviations from the single-exponential behavior result. At the highest concentrations, a single-exponential rise of the 1-MN triplet absorption is found with the time constant of the xanthone triplet formation (see above). This single exponentiality and the low transient concentration of the precursor state (see lower part Figure 6, curve e), the xanthone triplet, indicate that the transition rate $k^{3}{}_{X\rightarrow{}^3(1\text{-MN})} = 1/\tau^{3}{}_{X\rightarrow{}^3(1\text{-MN})}$ from the triplet of xanthone to 1-MN is considerably faster ($\tau < 1$ ps) than the formation time (1.5 ps) of the xanthone triplet itself. From the experiments with neat 1-MN as a solvent, we cannot decide whether the fast quenching rate is due to single, well-placed quenching molecules or due to the large number of 1-MN molecules in contact with the triplet donor.

A distinction between the two scenarios should be possible based on the quenching experiments at lower 1-MN concentrations. Lowering this concentration decreases the average number of acceptor molecules surrounding the xanthone donor. If the rate constant of the static quenching were dependent on that number, one would expect a decrease of the rate constant of the fastest component. Let us consider the experiments with a 1-MN concentration of 0.6 M. The rise of the 1-MN triplet absorption, which is directly related to the energy transfer, can be described by three time constants: 2 ps (relative contribution of 30%), 15 ps (40%), and 120 ps (30%). The process associated with the longest time constant obeys eq 2 and is therefore assigned to dynamic quenching. The 15 ps component is assigned to the transition regime between static and dynamic quenching. The 2 ps contribution finally is due to purely static quenching. This time constant is identical to the one observed for neat 1-MN, that is, with a quencher concentration 10 times higher. In other words, only the amplitude of the static quenching but not its rate constant decreases with concentration. Thus, the rate constant for the static quenching does not scale with the number of acceptors in close contact. It seems to be sufficient to have a single 1-MN in contact with triplet excited xanthone for energy transfer within ≤ 1 ps to occur. Such a behavior is not covered by the usual treatments of bimolecular quenching such as the Collins−Kimball approach[31] and the more sophisticated models mentioned in ref 22.

5. Conclusion

The investigation of transient emission and absorption in a wide range of wavelengths on xanthone and xanthone/1-methylnaphthalene solutions yielded important new information on the ISC in xanthone and on triplet quenching. It was shown that triplet formation after optical excitation of xanthone is an ultrafast process. The reaction is sequential, proceeding from the $^1\pi\pi^*$ to the $^3n\pi^*$ state within 1.5 ps and followed by a slower (12 ps) internal conversion in the triplet manifold to the $^3\pi\pi^*$ state. 1-Methyl-naphthalene acts as an efficient and ultrafast quencher for the xanthone triplet state. Quenching occurs on the 1 ps time scale. The experiments show that the system xanthone/1-methyl-naphthalene can be used for the study of very fast structural dynamics of peptides even on the picosecond time scale.

Acknowledgment. Dedicated to Professor Ulrich E. Steiner on the occasion of his 60th birthday.

References and Notes

(1) Bieri, O.; Wirz, J.; Hellrung, B.; Schutkowski, M.; Drewello M.; Kiefhaber, T. *Proc. Natl. Acad. Sci. U.S.A.* **1999**, *96*, 9597.
(2) Krieger, F.; Fierz, B.; Bieri, O.; Drewello, M.; Kiefhaber, T. *J. Mol. Biol.* **2003**, *332*, 265.
(3) Krieger, F.; Fierz, B.; Axthelm, F.; Joder, K.; Meyer, D.; Kiefhaber, T. *Chem. Phys.*, in press.
(4) Scaiano, J. C. *J. Am. Chem. Soc.* **1980**, *102*, 7747.
(5) *Modern Molecular Photochemistry*; Turro, N., Ed.; Benjamin/Cummings: Menlo Park, CA, 1978.
(6) Damschen, D. E.; Merritt, C. D.; Perry, D. L.; Scott, G. W.; Talley, L. D. *J. Phys. Chem.* **1978**, *82*, 2268.
(7) Greene, B. I.; Hochstrasser, R. M.; Weisman, R. B. *J. Chem. Phys.* **1979**, *70*, 1247.
(8) Cavaleri, J.; Prater, K.; Bowman, R. *Chem. Phys. Lett.* **1996**, *259*, 495.
(9) El-Sayed, M. *J. Chem. Phys.* **1963**, *38*, 2834.
(10) Schmidt, B.; Laimgruber, S.; Zinth, W.; Gilch, P. *Appl. Phys. B* **2003**, *76*, 809.
(11) Satzger, H.; Spörlein, S.; Root, C.; Wachtveitl, J.; Zinth, W.; Gilch, P. *Chem. Phys. Lett.* **2003**, *372*, 216.
(12) Seel, M.; Wildermuth, E.; Zinth, W. *Meas. Sci. Technol.* **1997**, *8*, 449.
(13) Strickler, S.; Berg, R. *J. Chem. Phys.* **1962**, *37*, 814.
(14) Ley, C.; Morlet-Savary, F.; Fouassier, J. P.; Jacques, P. *J. Photochem. Photobiol., A* **2000**, *137*, 87.
(15) Hochstrasser, R. A., Jr.; Lutz, H.; Scott, G. W. *J. Chem. Phys.* **1974**, *61*, 2500.
(16) Högemann, C.; Vauthey, E. *J. Phys. Chem. A* **1998**, *102*, 10051.
(17) Melhuish, W. *J. Chem. Phys.* **1969**, *50*, 2779.
(18) Wang, X.; Kofron, W.; Kong, S.; Rajesh, C.; Modarelli, D.; Lim, E. *J. Phys. Chem. A* **2000**, *104*, 1461.
(19) Pownall, H. J.; Huber, J. R. *J. Am. Chem. Soc.* **1971**, *93*, 6249.
(20) Morlet-Savary, F.; Ley, C.; Jacques, P.; Wieder, F.; Fouassier, J. P. *J. Photochem. Photobiol., A* **1999**, *126*, 7.
(21) *Handbook of Photochemistry*; Murov, S. L., Carmichael, I., Hug, G. L., Eds.; Marcel Dekker: New York, 1993.
(22) Sikorski, M.; Krystkowiak, E.; Steer, R. *J. Photochem. Photobiol., A* **1998**, *117*, 1.
(23) Ott, J.; Sipowska, J. *J. Chem. Eng. Data* **1996**, *41*, 987.
(24) Lien, P.; Lin, H.; Lee, M. *Fluid Phase Equilib.* **2004**, *215*, 187.
(25) Atkins, P.; de Paula, J. *Physical Chemistry*, 7th ed.; Oxford University Press: Oxford, 2002.
(26) Jozefowicz, M.; Heldt, J. *Chem. Phys.* **2003**, *294*, 105.
(27) Steiner, U. E.; Ulrich, T. *Chem. Rev.* **1989**, *89*, 51.
(28) Connors, R. E.; Christian, W. R. *J. Phys. Chem.* **1982**, *86*, 1524.
(29) Connors, R. E.; Sweeney, R. J.; Cerio, F. *J. Phys. Chem.* **1987**, *91*, 819.
(30) Ohshima, Y.; Fujii, T.; Fujita, T.; Inaba, D.; Baba, M. *J. Phys. Chem. A* **2003**, *107*, 8851.
(31) Collins, F. C.; Kimball, G. E. *J. Colloid. Sci.* **1949**, *4*, 425.
(32) The time constant determined by transient absorption is 1.3 ps, and by fluorescence spectroscopy 1.5 ps. In the following we will refer to both as the 1.5 ps component.

PAPER www.rsc.org/pccp | Physical Chemistry Chemical Physics

On the unusual fluorescence properties of xanthone in water†

B. Heinz,[a] B. Schmidt,[a] C. Root,[a] H. Satzger,[ab] F. Milota,[c] B. Fierz,[d] T. Kiefhaber,[d] W. Zinth[a] and P. Gilch*[a]

Received 9th March 2006, Accepted 6th June 2006
First published as an Advance Article on the web
DOI: 10.1039/b603560d

Photo-excited xanthone is known to undergo ultrafast intersystem crossing (ISC) in the 1 ps time domain. Correspondingly, its fluorescence quantum yield in most solvents is very small ($\sim 10^{-4}$). Surprisingly, the quantum yield in water is 100 times larger, while ISC is still rapid (~ 1 ps), as seen by ultrafast pump probe absorption spectroscopy. Temperature dependent steady state and time resolved fluorescence experiments point to a delayed fluorescence mechanism, where the triplet $^3n\pi^*$ state primarily accessed by ISC is nearly isoenergetic with the photo-excited $^1\pi\pi^*$ state. The delayed fluorescence of xanthone in water decays with a time constant of 700 ps, apparently by internal conversion between the $^3n\pi^*$ state and the lowest lying triplet state $^3\pi\pi^*$.

1. Introduction

In his classic 1963 paper[1] M. El-Sayed formulated rules for the intersystem crossing (ISC) efficiencies of photo-excited molecules. These rules, which have become part of photochemistry textbooks,[2,3] state that ISC can be highly efficient if the spin flip is accompanied by a change of the orbital character of the electronic wavefunction. For instance, if the photo-excited state is a singlet $^1\pi\pi^*$ state the ISC will be efficient provided that a triplet $^3n\pi^*$ state is energetically accessible. In aromatic carbonyl compounds such a situation prevails and they have indeed become textbook examples for molecules undergoing fast ISC. At the time of publication of the El-Sayed rules the time scales for ISC could only be inferred indirectly either from low fluorescence or high triplet quantum yields. Meanwhile numerous time resolved experiments have been performed and underscore El-Sayed's findings.[2]

Xanthone has been among the aromatic carbonyl compounds studied by a variety of techniques.[4–11] Due to its planar[12] and rigid structure n or π character can clearly be assigned to the orbitals. Furthermore, photo-induced molecular rearrangements are not expected to play an important role. The first ultrafast time resolved studies on ISC in xanthone afforded a time constant of ~ 10 ps.[6,7] In these picosecond pump probe experiments the ISC time constant was obtained by deconvolution. In later femtosecond experiments[10] it was demonstrated that the rise of the triplet state absorption is in fact bi-exponential with time constants of 1.3 and 12 ps. Some of the present authors[11] had a closer look at this rise. For xanthone in ethanol components of 1 and 10 ps carrying nearly equal amplitudes were found. To assign these components triplet quenching experiments were performed. In the presence of high concentrations of the triplet quencher 1-methylnaphthalene the 10 ps component "vanishes". From this it was deduced that after 1 ps the transfer of the excited population to *one* triplet state is complete. According to El-Sayed's rules the decay of the photo-excited $^1\pi\pi^*$ state seems to start with an ISC process populating an $^3n\pi^*$ state (time constant of ~ 1 ps). In ref. 11, the 10 ps time constant has been associated with the subsequent internal conversion (IC) step to the lowest $^3\pi\pi^*$ state (*cf.* Fig. 1a, Fig. 3a and c). The population of this state is followed by a further process which manifests itself by a blue shift of the triplet absorption spectrum. This 60 ps process has tentatively been assigned to the dielectric relaxation of the solvent.[11]

For xanthone in ethanol this delivers a consistent picture which is in line with steady state and femtosecond fluorescence experiments.[11] A puzzle arises when one looks at the fluorescence behavior of xanthone dissolved in water. Our interest in this arose since peptides bearing xanthone and naphthyl moieties as markers are used to monitor intramolecular contact formation in polypeptide chains.[13–15] For such experiments water is the solvent of choice. The apparent inconsistency observed is that even though ISC is very fast in xanthone, the fluorescence quantum yield of xanthone in water is $\sim 4\%$, *i.e.* two orders of magnitude higher than expected. This high quantum yield in water was first described by Pownall and Huber,[4] but not further investigated. Resolving this puzzle is hampered by the low solubility of xanthone in water, which may be the reason why this issue has not been addressed in detail. Still, this solubility is sufficient to perform steady state and picosecond fluorescence experiments but renders femtosecond experiments difficult. For the femtosecond experiments we resorted to a xanthone derivative (a peptide bound to the xanthone, in the following referred to as xanthone peptide) which in terms of fluorescence behavior in water is very similar to xanthone but features a higher solubility.

[a] *Department für Physik, Ludwig-Maximilians-Universität, Oettingenstr. 67, D-80538 München, Germany. E-mail: Peter.Gilch@physik.uni-muenchen.de; Fax: +49-89-2180-9202*
[b] *Steacie Institute for Molecular Sciences, National Research Council of Canada, 100 Sussex Drive, Ottawa, Ontario, Canada K1A OR6*
[c] *Institut für Physikalische Chemie der Universität Wien Währingerstraße 42, A-1090 Wien, Austria*
[d] *Division of Biophysical Chemistry, Biozentrum, University of Basel, Klingelbergstrasse 50/70, CH-4056 Basel, Switzerland*
† The HTML version of this article has been enhanced with colour images.

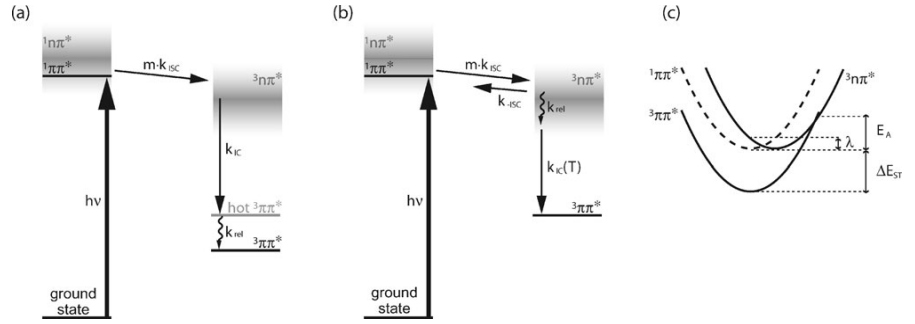

Fig. 1 Schematic Jablonski diagrams depicting the excited states of xanthone. Bold lines symbolize states with energies defined spectroscopically ($^1\pi\pi^*$ and $^3\pi\pi^*$), grey shades stand for states ($^1n\pi^*$ and $^3\pi\pi^*$) for which the energetic positions are deduced indirectly and are not well defined. Transitions among these states considered here are indicated by arrows. (a) Mechanism as discussed in ref. 11. (b) Mechanism incorporating the findings of this study. (c) Schematic potential energy curves illustrating the origin of a barrier for the IC.

2. Experimental

Steady state fluorescence spectra were recorded with a commercial fluorimeter (Fluorolog 1680 0.22 m from Spex). The reported fluorescence spectra were corrected for the spectral sensitivity of the fluorimeter. 2-(1-Naphthyl)-5-phenyloxazol (1-NPO) in cyclohexane was used as a reference dye for the determination of the fluorescence quantum yields.[16]

A detailed description of the femtosecond pump probe setup is given in ref. 17. A 1 kHz Ti:Sa laser/amplifier system served as a light source. Pump and probe pulses in the desired frequency range were generated by non-linear techniques (NOPA, SHG, and white light generation). The pertinent parameters for the pump probe experiment were the following: The pump light was tuned to 340 nm, had an energy of $\sim$350 nJ pulse^{-1} and a diameter of $\sim$150 μM at the sample location. Its polarization plane lay at the magic angle with respect to the white light probe. Multi-channel probing[18] spanned a spectral range from 400–700 nm. The experimental response time was $\sim$200 fs (FWHM). The sample was exchanged between consecutive laser shots by a flow system. The fused silica sample cell had a pathlength of 0.5 mm and the optical density at the excitation wavelength amounted to 0.5.

The picosecond fluorescence lifetime measurements were recorded with a standard time-correlated single photon counting setup.[19] The excitation light was provided by a regeneratively amplified fs-laser system (Mira 900F, RegA 9000, and OPA 9400, all from Coherent Inc.), yielding 70 fs pulses at 680 nm with a repetition rate of 200 kHz. This output was frequency doubled in a 300 μm β-barium borate crystal, resulting in 100 fs pulses at 340 nm with 50 nJ pulse energy. Samples of xanthone and the xanthone peptide dissolved in water or ethanol were kept in fused silica cells (1 cm path length). For the temperature dependent measurements a flow cell, pumped by a gear pump whose 40 ml reservoir was kept in a thermostat, was used. Fluorescence photons were collected in 90° geometry and after passing a monochromator (SPEX 1681), detected at 400 nm (xanthone) and 417 nm (xanthone peptide), respectively, by a Peltier-cooled photomultiplier (Hamamatsu, type 3809). The instrument response function (52 ps at FWHM) was measured with stray light and deconvoluted from the fluorescence decay using commercially available software (Fluofit from PicoQuant).

Xanthone (Fluka), 1-NPO (Lambdachrome), cyclohexane (Merck, Uvasolv), ethanol (Merck Seccosolv), and water (Merck LiChrosolv) were used as received. The xanthone peptide (Xanthone-$(Pro)_5$-Phe-Ser-Arg-Ser-Arg-Gly-$CONH_2$) was synthesized and purified as described in ref. 14.

3. Results

3.1. Steady state fluorescence spectroscopy

The fluorescence spectra of xanthone in ethanol and water (Fig. 2) already reveal the striking anomaly dealt with in this paper. The fluorescence intensities of the molecule in the two solvents differ by two orders of magnitude. Absolute numbers for the fluorescence quantum yields ϕ_{fl} are determined by comparing the spectrally integrated fluorescence intensity with that of a reference dye (2-(1-naphthyl)-5-phenyloxazol,1-NPO). The quantum yield of 1-NPO is taken to be 0.7.‡ Based on this reference value the fluorescence quantum yields ϕ_{fl} at room temperature are 4.9×10^{-4} for xanthone in ethanol, 4.2×10^{-2} in water, and 1.5×10^{-2} for the xanthone peptide in water (see also Table 1). The quantum yield of xanthone in water closely matches the one reported by Pownall and Huber (3.0×10^{-2}).[4] The similarity of the values of xanthone and the xanthone peptide in water confirms that the xanthone peptide can be used as a "placeholder" for xanthone in femtosecond experiments. The quantum yield for the prompt fluorescence ϕ_{fl}^{p} of xanthone in ethanol can be compared with a calculation based on the relation

$$\phi_{fl}^{p} = \frac{\tau_{fl}^{p}}{\tau_{rad}}. \quad (1)$$

The prompt fluorescence lifetime τ_{fl}^{p} was determined by a femtosecond Kerr gate experiment[11] to be 1.5 ps. The radiative lifetime τ_{rad} of the ππ* transition obtained by a Strickler–Berg analysis[21] is 15 ns. This yields a value for ϕ_{fl}^{p} of 1×10^{-4}, which

‡ In his handbook of fluorescence spectra Berlman[20] reported a quantum yield of 0.94 for 1-NPO. The lifetime data compiled in this book afforded a somewhat lower yield of 0.74. This is very close to the quantum yield of 0.70 reported in another study.[16]

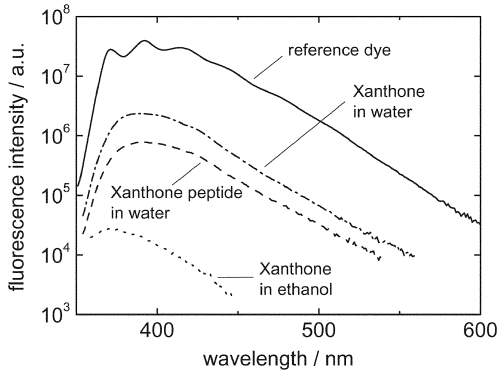

Fig. 2 Fluorescene spectra of the xanthone samples investigated in this study in comparison with the reference dye. The excitation light was tuned to 344 nm and was in resonance with the $^1\pi\pi^*$ transition of xanthone. The absorbances of the samples at 344 nm were matched (A = 0.15 OD), so that the intensities of the spectra can be directly compared. Note the logarithmic intensity axis.

is of the right magnitude. The experimental value of the total fluorescence quantum yield $\phi_{fl} = 4.9 \times 10^{-4}$ (see above) is somewhat larger, pointing to the existence of an additional fluorescence component.

The high fluorescence quantum yield of xanthone in water can be explained by two alternative models: (i) A much longer ISC time would directly translate into a longer fluorescence lifetime and thus to a larger value of ϕ_{fl}. (ii) A delayed fluorescence scheme with a triplet state in energetic vicinity to the fluorescent singlet state would also lead to a large value of ϕ_{fl} in water. A comparison of femtosecond pump probe experiments of xanthone in ethanol and the xanthone peptide in water (see below) will support explanation (ii).

3.2. Femtosecond pump probe spectroscopy

Samples of xanthone in ethanol and the xanthone peptide in water were excited with 340 nm femtosecond pump pulses. The spectral response was probed by a white light continuum in a multi-channel fashion. The detection range covers the absorption band of the xanthone triplet[22] peaking around 600 nm (Fig. 3). The data for xanthone in ethanol, already published in ref. 11, are included here for the sake of comparison. Immediately after photo-excitation xanthone in ethanol shows a weak and broad induced absorption of the excited singlet state (Fig. 3a). Subsequently the transient absorption rises in the aforementioned bi-phasic fashion (time constants of 1.3 and 12 ps, see amplitude spectra in Fig. 3c). Triplet quenching experiments[11] have shown that the ISC process is related to the 1.3 ps kinetic component. These fast kinetics are followed by an apparent blue shift of the triplet spectrum occurring with a characteristic time of 62 ps. This spectral change can alternatively be described by the decay of a red absorption band and the concomitant rise of a blue band.

Table 1 Compilation of the fluorescence properties of xanthone determined is this study. For the calculation of the fluorescence quantum yield ϕ_{fl} a value of 0.7 for the yield of the reference dye 1-NPO was assumed. The lifetimes of the delayed fluorescence τ_{fl}^{d} stem from the single photon counting experiments. The singlet fraction s was calculated using eqn (4)

	ϕ_{fl}	τ_{fl}^{d}/ps	s
Xanthone in ethanol			
294 K	4.9×10^{-4}	57	0.1
Xanthone in water			
280 K	5.8×10^{-2}	998	1.16
294 K	4.2×10^{-2}	706	1.18
307 K	2.8×10^{-2}	480	1.16
320 K	1.9×10^{-2}	30^{-2}	1.25
332 K	1.1×10^{-2}	188	1.16
Xanthone peptide in water			
294 K	1.5×10^{-2}	316	0.94

For the xanthone peptide in water similar features are observed. There is a transient absorption around 600 nm at early delay times, which also points to a rapid formation of the triplet state (Fig. 3b). The rise of this absorption can be modelled with two time constants of 0.35 and 3 ps (Fig. 3d). The apparent blue shift here develops on a longer time scale with a dominant 320 ps component. The spectral evolution here clearly features an isosbestic point around 630 nm, suggesting a transition between two distinct states—and not a spectral shift.

The picosecond rise of an induced absorption band around 600 nm gives evidence that the xanthone peptide in water as well as xanthone in ethanol *both* rapidly populate a triplet state. To sum up, a longer ISC time for the xanthone peptide in water as compared to xanthone in ethanol is not observed. Thus, the duration of the ISC cannot be responsible for the high fluorescence quantum yield of the xanthone peptide (or xanthone) in water contrary to model (i). Our proposed model of a delayed fluorescence mechanism would call for an emissive singlet state and a triplet state being populated at the same time. To support this explanation, we studied the fluorescence emission of xanthone in greater detail.

3.3. Picosecond fluorescence spectroscopy

Temperature controlled xanthone samples were excited with 340 nm pulses (duration 100 fs, repetition rate 200 kHz). Time dependent fluorescence emission at 400 nm (xanthone in water and ethanol) and at 417 nm (xanthone peptide) was detected *via* time correlated single photon counting. The time resolution of the set-up was ~50 ps and thus the ultrafast (~1 ps) fluorescence component as the one reported in ref. 11 could not be resolved. The xanthone samples feature fluorescence decay times on the 100 ps time scale (Fig. 4). The time traces were subject to single exponential, or—where appropriate—bi-exponential fits. At room temperature xanthone in water features the slowest decay time with 706 ps, followed by the xanthone peptide in water (316 ps (84%) and 948 ps (16%)), and xanthone in ethanol (57 ps). The values for the xanthone peptide in water and xanthone in ethanol agree with the characteristic times for the blue shifts observed in the pump probe experiments.

For xanthone both in water and ethanol (data for ethanol not shown) the fluorescence decay speeds up with rising temperature (Fig. 4). For xanthone in water we find values between 998 ps at 280 K and 188 ps at 332 K. This decrease in

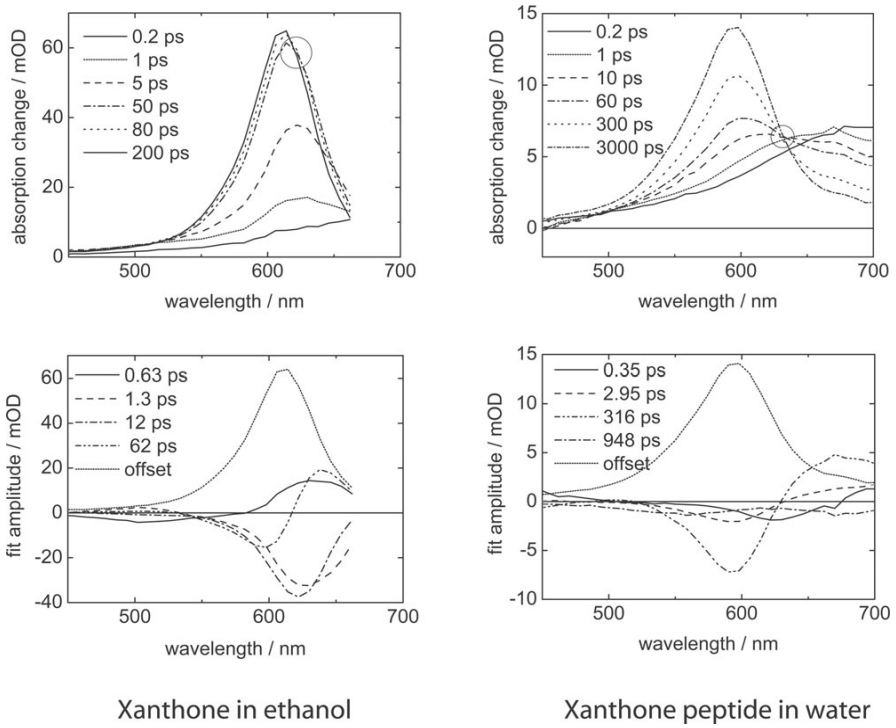

Fig. 3 Femtosecond pump probe experiments on xanthone in ethanol (left panel, taken from ref. 11) and the xanthone peptide in water (right panel). In the upper panel the experimental data are given as transient absorption spectra at delay times indicated. The circles mark the isosbestic points. In the lower panel decay associated spectra retrieved from a global fit are depicted. The 316 ps and 948 ps time constants were taken from the fluorescence experiment. A fit with free floating parameters yielded comparable results.

fluorescence lifetime with rising temperature nicely correlates with the decrease in fluorescence intensity (Fig. 4c). Due to the limited time resolution of the single photon counting experiment a corresponding graph for xanthone in ethanol could not be recorded. Yet, the qualitative behavior—decrease of lifetime and intensity—is the same.

4. Discussion

The quenching experiments on xanthone in ethanol[11] mentioned in the Introduction have given evidence for a complete transfer of the photo-excited population into a triplet state within $\sim$1.5 ps. The pump probe spectra of xanthone in ethanol and the xanthone peptide in water both show an absorption band around 600 nm characteristic for the xanthone triplet. Thus, it is very likely that for the xanthone peptide in water some picoseconds after the pump pulse at least a portion of the excited state population must also reside in a triplet state. So it is quite surprising that at the same time we are seeing fluorescence emission of the molecule. In fact, these two at first glance contradictive observations were already made for xanthone in water by Mohtat *et al.*[23]—though they did not further comment on it. As mentioned above this apparent contradiction can be resolved by a delayed fluorescence mechanism[2] (see Fig. 1b), where the following processes occur: The primarily excited singlet state undergoes fast ISC characterized by a rate constant mk_{ISC}. Thereby m is the number of triplet product states involved in the ISC process, and k_{ISC} is the rate constant for the transfer to one triplet substate. A rate constant k_{-ISC} is assigned to the backward ISC process from one triplet state to the singlet state. Due to detailed balance this constant obeys the relation

$$k_{-ISC} = k_{ISC} e^{\frac{-\Delta E_{ST}}{kT}}. \quad (2)$$

Here, ΔE_{ST} is the energy gap between the singlet and triplet states (which is taken to be a positive quantity and we assume that the entropy does not change during the singlet triplet transition). In this scheme an equilibrium between singlet and triplet states is approached with an observed rate constant $k_{obs} = mk_{ISC} + k_{-ISC}$. The fractional population s of the singlet state in equilibrium is given by

$$s = \frac{1}{m + e^{\frac{-\Delta E_{ST}}{kT}}} e^{\frac{-\Delta E_{ST}}{kT}}. \quad (3)$$

Processes depleting either the singlet or triplet state will limit the time for which the equilibrium prevails and for which delayed fluorescence can be observed. As the radiative lifetime of xanthone in water is long ($\tau_{rad} \approx 20$ ns), it is obvious that radiative depletion does not significantly contribute to the delayed fluorescence lifetime. Internal conversion between the $^1\pi\pi^*$ state and the ground state might contribute to the decay

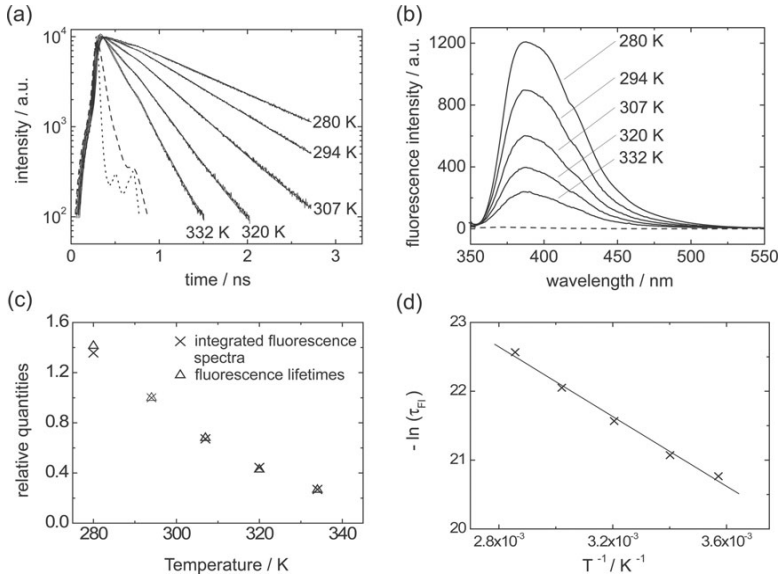

Fig. 4 Time correlated single photon counting experiment on xanthone in water and ethanol (a) in comparison with steady state fluorescence data (b). (a) The data recorded at different temperatures and the respective fits are shown. The dotted line represents the instrumental response function. The dashed line depicts the data from xanthone in ethanol at 294 K, whereas all other curves show the fluorescence of xanthone in water. The time constants obtained from the fits are compiled in Table 1. (b) All fluorescence spectra presented by solid lines refer to xanthone in water at temperatures indicated, the dashed line represents the fluorescence spectrum of xanthone in ethanol at room temperature (note that the amplitude of this spectrum is two orders of magnitude smaller that those in water). (c) Correlation between the temperature dependencies of the fluorescence intensity and the fluorescence lifetime for xanthone in water. (d) Arrhenius analysis of the fluorescence lifetime for xanthone in water.

of the delayed fluorescence. Such an internal conversion would compete with the population of the lowest (long-lived) triplet state and the yield of this state would depend on the delayed fluorescence lifetime. This lifetime is a factor of 10 shorter for xanthone in ethanol as compared to xanthone in water. The relative triplet yield for the two samples was determined by recording the transient absorption spectra for a delay time of $\sim$1 ns (data not shown, the transient spectra depicted in Fig. 4 should not be compared, since the experimental conditions for both solutions were not identical). Under the assumption that the extinction coefficients are equal for both samples their triplet yields are very close to each other (within $\sim$50%). Thus, the internal conversion to the ground state does not seem to contribute to the delayed fluorescence lifetime. Neither can the decay of the *lowest* triplet state of xanthone hold responsible for the delayed fluorescence lifetime. Even with oxygen quenching taken into account this triplet lifetime is $\sim$0.5 μs.[24] This is orders of magnitude too long to explain the $\sim$700 ps fluorescence decay. From this we can conclude that the triplet state involved in the delayed fluorescence is not the lowest triplet state. Some information on the nature of this triplet state can be gained from the singlet fraction s which is in turn related with the energy gap ΔE_{ST} (see eqn (3)). The fraction s is connected to the fluorescence quantum yield ϕ_{fl} and the experimentally accessed lifetimes by

$$\phi_{fl} = \frac{\tau_{fl}^{p} + s\tau_{fl}^{d}}{\tau_{rad}}. \qquad (4)$$

The lifetime of the prompt fluorescence τ_{fl}^{p} we take to be 1.5 ps which is the value determined for xanthone in ethanol by the Kerr gate experiment.[11] Pump probe experiments on the xanthone peptide in water feature a shortest time constant of roughly the same magnitude (0.35 ps). Xanthone in water is assumed to behave like the xanthone peptide in water. And thus, the value for τ_{fl}^{p} of 1.5 ps is used for all samples. The delayed fluorescence decays with a characteristic time τ_{fl}^{d} measured in the single photon counting experiment. The computed fractions s are compiled in Table 1. It turns out that for xanthone in water τ_{fl}^{p} is much smaller than the term $s\,\tau_{fl}^{d}$. Thus, the latter term mainly determines the value of ϕ_{fl}.

For xanthone and the xanthone peptide in water values for $s \approx 1$ are determined. It has to be stressed that if the energy gap ΔE_{ST} is taken to be positive—that is the triplet state lies below the singlet state—the maximum value of s is 0.5. It should be noted that the determination of fluorescence quantum yields is subject to appreciable uncertainties (note that we only performed a relative determination). Therefore the basic information retrieved from the evaluation of s should only be that within this model the energy gap ΔE_{ST} is close to zero. The temperature independence of s (see Table 1) is a further indication of the fact that ΔE_{ST} is close to zero.

Considering the aforementioned findings the temperature dependence of the fluorescence quantum yield ϕ_{fl}—defined in eqn (4)—is solely due to the change of the lifetime τ_{fl}^{d}. In our model this lifetime is given by the time for which the equilibrium between excited singlet and triplet states lasts. Thus, the depletion of the triplet state in equilibrium has to be temperature dependent. It is important to note that for xanthone in ethanol the same situation prevails. In ethanol the equilibrium lasts for only 60 ps and the singlet fraction s in equilibrium

only amounts to 0.1 leading to a value of $\Delta E_{ST} = 440\ cm^{-1}$. In contrast to the situation in water this results in a considerable contribution of the prompt fluorescence to the total emission. Nevertheless, the difference in fluorescence behavior between the two solvents is of quantitative and not qualitative nature.

The questions to be addressed now are: (i) Which triplet state is so close to the singlet state that delayed fluorescence is so effective? (ii) Which mechanism depletes this state? To (i): In the spectral range of the photo-excitation only the singlet $^1\pi\pi^*$ carries appreciable oscillator strength,[4] so this is the state photo-excited in our experiment (*cf.* Fig. 1b). The singlet $^1n\pi^*$ state is in energetic vicinity to the $^1\pi\pi^*$ state. In the gas phase[25] or non-polar surroundings[4] the $^1n\pi^*$ state lies below the bright $^1\pi\pi^*$ state by some few 1000 cm^{-1}. In polar surroundings the transition to the $^1n\pi^*$ state has not been located,[4,10] presumably, because it is hidden below the much stronger $^1\pi\pi^*$ transition. Such solvent induced hypsochromic shifts of $n\pi^*$ transitions are also observed or deduced in closely related molecules like benzophenone,[2] thioxanthone,[26] and acridone.[27] Similarly, Mg^{2+} ions acting as Lewis acids have been shown to influence the fluorescence properties of aromatic aldehydes.[28] This has been rationalized by an increase of the $^3n\pi^*$ energy induced by the ions.[28] In this case the $^1n\pi^*$ state is either isoenergetic or lies at a higher energy than the $^1\pi\pi^*$ state. Singlet–triplet splitting is known to be small for $n\pi^*$ states and high for $\pi\pi^*$ states,[3] which implies that the lowest triplet state in polar media is of $\pi\pi^*$ character. In fact, the phosphorescence spectrum and lifetime measurements[4] as well as ESR spectroscopy[29] of the xanthone triplet in polar media indicate that the lowest triplet state is of $\pi\pi^*$ nature. The phosphorescence experiment[4] places the triplet $^3\pi\pi^*$ state about 3300 cm^{-1} below the singlet $^1\pi\pi^*$ state—an energy gap by far too large to account for the observed delayed fluorescence. Thus, the triplet state involved should be the $^3n\pi^*$ state. According to El-Sayed's rules for ISC this is also the triplet state which is preferentially populated when starting with a $^1\pi\pi^*$ state. Its energetic position has not yet been determined spectroscopically, presumably because it is too short lived. Based on our findings the $^3n\pi^*$ state is isoenergetic with the singlet $^1\pi\pi^*$ state in water and lies $\sim$400 cm^{-1} below it in ethanol. These estimates are based on eqn (3) and (4). For the multiplicity m entering eqn (3) we use a value of 1 and not the common value of 3 for a triplet state. This relies on the fact that ISC often does not distribute population evenly among the substates of one triplet (usually referred to as T_x, T_y, and T_z).[30] For xanthone such a preferential population of the T_z by a factor of 5–10 was inferred from ESR[29] and ODMR spectroscopy.[5] The ESR spectroscopy, however, was performed on $^3\pi\pi^*$. Still, if a preferential population is observed in a substate of a certain triplet ($^3\pi\pi^*$) which is populated *after* the $^3n\pi^*$ then it is very likely that a substate of $^3n\pi^*$ itself is preferentially occupied as well. In conclusion, the state participating in the delayed fluorescence seems to be one substate of the $^3n\pi^*$ state.

To (ii): How is the initially populated $^3n\pi^*$ state depleted and the delayed fluorescence "switched off"? We note that at present we cannot give a completely consistent explanation. In the following we draw a picture of the photo-physics that tries to incorporate most of the experimental findings. As inferred from the single photon counting experiment the $^3n\pi^*$ state is—depending on temperature and solvent—depleted on the time scale of $\sim$100–1000 ps. The fluorescence decay times nicely match the time constants of the blue shift observed in the pump probe data (Fig. 3c and d). In analogy to the interpretation of results on thioxanthone[31] this shift was associated with the dielectric relaxation of the solvent.[11] Two observations question this assignment. First, during dielectric relaxation a molecule experiences a continuous change of its solvent surroundings resulting in a smooth shift of its spectral features (*e.g.* first moment of the spectrum).[32] Yet, the presence of isosbestic points in the pump probe data speak in favor of a transition between two distinct states (Fig. 3a and b). Second, the time constants of the apparent shift at room temperature are $\sim$100 ps or longer. This is one order of magnitude larger than the average relaxation time measured with a different solvation probe, coumarin 153.[32] Thus, a more likely assignment for the apparent shift is the $^3n\pi^* \rightarrow {}^3\pi\pi^*$ transition. As stated above, the energy gap between singlet and triplet $\pi\pi^*$ states is so large that no delayed fluorescence will occur from the $^3\pi\pi^*$ state. The delayed fluorescence should then be switched off with this transition.

The transient absorption experiment gives further evidence that the transition involves the $^3n\pi^*$ and $^3\pi\pi^*$ states. Absorption spectra of the *relaxed* triplet state of xanthone vary with the solvent polarity.[22] In polar solvents in which the lowest triplet state is of $^3\pi\pi^*$ character[4,29] the absorption peaks around 610 nm. In nonpolar solvents where the $^3n\pi^*$ and $^3\pi\pi^*$ states are in energetic vicinity[8] two absorption bands are observed. One close to the location of the "polar" band and one at higher wavelengths ($\sim$670 nm). The latter was assigned to the $^3n\pi^*$ state. These results predict a decay of an absorption band at high wavelengths and a concomitant rise of a band at lower wavelengths during the $^3n\pi^* \rightarrow {}^3\pi\pi^*$ transition. This is exactly what is observed in the pump probe data presented here. Thus, the process underlying the decay of the delayed fluorescence seems to be the IC process between the two triplet states.

This transition proceeds with a temperature dependent rate constant $k_{IC}(T)$ (Fig. 1b). For a temperature independent fractional singlet population s as observed here (see Table 1) $k_{IC}(T)$ is inversely proportional to the value of τ_{fl}^{d} derived from the time correlated single photon counting experiment. Plotting $\frac{1}{\tau_{fl}^{d}(T)} \approx k_{IC}(T)$ according to the Arrhenius law (Fig. 4d) gives a reasonable linear dependency between ln k_{IC} and $1/T$. The slope of the Arrhenius plot affords an activation energy E_A of 2000 cm^{-1}. An Arrhenius analysis based on the fluorescence quantum yield results in a very similar value (1800 cm^{-1}). The linear correlation between ln k_{IC} and $1/T$ indicates that temperature independent processes do not contribute significantly to the decay of the delayed fluorescence. Such a temperature independent process might have been the internal conversion between the $^1\pi\pi^*$ and the ground state. From the Arrhenius analysis of k_{IC} one also obtains a pre-exponential factor of 10^{13} s^{-1}. This implies that the rather slow room temperature IC between the two triplet states is not due to a weak coupling mediating the transition between the two triplet states but due to a barrier. In a classical single mode picture the barrier E_A can be related to the total re-organization

energy λ and the difference ΔE_{TT} between the $^3\pi\pi^*$ and the $^3n\pi^*$ state (Fig. 1c) (we again assume that the entropy difference is zero):[33]

$$E_A = \frac{(-\Delta E_{TT} + \lambda)^2}{4\lambda} \quad (5)$$

Values for this energy difference can be obtained based on the following considerations. The energy gap between the $^1\pi\pi^*$ state and the $^3\pi\pi^*$ state has been determined spectroscopically to be 3300 cm^{-1}.[4] This energy gap has been reported for xanthone in ethanol, we assume the value to be the same for xanthone in water. The present findings indicate that the $^1\pi\pi^*$ and the $^3n\pi^*$ state are iso-energetic in water and are 400 cm^{-1} apart in ethanol. So the pertinent energy difference ΔE_{TT} is 3300 cm^{-1} for water and 2900 cm^{-1} for ethanol. Using the values for water eqn (5) yields the following two solutions for the re-organization energy, λ_1 = 790 cm^{-1} and λ_2 = 13 800 cm^{-1}. Spectroscopic results support the first, smaller value. In the classical single mode picture used here the re-organization energy λ is given by[34]

$$\lambda = \frac{\Delta\nu_s}{2}. \quad (6)$$

Here, $\Delta\nu_s$ is the Stokes shift between the absorption and emission band of the respective transition. Absorption and emission bands related with $^3\pi\pi^* \rightarrow {}^3n\pi^*$ cannot be (easily) recorded since they lie in the IR. Yet, there is information on the Stokes shift associated with the $S_0 \rightarrow {}^1\pi\pi^*$ transition which should tell us about the expected order of magnitude. In water the absorption and emission bands due to the $S_0 \rightarrow {}^1\pi\pi^*$ transition peak at 344 and 386 nm, respectively. This translates into a Stokes shift $\Delta\nu_s$ of 3200 cm^{-1} or a re-organization energy of 1600 cm^{-1}. Only the first solution of eqn (5) λ_1 = 790 cm^{-1} is of this magnitude. So within this picture, the barrier of the $^3n\pi^* \rightarrow {}^3\pi\pi^*$ transition is due to a small re-organization energy λ and a comparatively high energy difference ΔE_{TT}.

The observed solvent dependence of the rate constant k_{IC} is in line with this model. Changing the solvent from water to ethanol increases k_{IC} at room temperature by a factor of 10. For equal pre-exponential factors this is equivalent to a *difference* in activation energies E_A of 460 cm^{-1}. Using Eqn (5) and ΔE_{TT} = 2900 cm^{-1} and λ = 790 cm^{-1} (the value for water) one obtains a difference of the same magnitude (590 cm^{-1}). The small re-organization energy can also explain the ultrafast—and thereby close to barrierless—ISC process. In terms of re-organization the ISC and IC process should be similar. In either process $n\pi^*$ and $\pi\pi^*$ states are involved. For the ISC process the energy gap (ΔE_{ST}) is close to zero and thus $E_A \approx \lambda/4 \approx 200$ cm^{-1}, *i.e.* ISC is close to barrierless.

Despite these arguments in favor of a small re-organization energy the picture has one drawback. The solution λ_1 = 790 cm^{-1} of eqn (5) places the process in the Marcus inverted region. In the inverted region temperature dependencies are often weak when high frequency quantum modes couple strongly to the transition. This would contradict the observed temperature dependencies seen in Fig. 4. An evaluation of the degree of high frequency coupling would require equilibrium structures and normal modes of both the $^3n\pi^*$ and the $^3\pi\pi^*$ state. As this information is presently not available this issue cannot be settled yet. The presented model and experimental data indicate that this coupling is weak.

Associating the ~700 ps/60 ps process for xanthone in water/ethanol with an activated IC between the two triplet states requires a re-assignment of the 3–10 ps processes in these samples. The time scale of these processes matches with the slower phases of dielectric relaxation seen in dynamic Stokes shift experiments.[32] Compared to the ordering put forth in ref. 11 (*cf.* Fig. 1a), it seems that dielectric relaxation proceeds the IC (*cf.* Fig. 1b).

In conclusion, the abnormally high fluorescence quantum yield of xanthone in water is assigned to a delayed fluorescence mechanism. The dark state in this mechanism has to be isoenergetic with the bright $^1\pi\pi^*$ state. The most likely candidate for this dark state is a substate (T_z) of the triplet $^3n\pi^*$. This state would then be populated in an ultrafast (~1 ps) ISC process. The decay of the delayed fluorescence proceeds with time constants of ~700 ps in water, ~60 ps in ethanol and ~300 ps for the xanthone peptide in water and is connected with considerable changes in the transient absorption spectrum. These changes bear the signature of an internal conversion from the $^3\pi\pi^*$ to the $^3\pi\pi^*$ state.

Acknowledgements

We are thankful to Prof. H. F. Kauffmann (Universität Wien) for the possibility to record time resolved fluorescence spectra at his laboratory. Further, we would like to thank our undergraduate students Katrin Vu and Ossian Karch for their work on the steady state fluorescence. B. Heinz gratefully appreciates a scholarship donated by the Fonds der Chemischen Industrie.

References

1 M. El-Sayed, *J. Chem. Phys.*, 1963, **38**, 2834–2838.
2 N. Turro, *Modern Molecular Photochemistry*, The Benjamin/Cummings Publishing Co Inc., Menlo Park, CA, 1978.
3 J. Kopecky, *Photochemistry. A Visual Approach*, VCH, Weinheim, 1992.
4 H. J. Pownall and J. R. Huber, *J. Am. Chem. Soc.*, 1971, **93**, 6429–6436.
5 A. Chakrabarti and J. R. Huber, *J. Phys. Chem.*, 1976, **80**, 2966–2973.
6 D. E. Damschen, C. D. Merritt, D. L. Perry, G. W. Scott and L. D. Talley, *J. Phys. Chem.*, 1978, **82**, 2268–2272.
7 B. I. Greene, R. M. Hochstrasser and R. B. Weisman, *J. Chem. Phys.*, 1979, **70**, 1247–1259.
8 R. E. Connors and W. R. Christian, *J. Phys. Chem.*, 1982, **86**, 1524–1528.
9 R. E. Connors, R. J. Sweeney and F. Cerio, *J. Phys. Chem.*, 1987, **91**, 819–822.
10 J. Cavaleri, K. Prater and R. Bowman, *Chem. Phys. Lett.*, 1996, **259**, 495–502.
11 H. Satzger, B. Schmidt, C. Root, W. Zinth, B. Fierz, F. Krieger, T. Kiefhaber and P. Gilch, *J. Phys. Chem. A*, 2004, **108**, 10072–10079.
12 K. Iijima, T. Misu, S. Ohnishi and S. Onuma, *J. Mol. Struct.*, 1989, **213**, 263–269.
13 O. Bieri, J. Wirz, B. Hellrung, M. Schutkowski, M. Drewello and T. Kiefhaber, *Proc. Natl. Acad. Sci. U. S. A.*, 1999, **96**, 9597–9601.
14 F. Krieger, B. Fierz, O. Bieri, M. Drewello and T. Kiefhaber, *J. Mol. Biol.*, 2003, **332**, 265–274.
15 F. Krieger, B. Fierz, F. Axthelm, K. Joder, D. Meyer and T. Kiefhaber, *Chem. Phys.*, 2004, **307**, 209–215.

16 H. Lami, G. Pfeffer and G. Laustria, *J. Phys. (Paris)*, 1966, **27**, 398–404.
17 H. Satzger, S. Spörlein, C. Root, J. Wachtveitl, W. Zinth and P. Gilch, *Chem. Phys. Lett*., 2003, **372**, 216–223.
18 M. Seel, E. Wildermuth and W. Zinth, *Meas. Sci. Technol*., 1997, **8**, 449–452.
19 D. O'Connor and D. Phillips, *Time Correlated Single Photon Counting*, Academic Press, London, 1984.
20 I. Berlman, *Handbook of Fluorescence Spectra of Aromatic Molecules*, 2nd edn, Academic Press, New York, 1971.
21 S. Strickler and R. Berg, *J. Chem. Phys*., 1962, **37**, 814–822.
22 C. Ley, F. Morlet-Savary, J. P. Fouassier and P. Jacques, *J. Photochem. Photobiol. A*, 2000, **137**, 87–92.
23 N. Mohtat, F. Cozens and J. Scaiano, *J. Phys. Chem. B*, 1998, **102**, 7557–7562.
24 S. L. Murov, I. Carmichael and G. L. Hug, *Handbook of Photochemistry*, Marcel Dekker Inc, New York, 1993.
25 Y. Ohshima, T. Fujii, T. Fujita, D. Inaba and M. Baba, *J. Phys. Chem. A*, 2003, **107**, 8851–8855.
26 C. Ley, F. Morlet-Savary, P. Jacques and J. P. Fouassier, *Chem. Phys*., 2000, **255**, 335–346.
27 M. Mitsui, Y. Ohshima and O. Kajimoto, *J. Phys. Chem. A*, 2000, **104**, 8660–8670.
28 S. Fukuzumi, N. Satoh, T. Okamoto, K. Yasui, T. Suenobu, Y. Seko, M. Fujitsuka and O. Ito, *J. Am. Chem. Soc*., 2001, **123**, 7756–7766.
29 H. Murai, M. Minami and Y. Ihaya, *J. Phys. Chem*., 1988, **92**, 2120–2124.
30 D. Astruc, *Triplet State ODMR Spectroscopy*, John Wiley & Sons, New York, 1982.
31 F. Morlet-Savary, C. Ley, P. Jacques, F. Wieder and J. P. Fouassier, *J. Photochem. Photobiol. A*, 1999, **126**, 7–14.
32 M. L. Horng, J. A. Gardecki, A. Papazyan and M. Maroncelli, *J. Phys. Chem*., 1995, **99**, 17311–17337.
33 D. DeVault, *Quantum-mechanical tunnelling in biological systems*, Cambridge University Press, Cambridge, 1984.
34 R. A. Marcus, *J. Phys. Chem*., 1989, **93**, 3078–3086.

Loop formation in unfolded polypeptide chains on the picoseconds to microseconds time scale

Beat Fierz[†], Helmut Satzger[‡§], Christopher Root[‡], Peter Gilch[‡], Wolfgang Zinth[‡], and Thomas Kiefhaber[†¶]

[†]Division of Biophysical Chemistry, Biozentrum der Universität Basel, Klingelbergstrasse 70, CH-4056 Basel, Switzerland; and [‡]Lehrstuhl für BioMolekulare Optik, Department für Physik, Ludwig-Maximilians-Universität, Oettingerstrasse 67, D-80538 Munich, Germany

Communicated by Wolfgang Kaiser, Technical University of Munich, Garching, Germany, December 13, 2006 (received for review October 3, 2006)

Intrachain loop formation allows unfolded polypeptide chains to search for favorable interactions during protein folding. We applied triplet–triplet energy transfer between a xanthone moiety and naphthylalanine to directly measure loop formation in various unfolded polypeptide chains with loop regions consisting of polyserine, poly(glycine–serine) or polyproline. By combination of femtosecond and nanosecond laserflash experiments loop formation could be studied over many orders of magnitude in time from picoseconds to microseconds. The results reveal processes on different time scales indicating motions on different hierarchical levels of the free energy surface. A minor (<15%) very fast reaction with a time constant of ≈3 ps indicates equilibrium conformations with donor and acceptor in contact at the time of the laserflash. Complex kinetics of loop formation were observed on the 50- to 500-ps time scale, which indicate motions within a local well on the energy landscape. Conformations within this well can form loops by undergoing local motions without having to cross major barriers. Exponential kinetics observed on the 10- to 100-ns time scale are caused by diffusional processes involving large-scale motions that allow the polypeptide chain to explore the complete conformational space. These results indicate that the free energy landscape for unfolded polypeptide chains and native proteins have similar properties. The presence of local energy minima reduces the conformational space and accelerates the conformational search for energetically favorable local intrachain contacts.

conformational substates | femtoseconds spectroscopy | peptide dynamics | protein folding | triplet–triplet energy transfer

Understanding the protein folding process requires the characterization of the structure and dynamics of all states along the reaction coordinate and the transition states separating them. Properties of native proteins have been extensively characterized by x-ray crystallography and NMR spectroscopy. Detailed structural information on partially folded states has been obtained by hydrogen exchange and NMR techniques. The properties of unfolded proteins are much less understood, although a detailed characterization of the structure and dynamics of the unfolded state is essential for a better understanding of the early steps in protein folding and the free energy landscape of the folding reaction. A major problem in the characterization of unfolded proteins is the nonphysiological solvent conditions that are required to populate the unfolded state in equilibrium. NMR studies (1–9) and the analysis of the effect of mutations on the solvent accessibility of the unfolded state (10) have revealed the presence of both native and non-native interactions in unfolded states of several proteins. In addition, steric constraints and intramolecular hydrogen bonding were suggested to promote the folding reaction by restricting the conformational space of unfolded polypeptide chains (11, 12). Recently, the dynamics of the unfolded state have become accessible to experimental investigations using NMR spectroscopy and electron transfer reactions (13–15).

Intrachain loop formation between protein side chains is a particularly important process in unfolded proteins because it allows a folding polypeptide chain to search for energetically favorable interactions. Fast electron transfer reactions have recently been applied to investigate the kinetics of intrachain loop formation in polypeptide chains (13, 15–17). We have used triplet–triplet energy transfer (TTET) between a xanthone (Xan) donor moiety and a naphthylalanine (NAla) acceptor to measure loop formation in a variety of polypeptide chains (13, 15, 16, 18–20). TTET is a two-electron exchange reaction (Dexter mechanism) operating only between molecules in close contact and is thus fundamentally different from FRET, which is based on dipole–dipole interactions extending to the nanometer range. The photophysical reactions involved in TTET from Xan to Nala occur on the time scale of a few picoseconds (21, 22) and have a strong distance dependence with a reactive boundary of 4.4 Å (23). These properties allow the use of TTET to measure absolute rate constants for loop formation reactions slower than ≈5 ps (see Fig. 1) (15, 21). Applying TTET to study loop formation between the ends of unfolded polypeptide chains with repetitive sequences and in fragments derived from natural proteins revealed exponential kinetics with time constants on the 5-to 100-ns time scale depending on loop length and amino acid sequence (13, 15–17). The observed single exponential kinetics indicate fast interconversion processes between individual conformations of the polypeptide chains (24). All previous experiments on loop formation were restricted to the nanosecond time scale because of the experimental systems or setups applied (15). These experiments could, however, not rule out faster processes, which may occur in the experimental dead time. Because TTET from Xan to Nala allows the measurement of subnanosecond processes (Fig. 1) (21, 22) we combined femtosecond and nanosecond laserflash experiments to study loop formation reactions in several polypeptide chains with loop regions consisting of polyserine, poly(glycine–serine), or polyproline. This combination of experiments allowed us to monitor loop formation processes over six orders of magnitude in time from picoseconds to microseconds.

Results and Discussion

Nanosecond and Subnanosecond Intramolecular Contact Formation. TTET between Xan and Nala can be monitored either by the decrease in the Xan triplet absorbance band centered at 590 nm or the increase in the Nala triplet absorbance at ≈420 nm (16). Typically the reaction is monitored at 590 nm because of the stronger Xan triplet absorbance band. Our previously performed nanoseconds laserflash TTET experiments had a dead time of ≈12 ns, which allowed us to measure nanosecond to microsecond loop formation dynamics in peptides of different length and sequence (16). To test for the existence of faster loop formation processes on the subnanosecond time scale, we recorded the donor triplet

Author contributions: W.Z. and T.K. designed research; B.F., H.S., and C.R. performed research; B.F. and P.G. contributed new reagents/analytic tools; B.F., H.S., C.R., W.Z., and T.K. analyzed data; and B.F., W.Z., and T.K. wrote the paper.

The authors declare no conflict of interest.

Freely available online through the PNAS open access option.

Abbreviations: TTET, triplet–triplet energy transfer; Xan, xanthone; Nala, naphthylalanine.

[§]Present address: Steacie Institute for Molecular Sciences, National Council of Canada, 100 Sussex Drive, Ottawa, ON, Canada K1A OR6.

[¶]To whom correspondence should be addressed. E-mail: t.kiefhaber@unibas.ch.

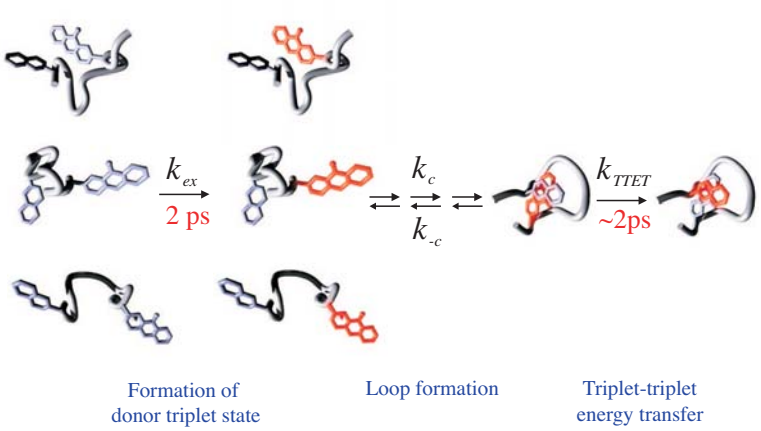

Fig. 1. Schematic representation of intramolecular triplet–triplet energy transfer between Xan and Nala used to monitor loop formation in unfolded polypeptide chains (15, 21, 22). The red labels indicate groups that are in the triplet state.

absorbance change at 590 nm in peptides containing donor and acceptor groups separated by polypeptide chains of different length and sequence. The observed kinetics of absorbance decay on the nanosecond to microsecond time scale were analyzed and the amplitudes of the decay were compared with the respective amplitudes measured in donor-only reference peptides (Fig. 2). In these peptides Nala was replaced by phenylalanine, which cannot undergo TTET with Xan (18). Fig. 2 shows that all chains containing Xan and naphthalene exhibit smaller amplitudes for the kinetics of the Xan triplet decay compared with the donor-only reference peptides. The effect is more pronounced for the *Xan*–Ser_2–*NAla* and *Xan*–Ser_6–*NAla* loops compared with the long and flexible *Xan*–$(Gly\text{-}Ser)_{12}$–*NAla* loop (Fig. 2). When donor and acceptor are separated by five proline residues, which should result in a stiff and rod-like structure, only very little Xan triplet decay occurs within the dead time. These results reveal that subnanosecond dynamics of loop formation occur in all investigated polypeptide chains and that the extent of these fast reactions depends on loop size and amino acid sequence.

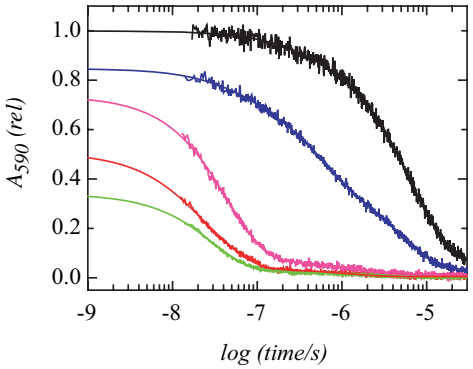

Fig. 2. Kinetics of loop formation in different peptides measured by TTET from Xan to Nala induced by a 4-ns laserflash. The kinetics were monitored by the change in Xan triplet absorbance at 590 nm. Kinetics of a *Xan*-Ser_2-*NAla* loop (red line), a *Xan*–Ser_6–*NAla* loop (green line), a *Xan*–$(Gly\text{-}Ser)_{12}$–*NAla* loop (magenta line), and a *Xan*–Pro_5–*NAla* loop (blue line) are shown. For comparison, the triplet decay in a donor-only reference peptide (black line) with NAla replaced by Phe is displayed (for peptide sequences see Table 1). In the donor-only peptides the Xan triplet state decays by oxygen quenching and intersystem crossing pathways, which occurs on the 20- to 50-μs time scale. Data were corrected for small differences in peptide concentration and normalized to the absorbance of the reference peptide. The solid lines are exponential fits to the data with the time constants given in Table 1.

Femtosecond-Laserflash TTET Experiments. To resolve the dynamics of the processes occurring within the dead time of the nanosecond experiments we induced TTET by a 100-fs laserflash. Formation of the Xan triplet state ($\pi\pi^* \rightarrow {}^3n\pi^*$ transition) and TTET from Xan to Nala were shown to have time constants ≈2 ps (21, 22). The photophysics of Xan involves an additional relaxation process from the initially formed ${}^3n\pi^*$ state to the ${}^3\pi\pi^*$ state, which has a time constant of ≈300 ps in water (22). However, the originally formed ${}^3n\pi^*$ state can already undergo TTET with Nala (21). This fact allows the observation of loop formation reactions with time constants lower than ≈5 ps (see Fig. 1). To discriminate processes caused by TTET from photophysical reactions in the Xan donor group we compared changes in the Xan triplet absorbance band at ≈590 nm in peptides bearing donor and acceptor to the changes in a donor-only reference peptide. Fig. 3 shows time-resolved Xan triplet absorbance spectra for the *Xan*–Ser_2–*NAla* peptide (Fig. 3*A*) and the donor-only reference peptide (Fig. 3*B*). The sum of four exponentials is required to fit the data. Analysis of the amplitude spectra (Fig. 3 *C* and *D*) reveals the spectral changes associated with the individual kinetic phases. In these plots the amplitude changes associated with a kinetic process are shown at different wavelengths. Negative values indicate an increase in absorbance, whereas positive values indicate a decrease in absorbance. In both peptides formation of the relaxed singlet state ($\pi\pi^*$) occurs with a time constant ≈0.3 ps. Subsequently, a high energy triplet state (${}^3n\pi^*$) is formed on the 2- to 3-ps time scale as seen from the blue shift of the absorbance spectrum associated with an increase in absorbance. The ${}^3n\pi^*$ state is in equilibrium with the relaxed singlet state, which leads to delayed fluorescence processes (21, 22). In the donor-only reference peptide a significant increase in triplet absorbance in combination with a blue shift of the absorbance maximum is observed with a time constant of 280 ps (Fig. 3 *B* and *D*). As discussed in more detail in refs. 21 and 22, this process is caused by the ${}^3n\pi^* \rightarrow {}^3\pi\pi^*$ transition in Xan and shows an isosbestic point ≈630 nm. The *Xan*–Ser_2–*NAla* peptide shows a similar blue shift in the Xan triplet absorbance band with a time constant of 320 ps. In contrast to the donor-only peptide, this process is associated with only very little change in

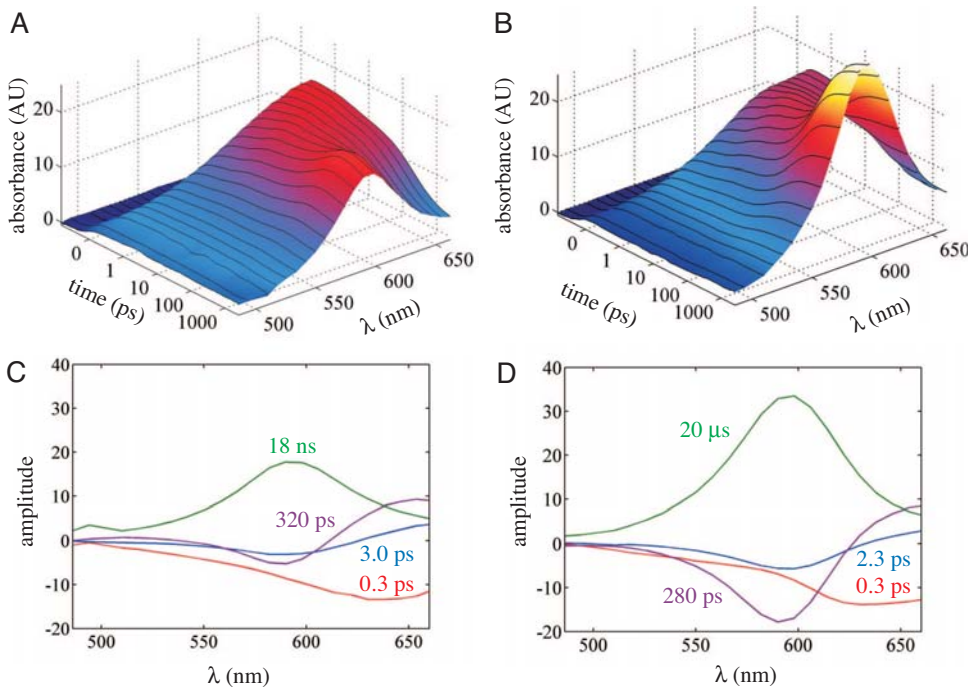

Fig. 3. TTET experiments induced by a 200-fs laser flash. (*A*) Kinetics of formation of the *Xan*–Ser_2–*NAla* loop measured by TTET from Xan to Nala induced by an ultrashort laserflash (time resolution of the experiment, 200 fs). Spectral changes in the Xan triplet absorbance band are displayed on a split time base. The time range from −1 ps to 1 ps is shown on a linear time scale, and the time range from 1 ps to 4 ns is shown on a log time scale. The time of the laserflash is defined as $t = 0$. (*B*) Corresponding spectral changes in the Xan triplet absorbance band of the donor-only reference peptide. (*C* and *D*) Amplitude spectra obtained from a triple exponential fit of the data with the associated time constants as indicated. The slowest time constant for triplet decay in the *Xan*–Ser_2–*NAla* loop corresponds to the kinetics observed in nanosecond experiments (Fig. 2). In the reference peptide the amplitude spectrum for $\tau = 20$ μs was taken from the fit of the data shown in Fig. 2.

absorbance at 590 nm and shows an isosbestic point ≈600 nm (Fig. 3 *A* and *C*). Subsequently, a slow decrease in Xan triplet absorbance on the nanosecond time scale is observed in the *Xan*–Ser_2–*NAla* peptide in agreement with the nanosecond laserflash experiments (see Fig. 2). In the reference peptide no relaxation from the triplet state to the ground state is observed within the first 4 ns, because this process occurs on the 20- to 50-μs time scale (see Fig. 2). The time constant and the amplitude spectrum of this slow decay were determined in a nanosecond experiment and are indicated in Fig. 3*D*.

The time-dependent changes in the triplet absorbance bands reveal a major loss in the population of Xan triplet states on the time scale from 50 to 500 ps in the *Xan*–Ser_2–*NAla* peptide as compared with the donor-only peptide. This loss in Xan triplet states is associated with an increase in naphthalene triplet absorbance at 420 nm (data not shown), confirming that this effect is caused by TTET between Xan and naphthalene in a subpopulation of conformations. However, the time dependence of the absorbance changes at 420 nm cannot be analyzed quantitatively, because a $^1\pi\pi^*$ Xan fluorescence band (delayed fluorescence) and a second, weaker Xan triplet absorbance band are located in the same spectral region.

Loop Formation Dynamics from Picoseconds to Microseconds. The kinetics of TTET between Xan and Nala differ significantly from the photophysics in the donor-only reference peptide (Fig. 3). There are two possibilities to separate TTET reactions from photophysics in Xan to gain information on the dynamics of loop formation. One way is to monitor kinetics at the isosbestic point for the triplet relaxation at 630 nm. A second possibility is to normalize the time-dependent spectral changes at the Xan triplet absorbance maximum (590 nm) in the *Xan*–Ser_2–*NAla* peptide (Fig. 3*A*) against the changes in the donor-only reference peptide (Fig. 3*B*) according to

$$A_{590}(rel) = \frac{A_{590}^{D/A}}{A_{590}^{D}}, \qquad [1]$$

where A_{590}^{D} denotes the absorbance of the donor-only reference peptide at a given time and $A_{590}^{D/A}$ the respective absorbance of the peptide-bearing donor and acceptor. Both procedures yield identical results. However, because of the stronger absorbance changes at 590 nm the normalization of the data according to Eq. **1** gave better signal-to-noise ratios compared with measurements at the isosbestic point at 630 nm. Thus, in the following we will present and discuss the time course of changes in $A_{590}(rel)$. To gain information on loop formation in the time range from picoseconds to microseconds, we combined the data from the femtosecond experiments with changes in $A_{590}(rel)$ measured in nanosecond investigations. Fig. 4 shows changes in $A_{590}(rel)$ from 1 ps to 30 μs. Several subnanosecond processes can be distinguished. For *Xan*–Ser_2–*NAla* ≈12% of the Xan triplet states decay very fast with a time constant of ≈3 ps, indicating a process that is limited by the photophysics of the system. This rapid decay may either be caused by loop formation reactions on the low picosecond or subpicosecond time scale or, more likely, indicates that ≈12% of the peptide conformations have donor and acceptor in contact when Xan is excited by the laserflash. Additional processes occur on the 50- to 500-ps time scale (Fig. 4),

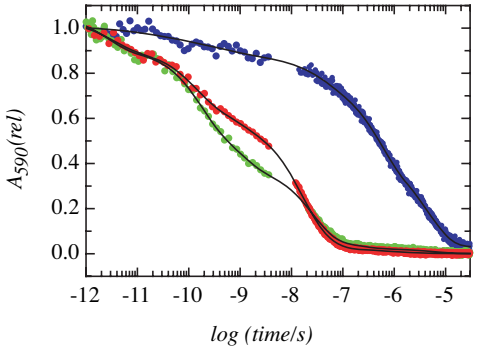

Fig. 4. Kinetics of loop formation on the time scale from 1 ps to 30 μs measured in TTET experiments and monitored by changes in Xan triplet absorbance at 590 nm. The kinetics of a *Xan*–Ser_2–*NAla* loop (red dots), a *Xan*–Ser_6–*NAla* loop (green dots), and a *Xan*–Pro_5–*NAla* loop (blue dots) are shown. The kinetic traces were obtained from a combination of data measured in femtosecond and nanosecond laserflash experiments (Figs. 2 and 3). $A_{590}(rel)$ was determined for each peptide according to Eq. **1** to correct for effects from photophysics in Xan (Fig. 3*B*) and the different peptide concentrations required in nanosecond and femtosecond experiments. The lines represent the results of fits to the data to the sum of a stretched exponential function (see Eq. **2**) and exponential functions with the parameters given in Table 1.

which can either be fitted by the sum of several exponentials or with a stretched exponential function (Kohlrausch–William–Watts function) according to

$$A(t) = A_0 \cdot e^{-(k_{KWWt})^{\beta}}, \qquad [2]$$

where β indicates the stretching parameter and k_{KWW} denotes the apparent rate constant of this reaction. Accordingly after $1/k_{KWW} = \tau_{app}$ the signal has decreased to 37% (1/e) of the original signal (A_0). Because the $^3n\pi^* \rightarrow {}^3\pi\pi^*$ relaxation occurs with a time constant of 300 ps (Fig. 3), kinetic coupling between triplet relaxation and TTET processes occurs, which complicates the quantitative evaluation of the fast TTET kinetics. For a qualitative evaluation of the data and comparison of different loop sequences we used the τ_{app} values of this reaction obtained by fitting the data according to Eq. **2**. For the *Xan*–Ser_2–*NAla* loop a τ_{app} of 170 ps is observed and 32% of the total absorbance change occurs on this time scale. In the remaining molecules the triplet states decay on the nanosecond time scale as observed in nanosecond laserflash experiments (see Table 1) (16).

In an alternative analysis of the absorbance changes over the complete time range from picoseconds to microseconds (Fig. 4) we determined the distribution of time scales (25). The results indicate three separated time regimes on the low-picosecond, hundreds of picoseconds, and nanosecond time scale for TTET in the *Xan*–Ser_2–*NAla* peptide (data not shown), which confirms the findings obtained by fitting the data to a combination of exponential and stretched exponential functions.

Effect of Chain Length and Chain Stiffness on Subnanosecond Dynamics of Loop Formation. To further characterize the subnanosecond TTET reactions, we tested their sensitivity toward chain length and chain stiffness. Fig. 4 compares TTET kinetics in the *Xan*–Ser_2–*NAla* peptide with the kinetics in the *Xan*–Ser_6–*NAla* and the stiff *Xan*–Pro_5–*NAla* peptides. All peptides show TTET reactions on the picosecond time scale, but the kinetics depend on the loop size and sequence (see Table 1). Similar to the *Xan*–Ser_2–*NAla* peptide, the *Xan*–Ser_6–*NAla* peptide shows ≈15% of very rapid Xan triplet decay with a time constant of ≈3 ps. Subsequently, a process with τ_{app} = 260 ps is observed, which is on the same time scale as for the *Xan*–Ser_2–*NAla* peptide. The amplitude of this reaction is 48%, which is larger than in the *Xan*–Ser_2–*NAla* peptide, in agreement with the results from the dead-time absorbance changes observed in the nanosecond laserflash experiments (Fig. 2). The dynamics of nanosecond loop formation reactions are slightly slower for the *Xan*–Ser_6–*NAla* loop compared with the *Xan*–Ser_2–*NAla* loop. The *Xan*–Pro_5–*NAla* peptide, which is significantly stiffer than the polyserine loops, does not show any evidence for very rapid TTET within the first 10 ps. It shows, however, subnanosecond loop formation kinetics with τ_{app} = 210 ps and a largely reduced amplitude (13%) compared with the polyserine loops. The majority of *Xan*–Pro_5–*NAla* conformations form loops on the 10-ns to μs time scale in a complex multiexponential process.

Origin of Loop Formation Processes on the Different Time Scales. The combination of femtosecond and nanosecond TTET experiments shows that loop formation in a polypeptide chain occurs on different time scales. In both polyserine loops 10–15% of the molecules undergo very fast TTET limited by the ultrafast photophysics (intersystem crossing) of the system (Fig. 4). This finding suggests that a subpopulation of the ensemble of chain conformations have donor and acceptor in contact at the time point of the laserflash, which may be partly caused by the hydrophobic nature of the TTET labels. The absence of this reaction in the *Xan*–Pro_5–

Table 1. Time constants for loop formation obtained from the combination of femtosecond and nanosecond experiments

Loop	τ_1, ps	A_1, %	$\tau_2(app)$, ps*	A_2, %	β	τ_3, ns	A_3, %	τ_4, ns	A_4, %
Xan–Ser$_2$–NAla	3.3	12	170	32	0.72	12	40	37†	16
Xan–Ser_6–*NAla*	2.5	15	260	48	0.70	20	37		
Xan–$(Gly–Ser)_{12}$–*NAla*‡						45	72		
Xan–Pro_5–*NAla*	—	—	210	13	0.43	34–5,000§	87		

Note that ultrafast loop formation dynamics well below 1 ns are present. All investigated peptides contain the additional sequence Ser–Arg–Ser–Arg–Gly–$CONH_2$ C-terminal from the NAla group to increase solubility.

*The parameters $\tau_2(app) = 1/k_{KWW}$, β, and A_2 give results from a stretched exponential function (Eq. **2**) used to fit the kinetics on the 50- to 500-ps time scale.

†In previous nanosecond experiments on the kinetics of formation of a *Xan*–Ser_2–*NAla* loop we observed a single time constant of 12.5 ns (16), whereas a double exponential function is required for the fitting the present data from nanosecond experiments. This finding may be connected with the additional C-terminal amino acids required to increase solubility of the peptide for femtosecond experiments. It may, however, also be caused by the improved signal-to-noise ratio based on the higher solubility.

‡No femtosecond experiments were performed on the *Xan*–$(Gly–Ser)_{12}$–*NAla* loop.

§The kinetics of formation of the *Xan*–Pro_5–*NAla* loop on the nanosecond time scale are complex and require at least three exponentials with time constants in the indicated range. These complex kinetics are caused by heterogeneity caused by cis–trans equilibria at the prolyl peptide bonds (F. Krieger and T.K., unpublished work).

NAla peptide indicates only a negligible fraction of closed loop conformations in equilibrium in this peptide, in agreement with the increased stiffness of polyproline chains (26).

In all peptides investigated in this study loop formation reactions that are not limited by photophysics occur on two well separated time scales. For all peptides reactions with an apparent time constant on the 200-ps time scale are observed (see Table 1). For the *Xan*–Pro_5–*NAla* loop this process has a lower amplitude (13%) compared with the *Xan*–Ser_2–*NAla* loop (32%) and the *Xan*–Ser_6–*NAla* loop (48%). The time scale of these reactions is similar to the dynamics of local motions in the polypeptide backbone observed in a photoswitchable cyclic peptide (27, 28) and only slightly slower than expected for single-bond rotations in the polypeptide backbone in water. This observation suggests that a significant subpopulation of molecules can form loops by performing just a few bond rotations without having to explore the complete free energy landscape.

The remaining conformations in the ensemble of unfolded states show loop formation on the 10- to 100-ns time scale in all peptides. This reaction becomes slower with increasing loop length in agreement with our previous findings (16). The dynamics on the nanosecond time scale were shown to be caused by diffusional processes exploring the complete accessible free energy landscape for the polypeptide chains as shown by their length and sequence dependence, which are in agreement with predictions from polymer theory (24). These reactions are very slow and complex for the polyproline loop, which is caused by cis–trans equilibria at the five prolyl peptide bonds and leads to different populations of molecules that interconvert on the second to minute time scale. Thus, loop formation on the nanosecond time scale is observed for the individual populations giving rise to complex kinetics.

Hierarchy of Peptide Motions. The observed separation of time scales in the dynamics of loop formation indicates motions on different hierarchical levels (tiers) of the free energy landscape for a flexible polypeptide chain (Fig. 5). The dynamics on the nanosecond time scale represent chain diffusion exploring different local minima on the free energy landscape (13, 15, 16). Loop formation on the 50- to 500-ps time scale, in contrast, most likely represents motions within local wells on the free energy landscape that contain loop structures (Fig. 5). Thus, all conformations within such a well can form a loop by undergoing local motions and do not have to cross major barriers. The amplitude of this reaction is larger for the *Xan*–Ser_6–*NAla* loop compared with the *Xan*–Ser_2–*NAla* loop, in agreement with the properties of polyserine chains, which have a persistence length of ≈5 aa (29). Thus, the *Xan*–Ser_6–*NAla* peptide should be able to form a turn with less conformational strain as compared with the *Xan*–Ser_2–*NAla* peptide. As a consequence, the *Xan*–Ser_6–*NAla* peptide has a higher equilibrium population of conformations with close donor–acceptor distances. This model is confirmed by the results of the *Xan*–Pro_5–*NAla* peptide, which shows largely increased chain stiffness and only a small fraction of conformations that can form a loop on the subnanosecond time scale. Another aspect is highlighted by the *Xan*–$(Gly–Ser)_{12}$–*NAla* peptide. Here, the smaller amplitude of the subnanosecond reactions compared with the serine loops (Fig. 2 and Table 1) shows that a further increase in chain length leads to a smaller population of conformations that can form loops on the subnanosecond time scale, despite the larger flexibility of poly Gly-Ser.

The observed organization of peptide motions in different hierarchical levels suggests that the free energy landscapes of unfolded polypeptide chains and folded proteins (30–36) have similar features. For native myoglobin the highest tier contains several taxonomic substates separated by significant energy barriers. Transitions between these substates require major structural rearrangements and are important for protein function (37, 38). Each taxonomic substate contains a large number of statistical substates. Transitions between statistical substates correspond to local rearrangements of the polypeptide chain and are much faster than transitions between taxonomic substates. Within the statistical substates further tiers with decreasing barrier height can be discriminated (36). Our results show that this concept does not only apply to folded proteins but also to the ensemble of unfolded peptide conformations (Fig. 5). Obviously, the functionally important and structurally well defined taxonomic substates are absent in flexible chains. However, the free energy landscape includes a number of local wells that are separated from each other by significant free energy barriers. At room temperature interconversion between substates from different wells is fast compared with the time scale of loop formation, which leads to the observed exponential dynamics on the nanosecond time scale (24). The observed rate constants for these reactions depend on chain stiffness and chain length, i.e., on the size of the available conformational space (19). The barriers separating the different wells may be caused by breakage of intramolecular hydrogen bonds, which were shown to exist in unfolded model polypeptide chains in water (23). Conformational space within a well can be explored without encountering major barriers, which leads to loop formation on the 50- to 500-ps time scale. These rate constants only weakly depend on chain length and amino acid sequence but the population of conformations within the different substates is strongly affected by chain length and chain stiffness.

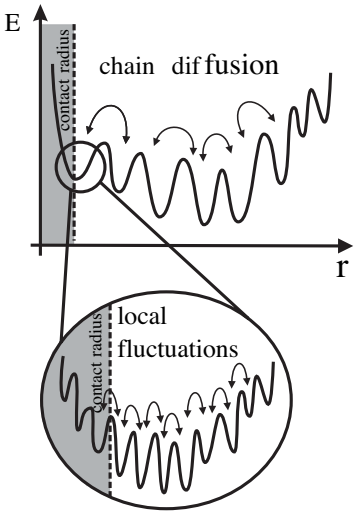

Fig. 5. Schematic representation of the hierarchical organization of the energy landscape for unfolded polypeptide chains. The highest tier of conformational substates contains different wells on the free energy landscape separated by energy barriers. Chain diffusion over the complete free energy surface is governed by transitions between these wells and includes major structural rearrangements of the polypeptide chain. Within each well a number of substates exist. Interconversion between these substates occurs by local structural changes. Motions on the highest tier lead to loop formation on the nanosecond time scale, whereas fluctuations within the local wells are much faster and result in loop formation on the 50- to 500-ps time scale. The dashed line indicates conformations with donor–acceptor in contact, which undergo TTET limited by the photophysical processes.

The observation of complex free energy landscapes for unfolded polypeptide chains is supported by recent results from experiments using a combination of FRET and electron transfer reactions. Results on different donor/acceptor positions in α-synuclein, a natively unfolded protein, indicated complex pairwise distance distribution functions containing several maxima and minima (39).

Implications for Protein Folding. The observed kinetics on different time scales show that loop formation in polypeptide chains is a

hierarchical process and that the free energy landscape of an unfolded polypeptide chain is complex and contains local minima. This hierarchical organization may play a major role for the protein folding process by allowing a fraction of molecules to form loop structures very rapidly, on the 50- to 500-ps time scale, and producing a significant fraction of loop conformations within the ensemble of unfolded conformations. This large fraction of loop conformations might serve as initiation sites for the folding reaction. The frequently observed hydrophobic zipper motif in β-hairpins (40), where the interacting side chains have similar hydrophobicity as the TTET labels of our model loops, should lead to similar fractions of loop conformations in equilibrium. In addition to the effects on the equilibrium properties of the unfolded state, the presence of a number of local minima accelerates conformational search and barrier crossing during the folding process by reducing the entropic contributions to the free energy barriers (41).

It is unlikely that the fast loop formation reactions on the 50- to 500-ps time scale are strongly influenced by the nature of the side chains, because van der Waals interactions are short-range interactions and operate on similar distances as TTET. Fast loop formation rather reflects reactions that only require a few bond rotations or breakage of just a few hydrogen bonds to form a loop without the necessity for major rearrangements of the intramolecular hydrogen-bonding network. The dynamics of loop formation on different time scales should lead to kinetic heterogeneity in very fast folding processes like formation of α-helices and β-hairpins or acquisition of the 3D structure for fast folding proteins. Our results may explain the findings from temperature jump studies on λ-repressor, which was shown to fold in complex kinetics on the low microsecond time scale that could be described by either a double exponential or a stretched exponential function (42).

Materials and Methods

Peptide Synthesis. Peptides and 9-oxoxanthen-2-carboxylic acid (Xan acid) were synthesized as described (16). Purity and mass were tested by analytical HPLC and mass spectrometry, respectively. For all measurements peptides were dissolved in 10 mM phosphate buffer, pH 7 or pure H_2O at 22.5°C.

Laserflash Experiments. The setup of the nanosecond laserflash experiments has been described (16). A Nd:YAG pulsed laser (354.6 nm, 4-ns pulse of 50 mJ; Quantel, Santa Clara, CA) was used to excite the samples, a Laser Flash Photolysis Reaction Analyzer (LKS.60; Applied Photophysics, Leatherhead, U.K.) was used to collect the absorption data. Peptide concentrations in the nanosecond experiments were ≈50 μM. Concentrations were determined by UV spectroscopy using Xan absorption at 343 nm (ε = 3,900 $cm^{-1}\cdot M^{-1}$).

The setup of the femtosecond pump probe experiments has been described (43). A 1-kHz Ti:Sa laser/amplifier system was used as a light source. Pump pulses at 340 nm were generated by frequency doubling the output of a noncollinear optical parametic amplifier (44, 45). White light generation supplied the broadband probing pulses. The pertinent parameters for the pump probe experiment were the following: The pump light had an energy of 350 nJ per pulse and a diameter of ≈150 μm at the sample location. Its polarization plane was at magic angle with respect to the white light probe [experimental response time was ≈200 fs (FWHM)]. Multichannel probing recorded the absorption changes from 400 to 700 nm. The sample was exchanged between consecutive laser shots by a peristaltic pump. The fused silica sample cell had a path length of 0.5 mm. The concentrations in femtosecond experiments were ≈2 mM.

Test for Intermolecular Reactions. To test for intermolecular TTET as the origin for the difference in kinetics between the *Xan*–Ser_2–*NAla* peptide and the donor-only peptide we measured a 1:1 mixture of a donor-only and an acceptor-only peptide at the same concentrations as in the TTET experiments. In this control experiment the Xan triplet decay was identical to the kinetics in the donor-only peptide, ruling out intermolecular TTET in associated or aggregated peptides on the picosecond time scale.

Data Analysis. Data were analyzed by using MATLAB (Mathworks, Natick, MA) and proFit (QuantumSoft, Uetikon am See, Switzerland).

We thank Hans Frauenfelder for discussion and comments on the manuscript. This work was supported by a grant from the Volkswagen Stiftung (to B.F.).

1. Evans PA, Topping KD, Woolfson DN, Dobson CM (1991) *Proteins* 9:248–266.
2. Neri D, Billeter M, Wider G, Wuthrich K (1992) *Science* 257:1559–1563.
3. Logan TM, Theriault Y, Fesik SW (1994) *J Mol Biol* 236:637–648.
4. Wong KB, Clarke J, Bond CJ, Neira JL, Freund SM, Fersht AR, Daggett V (2000) *J Mol Biol* 296:1257–1282.
5. Kazmirski SL, Wong KB, Freund SM, Tan YJ, Fersht AR, Daggett V (2001) *Proc Natl Acad Sci USA* 98:4349–4354.
6. Garcia P, Serrano L, Durand D, Rico M, Bruix M (2001) *Protein Sci* 10:1100–1112.
7. Sari N, Alexander P, Bryan PN, Orban J (2000) *Biochemistry* 39:965–977.
8. Yi Q, Scalley-Kim ML, Alm EJ, Baker D (2000) *J Mol Biol* 299:1341–1351.
9. Kortemme T, Kelly MJ, Kay LE, Forman-Kay JD, Serrano L (2000) *J Mol Biol* 297:1217–1229.
10. Sánchez IE, Kiefhaber T (2003) *J Mol Biol* 327:867–884.
11. Fitzkee NC, Rose GD (2004) *Proc Natl Acad Sci USA* 101:12497–12502.
12. Fleming PJ, Rose GD (2005) in *Protein Folding Handbook*, eds Buchner J, Kiefhaber T (Wiley, Weinheim, Germany), Vol 2, pp 710–736.
13. Bieri O, Wirz J, Hellrung B, Schutkowski M, Drewello M, Kiefhaber T (1999) *Proc Natl Acad Sci USA* 96:9597–9601.
14. Klein-Seetharaman J, Oikawa M, Grimshaw SB, Wirmer J, Duchardt E, Ueda T, Imoto T, Smith LJ, Dobson CM, Schwalbe H (2002) *Science* 295:1719–1722.
15. Fierz B, Kiefhaber T (2005) in *Protein Folding Handbook*, eds Buchner J, Kiefhaber T (Wiley, Weinheim, Germany), pp 805–851.
16. Krieger F, Fierz B, Bieri O, Drewello M, Kiefhaber T (2003) *J Mol Biol* 332:265–274.
17. Chang I-J, Lee JC, Winkler JR, Gray HB (2003) *Proc Natl Acad Sci USA* 100:3838–3840.
18. Krieger F, Fierz B, Axthelm F, Joder K, Meyer D, Kiefhaber T (2004) *Chem Phys* 307:209–215.
19. Krieger F, Möglich A, Kiefhaber T (2005) *J Am Chem Soc* 127:3346–3352.
20. Möglich A, Krieger F, Kiefhaber T (2005) *J Mol Biol* 345:153–162.
21. Satzger H, Schmidt B, Root C, Zinth W, Fierz B, Krieger F, Kiefhaber T, Gilch P (2004) *J Phys Chem A* 108:10072–10079.
22. Heinz B, Schmidt B, Root C, Satzger H, Milota F, Fierz B, Kiefhaber T, Zinth W, Gilch P (2006) *Phys Chem Chem Phys* 8:3432–3439.
23. Möglich A, Joder K, Kiefhaber T (2006) *Proc Natl Acad Sci USA* 103:12394–12399.
24. Szabo A, Schulten K, Schulten Z (1980) *J Chem Phys* 72:4350–4357.
25. Provencher SW (1982) *Comput Phys Commun* 27:213–227.
26. Schimmel PR, Flory PJ (1967) *Proc Natl Acad Sci USA* 58:52–59.
27. Spörlein S, Carstens H, Satzger H, Renner C, Behrendt R, Moroder L, Tavan P, Zinth W, Wachtveitl J (2002) *Proc Natl Acad Sci USA* 99:7998–8002.
28. Bredenbeck J, Helbing J, Sieg A, Schrader T, Zinth W, Renner C, Behrendt R, Moroder L, Wachtveitl J, Hamm P (2003) *Proc Natl Acad Sci USA* 100:6452–6457.
29. Miller WG, Brant DA, Flory PJ (1967) *J Mol Biol* 23:67–80.
30. Beece D, Eisenstein L, Frauenfelder H, Good D, Marden MC, Reinisch L, Reynolds AH, Sorensen LB, Yue KT (1980) *Biochemistry* 19:5147–5157.
31. Ansari A, Berendzen J, Bowne SF, Frauenfelder H, Iben IE, Sauke TB, Shyamsunder E, Young RD (1985) *Proc Natl Acad Sci USA* 82:5000–5004.
32. Frauenfelder H, Petsko GA, Tsernoglou D (1979) *Nature* 280:558–563.
33. Frauenfelder H, Sligar SG, Wolynes PG (1991) *Science* 254:1598–1603.
34. Austin RH, Beeson KW, Eisenstein L, Frauenfelder H, Gunsalus IC (1975) *Biochemistry* 14:5355–5373.
35. Fenimore PW, Frauenfelder H, McMahon BH, Parak FG (2002) *Proc Natl Acad Sci USA* 99:16047–16051.
36. Fenimore PW, Frauenfelder H, McMahon BH, Young RD (2004) *Proc Natl Acad Sci USA* 101:14408–14413.
37. Frauenfelder H, McMahon BH, Austin RH, Chu K, Groves JT (2001) *Proc Natl Acad Sci USA* 98:2370–2374.
38. Eisenmesser EZ, Millet O, Labeikovsky W, Korzhnev DM, Wolf-Watz M, Bosco DA, Skalicky JJ, Kay LE, Kern D (2005) *Nature* 438:117–121.
39. Lee JC, Gray HB, Winkler JR (2005) *J Am Chem Soc* 127:16388–16389.
40. Hazes B, Hol WGJ (1992) *Proteins Struct Funct Genet* 12:278–298.
41. Wagner C, Kiefhaber T (1999) *Proc Natl Acad Sci USA* 96:6716–6721.
42. Yang WY, Gruebele M (2003) *Nature* 423:193–197.
43. Satzger H, Spörlein S, Root C, Wachtveitl J, Zinth W, Gilch P (2003) *Chem Phys Lett* 372:216–223.
44. Wilhelm T, Piel J, Riedle E (1997) *Opt Lett* 22:1494–1496.
45. Riedle E, Beutter M, Lochbrunner S, Piel J, Schenkl S, Spörlein S, Zinth W (2000) *Appl Phys B* 71:457–465.

Non-exponential Kinetics of Intrachain Contact Formation in Unstructured Peptides at Low Temperature

Beat Fierz and Thomas Kiefhaber
Biozentrum der Universität Basel
Division of Biophysical Chemistry,
Klingelbergstr. 70
CH-4056 Basel
Switzerland

*corresponding author. Phone: ++41-61-267 2194; fax: ++41-61-267 2189; e-mail: t.kiefhaber@unibas.ch

Abstract

Intrachain loop formation is an elementary process in protein folding. We used diffusion-controlled triplet triplet energy transfer (TTET) from xanthone to naphthylanine to study the kinetics of loop formation in unfolded polypeptide chains. Previous experiments on loops of different length and amino acid sequence had revealed kinetics on different time scales at room temperature. Rapid kinetics on the 100's of ps time scale indicated motions within a local minimum on the energy landscape. Exponential kinetics with time constants on the 10 to 100 nanosecond time scale resulted from diffusional processes over the complete free energy landscape. The observed exponential kinetics indicated rapid equilibration between different unfolded conformations. To learn more about the properties of the free energy landscape governing polypeptide dynamics we investigated whether slowing-down conformations affects the kinetics of loop formation. We studied TTET between xanthone and naphthylalanine in two unfolded model peptides of the sequence Xan-(Gly-Ser)$_n$-NAla (n=1 and 12) at low temperature (298-208 K) and high viscosity. Above 240 K exponential kinetics are observed in both peptides. At lower temperature the kinetics become complex and can be described by an initial exponential decay followed by a slower process that exhibits stretched kinetics. The rate constants of the initial decay agree well with the expected value for motions within a local minimum. The slower stretched decay represents large scale diffusional processes that have become non-exonential due to increased relative barrier heights separating individual conformational substates. In the long peptide, the observed average rate constants from the stretched decay follow the dielectric relaxation of the solvent, indicating a solvent activated process. In the short peptide a decoupling of contact formation from solvent dynamics is observed due to barrier controlled dynamics. The same complex kinetics can be induced by increasing solvent viscosity at 253 K. These results indicate the presence of local minima on the free energy landscape of unfolded polypeptide chains that are separated by significant barriers.

Introduction

To understand the mechanism of protein folding the structure and dynamics of the denatured state have to be characterized. During the transition from a disordered and dynamic ensemble of unfolded conformations to a highly structured native state, interactions are formed between amino acids. These contact formation processes are viewed as the elementary steps of protein folding and set an upper limit to the rate at which the protein can explore its conformational space.

Fast electron transfer processes between groups in the polypeptide chain have been applied to observe loop closure reactions in proteins or unfolded peptides (1-4). We used the method of triplet triplet energy transfer (TTET) from xanthone to naphthalene to study the kinetics of loop formation in model peptides and fragments derived from proteins (1; 2; 4). This reaction can be monitored by following the decay of xanthone triplet absorption or the concomitant increase of naphthalene triplets. An overview of the experiment is shown in fig 1. Single exponential kinetics were observed for all unstructured peptides yielding time constants for contact formation in the 10 – 100 ns timescale. In *poly-(Gly-Ser)* chains the contact formation rate constant has been found to scale with the number of amino acids *N* between the labels with $k_c = N^{-1.7\pm0.08}$ for sufficiently long chains *(N > 20)* consistent with theoretical scaling laws for excluded volume chains (5). These rate constants, however, level off when the chains get shorter *(N < 10)* and approach an asymptotic limit at $1.8 \cdot 10^8 s^{-1}$. This effect is due to different processes that limit chain motion over short and long distances. For short loops, chain motion is dominated by chain stiffness whereas the chain exhibits diffusional behavior over long distances.

The picosecond time resolution of TTET (6; 7) enabled us to probe for dynamics on the sub-nanosecond timescale. An initial fast reaction on the 100's of picoseconds

timescale has been detected in short unstructured peptides (8) at room temperature, which can be interpreted as the fast depletion of species within the same local minimum on the free energy surface. Within this conformational substate, contact can be established without the crossing of any major barriers. The remaining peptide population has to cross several small barriers while sampling the whole accessible free energy surface to establish contact. At room temperature equilibration is fast and exponential kinetics in the nanosecond time scale are observed. Conformational substates have been observed in proteins (9-15) leading to non-exponential kinetics for conformational transitions at low temperature (13) when equilibration is slow because of high barriers compared to the available thermal energy.

The picosecond dynamics for loop closure in peptides suggest the existence of conformational substates for peptide dynamics. Non-exponential kinetics for solvent activated chain motions at low temperature would indicate a complex free energy landscape. Thus, we study the kinetics of loop formation by TTET in peptides at conditions where barrier crossing is slow by decreasing the thermal energy and increasing the viscosity of the solvent.

Results and Discussion

Complex kinetics at of Loop Formation at Low Temperature

We used two different peptide systems to study loop formation at low temperature. The *(Gly-Ser)*$_{12}$ peptide was used as a model for long and flexible chains. In this peptide end-to-end loop formation is limited by diffusive motions. A very short peptide with only one *(Ser-Gly)* unit between the labels served as a model for close contacts (e.g. in β-hairpins). This peptide was used to probe local kinetics in a system that is dominated by chain stiffness. The general structure of the peptides is shown in fig. 2.

At room temperature both peptides exhibit exponential kinetics on the nanosecond timescale (2). At 0° C, the kinetics are still exponential and higher viscosity the kinetics are still exponential (see Fig. 3). However, at lower temperature the kinetics of loop formation become increasingly complex. Figure 3 shows a direct comparison between two kinetic traces of *(Gly-Ser)$_{12}$* loop formation at 273 K and at 237 K in a 60% glycerol/water mixture. At 273 K the kinetics of loop closure in *(Gly-Ser)$_{12}$* are single exponential with a rate constant of $k_c = 8.2 \cdot 10^5$ s^{-1}. At 237 K the loop formation reaction is much slower and the kinetics are complex. A fast initial decay is followed by a slower process that is non-exponential in nature. A superposition of several exponential functions can describe the data within experimental error at 237 K. Alternatively, the kinetic traces can be fitted to a superposition of a fast exponential decay and a slow stretched exponential contribution (solid line in fig. 3).

$$y = A_{\exp} \cdot \exp\left(-k_{\exp} \cdot t\right) + A_{KWW} \cdot \exp\left(-\left[k_{KWW} \cdot t\right]^{\beta_{KWW}}\right) \qquad [1]$$

where *kexp* and *Aexp* characterize the rate and amplitude of the fast exponential decay, k_{KWW} and A_{KWW} denote the rate and amplitude of the stretched exponential contribution and β_{KWW} is the stretching parameter. The fit to the kinetic trace at 237 K in fig. 3 yields a value for $k_{exp} = 1.4 \cdot 10^6$ s^{-1} and $k_{KWW} = 1.5 \cdot 10^4$ s^{-1} with a stretching parameter of $\beta_{KWW} = 0.65$.

The stretched exponential function is often called Kohlrausch-William-Watts function (KWW) and has been used earlier to analyze segmental relaxation in polymers.(16-19) Several models can explain the appearance of Kohlrausch relaxation. The underlying process can be intrinsically non-exponential for all particles in the

system, the "homogenous" scenario. On the other hand, a Laplace transform resolves the KWW function into a superposition of exponential relaxations decaying with a broad distribution of relaxation times, the "heterogeneous" scenario (20). In this case, the β_{KWW} parameter is a measure for the width of the distribution of timescales involved in the decay. The fitted KWW rate constants can then be converted to an average rate $<k>$ by integration, which leads to

$$< k >^{-1} = \frac{k_{KWW}{}^{-1}}{\beta_{KWW}} \Gamma\left(\frac{1}{\beta_{KWW}}\right) \qquad [2]$$

where Γ is the gamma-function (21). Using equation [2] the fitted rate constant k_{KWW} from the trace in fig. 3 can be converted to an average rate for loop formation of $<k> = 1.1 \cdot 10^4\ s^{-1}$.

Temperature Dependence of Loop Formation

To characterize the temperature dependence of loop formation experiments have been performed between 298 K and 206 K in the presence of 60% glycerol (fig. 4). Above 280 K contact formation kinetics can be described by single exponential kinetics in both peptide systems while at low temperature, kinetics become more complex. In *(Gly-Ser)$_{12}$* an initial fast phase appears below 273 K and the slow main phase begins to show stretched behavior as indicated by a β_{KWW}-value significantly smaller than unity (see equation [1]). In the *(Ser-Gly)* peptide, the kinetic traces show similar characteristics as in *(Gly-Ser)$_{12}$*. A fast initial decay followed by a slower and increasingly complex reaction was detected below 274 K and could best be fitted to equation [1]. In *(Gly-Ser)$_{12}$* $<k>$ was decreased over four orders of magnitude from $5 \cdot 10^6\ s^{-1}$ to $500\ s^{-1}$ at 208 K. In the same temperature range β_{KWW} was decreased to a

value of 0.6 at the lowest temperatures. The decay of xanthone triplets in the absence of an acceptor was measured under the same conditions and was found to be slower by at least one order of magnitude at the lowest temperatures. Thus, the decay in xanthone triplet absorption results from TTET to naphthalene due to contact formation even at the lowest temperature. The temperature dependence of k_{exp} and $<k>$ is different. While k_{exp} shows Arrhenius behavior, the temperature dependence of $<k>$ exhibits a curvature and has a steeper slope.

In *(Ser-Gly)* $<k>$ was found to be faster over the whole range of temperature compared to $(Gly\text{-}Ser)_{12}$, as expected for a shorter peptide. The β_{KWW} – parameters were found to be generally smaller in the *(Ser-Gly)* peptide compared to $(Gly\text{-}Ser)_{12}$ with a value of 0.5 for the lowest accessible temperature.

The Free Energy Landscape

These results indicate a complex free energy landscape containing various local minima which governs the diffusional motion of the peptide. At high temperature, exchange between substates is fast (see fig. 5.A) since the barriers separating the local minima are small compared to the available thermal energy. Exponential kinetics for contact formation are observed under these conditions because the conformational distribution of molecules carrying an excited donor molecule remains constant during the course of the reaction (5). By decreasing the temperature on the one hand the available thermal energy that is decreased which leads to slower barrier crossing. On the other hand the dynamics of the solvent molecules slow down and thus the viscosity is increased. Both effects enter the theory of activated barrier crossing in solution by Kramers (22). Thus upon lowering the temperature, the transition rate of a molecule from one conformational substate to another is decreased (see fig. 5.B). If the

interchange of conformations is slow on the timescale of the experiment the kinetics are expected to deviate from exponential behavior (5) because excited donor molecules are locally depleted and the equilibrium distribution is not retained. As a result, different peptide populations starting in different wells on the conformational energy surface establish contact with different kinetics. This is consistent with the "heterogeneous" scenario leading to stretched exponential relaxation.

A fast exponential decay in the early time region is a feature commonly observed in relaxation data (23) and can be attributed to a transient phenomenon which decays on a short time-scale compared to the relaxation itself. In contact formation kinetics of short peptides we found such behavior at room temperature on the sub nanosecond time scale (8). In equilibrium, a multitude of subpopulations of peptide molecules with different donor-acceptor distances are present in the solution. A certain conformational substate on the free energy surface includes the population of peptides that have labels at close distance. These peptides can form donor-acceptor contacts faster than peptides in other local minima, because only a few torsional angles have to be rearranged and no major barriers have to be crossed (see fig 5.C). The depletion of species in this local minimum produces a fast initial decay in the kinetics. At room temperature the initial decay takes place on the sub-nanosecond timescale, upon lowering the temperature the kinetics are slowed down to the nanosecond time regime.

Femtosecond experiments detected an additional population of peptides with the labels already in contact at the beginning of the experiment. This population transfers the triplet energy within the first picoseconds of the experiment (8) and the kinetics can thus not be resolved using an experimental setup with nanosecond resolution independent of temperature.

Origin of the Temperature Dependence

The average rate constant for loop formation <*k*> of *(Gly-Ser)*$_{12}$ does not follow a linear Arrhenius type temperature dependence. The curvature can be described by a Vogel-Fulcher-Tamman (VFT) relation

$$k(T) = Ae^{H/k_B(T-T_o)} \qquad [3]$$

This empirical equation has been used to describe the α-relaxation of glass forming liquids over large ranges of temperatures. Solvent activated process like conformational rearrangements in proteins have been shown to follow VFT temperature dependencies (14; 24). In our experiments, the loop closure reactions in long peptides were found to exhibit VFT behavior indicating that chain dynamics are controlled by solvent motions just like large scale motions in proteins.

The fluctuating dipoles of the water molecules transfer momentum onto the solvated peptide bonds, thereby supplying the energy that drives chain motions. At the same time, energy is dissipated via friction. This leads to strong coupling of peptide and of solvent motion. Solvent dynamics can be determined via the dielectric relaxation rate k_{diel} which is a measure for the average solvent molecule reorientation time (25) and related to viscosity in a first approximation by

$$k_{diel} = \frac{k_B T}{4\pi\eta R^3} \qquad [4]$$

where k_B is he Boltzmann constant, T is the absolute temperature, R is the molecular radius and η is the solvent viscosity. A direct comparison of peptide dynamics and

dielectric relaxation is shown in fig. 6.A. The average contact formation rate constants of *(Gly-Ser)$_{12}$* follow the dielectric relaxation over the whole range of temperatures as expected for a solvent activated process. A conformational transition of the peptide can only occur if the solvent moves. Thus solvent dynamics limit peptide motion. It has been proposed that the ratio of k_{diel} and the rate constant of a solvent activated process

$$n(T) = k_{diel} / k \qquad [5]$$

is a measure for the number of steps on the free energy surface that are required for the reaction (14). In the case of the *(Gly-Ser)$_{12}$* peptide this ratio increases from $n = 1.4 \cdot 10^4$ at 270 K to $n = 4.0 \cdot 10^4$ at 208 K as shown in fig. 6.B.

No deviation from Arrhenius behaviour was detected for the temperature dependence of $<k>$ in the *(Ser-Gly)* peptide (see fig. 6). A comparison to the dielectric relaxation rate yields a ratio of $n = 3.1 \cdot 10^3$ at 270 K that is increased with decreasing temperature. Below 230 K however, the rate constants of *(Ser-Gly)* contact formation do not follow the motions of the solvent any more. Below this temperature peptide and solvent motions are partially decoupled and the value for *n* drops significantly.

There are several concepts to explain the temperature dependence of both peptides. The increase in the number of steps to form contact upon lowering the temperature for *(Gly-Ser)$_{12}$* and *(Ser-Gly)* above 230 K might be due to a transient trapping of the peptide in local minima on the free energy surface. Thus, escape from these wells slows contact formation down even more and the number of solvent rearrangement steps which are required to sample the free energy landscape is increased.

In the short peptide, however, the decrease in *n* leads to a different scenario below 230 K. An explanation for the apparent decoupling from solvent dynamics of *(Ser-Gly)* is provided by a mechanism for contact formation controlled by high barriers in comparison the diffusional motions of long molecules. In Kramers theory (22) it is shown that the rate constants for activated barrier crossing are inversely proportional to solvent viscosity. For contact formation reactions in peptides this relationship is more complex as the rate constants have been found to exhibit fractional viscosity dependence

$$k = k_0 \left(\frac{\eta}{\eta_0} \right)^{-\beta} \qquad [6]$$

with $\beta \leq 1$. In long peptides, like *(Gly-Ser)*$_{12}$ β approaches 1 (26). The contact formation rates of shorter peptides on the other hand scale with a reduced viscosity dependence ($\beta < 1$) indicating a partial decoupling from solvent viscosity. Such behaviour has been observed in relaxation kinetics for many polymers (27-29) and has been explained by various concepts like position dependent (30) or frequency dependent friction coefficients (31; 32), barrier shape (33) or different micro viscosity around the molecule due to preferential hydration effects (34).

Temperature dependent micro-viscosity is an alternative explanation as viscosity is coupled to dielectric relaxation via equation [4]. At lower temperature a stronger decoupling from solvent motion is observed in the *(Ser-Gly)* peptide. It has been proposed regions exist supercooled solutions contain regions with different degrees of fluidity (35; 36). The size of such domains is estimated to be of the nanometer scale (37-40). Contact formation is determined by the local environment of the mole-

cules. As this process takes place at much shorter at very short length scales in a short peptide, kinetics of *(Ser-Gly)* are more influenced by solvent inhomogeneities and a decoupling can be observed at low temperatures. In addition, inhomogeneities in the solvent can lead to a further lowering of the KWW stretching parameter β_{KWW}, which is consistent with the generally lower values for β_{KWW} in the *(Ser-Gly)* peptide.

Increasing the Friction

By lowering thermal energy, complex kinetics are observed due to slow exchange between local minima on the free energy landscape (see fig. 4). Increasing the friction on the energy surface by increasing the solvent viscosity at a given temperature is another possibility to slow down barrier crossing dynamics. To test if complex contact formation kinetics can also be produced at a constant temperature by increasing the viscosity and thus decelerate conformational equilibration, contact formation of $(Gly\text{-}Ser)_{12}$ kinetics were measured at different glycerol concentrations.

Figure 7.A shows the results of the results of the viscosity dependence of loop formation for $(Gly\text{-}Ser)_{12}$ at 253 K. In 40% glycerol which corresponds to a viscosity of 20 cp loop formation kinetics are described by a single exponential decay. At higher glycerol concentrations and thus higher viscosities (η = 188 cp, 500 cp and ~ 3000cp) an initial fast decay is detected followed by a process exhibiting complex kinetics. The rates constants k_{exp} and $\langle k \rangle$ from the fit to equation [1] are shown in fig. 7.B. A fit of the viscosity dependence of $\langle k \rangle$ with equation [6] exhibits a fractional viscosity dependence of $(Gly\text{-}Ser)_{12}$ of β = 0.84, which is lower than the value obtained for the viscosity dependence of loop formation at room temperature (β = 0.98). The extreme values of viscosity lead to a less pronounced effect than observed at room temperature. Due to the increased complexity of the kinetics such behavior is however expected.

These results show that the effect of increased viscosity leads to similar results in terms of complex kinetic behavior of loop formation than lowering the thermal energy. These findings argue for the mechanism of a diffusional search on a rough surface containing local traps for a loop formation reaction in polypeptides.

Conclusions

At low temperature the contact formation kinetics of short and long peptides become increasingly complex. A combination of a fast initial exponential decay and a slower stretched component describe the loop formation kinetics in both peptides. The fast process can be interpreted as the fast depletion of species in a local minimum on the free energy surface that allows contact without the crossing of any major barriers. If the rate constants k_{exp} of the fast phase in the *(Ser-Gly)* peptide are extrapolated to room temperature a value of ~ $7 \cdot 10^8$ s^{-1} is obtained. Correcting for the viscosity in 60% glycerol, the fast process proceeds with a time constant in the 100's of picoseconds. This is consistent with an initial fast phase for contact formation observed in ps-time resolution experiments(8)in a similar peptide system whose rate constant lies as well in this time regime.

The following slower process can be attributed to contact formation of the remaining molecules that populate local minima on the free energy surface and have to cross several barriers to establish contact. These small barriers arise from intramolecular interactions, bond rotation potentials and steric effects that become significant at low temperature. The complex kinetics of contact formation at low temperature can be explained by slow equilibration of peptide conformations leading to different loop formation rate constants for different peptide subensembles. Increasing the viscosity leads to high friction of the peptide on the energy landscape thereby slowing down

barrier crossing. Thus, conformational equilibration is equally slowed down and complex kinetics for contact formation are observed.

Loop formation is coupled to solvent motion. This is reflected in a non-Arrhenius temperature dependence in long peptides, following the dielectric relaxation of the solvent. Two different mechanisms for peptide motion can be discriminated. For large scale conformational transitions, solvent motion determines peptide dynamics at all accessible temperatures. Small scale motions, like contact formation in the *(Ser-Gly)* peptide however are governed by barriers and are decoupled from solvent dynamics at low temperature. This might be due to either the barrier limited dynamics leading to an Arrhenius type temperature dependence. On the other hand, small inhomogeneities in the solvent at low temperature might lead to smaller local viscosity and thus to faster dynamics.

The ratio between the dielectric relaxation and contact formation rate constant can be interpreted as the number of steps needed to bring the labels into contact. This number lies in the 10^4 for a long and flexible peptide and 10^3 for a very short peptide. This gives a picture of the conformational search an unfolded protein has to perform in order to establish short and long range interactions upon folding. It is thus shown that the picture of conformational substates is valid for conformational transitions in unstructured polypeptides corresponding to observations in proteins.

Materials and Methods

Peptides. The peptides used in the study were the *(Ser-Gly)* peptide Xan-*Ser-Gly*-NAla-Ser-Arg-Gly-OH as a model for short peptides and the $(Gly\text{-}Ser)_{12}$ peptide Xan-$(Gly\text{-}Ser)_{12}$-NAla-Ser-Arg-Gly-OH as a model peptide in the long chain limit. The C-terminal arginines were included to enhance solubility of the peptides. Xan

stands for 9-oxoxanthen-2-carboxylic acid and was synthesized as described before (2) (xanthone acid) NAla is 1-naphthylalanine and was purchased from BACHEM. All peptides were synthesized by solid phase peptide synthesis (SPPS) as described before (2), purified by RP-HPLC on a Merck LiChrosorp® RP-8 column and the purity was confirmed by MALDI-MS and analytical HPLC.

Solvents. All traces were recorded in water/glycerol mixtures to vary solvent viscosity and prevent freezing of the solvent (water: *for UV spectroscopy*, purchased from FLUKA, glycerol: *99.5+% spectrophotometric grade*, purchased from SIGMA-ALDRICH, the solvents were used without further purification). The viscosity of the solutions were measured using a falling ball viscosimeter (Haake) at temperatures down to 263 K or taken from literature.(41; 42)

Measurements. Concentrations of around 100µM of peptide were used for the experiment. At this concentration the rate of intermolecular quenching is negligible compared to intramolecular quenching. The measurements were performed using an Applied Photophysics Laser Photolysis Spectrometer (LKS.60). To keep the samples at a defined temperature, a cooling unit by Oxford Instruments (DN704) was used.

References

1. Bieri, O., Wirz, J., Hellrung, B., Schutkowski, M., Drewello, M. & Kiefhaber, T. (1999). The speed limit for protein folding measured by triplet-triplet energy transfer. *Proc. Natl. Acad. Sci. USA* 96, 9597-9601.
2. Krieger, F., Fierz, B., Bieri, O., Drewello, M. & Kiefhaber, T. (2003). Dynamics of Unfolded Polypeptide Chains as a Model for the Earliest Steps in Protein Folding. *J Mol Biol* 332, 265-274.
3. Chang, I. J., Lee, J. C., Winkler, J. R. & Gray, H. B. (2003). The protein-folding speed limit: intrachain diffusion times set by electron-transfer rates in denatured Ru(NH3)5(His-33)-Zn-cytochrome c. *Proc Natl Acad Sci U S A* 100, 3838-40.
4. Krieger, F., Fierz, B., Axthelm, F., Joder, K., Meyer, D. & Kiefhaber, T. (2004). Intrachain diffusion in a protein loop fragment from carp parvalbumin. *Chem. Phys.* 307, 209-215.
5. Szabo, A., Schulten, K. & Schulten, Z. (1980). First passage time approach to diffusion controlled reactions. *J. Chem. Phys.* 72, 4350-4357.
6. Satzger, H., Schmidt, B., Root, C., Zinth, W., Fierz, B., Krieger, F., Kiefhaber, T. & Gilch, P. (2004). Ultrafast Quenching of the Xanthone Triplet by Energy Transfer: New Insight into the Intersystem Crossing Kinetics. *J. Phys. Chem. A* 108, 10072-10079.
7. Heinz, B., Schmidt, B., Root, C., Satzger, H., Milota, F., Fierz, B., Kiefhaber, T., Zinth, W. & Gilch, P. (2006). On the Unusual Fluorescence Properties of Xanthone in Water. *To be submitted*.
8. Fierz, B., Satzger, H., Root, C., Zinth, W. & Kiefhaber, T. (2006). Hierarchy of Conformational Dynamics of Unfolded Polypeptide Chains Revealed by Loop Formation on the Picoseconds to Microseconds Time Scale. *submitted*.
9. Ansari, A., Berendzen, J., Bowne, S. F., Frauenfelder, H., Iben, I. E., Sauke, T. B., Shyamsunder, E. & Young, R. D. (1985). Protein states and proteinquakes. *Proc Natl Acad Sci U S A* 82, 5000-4.
10. Frauenfelder, H., Petsko, G. A. & Tsernoglou, D. (1979). Temperature-dependent X-ray diffraction as a probe of protein structural dynamics. *Nature* 280, 558-63.
11. Frauenfelder, H., Sligar, S. G. & Wolynes, P. G. (1991). The energy landscapes and motions of proteins. *Science* 254, 1598-603.
12. Onuchic, J. N. & Wolynes, P. G. (1993). Energy landscapes, glass transitions, and chemical reaction dynamics in biomolecular or solvent environment. *J. Chem. Phys.* 98, 2218-2224.
13. Austin, R. H., Beeson, K. W., Eisenstein, L., Frauenfelder, H. & Gunsalus, I. C. (1975). Dynamics of ligand binding to myoglobin. *Biochemistry* 14, 5355-5373.
14. Fenimore, P. W., Frauenfelder, H., McMahon, B. H. & Parak, F. G. (2002). Slaving: Solvent fluctuations dominate protein dynamics and functions. *Proc Natl Acad Sci U S A* 99, 16047-16051.
15. Beece, D., Eisenstein, L., Frauenfelder, H., Good, D., Marden, M. C., Reinisch, L., Reynolds, A. H., Sorensen, L. B. & Yue, K. T. (1980). Solvent Viscosity and Protein Dynamics. *Biochemistry* 19, 5147-5157.
16. Bandis, A., Wen, W. Y., Jones, E. B., Kaskan, P., Jones, A. A., Inglefield, P. T. & Bendler, J. T. (1994). An NMR study of segmental motion in polyisobutylene and the relationship to translational diffusion of sorbed CO2. *J. Polym. Sci., Polym. Phys. Ed.* 32, 1707-1717.

17. Yiyong, H., Lutz, T. R., Ediger, M. D., Ayyagari, C., Bedrov, D. & Smith, G. D. (2004). NMR Experiments and Molecular Dynamics Simulations of the Segmental Dynamics of Polystyrene. *Macromolecules* 37, 5032-5039.
18. Moe, N. E., Qiu, X. H. & Ediger, M. D. (2000). 13C NMR Study of Segmental Dynamics of Atactic Polypropylene Melts. *Macromolecules* 33, 2145-2152.
19. Qiu, X. H., Moe, N. E., Ediger, M. D. & Fetters, L. J. (2000). Local and global dynamics of atactic polypropylene melts by multiple filed 13C nuclear magnetic resonance. *J. Chem. Phys.* 113, 2918-2926.
20. Arbe, A., Colmenero, J., Monkenbusch, M. & Richter, D. (1998). Dynamics of Glass-Forming Polymers: "Homogeneous" versus "Heterogenous" Scenario. *Physical Review Letters* 81, 590-593.
21. Lindsey, C. P. & Patterson, G. D. (1980). Detailed comparison of the Williams-Watts and Cole-Davidson functions. *J. Chem. Phys.* 73, 3348-3357.
22. Kramers, H. A. (1940). Brownian motion in a field of force and the diffusion model of chemical reactions. *Physica* 4, 284-304.
23. Phillips, J. C. (1996). Stretched exponential relaxation in molecular and electronic glasses. *Rep. Prog. Phys* 59, 1133-1207.
24. Iben, I. E., Braunstein, D., Doster, W., Frauenfelder, H., Hong, M. K., Johnson, J. B., Luck, S., Ormos, P., Schulte, A., Steinbach, P. J. & Xie, A. H. (1989). Glassy Behavior of a Protein. *Phys. Rev. Lett.* 62, 1916-1919.
25. Debye, P. (1929). *Polar Molecules*, Dover, New York.
26. Moglich, A., Krieger, F. & Kiefhaber, T. (2005). Molecular basis for the effect of urea and guanidinium chloride on the dynamics of unfolded polypeptide chains. *J Mol Biol* 345, 153-62.
27. Zhu, W. & Ediger, M. D. (1997). Viscosity Dependence of Polystyrene Local Dynamics in Dilute Solutions. *Macromolecules* 30, 1205-1210.
28. Punchard, B. J. & Adolf, D. B. (2002). Pressure and Temperature Dependence of the Dilute Solution Segmental Dynamics of Anthracene-Labeled Polyisoprene. *Macromolecules* 35, 3281-3287.
29. Pilar, J. & Labsky, J. (2003). Solvent Dependence of Polystyrene Local Segmental Dynamics in Dilute Solution by Spin-Label X-Band ESR. *Macromolecules* 36, 913-920.
30. Gavish, B. (1980). Position-Dependent Viscosity Effects on Rate Coefficients. *Physical Review Letters* 44, 1160-1163.
31. Doster, W. (1983). Viscosity Scaling and Protein Dynamics. *Biophysical Chemistry* 17, 97-103.
32. Schlitter, J. (1988). Viscosity Dependence of Intramolecular Activated Processes. *Chemical Physics* 120, 187-197.
33. Grote, R. F. & Hynes, J. T. (1980). The stable states picture of chemical reactions. II. Rate constants for condensed and gas phase reaction models. *J. Chem. Phys.* 73, 2715-2732.
34. Kleinert, T., Doster, W., Leyser, H., Petry, W., Schwarz, V. & Settles, M. (1998). Solvent Composition and Viscosity Effects on the Kinetics of CO Binding to Horse Myoglobin. *Biochemistry* 37, 717-733.
35. Adam, G. & Gibbs, J. H. (1965). On the Temperature Dependence of Cooperative Relaxation Properties in Glass-Forming Liquids. *J. Chem. Phys.* 43, 139-146.
36. Bhattacharyya, S. & Bagchi, B. (1997). Decoupling of tracer diffusion from viscosity in a supercooled liquid near the glass transition. *J. Chem. Phys.* 107, 5852-5862.

37. Kirkpatrik, T. R. (1985). Mode-coupling theory of the glass transition. *Phys. Rev. A* 31, 939-944.
38. Tarjus, G. & Kivelson, D. (1995). Breakdown of the Stokes-Einstein relation in supercooled liquids. *J. Chem. Phys.* 103, 3071-3073.
39. Cicerone, M. T. & Ediger, M. D. (1996). Enhanced translation of probe molecules in supercooled o-terphenyl: Signature of spatially heterogeneous dynamics? *J. Chem. Phys.* 104, 7210-7218.
40. Cicerone, M. T., Blackburn, F. R. & Ediger, M. D. (1995). How do molecules move near Tg? Moleculare rotation of six probes in o-terphenyl across 14 decades in time. *J. Chem. Phys.* 102, 471-479.
41. Green, E. & Parke, J. P. (1939). The density and viscosity of glycerol solutions at low temperatures. *J. Soc. Chem. Ind.* 58, 319-20.
42. Segur, J. B. & Oberstar, H. E. (1951). Viscosity of Glycerol and Its Aqueous Solutions. *Ind. Eng. Chem.* 43, 2117-2120.
43. Huck, J. R., Noyel, G. A. & Jorat, L. J. (1988). Dielectric Properties of Supercooled Glycerol-Water Solutions. *IEEE Trans. Electr. Insul.* 23, 627-638.

Figure captions

Figure 1: Scheme of a TTET experiment. The polypeptide carrying an excited triplet donor label moves in the solvent until upon establishing van der Waals contact between the labels the triplet is transferred on the acceptor label by a two electron exchange mechanism. The reaction is monitored spectroscopically. As excitation and transfer lie in the 2ps time region (6; 7) and the contact complex is very short lived the experiment directly yields the rate constant of contact formation.

Figure 2: General scheme of the peptides used in this study. The xanthone moiety is coupled to the N-terminus, the naphthalene is included as the non – natural amino acid naphtylalanine. Between donor and acceptor glycine and serine sequences are used. The C-terminal arginine was included to increase solubility.

Figure 3: Comparison of experimental traces of *(Gly-Ser)*$_{12}$ contact formation recorded at 273 K (—) and 237 K (—). The trace at 273 K follows single exponential kinetics with a rate constant of $k = 8.2 \cdot 10^5 s^{-1}$. At high temperature not the whole amplitude of the reaction is observed because of a fast process occurring within the dead time (~15 ns) of the experiment. At low temperature, the fast process is observable. The trace at 237 K shows complex kinetics. A fast exponential reaction in the early time region is followed by a multi - or stretched exponential decay. Fitting to equation [1] yields for the fast initial rate constant $k_1 = 1.38 \cdot 10^6 s^{-1}$ and for the stretched decay $k_2 = 1.5 \cdot 10^4 s^{-1}$ with a stretch factor $\beta_{KWW} = 0.65$.

Figure 4: Temperature dependence of the contact formation kinetics of the **A)** *(Gly-Ser)*$_{12}$ peptide and **B)** *(Ser-Gly)* peptide. All data were recorded in 60% glycerol wa-

ter mixtures. The rate constants were obtained by fitting the experimental trace to equation [1]. The open symbols correspond to the exponential phase (k_{exp}), the full symbols are the average rates constants $<k>$ obtained by converting the fitted rate constants using equation [2]. The solid line are VFT fits to the data (see equation [3]) yielding for *(Gly-Ser)*$_{12}$ $A = 5.23 \cdot 10^{10}$ s^{-1}, $H = 1.4 \cdot 10^4$ kJ/mol and $T_0 = 121$ K and for *(Ser-Gly)* $A = 1.49 \cdot 10^{16}$ s^{-1}, $H = 4.88 \cdot 10^4$ kJ/mol and $T_0 = 12.1$ K. For comparison the dielectric relaxation rate k_{diel} of the solvent is shown as dotted line. The data is taken from ref (43). It is shown that for the average rates constants for contact formation of *(Gly-Ser)12* follow the dielectric relaxation rate over the whole temperature range, while the rate constants of *(Ser-Gly)* deviate at low temperature.

The temperature dependencies of the β_{KWW} parameters for both peptides are shown in the separate panels below. The value for β_{KWW} decreases monotonically in both cases to reach a value around 0.5

Figure 5: A hypothetical energy surface depending on the distance between two reactive groups in a polymer is shown for different temperatures. **A)** High temperature: The interchange of conformations is fast. For a reaction that occurs if the polymer enters the reactive well on the left (i.e. a contact between the reactive groups is established) exponential kinetics are expected(5). **B)** Low temperature: The interchange of conformations is slow due the height of the barriers relative to the available energy. Thus the system cannot retain equilibrium during the course of the contact formation reaction and non-exponential kinetics are expected. **C)** Due to the hierarchical organization of the free energy landscape each conformational substate contains a high number of lower tier substates separated by lower barriers that interchange on a shorter timescale. Small scale fluctuations around bond angles are governed by the

lower tier barriers. Motions within a certain conformational substate are detected as fast initial decay in the kinetics of contact formation.

Figure 6: A) Temperature dependence of contact formation of peptides compared to the dielectric relaxation rate k_{diel}. It is shown that for the average rates constants for contact formation of *(Gly-Ser)*$_{12}$ (—) follow the dielectric relaxation rate over the whole temperature range, while the rate constants of *(Ser-Gly)* (—) deviate at low temperature. **B)** The ratio of k_{diel} and $<k>$ in both peptides

Figure 7: A) *(Gly-Ser)*$_{12}$ contact formation dynamics in solutions containing 40%(—), 64%(—), 72%(—) and 84%(—) glycerol (% by weight) leading to increasing viscosity at 253 K. The missing amplitude of the first and fastest trace corresponds to the fast initial decay that cannot be detected at this temperature and viscosity. The very slow process observed in the 40% glycerol trace corresponds to the lifetime of xanthone and arises from a population of molecules that are hindered to make contact.

B) The rate constant for fast and slow process are shown as a function of viscosity. The faster rates arise from loop formation, while the initial decay is followed by a stretched residual decay. The viscosity dependence of the main stretched phase was fitted to the following equation [6] commonly used to analyze viscosity dependencies of contact formation reactions (fit values are $k_0 = 6.6 \cdot 10^6$ s^{-1}, $\beta = 0.84$). The data shows a fractional viscosity dependence with a $\beta = 0.84$ which is lower than at room temperature.

C) Upon increasing viscosity the initial decay is observed and the β_{KWW} parameter of the residual kinetics is decreasing indicating a similar effect on contact formation than decreasing the temperature.

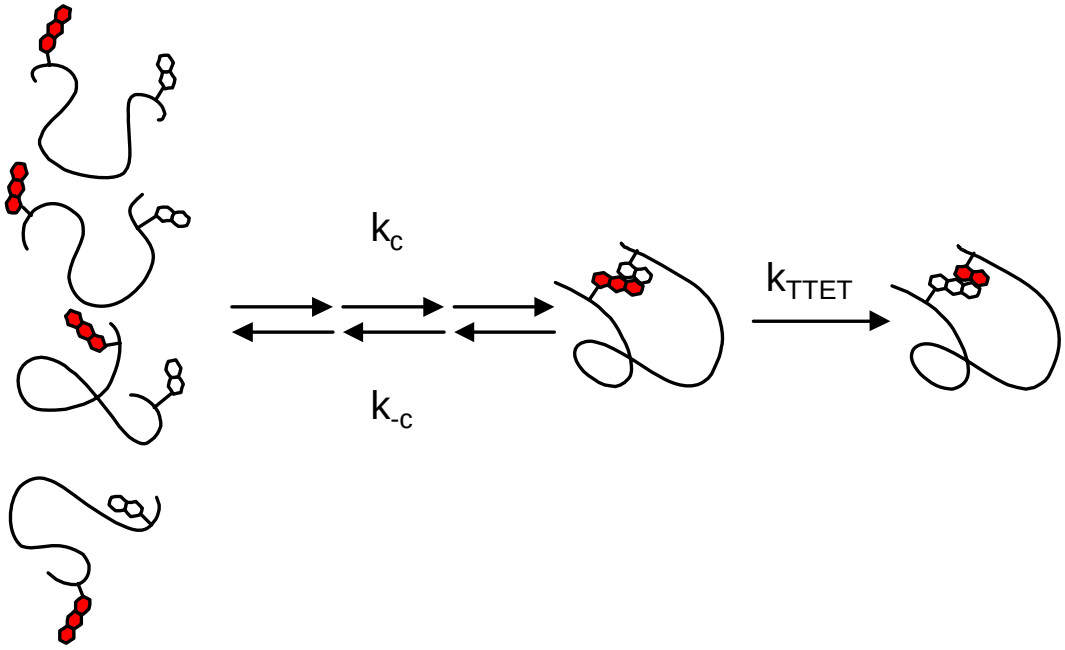

Figure 1

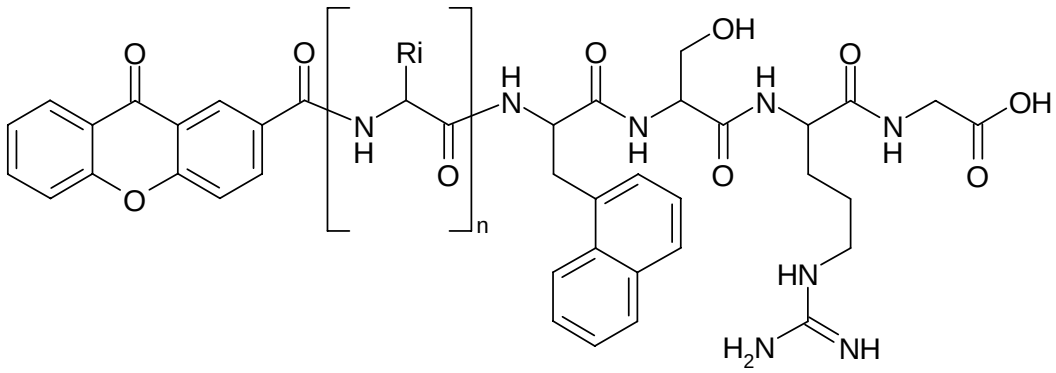

Figure 2

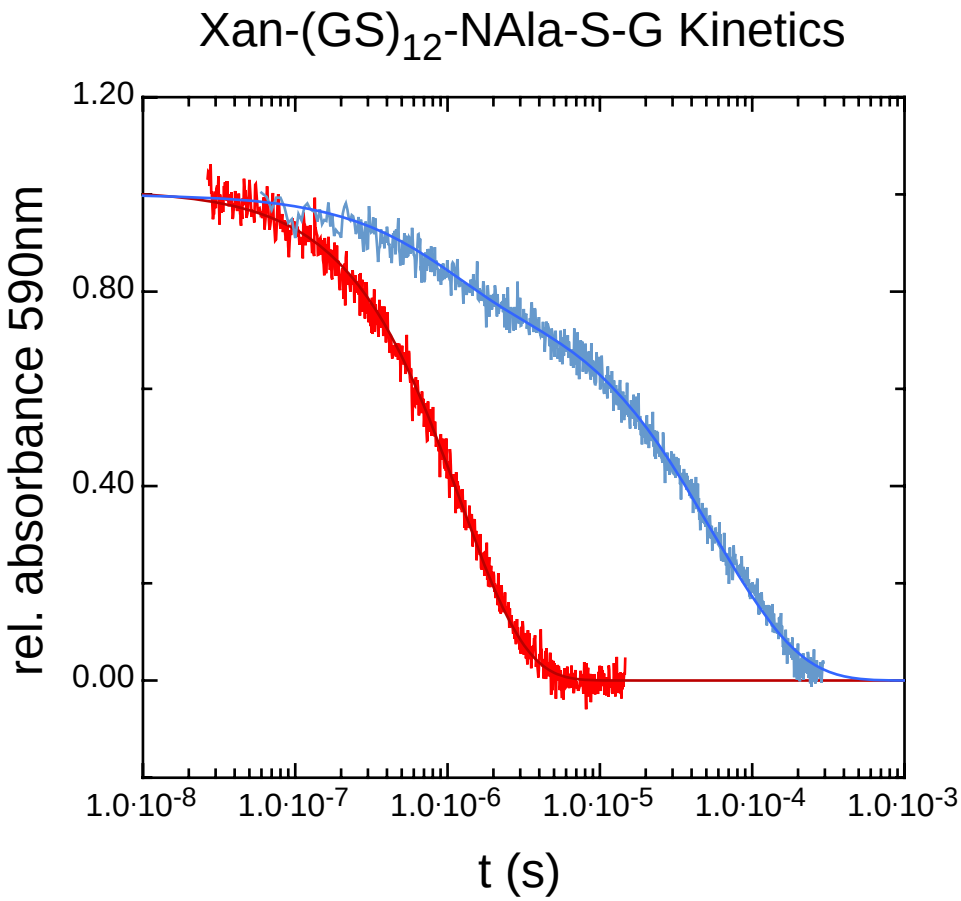
Xan-(GS)12-NAla-S-G Kinetics
rel. absorbance 590nm
1.20
0.80
0.40
0.00
1.0·10-8
1.0·10-7
1.0·10-6
1.0·10-5
1.0·10-4
1.0·10-3
t (s)

Figure 3

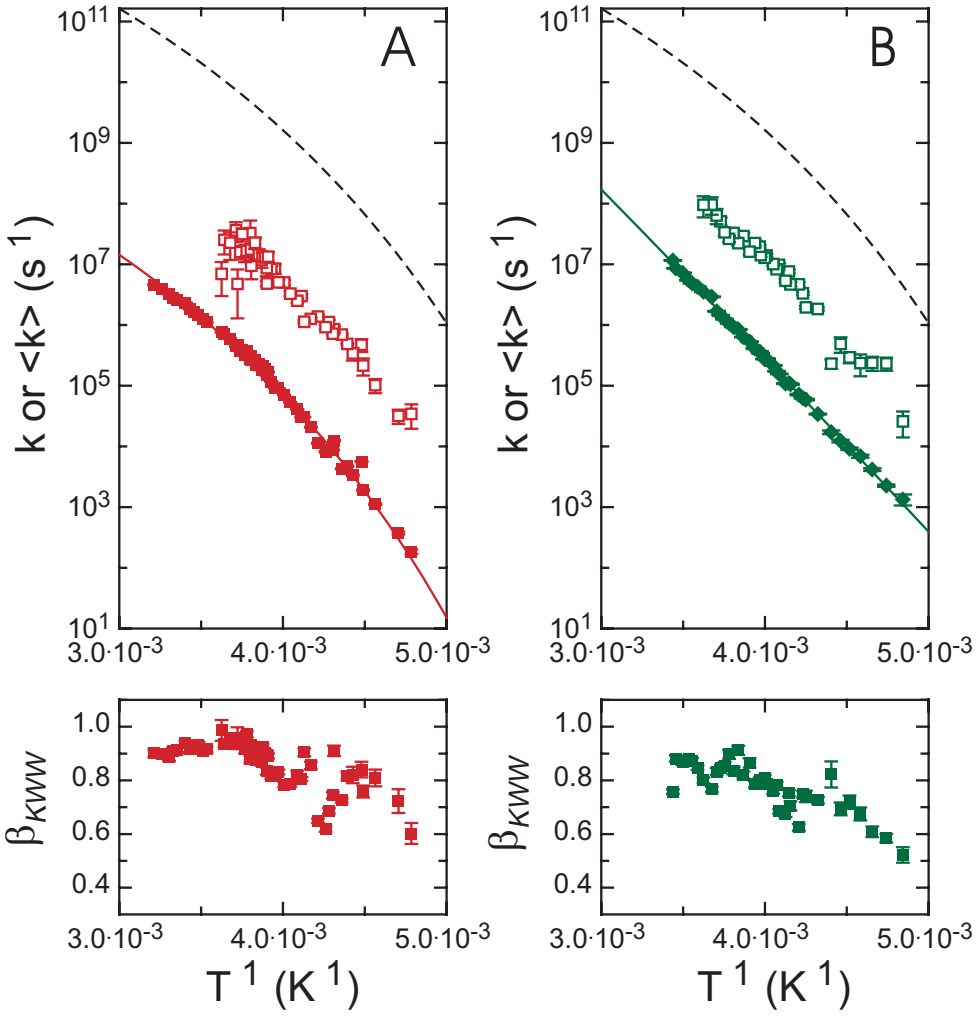
A
B
k or <k> (s 1)
βKWW
T 1 (K 1)
10^11
10^9
10^7
10^5
10^3
10^1
3.0·10-3
4.0·10-3
5.0·10-3
1.0
0.8
0.6
0.4

Figure 4

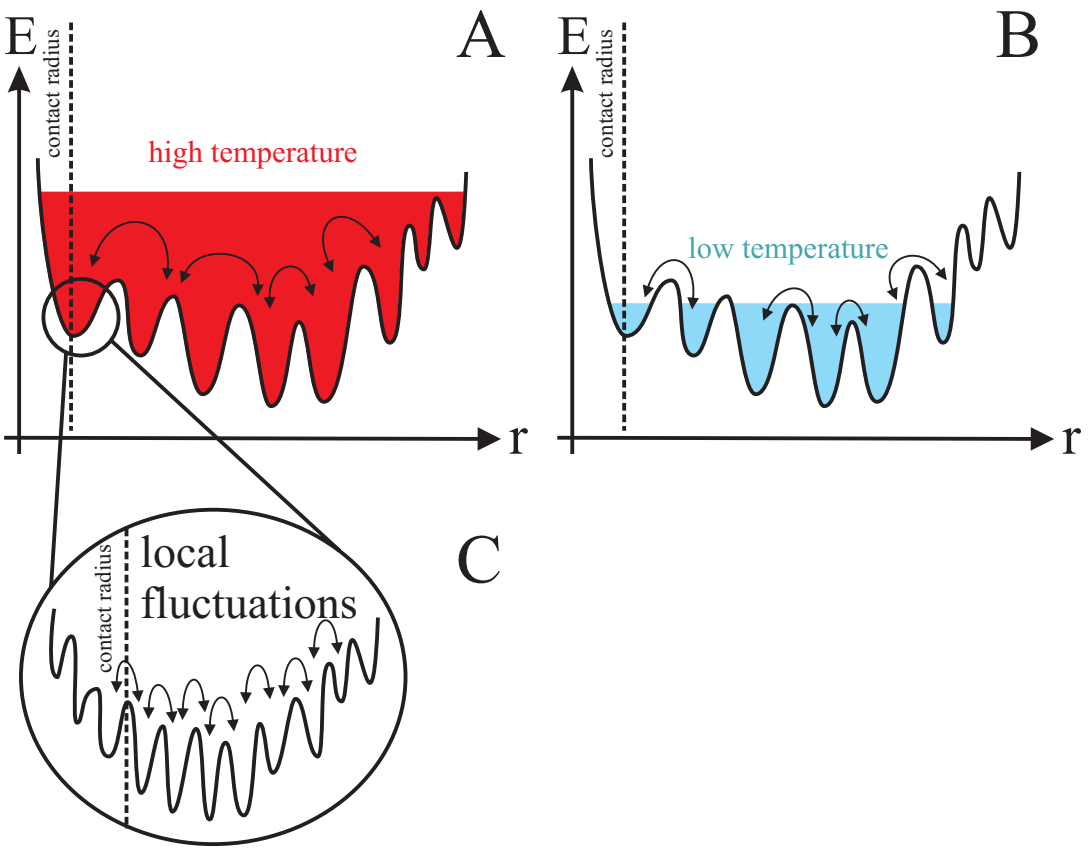
E
contact radius
A
high temperature
r
E
contact radius
B
low temperature
r
C
contact radius
local
fluctuations

Figure 5

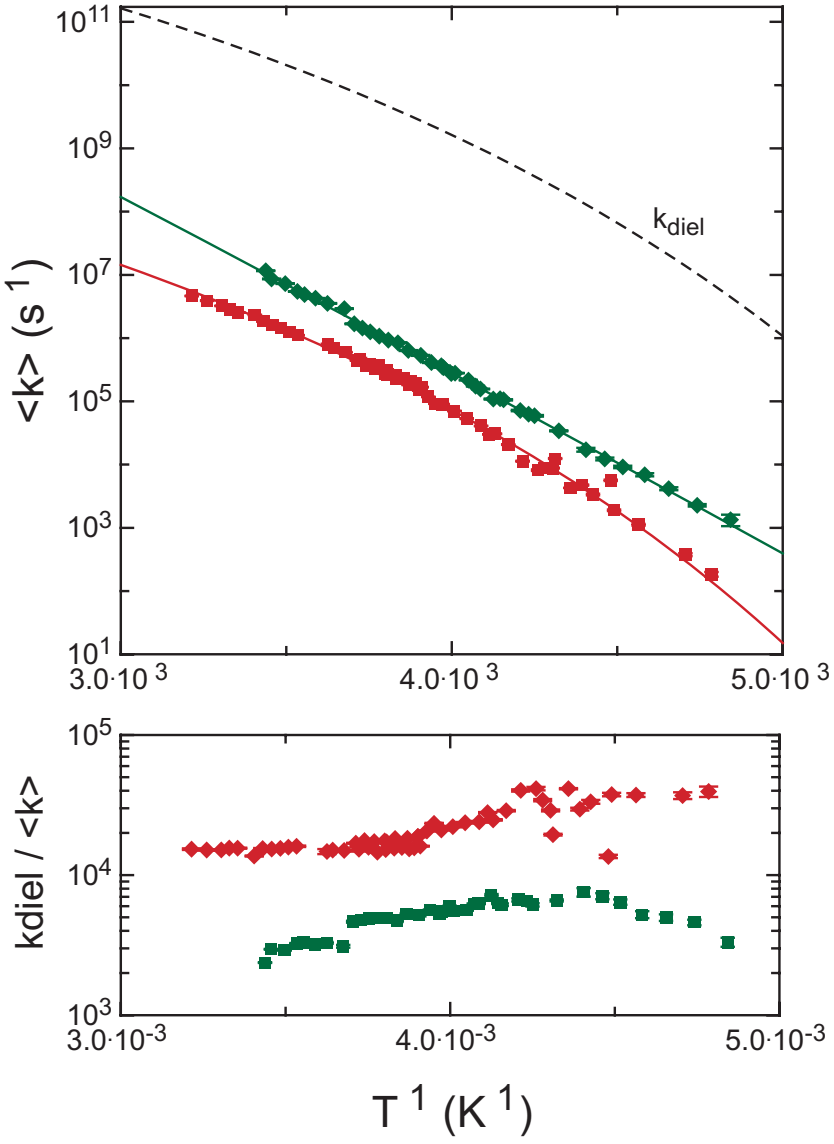
10^{11}
10^{9}
10^{7}
10^{5}
10^{3}
10^{1}
<k> (s^{-1})
k_{diel}
$3.0\cdot10^{3}$
$4.0\cdot10^{3}$
$5.0\cdot10^{3}$
10^{5}
10^{4}
10^{3}
kdiel / <k>
$3.0\cdot10^{-3}$
$4.0\cdot10^{-3}$
$5.0\cdot10^{-3}$
T^{-1} (K^{-1})

Figure 6

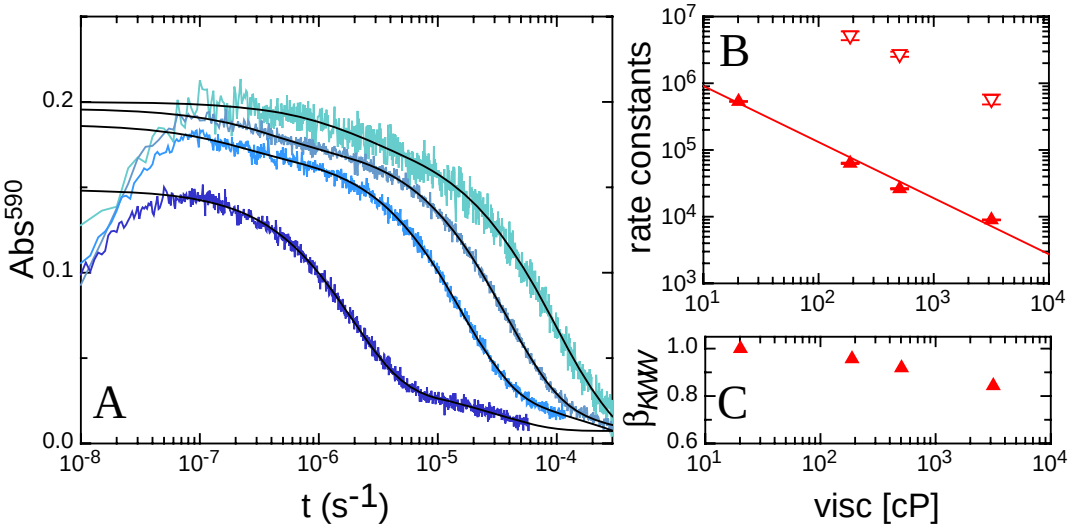

Figure 7

Global and Local α-Helix Dynamics and Stability Measured by Triplet-Triplet Energy Transfer

Beat Fierz, Andreas Reiner & Thomas Kiefhaber*
Biozentrum der Universität Basel
Division of Biophysical Chemistry,
Klingelbergstr. 70
CH-4056 Basel
Switzerland

*corresponding author. Phone: ++41-61-267 2194; fax: ++41-61-267 2189; e-mail: t.kiefhaber@unibas.ch

Abstract

We investigated local and global dynamics and stability in α-helices using triplet-triplet energy transfer between xanthone and naphthylalanine attached at different positions in helical peptides. The labels were introduced with (i, i+6) spacing at N-terminal, central and C-terminal positions or at both ends of alanine based helical peptide. All peptides exhibit double exponential TTET kinetics. This indicates an equilibrium between helical conformations in which intrachain contact formation is prevented and conformations with at least partially unfolded helices, which allow TTET by intrachain loop formation. The results revealed lower helical content at the ends of the peptides compared to the central part. In the terminal regions unfolding occurs with time constants around 300 ns at 5^{o} C which is faster than in the interior of the helix where time constants of 1-2 μs are observed. This argues for local un-folding events at the terminal regions. The unfolding kinetics at interior positions are similar to the dynamics observed for peptides with the labels attached at both ends, indicating that these reactions reflect global unfolding events. Measuring TTET as a function of urea concentration further gained position dependent rate constants for the transition from the partially unfolded states to the helical conformations. Time constants of 300-600 ns were observed for local helix formation with no clear posi-tion dependence. This argues for a similar probability for helix formation throughout the helix and indicates that helix formation from the coil state occurs in a single event involving major parts of the structure.

Introduction

Around 30% of all amino acid residues in protein structures are found in α-helices making the α-helix is the most abundant secondary structure (1). In many proteins helix formation has been shown to occur fast and before the establishment of the native tertiary structure (2; 3). The factors that govern stability in short model helices have been studied in great detail both theoretically and experimentally (for a review see (4)). The thermodynamics of helix stability are well understood and helix content can be predicted accurately for small peptides using Zimm-Bragg or Lifson-Roig theory (5-7). It has been found experimentally that small alanine based peptides can form stable α-helices (8-10) and helix propensities for all 20 amino acids have been determined (4).However, the kinetics of helix formation are still not very well characterized. In helix-coil transition models, the establishment of a first helical turn from a completely random peptide is assumed to be a very unlikely event and entropically unfavourable. Thus, helix nucleation is thought to occur on a slower timescale than the addition of further helical turns at both ends of the growing helix.

Despite numerous theoretical studies on the helix-coil transitions, little is known on the kinetics of helix formation starting from the ensemble of unfolded states. Helix dynamics in long homopolymers were measured using dielectric relaxation (11) and ultrasonic absorption techniques (12), which gave relaxation times on the 100's of nanoseconds time scale, depending on solvent and amino acid sequence. This gave helix growth time constants in the range of 0.1 to 10 ns,. With the development of nanosecond temperature jump methods studies on the helix-coil transition were continued on smaller model peptides. Using infrared spectroscopy (13-18) or UV Raman spectroscopy (19) relaxation time constants in the ten nanosecond to microsecond range were detected for unfolding of small alanine-based helices, corresponding well

to the earlier results from relaxation studies (11). Using fast relaxation experiments allowed to determine time-dependent changes in the overall helical content, but they did not yield any information on local helix stability and dynamics. Using fluorescence techniques the dynamics at the N-terminus of a helical peptide was probed, which gave different time constants compared to measurements of the average helix content (14). Other experiments to obtain site specific relaxation times applied IR-spectroscopy in ^{13}C labelled peptides, but did not obtain any clear-cut results (18; 20).

We recently applied diffusion controlled triplet-triplet energy transfer (TTET) to observe dynamics in unfolded polypeptides (21; 22) and in protein fragments (23). This method allows to determine rate constants for intrachain loop formation (k_c) between a triplet donor (xanthone) and a triplet acceptor label (naphthylalanine) attached to specific sites on a polypeptide chain. Xanthone is excited to the triplet state with a 4 ns laser flash and undergoes intersystem crossing with $1/k_{ISC}$=2 ps with a quantum yield of 99% (24). The xanthone triplet population is detected by the triplet absorption band at 590 nm. Upon van der Waals contact between the labels the triplet energy is rapidly transferred to naphthylalanine with a time constant for TTET of $1/k_{TTET} < 2$ ps. Similar to hydrogen/deuterium exchange, TTET should be able to measure dynamics in folded and partially folded structures, if the conformational transitions between the folded and the unfolded state are slower than loop formation between the labels in the unfolded state. A pre-requisite for this approach is that contact formation is prevented in the folded structure. The advantage of such a method is that measurements can be conducted in equilibrium, even if the equilibrium strongly favours the folded state and that dynamics in different parts of a folded structure can be monitored by changing the position of the triplet labels.

We wanted to test whether TTET from xanthone to naphthylalanine attached at different positions in an α-helical peptide can be used to measure local helix stability and dynamics. Earlier experiments by Lapidus *et al.* (25) had indicated that helix formation prevents contact formation between the ends of an α-helix. We introduced xanthone and naphthylalanine moieties at different positions and with different spacing into short helical peptides and measured TTET with ns resolution. The resulting kinetics were compared to global helix dynamics probed in a peptide where the TTET labels were attached to the ends of the same helix. We further used urea to destabilize the helices, which gained information on the unfolding and refolding rate constants for the helix-coil transition at different positions in the α-helix.

Results and Discussion

Design and helix content of the peptides

To observe local dynamics in an α-helix contact formation reactions were measured in peptides of the general design Ac-$(A)_5$-$(AAARA)_3$-A-NH_2. This peptide is reported to exhibit high helicity (> 80%) in solution around 0^oC (26; 27) and the unfolding kinetics of similar peptides have been probed in several relaxation studies (13; 14; 19; 28; 29). We introduced TTET labels at different positions of the α-helix using the non-natural amino acid 1-naphthlylalanine (NAla) and by attaching the xanthone moiety (Xan) to the N-terminus or to the side chain of the non-natural amino acid α,β-diaminopropionic acid (for sequences see table 1).

To monitor global helix unfolding and refolding the TTET labels were positioned at the ends of the helix (peptide X0N22, see fig. 1.A). To observe local dynamics the labels were separated by six residues (i, i+6) to prevent contact in the helical state

(fig. 1.B). The positions of the labels were varied throughout the sequence. Five different peptides were synthesized which probe local dynamics at the N-terminus (X1N7), in the interior (X5N11, X7N13), and at the C-terminus (X11N17, X21N15). For comparison, the naphtyl moiety was separated by four residues (i, i+4) from the xanthone group (X7N11). This results in both labels being at the same side of the helix and thus enabling contact in the helical state (fig. 1.C).

To test the effect of the labels on helical content we recorded circular dichroism (CD) spectra for all peptides at 5^{o} C (see fig. 2.A). Due to the contributions of NAla to the CD signal around 220 nm only relative differences in helical content can be determined. Figure 2.A shows that the peptide X7N11 with Xan and NAla in the (i, i+4) position exhibits the highest helical content, indicating stabilizing hydrophobic interactions of the labels. Introduction of (i, i+6) spaced labels into the helix interior or at the N-terminus has a destabilizing effect as seen from the spectra of X1N7, X5N11, X7N13 and X11N17 compared to the peptide which carries the labels at both ends. Only if the labels are situated directly at the C-terminus in X21N15 they do not affect helix stability. Temperature unfolding curves of all peptides were measured by CD at 222nm (fig. 2.B). The temperature transition curves are broad and a high temperature baseline for unfolded peptides is reached above 60^{o} C for the destabilized peptides with (i, i+6) spaced labels in the center. The other peptides show still some helical content up to 80^{o}C. The X7N11 peptide however exhibits very high stability and is not completely unfolded at 98^{o}C. These results show that the replacement of interior alanine residues by the labels has a large impact on global helicity, while the perturbation is smaller at end-positions. This is in agreement with experimental results on the position dependent effect of alanine to glycine substitutions on helix stability (30) and with predictions from Lifson-Roig theory (6; 7).

Contact formation experiments

To probe the influence of helical structure on intrachain contact formation we performed TTET experiments at 5° C. Figure 3 compares the decay of xanthone triplet absorbance at 590 nm in peptides carrying the labels at different positions in the helix. For all peptides, double exponential fits are required to fit the data. The fit results are given in table 2. The slowest kinetics are observed for end-to-end contact formation in X0N22 where the fit yields a main kinetic phase with a rate constant λ_2 = $2.2 \cdot 10^5$ s^{-1} (90% amplitude) and a faster phase with λ_1 = $2.0 \cdot 10^6$ s^{-1} (10% amplitude). In the case of local (i, i+6) contacts at the termini or in the interior of the helix, similar behavior is observed. In the X7N13 peptide the labels are in the central portion of the peptide. Here, a fast phase with a rate constant of λ_1 = $5.3 \cdot 10^6$ s^{-1} (17% amplitude) and a slower phase with λ_2 = $5.4 \cdot 10^5$ s^{-1} (83% amplitude) are observed. In the X1N7 peptide which probes the N-terminus, a faster process with λ_1 = $1.1 \cdot 10^7$ s^{-1} (29% amplitude) is followed by a slower process with λ_2 = $2.4 \cdot 10^6$ s^{-1} (71% amplitude). In the X11N17 peptide, reflecting local dynamics in the C-terminal portion of the helix, a fast phase with λ_1 = $2.4 \cdot 10^7$ s^{-1} (42% amplitude), and a slower phase with λ_2 = $2.9 \cdot 10^6$ s^{-1} (48% amplitude) are detected. Thus the observed dynamics are generally faster at the helix termini and the fast phase has a larger amplitude at these positions.

The X21N15 peptide, which probes local dynamics directly at the C-terminus, does not show pronounced double exponential kinetics and only a fast phase with λ_1 = $1.2 \cdot 10^7$ s^{-1} remains. The absence of double exponential behavior indicates that the C-terminal part of the peptide is mainly unstructured. These findings are corroborated by earlier results which show that the C-terminus of an α-helix is significantly less stable than the N-terminus (31-33).

The X7N11 peptide which carries the labels at the (i, i+4) position serves as a model for the case where contact is possible in the helical state. In this peptide no TTET on the nanosecond time scale could be observed since transfer already occurs in the dead time of the experiment (10 ns). The observed stabilization of helical structure seen in the CD spectra presumably results from interactions between the labels, which allows triplet transfer on a sub-nanosecond timescale. These findings show, that interactions between the triplet labels in the helical state lead to very fast TTET, which cannot be resolved by our measurements.

As TTET on the nanosecond to microsecond timescale is observed in peptides with the labels in (i, i+6) position, this shows that no contact is possible if helical structure is present at the label position. To establish contact, the helix has to unfold which results in the slow process observed in the kinetics. Thus, increased helix stability should increase the amplitude of the slow phase and further decrease observed contact formation kinetics.

To test this model, the helical conformation of the X7N13 peptide, having the labels at the ith and (i+6)th postions, was stabilized by addition of 40% TFE to the solution. TTET experiment on this peptide showed a single exponential decay of the xanthone triplet absorption with a rate constant $k = 9.1 \cdot 10^4$ s^{-1} at 5^o C. This shows that stabilization of the helix leads to a disappearance of the fast kinetic phase. In addition, the slow phase is further slowed down by two orders of magnitude compared to an unstructured peptide (see fig. 2). This leads to the conclusion that no contact is possible in the helical state and that the slow process monitors opening of helical structure. The time constants of the slow observed phases in all the peptides are in the 100's of nanoseconds to two microsecond time scale, which is in good agreement with relaxa-

tion time constants from temperature jump experiments. This is another indication that helix unfolding is monitored by λ_2.

Kinetic modeling and Urea Dependence

As the helical state does not allow contact formation but at least partial unfolding to the coil state is required to allow TTET we obtain a kinetic scheme (see equation [1]) which is similar to the situation in hydrogen exchange experiments. The helix-coil equilibrium is coupled to the fast reaction of contact formation which allows monitoring of the microscopic rate constants of helix unfolding and refolding. For contact formation in an α-helical peptide the kinetic system can be formulated as follows

$$H^* \underset{k_f}{\overset{k_u}{\rightleftarrows}} C^* \xrightarrow{k_c} C \qquad [1]$$

This model includes two ensembles of conformations. Peptides, which have helical structure formed and cannot establish contact between the labels denoted *H* are in equilibrium with another conformational ensemble, where contact is allowed by a partial opening of the structure, denoted *C*. The asterisk denotes an excited donor which transfers the triplet energy to the acceptor upon contact. The microscopic rate constants k_u and k_f report on the forth and back transitions between these two populations and contain information about the local dynamics of the α-helix, whereas k_c denotes the contact formation reaction due to chain diffusion. A kinetic three-state system has two eigenvalues (see equation [2]), the observable rate constants λ_1 and λ_2, which depend on the microscopic rate constants k_u, k_f and k_c.

$$\lambda_1 = \frac{1}{2}(p+q), \quad p = k_u + k_f + k_c, \quad q = \sqrt{p^2 - 4k_u k_c}$$
$$\lambda_2 = \frac{1}{2}(p-q) \qquad [2]$$

A special case for the kinetics arises if the folded helical state *H* is stable ($k_f >> k_u$). Then the slower eigenvalue λ_2 dominates the kinetics and only one phase is observed. If additionally contact formation is much faster than helix unfolding ($k_c >> k_f$) then λ_2 corresponds directly to k_u. This limit corresponds to the EX1 limit in hydrogen exchange (34). In the situation, where all microscopic rate constants are in the same range however, λ_1 and λ_2 and the corresponding amplitudes of the two kinetic phases can be used to gain information about all microscopic rate constants.

Such a regime can be reached for all peptides by varying the helix content upon changing the temperature or by addition of denaturants as urea. It has been shown that addition of urea leads to unfolding of helices (35) with the equilibrium constant of helix propagation depending linearly on urea concentration. The amplitudes of the two observed kinetic phases are functions of the microscopic rate constants (36). The dependence of the logarithm of the microscopic rate constants on urea concentration is assumed to be linear following the relation

$$\ln k_i = \ln k_0 - \frac{m_i \cdot [urea]}{RT} \qquad [3]$$

where k_i denotes any microscopic rate constant, k_0 is the rate constant of the reaction in the absence of urea and m_i is the kinetic *m*-value of the reaction. This behaviour is found for many protein folding reactions, where it is interpreted as the denaturant dependence of the free energy of activation (37). For contact formation reactions

linear relationships have been found as well, resulting from a superposition of viscosity effects and weak denaturant binding to the polypeptide chain (38).

Contact formation experiments were performed in solutions containing different concentrations of urea from 1 M to 7 M at 5°C. As in the absence of denaturant double exponential functions were necessary to describe the data. The rate constants and amplitudes obtained from fits to the experimental curves of four selected peptides are shown in fig. 3.

A global fit to the observed rate constants λ_1 and λ_2 and the corresponding amplitudes A_1 and A_2 of every peptide system was performed applying the three-state model including the urea dependence of the microscopic rate constants (equations [1] and [3]). The fit and the urea dependence of the microscopic rate constants are included in fig. 3 as solid lines. The slow observable rate constant λ_2 corresponds approximately to the helix opening rate constant k_u, while λ_1 corresponds to contact formation k_c. On the other hand, the rate constant which reports on local structure formation, k_f, is defined through the amplitudes of the observed kinetic phases. If the helical structure is stable, the slow phase dominates the kinetics. However, upon destabilization of the helix the kinetics become biphasic and a fast process appears which corresponds to the contact formation reaction. The amplitudes are a function of all microscopic rate constants but essentially report on the ratio of k_u over k_f.

End-to-end loop formation in the X0N22 peptide (fig. 3.A) gets increasingly faster as the helical structure is destabilized with urea. The slow rate constant λ_2 is accelerated with increasing urea concentration and the corresponding amplitude is decreased from 90% to around 60% at 7 M urea, while the fast rate constant remains almost constant but the corresponding amplitude increases. This results from a decrease in k_f with increasing urea concentration. At 3.9 M urea, the microscopic helix unfolding rate constant k_u equals the helix refolding k_f which reports on the unfolding equilib-

rium. At 7M urea the peptide seems largely unfolded as judged by CD spectroscopy. However, significant amounts of residual helical structure can be detected in the contact formation experiments by the ratio of slow and fast amplitude even at this high urea concentration.

In the X7N13 peptide (fig. 3.C), where local dynamics in the center of the helix are probed, λ_1 and λ_2 show a similar behavior as in the X0N22 peptide. However, the amplitudes have a much stronger dependence on the urea concentration. Compared to global helix unfolding as reported by TTET in the X0N22 peptide, the local structure is unfolded already at lower urea concentrations as judged by the equilibrium k_u/k_f which reaches unity at 1.8 M urea.

Helix dynamics at the helix termini, as seen in X1N7 and X11N17 (Fig 3.B and D), show a slightly different behavior. Here, λ_1 and λ_2 both get slower with increasing urea concentration. In both peptides, the local stability is much lower. The equilibrium constant for helix unfolding k_u/k_f reaches unity at 0.2 M urea for the X1N7. For the C-terminal part, k_u is larger under all conditions.

Results of the Global Fit. For all peptides which show helical structure in the region of the labels, the microscopic rate constants and urea m-values obtained from the global fits are shown in figure 5.A and B and are given in table 2. The rate constants of local helix opening k_u are faster at the termini compared to the peptides which probe motions at the center of the peptide. The corresponding m_u-values show an interesting behavior. While m_u is positive for the N- and C-terminal label positions resulting in a decrease of k_u with increasing denaturant concentration, it is negative in the center. At these positions, helix unfolding is accelerated by urea, pointing to a reaction that is limited by a free energy barrier. This is consistent with denaturant action observed in proteins (37).

Besides decreasing protein and helix stability, urea has pronounced effects on solvent properties and chain dynamics since it increases viscosity and slows down loop formation (38). If local structure is weakly formed and almost no unfolding barrier exists, viscosity and binding effects probably outbalance the acceleration caused by structure disruption leading to positive m_u-values in these peptides. For the global helix dynamics in the X0N22 peptide a negative m_u-value is found as well, indicating that a similar process is probed in X0N22 as at the center positions.

The microscopic rate constants for contact formation k_c in the coil state are lower in the center compared to the termini. This indicates that in the center chain dynamics are still influenced by structure even in the population of peptides that are able to establish contact. The m_c-values show strong urea dependent kinetics at the terminal positions, as expected for unstructured peptides where the *m*-value for end-to-end contact formation in homopolymers was determined as ~300 J $mol^{-1}M^{-1}$ (38). In the center and for global helix dynamics however urea has almost no influence on k_c. A possible cause for this discrepancy is a superposition of two effects. On the one hand, helical structure that hinders chain dynamics is dissolved leading to more flexibility. On the other hand, urea leads to extended chain conformations (A. Möglich, *et al.*, *to be submitted*), increased solvent viscosity and slows down chain dynamics. In combination, these effects cancel out leading to a low m_c-value. When extrapolated to 8 M urea the rate constants for intrachain contact formation k_c are all similar with $4.7(\pm0.06)\cdot10^6\ s^{-1}$ for X5N11, X7N13 and X11N17. X1N7 is slightly faster with k_c = $6.36\cdot10^6\ s^{-1}$ because the xanthone is attached at the N-terminal position and its motion is not hindered by tail effects (B. Fierz & T. Kiefhaber, *to be submitted*). This shows that when no local structure persists, chain dynamics are limiting and similar at all positions.

The rate constant k_f, which reports on helical structure formation, is similar throughout the peptide and is highly dependent on urea concentration at all positions shown by high m_f-values. Thus, addition of urea, which leads to disruption of helical structure, acts mainly on k_f. The similar values of k_f over the whole peptide suggest that the same process of helix formation is monitored at any position.

Local and global dynamics in short alanine based α-helices.

We obtained site specific information about equilibrium dynamics in short α-helices using TTET to probe local and global helix unfolding at different urea concentrations. Double exponential kinetics were observed for intrachain contact formation reactions and interpreted using a kinetic three-state model.

Using the ratio of the microscopic rate constants which probe helix unfolding (k_u) and refolding (k_f) as an equilibrium constant for a local helix-coil equilibrium, information about local stability could be obtained. In contrast to global stability as probed by CD, the stability of local helical structure was found to be lower at the helix termini. This is in agreement with helix-coil theory (5; 6) and has been experimentally observed by amide hydrogen exchange (31; 39), in mutational studies (30), by NMR spectroscopy (40-44) or using electron spin resonance (45; 46). In addition, it was observed that in a peptide which probed the C-terminus, only very small amounts of structure were detected. These results show that TTET is able to probe local helix stability.

It was shown that local helix opening reactions at the N- and C-termini of a peptide are three to four times faster with time constants of 300 ns than in the center of the helix where time constants up to 1.4 μs were measured. Thus, helices are not only less stable at the ends but the unfolding dynamics and fluctuations are faster. The obtained time constants are comparable with results from temperature-jump studies

which probe global relaxation kinetics of helix unfolding and yield time constants in the range of 120 – 600 ns (13; 14; 16-20; 28) at different temperatures.

The *m*-values of the unfolding rate constants m_u can be used to gain insight into the mechanism of helix unfolding. Negative m_u-values in the range of -120 to -260 J mol^{-1} M^{-1} are obtained for global and local helix unfolding in the center of the peptide, corresponding to an increase in the rate constant with increasing urea concentrations. However, the peptides probing dynamics at the termini show positive m_u-values of 80-160 J mol^{-1} M^{-1}. This points to the absence of barriers for helix opening at the termini.

Local helix formation occurs on the same time scale as unfolding with time constants of 300-600 ns which are independent of position. The *m*-values which report on structure formation have been found to be large and positive with m_f = 650–800 J mol^{-1} M^{-1} which results in a strong decrease in k_f at high urea concentrations and thus to helix unfolding. As urea can compete for hydrogen bonds, intrachain interactions are less favorable and extended conformations are preferred. This has been observed in model peptides by fluorescence resonance energy transfer studies (A. Möglich, *et al.*, *to be submitted*). The competition for hydrogen bonds by urea abolishes the stabilizing force of helical structure thus helix nucleation and propagation is slowed down.

The global *m*-value of the helix coil transition, m_f-m_u reaches values of around ~1000 J/mol/M for the center part of the helix and ~ 500 J/mol/M for the termini. For urea induced helix unfolding, global m-values of 96 J/mol/M per residue have been obtained (35). This yields for a six residue helix a value of 577 J/mol/M well within the value obtained for the termini, whereas in the interior the values are by a factor of two larger. This shows, that the local information obtained in the interior contains

contribution from global helix unfolding and refolding while at the ends local events are probed.

The timescales of helix formation are still slower as predictions from molecular dynamics simulations, where nucleation rate constants in the 100's of picoseconds time regime have been found (47). Thus, our results can serve as a direct benchmark for molecular dynamics simulations.

Materials and Methods

Peptide Synthesis: All peptides were synthesized using standard fluorenylmethoxy-carbonyl- (Fmoc) chemistry on an Applied Biosystems synthesizer. The detailed procedures have been described before (22). In the peptide X0N22 two additional glycines were introduced at the C-terminus to improve the yield of synthesis.

Peptide Modification: The xanthone derivative 9-Oxoxanthen-2-carboxylic acid was prepared according to Graham and Lewis (48) and introduced on resin by PyBOP (Novabiochem) mediated coupling in dimethylformamide (DMF) to either the N-terminus or the free amino group of a diaminopropionic-acid (Dpr) residue. Fmoc-Dpr(Mtt) (Novabiochem) was deprotected after peptide synthesis using 3% trifluoroacetic acid in DMF. The naphtalene moiety was introduced as the nonnatural aminoacid naphtylalanine (Bachem) by standard peptide synthesis.

Peptide Purification: All peptides were purified to >90% purity by preparative HPLC over RP-8 columns. The purity of the peptides was checked by analytical HPLC, the mass was confirmed by MALDI mass spectrometry.

Measurement Apparatus: All measurements were performed on a Laser Flash Photolysis Reaction Analyzer (LKS.60) from Applied Photophysics. A Quantel Nd:YAG Brilliant laser (354.6 nm, ~4 nm pulse width, ~50 mJ) was used to selectively excite the xanthone moiety. Transient absorption traces were recorded at 590nm for the xanthone and at 420nm for the naphtalene triplet band.

Measurement Conditions: The measurements were performed in 10mM phosphate buffer, pH 7 at 5^{O} C, the pepide concentration was 50 μM as determined by UV-absorption at 343 nm using a molar extinction coefficient of 3900 M^{-1} for the xanthone moiety. All solutions were degassed prior to the measurements to minimize

oxygen quenching. Urea from Fluka, Switzerland was used whereas the concentrations were detemined by measuring the refractive index according to Pace (49).

Evaluation: For evaluation of the experimental curves the ProFit™ software (QuantumSoft, Zürich, Switzerland) was used.

Acknowledgements

We thank Stefan Biedert, Lena Chang, Fabian Käslin, Raphael Küng and Cédric Lienhart for assistance during the measurements.

Tables

Table 1:

Name	Label pos.	Sequence
X0N22	end-to-end	Xan-AAAAAAAARAAAAARAAAARA-NAla-GG-NH_2
X7N11	(i, i+4)	Ac-AAAAAA-Dpr(Xan)-ARA-NAla-AARAAAARAA-NH_2
X1N7	(i, i+6)	Ac-Dpr(Xan)-AAAAA-NAla-ARAAAARAAAARAA-NH_2
X5N11	(i, i+6)	Ac-AAAA-Dpr(Xan)-AAARA-NAla-AARAAAARAA-NH_2
X7N13	(i, i+6)	Ac-AAAAAA-Dpr(Xan)-ARAAA-NAla-RAAAARAA-NH_2
X11N17	(i, i+6)	Ac-AAAAAAAARA-Dpr(Xan)-AARA-NAla-AARAA-NH_2
X21N15	(i, i+6)	Ac-AAAAAAAARAAAAR-NAla-AAARA- Dpr(Xan)-NH_2

Peptides used in the study Xan: xanthone, NAla: 1-naphtylalanine, Dpr: α,β-diaminopropionic acid

Table 2:

Peptide	observable rate constants and amplitudes				Fit results from global fit to three-state model, values given at buffer conditions					
	λ_1 $\cdot 10^6\ s^{-1}$	λ_1 $\cdot 10^6\ s^{-1}$	A_1	A_2	k_u $\cdot 10^6\ s^{-1}$	k_f $\cdot 10^6\ s^{-1}$	k_c $\cdot 10^6\ s^{-1}$	m_u (J mol^{-1} M^{-1})	m_f (J mol^{-1} M^{-1})	m_c (J mol^{-1} M^{-1})
X0N22	2.01	0.22	0.11	0.89	0.34	0.84	1.48	-137	3 95	5.85
X1N7	11.3	2.37	0.29	0.71	2.90	3.05	13.9	160	698	226
X5N11	5.25	0.60	0.11	0.89	0.91	2.94	5.62	-117	776	46.1
X7N13	5.27	0.54	0.17	0.83	0.73	1.63	5.67	-262	693	52.4
X11N17	24.5	2.94	0.42	0.48	2.86	2.38	18.3	85	652	394

Fit results of the kinetic traces in 10mM phosphate buffer at 5oC and results from a global fit of the observable rate constants and amplitudes to the kinetic three-state model (see equations [1], [3]). All peptides are shown that exhibit helical structure at the label positions.

References

1. Barlow, D. J. & Thornton, J. M. (1988). Helix geometry in proteins. *J Mol Biol* 201, 601-19.
2. Baldwin, R. L. & Rose, G. D. (1999). Is protein folding hierarchic? I. Local structure and peptide folding. *Trends Biochem. Sci.* 24, 26-33.
3. Karplus, M. & Weaver, D. L. (1994). Protein folding dynamics: The diffusion-collision model and experimental data. *Protein Sci.* 3, 650-668.
4. Doig, A. J., Errington, N. & Iqbalsyah, T. M. (2005). Stability and Design of alpha-Helices. In *Protein Folding Handbook* (Buchner, J. & Kiefhaber, T., eds.), Vol. 1, pp. 247-313. 2 vols. WILEY-VCH, Weinheim.
5. Zimm, B. H. & Bragg, J. K. (1959). Theory of phase transition between helix and random coil in polypeptide chains. *Journ. Chem. Phys.* 31, 526-535.
6. Lifson, S. & Roig, A. (1961). On the theory of helix-coil transitions in polypeptides. *J. Chem. Phys.* 34, 1963-1974.
7. Munoz, V. & Serrano, L. (1994). Elucidating the folding problem of helical peptides using empirical parameters. *Nature Struct. Biol.* 1, 399-409.
8. Shoemaker, K. R., Kim, Brems, Marqusee, York, Chaiken, Stewart & Baldwin, R. L. (1985). Nature of the charged group effect on the stability of the C-peptide helix. *Proc. Natl. Acad. Sci. USA* 82, 2349-2353.
9. Marqusee, S. & Baldwin, R. L. (1987). Helix stabilization by Glu-…Lys+ salt bridges in short peptides of de novo design. *Proc. Natl. Acad. Sci. USA* 84, 8898-8902.
10. Marqusee, S., Robbins, V. H. & Baldwin, R. L. (1989). Unusually stable helix formation in short alanine-based peptides. *Proc Natl Acad Sci U S A* 86, 5286-5290.
11. Schwarz, G. & Seelig, J. (1968). Kinetic Properties and the Electric Field Effect of the Helix-Coil Transition of Poly(g-benzyl L-Glutamate) Determined from Dielectric Relaxation Measurements. *Biopolymers* 6.
12. Gruenewald, B., Nicola, C. U., Lustig, A. & Schwarz, G. (1979). Kinetics of the helix-coil transition of a polypeptide with non-ionic side chain groups, derived from ultrasonic relaxation measurements. *Biopys. Chem.* 9, 137-147.
13. Williams, S., Causgrove, T. P., Gilmanshin, R., Fang, K. S., Callender, R. H., Woodruff, W. H. & Dyer, R. B. (1996). Fast events in protein folding: helix melting and formation in a small peptide. *Biochemistry* 35, 691-697.
14. Thompson, P., Eaton, W. & Hofrichter, J. (1997). Laser temperature jump study of the helix-coil kinetics of an alanine peptide interpreted with a "kinetic zipper" model. *Biochemistry* 36, 9200-9210.
15. Thompson, P. A., Munoz, V., Gouri, S. J., Henry, E., Eaton, W. A. & Hofrichter, J. (2000). The Helix-Coil Kinetics of a Heteropeptide. *J. Phys. Chem. B* 104, 378-389.
16. Huang, C. Y., Getahun, Z., Zhu, Y., Klemke, J. W., DeGrado, W. F. & Gai, F. (2002). Helix formation via conformation diffusion search. *Proc Natl Acad Sci U S A* 99, 2788-93.
17. Huang, C. Y., Klemke, J. W., Getahun, Z., DeGrado, W. F. & Gai, F. (2001). Temperature-dependent helix-coil transition of an alanine based peptide. *J Am Chem Soc* 123, 9235-8.
18. Huang, C. Y., Getahun, Z., Wang, T., DeGrado, W. F. & Gai, F. (2001). Time-resolved infrared study of the helix-coil transition using (13)C-labeled helical peptides. *J Am Chem Soc* 123, 12111-2.
19. Lednev, I. K., Karnoup, A. S., Sparrow, M. C. & Asher, S. A. (1999). Alpha-Helix Peptide Folding and Unfolding Activation Barriers: A Nanosecond UV Resonance Raman Study. *J Am Chem Soc* 121, 8074-8086.

20. Werner, J. H., Dyer, R. B., Fesinmeyer, R. M. & Andersen, N. H. (2002). Dynamics of the Primary Processes of Protein Folding: Helix Nucleation. *J. Phys. Chem. B* 106, 487-494.
21. Bieri, O., Wirz, J., Hellrung, B., Schutkowski, M., Drewello, M. & Kiefhaber, T. (1999). The speed limit for protein folding measured by triplet-triplet energy transfer. *Proc. Natl. Acad. Sci. USA* 96, 9597-9601.
22. Krieger, F., Fierz, B., Bieri, O., Drewello, M. & Kiefhaber, T. (2003). Dynamics of Unfolded Polypeptide Chains as a Model for the Earliest Steps in Protein Folding. *J Mol Biol* 332, 265-274.
23. Krieger, F., Fierz, B., Axthelm, F., Joder, K., Meyer, D. & Kiefhaber, T. (2004). Intrachain diffusion in a protein loop fragment from carp parvalbumin. *Chem. Phys.* 307, 209-215.
24. Satzger, H., Schmidt, B., Root, C., Zinth, W., Fierz, B., Krieger, F., Kiefhaber, T. & Gilch, P. (2004). Ultrafast Quenching of the Xanthone Triplet by Energy Transfer: New Insight into the Intersystem Crossing Kinetics. *J. Phys. Chem. A* 108, 10072-10079.
25. Lapidus, L. J., Eaton, W. A. & Hofrichter, J. (2002). Measuring dynamic flexibility of the coil state of a helix-forming peptide. *J Mol Biol* 319, 19-25.
26. Lockhart, D. J. & Kim, P. S. (1992). Internal stark effect measurement of the electric field at the amino terminus of an α-helix. *Science* 257, 947-951.
27. Lockhart, D. J. & Kim, P. S. (1993). Electrostatic screening of charge and dipole interactions with the helix backbone. *Science* 260, 198-202.
28. Thompson, P. A., Munoz, V., Jas, G. S., Henry, E. R., Eaton, W. A. & Hofrichter, J. (2000). The Helix-Coil Kinetics of a Heteropeptide. *J. Phys. Chem. B* 104, 378-389.
29. Huang, C. Y., He, S., DeGrado, W. F., McCafferty, D. G. & Gai, F. (2002). Light-induced helix formation. *J Am Chem Soc* 124, 12674-5.
30. Chakrabartty, A., Schellman, J. A. & Baldwin, R. L. (1991). Large differences in the helix propensities of alanine and glycine. *Nature* 351, 586-588.
31. Rohl, C. A. & Baldwin, R. L. (1994). Exchange kinetics of individual amide protons in 15N-labeled helical peptides measured by isotope-edited NMR. *Biochemistry* 33, 7760-7.
32. Silva, R. A., Kubelka, J., Bour, P., Decatur, S. M. & Keiderling, T. A. (2000). Site-specific conformational determination in thermal unfolding studies of helical peptides using vibrational circular dichroism with isotopic substitution. *Proc Natl Acad Sci U S A* 97, 8318-23.
33. Decatur, S. M. & Antonic, J. (1999). Isotope-Edited Infrared Spectroscopy of Helical Peptides. *J Am Chem Soc* 121, 11914-11915.
34. Hvidt, A. & Nielsen, S. O. (1966). Hydrogen exchange in proteins. *Advan. Prot. Chem.* 21, 287-386.
35. Scholtz, J. M., Barrick, D., York, E. J., Stewart, J. M. & Baldwin, R. L. (1995). Urea unfolding of peptide helices as a model for interpreting protein unfolding. *Proc Natl Acad Sci U S A* 92, 185-9.
36. Kiefhaber, T., Kohler, H. H. & Schmid, F. X. (1992). Kinetic coupling between protein folding and prolyl isomerization. I. Theoretical models. *J. Mol. Biol.* 224, 217-229.
37. Myers, J. K., Pace, C. N. & Scholtz, J. M. (1995). Denaturant m values and heat capacity changes: relation to changes in accessible surface areas of protein unfolding. *Protein Sci.* 4, 2138-2148.
38. Moglich, A., Krieger, F. & Kiefhaber, T. (2005). Molecular basis for the effect of urea and guanidinium chloride on the dynamics of unfolded polypeptide chains. *J Mol Biol* 345, 153-62.

39. Rohl, C. A., Scholtz, J. M., York, E. J., Stewart, J. M. & Baldwin, R. L. (1992). Kinetics of amide proton exchange in helical peptides of varying chain lengths. Interpretation by the Lifson-Roig equation. *Biochemistry* 31, 1263-1269.
40. Jimenez, M. A., Blanco, F. J., Rico, M., Santoro, J., Herranz, J. & Nieto, J. L. (1992). Periodic properties of proton conformational shifts in isolated protein helices. An experimental study. *Eur J Biochem* 207, 39-49.
41. Liff, M. I., Lyu, P. C. & Kallenbach, N. R. (1991). Local effect of glycine substitution in a model helical peptide. *J Am Chem Soc* 113, 1014-1019.
42. Bradley, E. K., Thomason, J. F., Cohen, F. E., Kosen, P. A. & Kuntz, I. D. (1990). Studies of synthetic helical peptides using circular dichroism and nuclear magnetic resonance. *J Mol Biol* 215, 607-22.
43. Pease, J. H., Storrs, R. W. & Wemmer, D. E. (1990). Folding and activity of hybrid sequence, disulfide-stabilized peptides. *Proc Natl Acad Sci U S A* 87, 5643-7.
44. Osterhout, J. J., Baldwin, R. L., York, E. J., Stewart, J. M., Dyson, H. J. & Wright, P. E. (1989). 1H NMR studies of the solution conformations of an analogue of the C-peptide of ribonuclease A. *Biochemistry* 28, 7059-7064.
45. Miick, S. M., Casteel, K. M. & Millhauser, G. L. (1993). Experimental molecular dynamics of an alanine-based helical peptide determined by spin label electron spin resonance. *Biochemistry* 32, 8014-21.
46. Miick, S. M., Todd, A. P. & Millhauser, G. L. (1991). Position-dependent local motions in spin-labeled analogues of a short alpha-helical peptide determined by electron spin resonance. *Biochemistry* 30, 9498-503.
47. Hummer, G., Garcia, A. E. & Garde, S. (2001). Helix nucleation kinetics from molecular simulations in explicit solvent. *Proteins* 42, 77-84.
48. Graham, R. & Lewis, J. R. (1978). Synthesis of 9-Oxoxanthen-2-carboxylic acids. *J. Chem. Soc. Perkin I*, 876-881.
49. Pace, C. N. (1986). Determination and analysis of urea and guanidine hydrochloride denaturation curves. *Meth. Enzymol.* 131, 266-280.

Figure Captions

Figure 1: Models of peptides in helical structure. **A)** X0N22 helix, the TTET labels xanthone and naphthalene are shown in red. The xanthone moiety was attached to the N-terminus of the peptide while the naphthalene is introduced by using the non-natural amino acid naphtylalanine **B)** X7N13 helix, the xanthone moiety is attached to the sidechain of diaminopropionic acid, due to the (i, i+6) spacing the labels are positioned at different sides of the helix **C)** X7N11 helix, the (i, i+4) spacing allows contact in the helical state. The arginines are shown in blue, the labels xanthone and naphthalene are shown in red

Figure 2: A) Far UV CD spectra of all peptides used in the study. The spectra were recorded in 10 mM phosphate buffer pH 7 at 22.5°C in 1 mm cells. **B)** Temperature transitions monitored at 222 nm of the same peptides (—) X0N22, (—) X7N11, (—) X1N7, (—) X5N11, (—) X7N13, (—) X11N17, (—)X21N15.

Figure 3: Normalized contact formation kinetics monitored by the decay of xanthone triplets at 590 nm due to TTET upon contact formation in (—) X0N22, (—) X1N7, (—) X7N13, (—) X11N17, (—)X21N15 and (—) X7N13 in 40% TFE.

The traces were recorded at 50 μM in 10 mM phosphate buffer pH 7 at 5°C. The black lines are double exponential fits to the data. The fit results are given in figure 4 for X0N22, X1N7, X7N13 and X11N17, while for X21N15 $\lambda_1 = 1.14 \cdot 10^7\ s^{-1}$ with $a_1 = 0.86$ and $\lambda_2 = 7.5 \cdot 10^5\ s^{-1}$ and $a_2 = 0.14$, and for X7N13 in 40% TFE $\lambda = 9.1 \cdot 10^4\ s^{-1}$ are obtained.

Figure 4: Upper panels: Observed rate constants (■)λ_1 and (●)λ_2 of contact formation in peptides which probe global helix dynamics in X0N22, local motions at the N-terminus in

X1N7, dynamics in the center in X7N13 and local motions at the C-terminus in X11N17. The solid lines (—) and (—) are the global fits of the observable rate constants λ_1 and λ_2 to the tree-state-model (equations [1], [3]) while the calculated dependence of the microscopic rate constants obtained from the fit is given for k_u by (—), for k_f by (—) and by k_c by (—). The fit results are given in figure 5 and table 2. **Middle panels:** Amplitudes (■) a_1 and (●) a_2 corresponding to the observed rates from the fits to the experimental decay curves. The solid lines (—) and (—) are the global fits of the amplitudes corresponding to the two observable exponential phases. **Lower panels:** The CD signal at 222 nm at different urea concentrations shows global helix unfolding in contrast to the local structure probed with the dynamic experiments.

Figure 5: A) Microscopic rate constants k_u (♦), k_f (♦), k_c (■) from the global fit to the three-state-model. The dashed lines show the values for global helix dynamics monitored by X0N22 **B)** The m – values m_u (♦), m_f (♦), m_c (■) corresponding to the microscopic rate constants. The dashed lines show the global *m*-values for helix dynamics monitored by X0N22

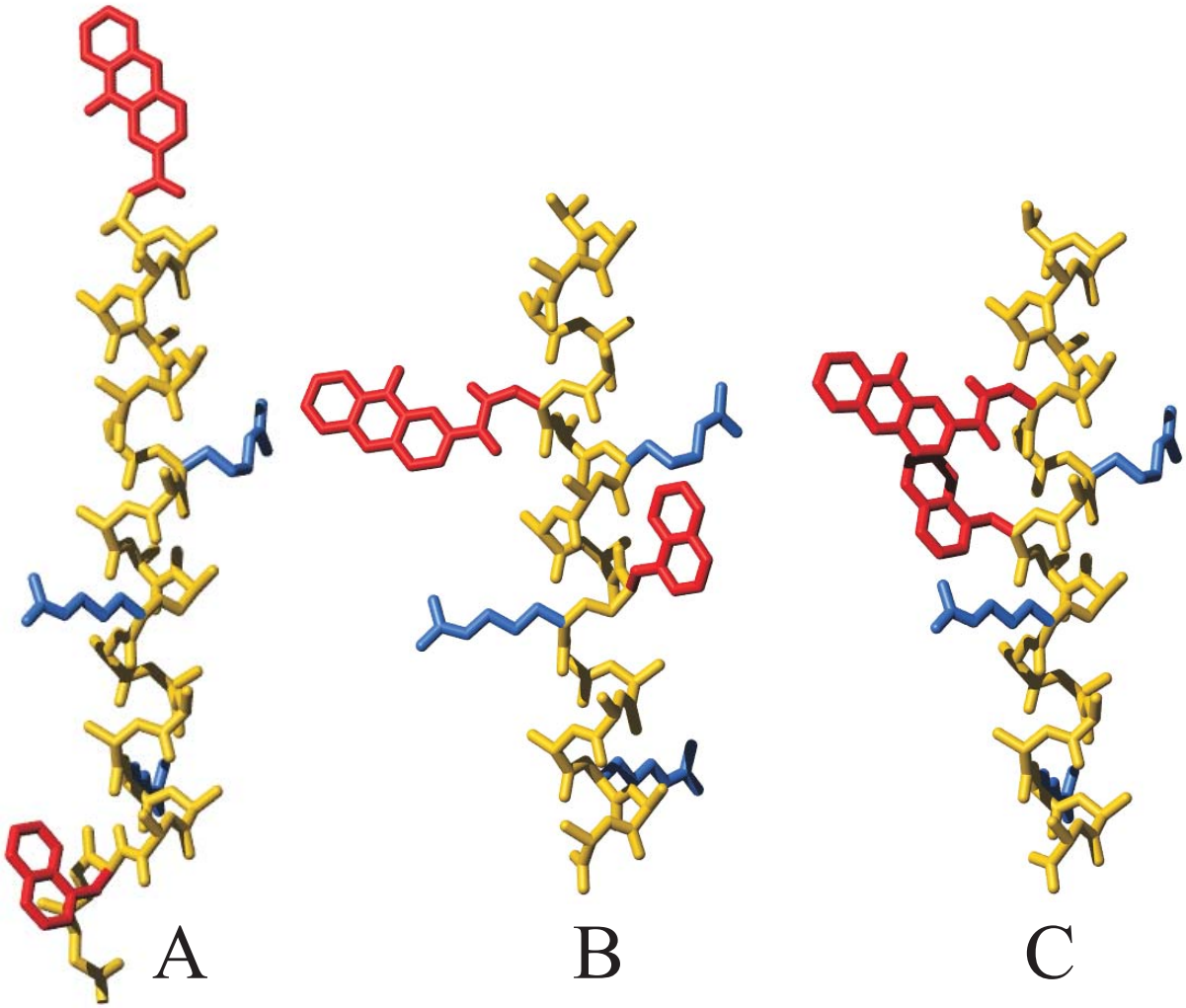

Figure 1

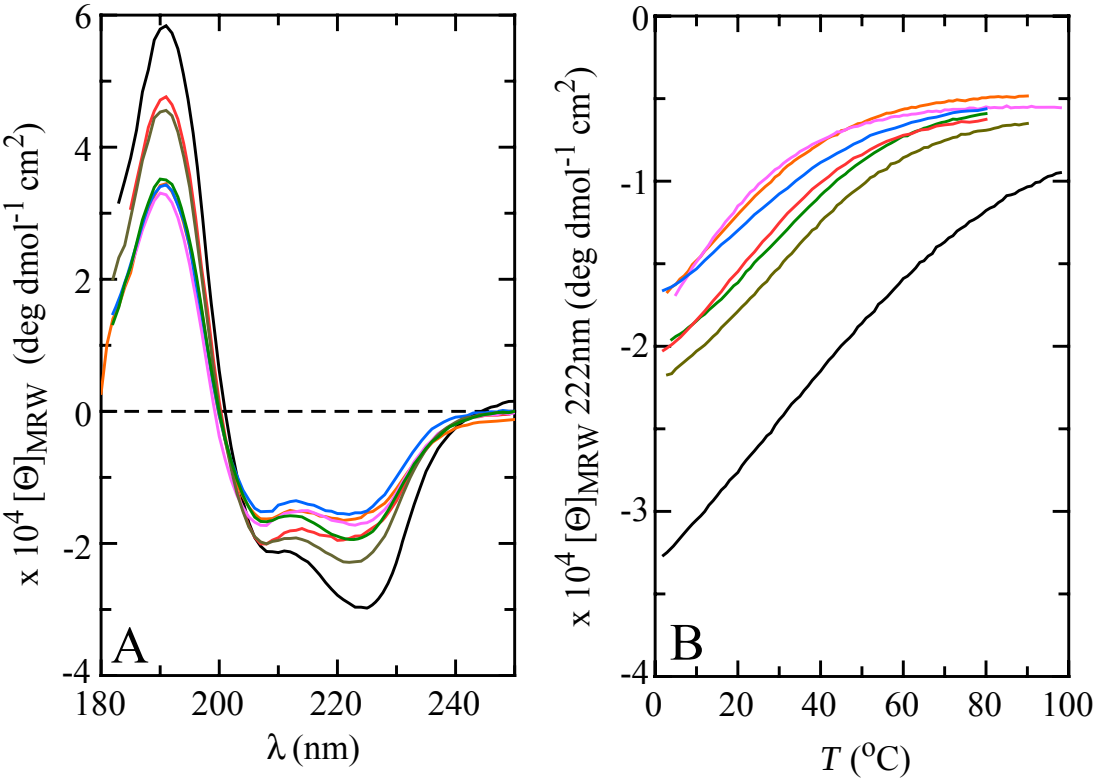
6
4
2
0
-2
-4
x 10^4 [Θ]MRW (deg dmol-1 cm2)
A
180
200
220
240
λ (nm)
0
-1
-2
-3
-4
x 10^4 [Θ]MRW 222nm (deg dmol-1 cm2)
B
0
20
40
60
80
100
T (°C)

Figure 2

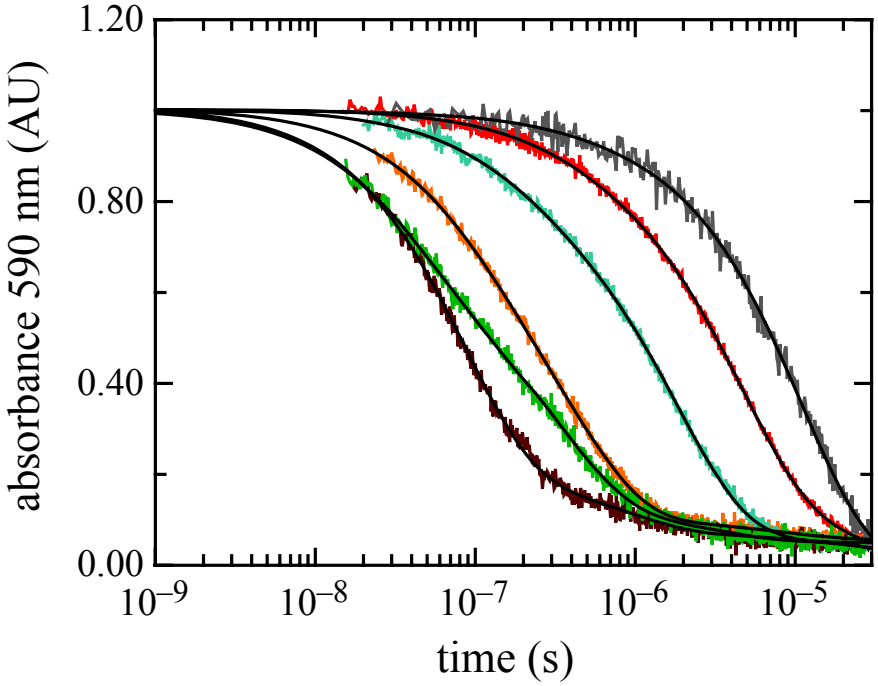

Figure 3

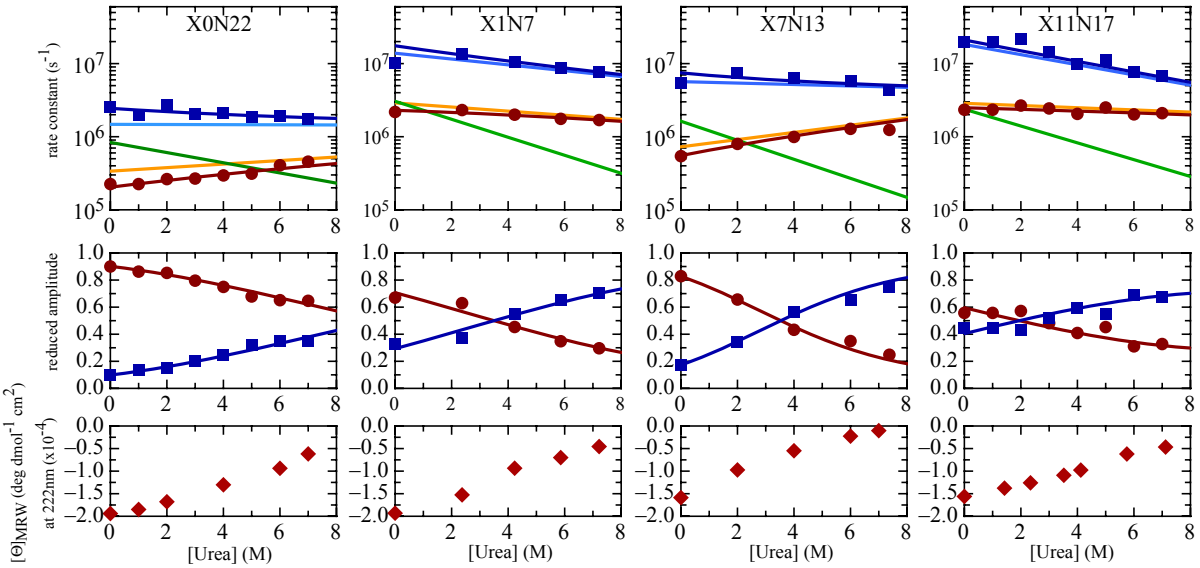
X0N22
X1N7
X7N13
X11N17
rate constant (s^{-1})
reduced amplitude
[Θ]$_{MRW}$ (deg dmol^{-1} cm^2) at 222nm (x10^{-4})
[Urea] (M)

Figure 4

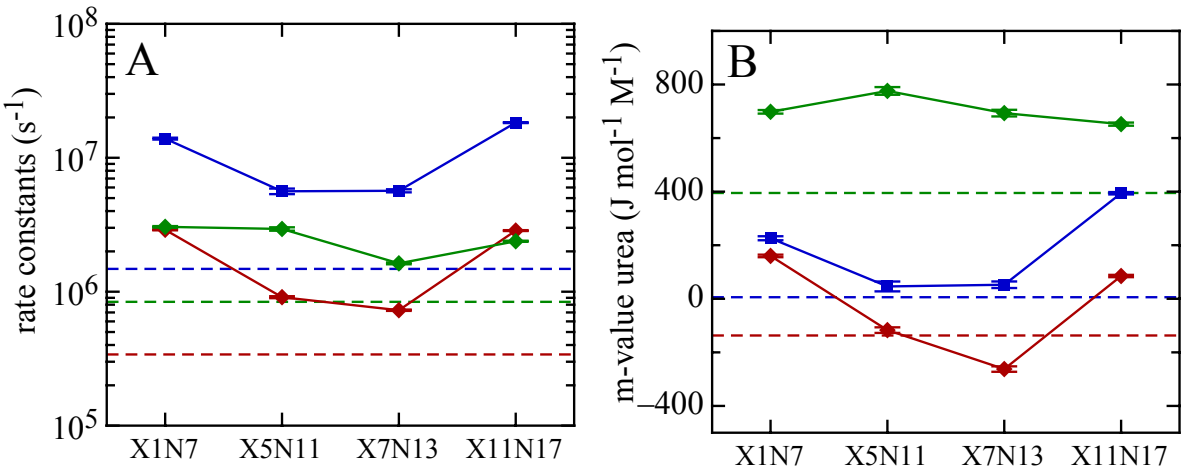
A
B
rate constants (s-1)
m-value urea (J mol-1 M-1)
10^8
10^7
10^6
10^5
800
400
0
–400
X1N7
X5N11
X7N13
X11N17

Figure 5

22
Dynamics of Unfolded Polypeptide Chains

Beat Fierz and Thomas Kiefhaber

22.1
Introduction

During protein folding the polypeptide chain has to form specific side-chain and backbone interactions on its way to the native state. An important issue in protein folding is the rate at which a folding polypeptide chain can explore conformational space in its search for energetically favorable interactions. Conformational search within a polypeptide chain is limited by intrachain diffusion processes, i.e., by the rate at which two points along the chain can form an interaction. The knowledge of the rates of intrachain contact formation in polypeptide chains and their dependence on amino acid sequence and chain length is therefore essential for an understanding of the dynamics of the earliest steps in protein folding and for the characterization of the free energy barriers for protein folding reactions. In addition, intrachain diffusion provides an upper limit for the speed at which a protein can reach its native state just like free diffusion provides an upper limit for the rate constant of bimolecular reactions. Free diffusion of particles in solution was treated extensively almost 100 years ago by Einstein and von Smoluchowski [1–3] but until recently, only little was known about the absolute time scales of intrachain diffusion in polypeptides. Numerous theoretical studies have been made to investigate the process of intrachain diffusion in polymers [4–10]. These studies derived scaling laws for intrachain diffusion and made predictions on the kinetic behavior of the diffusion process but they were not able to give absolute numbers. This chapter will briefly introduce some theoretical concepts used to treat chain diffusion and then discuss experimental results on intrachain diffusion from different model systems.

22.2
Equilibrium Properties of Chain Molecules

Since chain dynamics strongly depend on the chain conformation we will briefly present some polymer models for chain conformations. This topic is discussed in

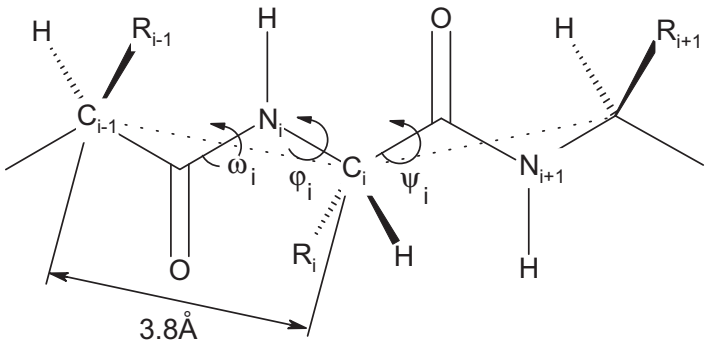

Fig. 22.1. Schematic representation of a polypeptide chain. The R_i denote the different amino acid side chains, the dashed lines denote the virtual chain segment. Adopted from Ref. [12].

more detail in Chapter 20 and in Refs [11–15]. The most simple description on an unfolded state of a protein is the idealized notion of a random coil. In a random coil no specific interactions between residues or more generally chain segments persist and a large conformational space is populated. Polypeptide chains are rather complex polymers as sketched in Figure 22.1. Usually simplified models are applied to calculate general properties of random coils.

22.2.1 The Freely Jointed Chain

The equilibrium properties of an ideal polymer can be described by a three-dimensional random walk. This hypothetical chain, the freely jointed chain, consists of n bonds of length l with equally probable angles at each joint. The chain is described by the $n+1$ position vectors of the joints (chain elements) $\mathbf{R_i}$ or the n bond vectors $\mathbf{r_i}$. The correlation of the bond vectors $\langle \mathbf{r_m} \cdot \mathbf{r_n} \rangle$ is zero for $n \neq m$ because of the independence of the bond vector direction. The average end-to-end distance $\langle r^2 \rangle$ for the freely jointed chain is given by

$$\langle r^2 \rangle = nl^2 \tag{1}$$

For such an ideal chain the end-to-end vectors are normally distributed. The often-used notion of a Gaussian chain, however, refers to a chain model with Gaussian distributed bond lengths. Thus the end-to-end vector distribution is also Gaussian and Eq. (1) holds. This chain model does not describe the local structure of a chain correctly but the global properties of long chains are modeled in a realistic way.

22.2.2 Chain Stiffness

In a chain with restricted angles between two neighboring segments the correlation between segments n, m is no longer zero for $n \neq m$ but asymptotically ap-

proaches zero with increasing distance. The chain is not as flexible as the freely jointed chain because every segment is influenced by its neighbors. This behavior can be described in terms of chain stiffness. The end-to-end distance for such a chain is larger than calculated from Eq. (1). Flory introduced the characteristic ratio (C_n) as a measure for the dimensions of a stiff chain compared to a freely jointed chain [12]

$$\langle r^2 \rangle = C_n n l^2 \tag{2}$$

For short chains C_n increases with chain length due to preferential chain propagation into one direction (see Figure 22.2). For long chains ($n \to \infty$) C_n reaches a constant limiting value (C_∞).

$$\langle r^2 \rangle = C_\infty n l^2 \tag{3}$$

In this limit $\langle r^2 \rangle$ grows proportional to n, like an ideal random-walk chain (see Eq. (1)). However, in a real chain $\langle r^2 \rangle$ increases by a factor of C_∞ more per segment compared with an ideal random-walk chain. The value of C_∞ gives the average number of consecutive chain segments that propagate in the same direction (''statistical segment''). Consequently, for an ideal Gaussian chain where there is no correlation between the bond vectors, the limiting characteristic ratio is 1 (see Eq. (1)). For real chains C_∞ is larger than 1 and larger values of C_∞ indicate stiffer chains.

Kuhn showed that for chains with limited flexibility and n bonds of length l an equivalent to the freely jointed chain can be defined introducing an hypothetical bond length b, the Kuhn length ($b > l$) [16, 17]. The Kuhn length is the length of chain segments that can move freely (i.e., without experiencing chain stiffness). The maximal length of the chain (r_{max}) is the same as for a freely jointed chain and thus $r_{max} = nl = n'b$ with $n' < n$. The Kuhn length b is defined as

$$b = \langle r^2 \rangle / r_{max} = C_\infty n l^2 / r_{max} = C_\infty l \tag{4}$$

Another widely used term is the persistence length l_p. It is a measure for the distance that an infinitely long chain continues in the same direction (i.e., is persistent). The Kuhn and the persistence lengths are connected by the simple relationship

$$b = 2 l_p \tag{5}$$

Both parameters are used as measures for chain stiffness.

22.2.3 Polypeptide Chains

Any real macromolecule like the polypeptide chain has defined segments which are connected by chemical bonds. Bond angles are constrained and the distribution

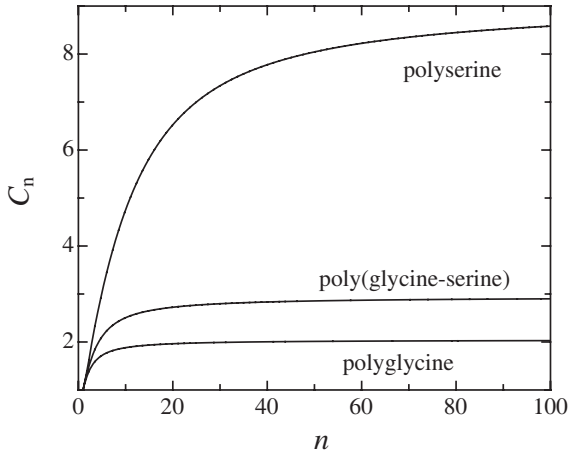

Fig. 22.2. Effect of chain length (n) on the characteristic ratio (C_n) for polyserine, polyglycine and a 50% mixture of serine and glycine. C_n was calculated using average transformation matrices given by Flory [12]. The transformation matrix for alanine was used to calculate the properties of serine.

of torsional angles is given by torsional potentials with several minima. In a peptide chain these torsional potentials are represented in conformational energy plots [18–21] or the Ramachandran map [22]. Flory and coworkers calculated statistical properties of various homopolypeptide chains [12, 18–21] based on the ϕ,ψ-angles from conformational energy plots. An average virtual bond length is defined from $C_{\alpha,i}$ to $C_{\alpha,i+1}$ and taken as 3.8 Å as shown in Figure 22.1 [12]. For polypeptide chains polyglycine represents the most flexible chain with $C_\infty = 2.2$ (see Figure 22.2) [12, 18, 19]. Poly-L-proline gives stiff chains with $C_\infty \approx 100$, due to the formation of a polyproline helix. For all other amino acids, C_∞ is between 8.5 and 9.5 [18]. These values correspond to persistence lengths around 19 Å for chains that do not contain glycine or proline and of 5.7 Å for poly-L-glycine [21]. It should be noted that these values apply for θ conditions, where the attractions between the chain segments (e.g., van der Waals or electrostatic interactions) compensate for the monomer–monomer repulsion due to excluded volume and the chain is apparently unperturbed. For details see Refs [11–15].

22.2.4
Excluded Volume Effects

In real (physical) chains two chain segments cannot occupy the same space. The excluded volume effect was first discussed by Kuhn [16] and leads to a non-ideal behavior of the chain. The chain dimensions increase as a result of the excluded volume, which leads to larger end-to-end distances. Flory obtained an approximate exponent for the chain dimensions including the contributions from the excluded volume effect by simple calculations [11].

$$\sqrt{\langle r^2 \rangle} \propto l \cdot n^{\nu}, \quad \nu = 0.59 \approx \text{or } 3/5 \tag{6}$$

This shows that the excluded volume effect is especially important for long chains. The excluded volume chain has been a subject of much research and is discussed in detail in the literature [13, 23–25] (see also Chapter 20).

For long real chains the end-to-end distribution function, $p(r)$, depends on the solvent conditions and on the temperature of the system if the intrachain interactions have enthalpic contributions. $p(r)$ for real chains can reasonably well be approximated by a skewed Gaussian function [26]

$$p(r) \propto 4\pi r^2 e^{-((r-r_0)/\sigma)^2} \tag{7}$$

where r is the end-to-end distance, σ is the half-width of the distribution and r_0 indicates the shift of the skewed Gaussian from the origin. Polypeptides in solution are complex molecules which may interact strongly with the solvent and with themselves enabling proteins to fold. The unfolded state of natural proteins was shown to contain both native and nonnative short-range and long-range interactions [27–39] (see Chapter 21). But many of the properties of GdmCl-unfolded proteins may be approximated by statistical chain models (see Section 22.4.2.4), although in some proteins specific intrachain interactions have also been found under strongly denaturing conditions [28, 39]. (see Chapter 21).

22.3 Theory of Polymer Dynamics

One of the major interests in polymer chemistry and biology is to elucidate the dynamic behavior of polymers in solution. Usually the dynamics of such molecules are complex and cannot be easily described by classical concepts. This is especially true for protein folding where the polypeptide chain not only moves freely in solution but also undergoes large cooperative structural transitions involving partially folded and native states. In the following we will give a short introduction to the theoretical concepts of polymer dynamics. More detailed information is given in Refs [8, 13, 23, 24].

22.3.1 The Langevin Equation

The energy surface on which a system moves is often complex with sequential and parallel events during the barrier crossing process (see Chapter 12.2). The motions of the system exhibit a diffusional character. The polymer chain in solution is immersed in solvent molecules which supply the energy for the movement by colliding with the polymer chain and at the same time dissipate this energy by exerting a frictional force on the molecule. The system can be described by the Langevin equation for Brownian motion if one assumes that the relaxation time scale for the solvent fluctuations is extremely short compared with the time scale of polymer motion [40]:

$$\ddot{x} = -M^{-1}\frac{\partial U(x)}{\partial x} - \gamma\dot{x} + M^{-1}F_{\text{fluc}}(t) \tag{8}$$

where M is the particle mass, x is the reaction coordinate, $U(x)$ denotes the energy, and γ is a friction coefficient, which is determined by the interactions of the system with its environment and couples the system to the environment. It can be related to solvent viscosity in real solutions. $F_{\text{fluc}}(t)$ is the random force which represents the thermal motion of the environment. The random force is modeled by Gaussian white noise of zero mean and a δ correlation function

$$\langle F_{\text{fluc}}(t)\rangle = 0$$
$$\langle F_{\text{fluc}}(t)\cdot F_{\text{fluc}}(t')\rangle = 2k_{\text{B}}T\gamma M\delta(t-t') \tag{9}$$

22.3.2 Rouse Model and Zimm Model

For long unfolded polypeptide chains, the simplified models used in polymer theory should be applicable. The system, i.e., the peptide immersed in the solvent, encounters no large barriers and undergoes random conformational changes. The dynamic behavior of Gaussian chains can be described analytically using classical polymer theory. Models of a higher complexity are only accessible, however, by solving the equations numerically in computer simulations. Two models have been initially proposed to describe polymer dynamics in dilute solutions: the Rouse model [5] and the Zimm model [6]. In both models the polymer is treated as a set of beads connected by harmonic springs. The Langevin equation (Eq. (8)) is used to describe the brownian motion of the connected beads in the Rouse model. The frictional and activating force from the solvent independently acts on all beads. The movement of the chain is described as a set of n relaxation modes. These modes can be compared to the vibrational modes of a violin string. Each mode p is coupled to a relaxation time τ_{p} and involves the motion of a section of the chain with n/p monomers. The mode with the longest relaxation time describes the overall motion (rotational relaxation) of the polymer chain. All other modes represent internal motions.

Yet, the scaling laws obtained for Rouse chains are not consistent with experimental results [24]. When a chain segment moves through a viscous solvent it has to drag surrounding solvent molecules along. This creates a flow field around the particle. Surrounding monomers are additionally affected by this flow field. As a result, the motion of one chain segment influences the motion of all other segments by hydrodynamic interactions.

The resulting chain model including hydrodynamic interactions was put forward by Zimm [6]. This model also gives internal relaxation modes, but the hydrodynamic interactions lead to significant deviations from the Rouse model. The solvent viscosity influences the system in two ways. First, it affects the random force that delivers the energy and dissipates it at the same time (γ, in the Langevin equa-

tion). Secondly, viscosity changes the strength of the hydrodynamic interactions. Many studies have been performed to compare the predictions of Rouse model, the Zimm model, and more refined models to actual experiments [41]. The overall chain motions including hydrodynamic interactions agree well with experiment [24]. Measurements of dynamics in DNA molecules using time-resolved optical microscopy directly showed internal relaxation modes [42].

22.3.3
Dynamics of Loop Closure and the Szabo-Schulten-Schulten Theory

One particularly intensively treated dynamic event in polymer chains is the loop closure or end-to-end diffusion reaction. Organic chemists are interested in loop closure probabilities for the synthesis of cyclic compounds. Also in nucleic acids end-to-end diffusion is important during formation of cyclic DNA. The kinetics of such cyclization reactions critically depend on the rate of intrachain contact formation. A similar situation is encountered in protein folding, where residues have to come together and form specific non-covalent interactions. Jacobsen and Stockmayer [4] derived a scaling law for end-to-end ring closure probability as a function of the length of the polymer chain. The calculations were based entirely on entropic contributions and yielded

$$p_{\text{ring}} \propto n^{-3/2} \tag{10}$$

where p_{ring} denotes the probability of ring formation and n is the number of monomers in such a ring.

Szabo, Schulten, and Schulten [7] discussed the kinetics that can be expected from a diffusion controlled encounter of two groups attached to the ends of a Gaussian chain (SSS theory). They treated the loop closure reaction as an end-to-end diffusion of a polymer on a potential surface. It was shown that the kinetics of such a process can be approximated by an exponential decay of the probability $\Sigma(t)$ that the system has not reacted (i.e., has not made contact) at time t

$$\Sigma(t) \approx \Sigma_{\text{approx}}(t) = \mathrm{e}^{(-t/\tau)} \tag{11}$$

This approximation holds if the distribution of chain conformations is stationary throughout the reaction, i.e., the interchange of conformations is fast compared with the rate of reaction, and the probability of reaction is small, i.e., the reactive radius is small compared with the chain length. The time constant τ is the mean first passage time of this reaction and depends on the equilibrium end-to-end distribution of the polymer chain $p(x)$, on the diffusion constant D of the chain ends relative to one another and on the reactive boundary r_a, i.e., the distance which leads to contact between the two ends.

$$\tau = \frac{1}{D}\int_{r_a}^{\infty} p(x)^{-1}\left(\int_{x}^{\infty} p(y)\,\mathrm{d}y\right)^2 \mathrm{d}x \Big/ \int_{r_a}^{\infty} p(x)\,\mathrm{d}x \tag{12}$$

The mean first passage time of contact formation can be related to the root mean square end-to-end distance, r, by expanding Eq. (12):

$$\tau^{-1} = k_{\text{contact}} \propto D(\sqrt{\langle r^2 \rangle})^{-3} \tag{13}$$

With Eq. (1) this gives the well-known relationship [4]:

$$k_{\text{contact}} \propto n^{-3/2} \tag{14}$$

for an ideal chain. The effect of viscosity on the rate of reaction is included in the diffusion coefficient D, which is assumed to be inversely proportional to the solvent viscosity. Hydrodynamic interactions, the excluded volume effect and other non-idealities (e.g., a diffusion coefficient dependent on chain conformation) are not considered in these approximations and probably contribute to the dynamics and scaling laws in real systems.

22.4 Experimental Studies on the Dynamics in Unfolded Polypeptide Chains

22.4.1 Experimental Systems for the Study of Intrachain Diffusion

It is now widely accepted that the description of the unfolded state as a complete random coil where the polypeptide chain behaves like an ideal polymer is not accurate. Short stretches along the polypeptide chain behave in a highly non-ideal manner because of chain stiffness, solvent interactions, and excluded volume. In addition, there is evidence for residual short-range and long-range interactions in unfolded proteins in water and even at high concentrations of urea and GdmCl [27, 28, 34, 43, 44]. For the understanding of the dynamic properties of unfolded proteins it is therefore essential to compare scaling laws and absolute rate constants for chain diffusion in homopolymer models with the results from unfolded proteins or protein fragments. Suitable experimental systems to study intrachain diffusion should allow direct measurements of the kinetics of formation of van der Waals contacts between specific groups on a polypeptide chain. To obtain absolute rate constants, the applied method must be faster than chain diffusion and the detection reaction itself should be diffusion controlled (see Appendix).

In the following, we will describe various experimental systems that have been used to study the dynamics of intrachain diffusion. In Section 22.4.2 results from these studies will be discussed in more detail in terms of dynamic properties of unfolded polypeptide chains. A summary of the results is given in Tables 22.1 and 22.2.

22.4.1.1 Early Experimental Studies

Dynamics of synthetic polymers in various organic solvents have been studied for a long time by different means. End-to-end contact formation has been examined

Tab. 22.1. Comparison of end-to-end contact formation rate constants observed in different systems.

k_{app} (s^{-1})	Loop size (n)[a]	Method	Labels[b]	Sequence	Conditions	Reference
$3.3 \cdot 10^8$–$1.1 \cdot 10^8$	4–8, 50[c]	FRET	Dansyl/naphthalene	$(heGln)_n$[d]	Glycerol/TFE	48, 50[c]
$2.8 \cdot 10^4$	60	Bond formation	Heme/Met	Unfolded cytochrome *c*	5.4 GdmCl, 40 °C	52
$5 \cdot 10^7$–$1.2 \cdot 10^7$	3–9	TTET	Thioxanthone/NAla	$(Gly\text{-}Ser)_x$	EtOH	50
$9.1 \cdot 10^6$	10	Triplet quenching	Trp/Cys	$(Ala\text{-}Gly\text{-}Gln)_3$	H_2O, phosphate	59
$1.1 \cdot 10^7$	10	Triplet quenching	Trp/cystine	$(Ala\text{-}Gly\text{-}Gln)_3$	H_2O, phosphate	59
$1.7 \cdot 10^7$	10	Triplet quenching	Trp/lipoate	$(Ala\text{-}Gly\text{-}Gln)_3$	H_2O, phosphate	59
$6.2 \cdot 10^4$	10	Triplet quenching	Trp/lipoate	Pro_9	H_2O, phosphate	59
$2.4 \cdot 10^7$	10	Triplet quenching	Trp/lipoate	$(Ala)_2Arg(Ala)_4ArgAla$	H_2O, phosphate	59
$4.1 \cdot 10^7$–$1.1 \cdot 10^7$	1–21	Fluor. quenching	DBO/Trp	$(Gly\text{-}Ser)_x$	D_2O	65
$3.9 \cdot 10^7$–$1 \cdot 10^5$	7	Fluor. quenching	DBO/Trp	Xaa_6[e]	D_2O	66
$6.6 \cdot 10^6$	8	Single molecule fluor. quenching	MR121/Trp	Part of human p53	H_2O, PBS, 25 °C	67
$8.3 \cdot 10^6$	9	Single molecule fluor. quenching	MR121/Trp	Part of human p53	H_2O, PBS, 25 °C	67
$1.8 \cdot 10^8$–$6.5 \cdot 10^6$	3–57	TTET	Xanthone/NAla	$(Gly\text{-}Ser)_x$	H_2O, 22.5 °C	54
$8 \cdot 10^7$–$3.4 \cdot 10^7$	3–12	TTET	Xanthone/NAla	$(Ser)_x$	H_2O, 22.5 °C	54
$2.5 \cdot 10^8$–$2.0 \cdot 10^7$	4	TTET	Xanthone/NAla	Ser-Xaa-Ser[f]	H_2O, 22.5 °C	54
$4.0 \cdot 10^6$	15	Triplet quenching	Zn-porphyrin/Ru	Unfolded cytochrome c	5.4 M GdmCl, 22 °C	64
$2.0 \cdot 10^7$	17	TTET	Xanthone/NAla	Carp parvalbumin	H_2O, 22.5 °C	55

[a] *n* is the number of peptide bonds between the reacting groups.
[b] The structures of the labels are shown in Figure 22.3.
[c] Calculated in Ref. [50] from the diffusion coefficients and the donor–acceptor distances given in Ref. [48].
[d] heGln = (N^5-(2-hydroxyethyl-)-L-glutamine).
[e] $(Xaa)_6$ = homohexapeptides of 16 different amino acids. The highest (Gly_6) and lowest values (Pro_6) for the observed rate constants are given.
[f] Xaa = Gly, Ala, Ser, Gly, Arg, His, Ile, Pro. The highest (*cis* Pro) and lowest values (*trans* Pro) for the observed rate constants are given. See Figure 22.9.

Tab. 22.2. Comparison of end-to-end contact formation rates observed in different systems measured or extrapolated to $n \approx 10$.

k_{app} (s^{-1})	Loop size (n)	Method	Labels	Sequence	Conditions[b]	Reference
$1 \cdot 10^6$	10[a]	Bond formation	Heme/Met	Unfolded cytochrome *c*	5.4 GdmCl, 40 °C	52
$1.2 \cdot 10^7$	9	TTET	Thioxanthone/NAla	$(GS)_4$	EtOH	50
$9.1 \cdot 10^6$	10	Triplet quenching	Trp/Cys	$(AGQ)_3$	H_2O, phosphate buffer	59
$1.1 \cdot 10^7$	10	Triplet quenching	Trp/cystine	$(AGQ)_3$	H_2O, phosphate buffer	59
$1.7 \cdot 10^7$	10	Triplet quenching	Trp/lipoate	$(AGQ)_3$	H_2O, phosphate buffer	59
$3.1 \cdot 10^7$	9	Fluor. quenching	DBO/Trp	$(GS)_4$	D_2O	65
$8.3 \cdot 10^6$	9	Single molecule Fluor. quenching	MR121/Trp	Fragment from human p53	H_2O, PBS, 25 °C	67
$8.3 \cdot 10^7$	9	TTET	Xanthone/NAla	$(GS)_4$	H_2O, 22.5 °C	54
$4.1 \cdot 10^7$	10	TTET	Xanthone/NAla	$(Ser)_9$	H_2O, 22.5 °C	54
$1 \cdot 10^7$	10[a]	Triplet quenching	Zn-porphyrin/Ru	Unfolded cytochrome *c*	5.4 M GdmCl, 22 °C	64

[a] Extrapolated from larger loops to 10 amino acids, as the average loop size in proteins. It should be noted that extrapolations used the Jacobsen Stockmeyer or SSS theory scaling law ($k_c \sim n^{-1.5}$), which gives a slightly smaller length dependence than the experimentally determined scaling laws (cf. Figure 22.8). This would result in larger extrapolated values of k_c.

[b] solvent was H_2O unless indicated. The data measured in concentrated GdmCl solutions or EtOH were not corrected for solvent effects. This would lead to a significant increase in k_c (see Figure 22.10).

using phosphorescence quenching of benzophenone in long hydrocarbon polymers [45] and by excimer formation of pyrene groups attached to poly(ethylene glycols) [46]. The dynamics of unfolded polypeptide chains have first been studied using fluorescence resonance energy transfer (FRET) from an energy donor to an energy acceptor group. FRET was shown to be a powerful tool to determine donor–acceptor distances [47], but time-resolved FRET kinetics also contain major contributions from the diffusion of the two FRET probes relative to each other [48, 49]. The number of excited donor molecules ($N^*(r,t)$) with donor–acceptor distance r changes with time in the presence of an acceptor group. This can be described by a second-order partial differential equation for the reduced distance distribution, $\bar{N}(r,t)$, normalized to $N_0(r)$:

$$\frac{\partial \bar{N}(r,t)}{\partial t} = -\frac{1}{\tau}\left\{\left(1+\left(\frac{R_0}{r}\right)^6\right)\bar{N}(r,t)\right\} + \frac{1}{N_0(r)}\frac{\partial}{\partial r}\left\{N_0(r)D\frac{\partial \bar{N}(r,t)}{\partial r}\right\}$$

$$\text{with } \bar{N}(r,t) = \frac{N^*(r,t)}{N_0(r,t)} \tag{15}$$

where R_0 is the distance of 50% FRET efficiency, which is a property of the FRET labels, $N_0(r)$ denotes the equilibrium distribution of distances between donor and acceptor, and τ is the fluorescence lifetime of the donor. The first term (equilibrium term) on the right-hand side describes the change of donor excitation with time through spontaneous decay and nonradiative energy transfer. The second term (diffusion term) describes the replenishment of excited labels through brownian motion. This dynamic component of FRET was exploited to determine diffusion coefficients of segmental motion in short homopolypeptide chains (poly-N^5-(2-hydroxyethyl)-L-glutamine) in glycerol and trifluoroethanol mixtures [48, 49] (see Chapter 17). Naphthyl- and dansyl-groups were used as donor and acceptor, respectively (Figure 22.3A).

These studies allowed the first estimates of the time scale of chain diffusion processes in polypeptide chains. Converting the reported average diffusion constants reported by Haas and coworkers [48] into time constants ($\tau = 1/k$) for contact formation at van der Waals distance gives values between 9 and 3 ns for a donor–acceptor separation of between 4 and 8 peptide bonds, respectively [50]. The dynamic component of FRET is sensitive to motions around the Förster distance (R_0), which is around 22 Å for the dansyl–naphthyl pair used in these studies. It therefore remained unclear whether the same diffusion constants represent the dynamics for formation of van der Waals contact between two groups. In addition, analysis of the FRET data critically depends on the shape of the donor–acceptor distribution function, which had to be introduced in the data analysis and thus did not allow model-free analysis of the data. It was found that this distribution can be described most accurately by the skewed Gaussian function mentioned above [51]. It later turned out that the chain dynamics measured by FRET are significantly faster than rate constants for contact formation (see below), which might indicate a distance-dependent diffusion constant in unfolded polypeptide chains.

A

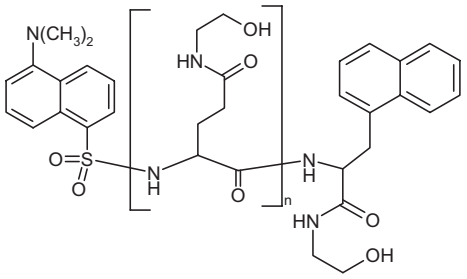
N(CH3)2
OH
HN
O
O=S=O
N
H
n
HN
OH

B

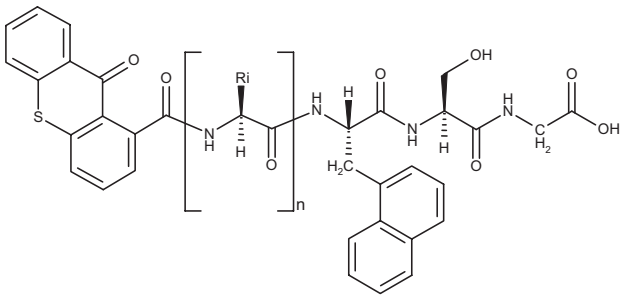
O
S
Ri
OH
OH
n

C

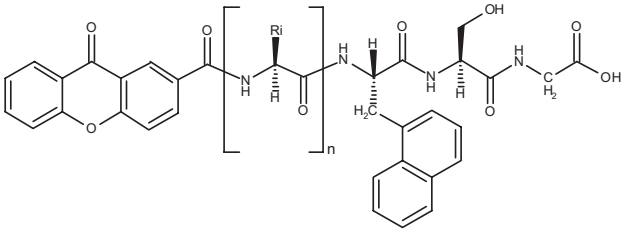
O
Ri
OH
OH
n

D

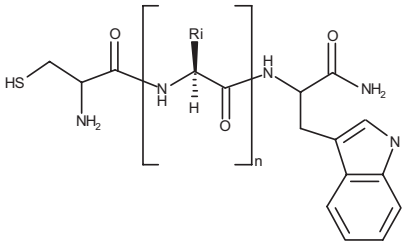
HS
NH2
Ri
O
NH2
N
n

E

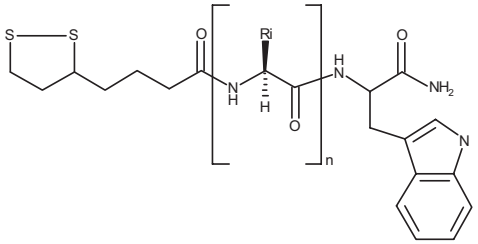
S
S
Ri
NH2
N
n

F

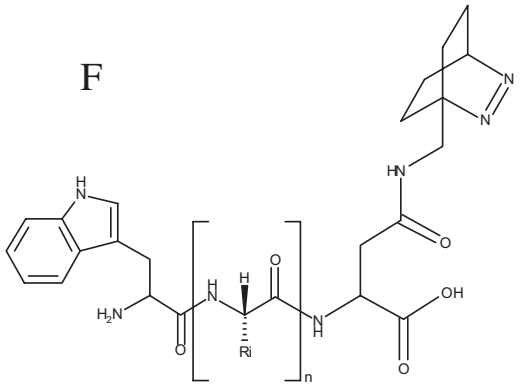
N
N
HN
O
H
N
H2N
Ri
OH
n

G

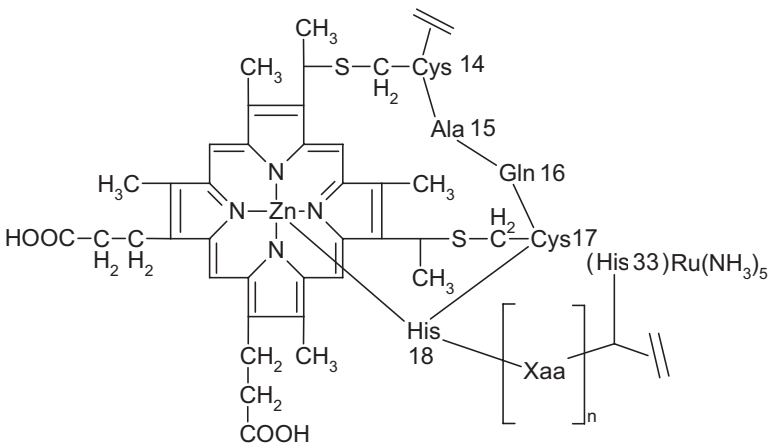
CH3
CH3
S
C
H2
Cys 14
Ala 15
Gln 16
H3C
CH3
N
N
Zn
N
HOOC
C
C
H2
H2
N
S
C
H2
Cys17
CH3
(His 33)Ru(NH3)5
His
18
Xaa
n
CH2
CH3
CH2
COOH

FRET was also used in several proteins to determine donor–acceptor distance distribution functions and diffusion coefficients (see Chapter 17).

Rates of intrachain diffusion have also been estimated from the rate constant for intramolecular bond formation in GdmCl-unfolded cytochrome *c* [52]. The reaction of a methionine with a heme group separated by 50–60 amino acids along the chain gave time constants around 35–40 μs. Extrapolating these data to shorter distances using SSS or Jacobsen-Stockmeyer theory ($k \sim n^{-1.5}$) gave an estimate of 1 μs for the time constant of contact formation at a distance of 10 peptide bonds, which was predicted to be the distance for the maximum rate of contact formation due to chain stiffness slowing down the diffusion process over shorter distances [53]. A problem with this experimental approach is that the recombination reaction of heme with methionine is not diffusion controlled. Thus, the chain dynamics allow a faster breakage of the heme–methionine contact than formation of the methionine–heme bond. Thus, not every contact was productive and the apparent rate constants obtained in these measurements were slower than the absolute rate constants measured with diffusion-controlled systems (see Experimental Protocols, Section 22.7).

22.4.1.2 **Triplet Transfer and Triplet Quenching Studies**

The early studies on intrachain diffusion did not yield absolute rate constants for contact formation, but they were important to trigger the development of more direct and model-free methods to study chain diffusion. Recently, several experimental systems using fast photochemical methods to directly monitor contact formation in model peptides and protein fragments have been introduced. Bieri et al. [50] and Krieger et al. [54, 55] used triplet–triplet transfer (TTET) between thioxanthone or xanthone derivatives and naphthalene (see Figure 22.3B,C) to directly measure rate constants for intrachain contact formation in synthetic polypeptide chains. A triplet donor and a triplet acceptor group are introduced at specific points in polypeptide chains. The donor is selectively excited by a laserflash and undergoes fast intersystem crossing into the triplet state (see Figure 22.4). Upon intrachain diffusion the triplet donor and triplet acceptor groups meet and the triplet state is transferred to the acceptor. Since TTET is a two electron exchange process (Dexter mechanism) it has a very strong distance dependence and usually requires

Fig. 22.3. Structures of different experimental systems used to measure intrachain contact formation. Results from these systems are summarized in Table 22.1. A) Dansyl and naphthyl-labeled poly-N^5-(2-hydroxyethyl)-L-glutamine used to determine diffusion constants by FRET [48]. B) Thioxanthone and naphthylalanine-labeled poly(Gly-Ser) peptides to measure contact formation by TTET [50]. C) Xanthone and naphthylalanine-labeled peptides to measure contact formation by TTET in various homopolymer chains and natural sequences with up to 57 amino acids between donor and acceptor [54, 55]. D,E) Tryptophan and cysteine or lipoate-labeled peptides to measure contact formation by Trp triplet quenching in various short peptide chains [59, 125, 126]. F) Short peptide chains ($n < 10$) for measuring DBO fluorescence quenching by tryptophan [65]. G) Quenching of Zn-porphyrin triplets by Ru-His complexes in unfolded cytochrome *c* [64].

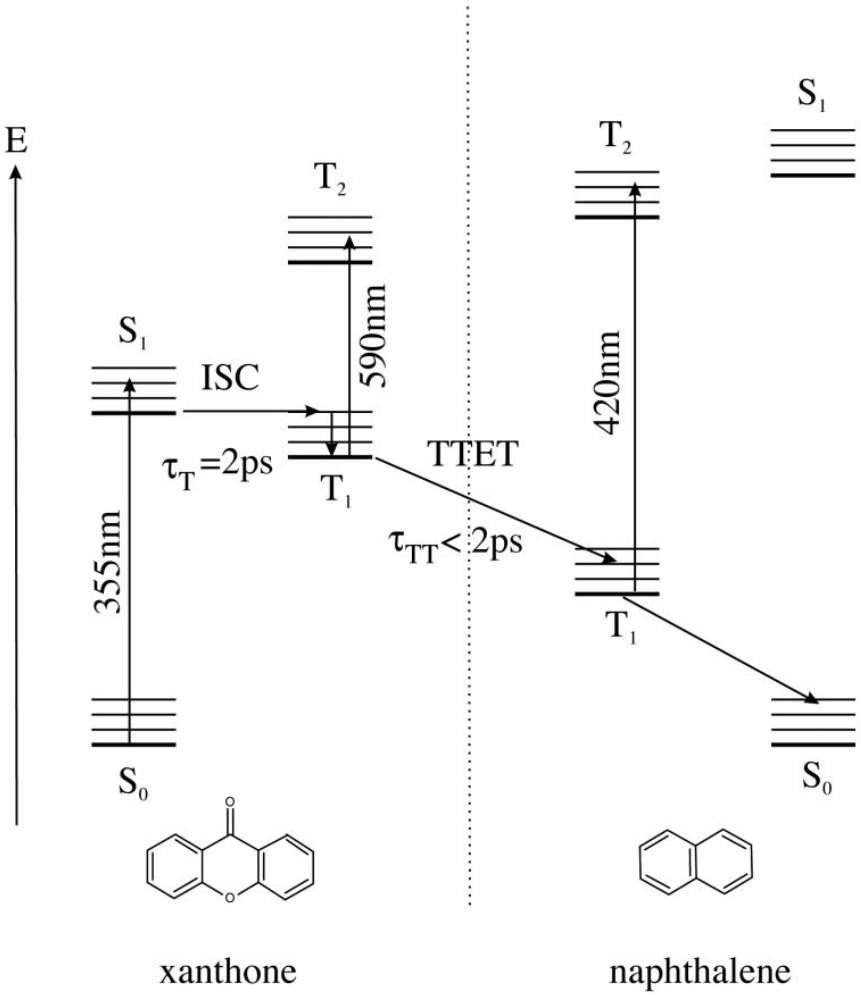

Fig. 22.4. Jablonski diagram for triplet–triplet energy transfer (TTET) from xanthone to naphthalene. Rate constants for triplet formation (k_T) and TTET (k_{TT}) were measured by laserflash photolysis using femtosecond pulses [56].

van der Waals contact to allow for electron transfer. This should be contrasted to FRET, which occurs through dipole–dipole interactions and thus allows energy transfer over larger distances (see above).

The triplet states of the labels have specific absorbance bands, which can easily be monitored to measure the decay of the donor triplet states and the concomitant increase of acceptor triplet states (Figure 22.5). The time constant for formation of xanthone triplet states is around 2 ps [56]. TTET between xanthone and naphthyl acetic acid is faster than 2 ps and has a bimolecular transfer rate constant of $4 \cdot 10^9$ M^{-1} s^{-1} [54, 56], which is the value expected for a diffusion-controlled reaction between small molecules in water (see Experimental Protocols, Section 22.7). Due to this fast photochemistry, TTET between xanthone and naphthalene allows measurements of absolute rate constants for diffusion processes slower than 10–20 ps (Figure 22.6 and Experimental Protocols, Section 22.7). The upper

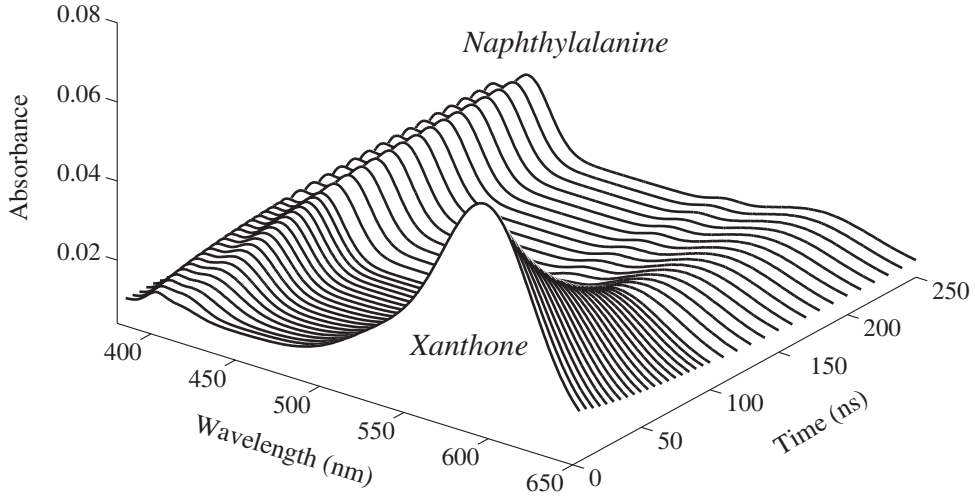

Fig. 22.5. Time-dependent change in the absorbance spectrum of a Xan-(Gly-Ser)$_{14}$-NAla-Ser-Gly peptide after a 4 ns laser flash at 355 nm. The decay in the intensity of the xanthone triplet absorbance band around 590 nm is accompanied by a corresponding increase in the naphthalene triplet absorbance band around 420 nm. Adapted from Ref. [54].

limit of the experimental time window accessible by TTET is set by the intrinsic lifetime of xanthone which is around 20–30 μs in water. Xanthone has a high quantum yield for intersystem crossing ($\phi_{ISC} = 0.99$, $\varepsilon \approx 4000$ M^{-1} cm^{-1}) and the triplet state has a strong absorbance band with a maximum around 590 nm in water ($\varepsilon^{T}_{590} \approx 10\,000$ M^{-1} cm^{-1}). This allows single-pulse measurements at rather low peptide concentrations (10–50 μM).

The low concentrations applied in the experiments also rule out contributions from intermolecular transfer reactions that would have half-times higher than 50 μs in this concentration range [50, 54]. Also contributions from through-bond transfer processes can be neglected, since this cannot occur over distances beyond eight bonds [57, 58] and even the shortest peptides used in TTET studies had donor and acceptor separated by 11 bonds.

Bieri et al. [50] initially used a derivate of thioxanthone as triplet donor and the nonnatural amino acid naphthylalanine (NAla) as triplet acceptor (see Figure 22.3B). Because of the sensitivity of the triplet energy of the donor on solvent polarity the measurements had to be carried out in ethanol. TTET detected single exponential kinetics in all peptides with time constants of 20 ns for the shortest loops in poly(glycine-serine)-based polypeptide chains [50]. The length dependence of contact formation in these peptides did not exhibit a maximum rate constant for transfer at $n = 10$, in contrast to the predicted behavior [53] (see Section 22.4.2.2). Based on these findings, the minimum time constant for intrachain contact formation was shown to be around 20 ns for short and flexible chains. The thioxanthone used in the initial experiments as triplet donor was later replaced by xanthone [54], which has a higher triplet energy than thioxanthone and thus allowed measurements in water (see Figure 22.3C). These results showed two- to threefold faster

rate constants for contact formation compared to the same peptides in ethanol [54], setting the time constant for intrachain diffusion in short flexible chains in water to 5–10 ns. The faster kinetics compared to the thioxanthone/NAla system could be attributed to the effect of ethanol [54] (see below).

A disadvantage of TTET from xanthone to NAla in its application to natural proteins is that Tyr, Trp, and Met interact with the xanthone triplet state either by TTET or by triplet quenching and thus should not be present in the studied polypeptide chains [55].

Lapidus et al. [59] used a related system to measure chain dynamics in short peptides. In this approach contact formation was measured by quenching of tryptophan triplet states by cysteine (see Figure 22.3D). Tryptophan can be selectively excited by a laserflash ($\phi_{ISC} = 0.18$, $\varepsilon_{266} \approx 3500\ M^{-1}\ cm^{-1}$, $\varepsilon^{T}_{460} \approx 5000\ M^{-1}\ cm^{-1}$) and its triplet decay can be monitored by absorbance spectroscopy [60]. The advantage of this system is that donor chromophore and quencher groups are naturally occurring amino acids, which can be introduced at any position in peptides and proteins. As in the case on TTET from xanthone to naphthalene some amino acids interfere with the measurements (e.g., Tyr, Met) since they interact with tryptophan triplets and should thus not be present in the studied polypeptide chains [61].

Major disadvantages of the Trp/Cys system are, (i) that the formation of tryptophan triplets is slow ($\tau = 3$ ns) [62], (ii) that triplet quenching is accompanied by the formation of S·radicals [59], and (iii) that the quenching process is not diffusion controlled [63]. These properties reduce the time window available for the kinetic measurements and do not allow direct and model-free analysis of the quenching time traces (see Experimental Protocols, Section 22.7). In addition, its low quantum yield makes the detection of the triplet states and the data analysis difficult, especially since the kinetics are obscured by radical absorbance bands. In addition to cysteine quenching, two other systems were presented by the same group [59] with cystine or the cyclic disulfide lipoate serving as quencher instead of cysteine (Figure 22.3E). The advantage of using lipoate is that the quenching kinetics are much closer to the diffusion limit. Thus, the rates measured with this system are generally faster. Still, all systems used for quenching of tryptophan triplets gave significantly slower kinetics of intrachain contact formation compared to TTET from xanthone to NAla in the same or in similar sequences (see Tables 22.1 and 22.2). This indicates that tryptophan triplet quenching does not allow measurements of chain dynamics on the absolute time scale [63].

Another recent experimental approach investigated intrachain contact formation in unfolded cytochrome *c* using electron transfer from a triplet excited Zn-porphyrine group to a Ru complex, which was bound to a specific histidine residue (His33; Figure 22.3G). Since electron transfer is fast and close to the diffusion limit these experiments should also yield absolute rate constants for chain diffusion. Contact formation in the 15-amino-acid loop from cytochrome *c* was observed with a time constant of 250 ns [64] in the presence of 5.4 M GdmCl. This is significantly faster than the dynamics in unfolded cytochrome *c* reported by Hagen et al. [52] under similar conditions. However, the dynamics measured by Chang et al. agree well with TTET measurements [50, 54, 55], when the kinetics are extrapolated from 5.4 M GdmCl to water (see below).

22.4.1.3 Fluorescence Quenching

Other approaches to measure contact formation applied quenching of long-lifetime fluorescence probes. Two studies used 2,3-diazabicyclo[2,2,2]oct-2-ene (DBO) as a fluorophore (see Figure 22.3F) [65, 66]. It has a lifetime of up to 1 μs and its excited singlet states can be quenched by tryptophan upon contact. The quenching rate of DBO by tryptophan lies close to the diffusion-controlled limit in water, yet the obtained rates are about a factor of 3 slower than the ones obtained with the xanthone/NAla system in the same peptides [54]. This suggests that the photochemistry of fluorescence quenching may not be faster than breakage of the van der Waals contact between DBO and Trp (see Figure 22.6 and Experimental Protocols, Section 22.7). Another disadvantage of this method is the rather short lifetime of the DBO excited state (< 1 μs), which limits the method to short peptides.

Recently, intrachain diffusion was measured using single molecule fluorescence quenching. Peptides were labeled with a fluorescent dye (MR121) which was quenched by tryptophan [67]. The quenching was reported to only occur efficiently via van der Waals contact. Contact formation between the labels resulted in fluorescence fluctuations, which were recorded by confocal fluorescence microscopy. The rate constants for contact formation were determined using time-correlated single-photon counting. The calculated rates are, however, significantly lower than those determined by more direct methods.

22.4.2 Experimental Results on Dynamic Properties of Unfolded Polypeptide Chains

The different systems presented above were applied to measure intrachain contact formation in a large variety of model peptides. The rates for contact formation have

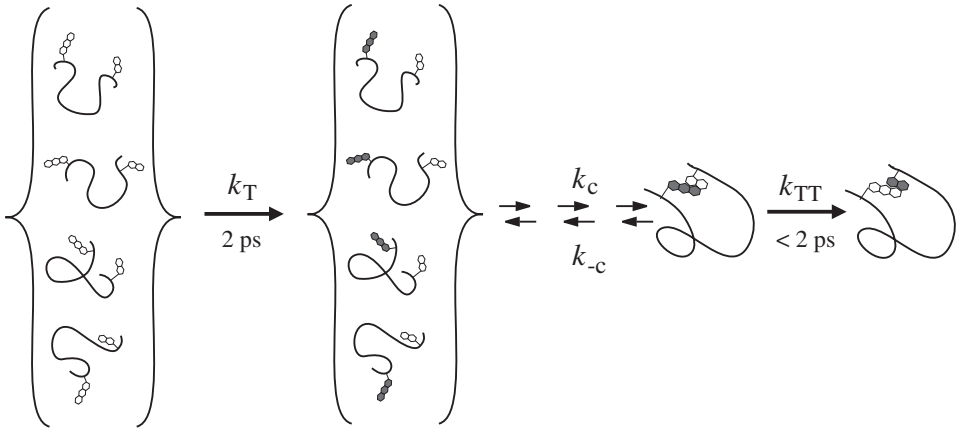

Fig. 22.6. Schematic representation of the triplet–triplet energy transfer (TTET) experiments. Triplet donor and acceptor groups are attached at specific positions on an unstructured polypeptide chain. Triplet states are produced in the donor group by a short laser flash and transferred to the acceptor upon encounter at van der Waals distance in a diffusion-controlled process. The experiments allow determination of the absolute rate constant for contact formation (k_c) in the ensemble of unfolded conformation, if formation of the triplet state (k_T) and the transfer process (k_{TT}) are much faster than chain dynamics ($k_T, k_{TT} \gg k_{-c}, k_c$; see Experimental Protocols, Section 22.7). The rate constants given for k_T and k_{TT} were taken from Ref. [56].

been found to vary depending on the method applied, on the sequence of the peptide and on the peptide length. Results from different groups are compared in Tables 22.1 and 22.2. The results reveal that TTET and electron transfer, which were shown to have fast photochemistry and diffusion-controlled transfer reactions, give virtually identical rate constants and have the fastest contact rates of all applied methods. These methods obviously allow the determination of absolute rate constants for contact formation. In the following, we will discuss results from experiments that used these methods to determine the effect of chain length, amino acid sequence and solvent properties on the rate constants of contact formation.

22.4.2.1 Kinetics of Intrachain Diffusion

All experiments applying TTET [50, 54] and electron transfer [64] to measure dynamics of unfolded polypeptide chains revealed single exponential kinetics on the ns time scale or slower (Figure 22.7). The only exception were short proline-containing peptides, where the kinetics of *cis* and *trans* Xaa-Pro peptide bonds could be resolved [54]. From the observation of single exponential kinetics several conclusions can be drawn. As observed by Szabo, Schulten, and Schulten [7] and pointed out by Zwanzig [68], single exponential kinetics indicate fast interconversion between the different conformations in the ensemble of unfolded states, thus allowing the chain to maintain the equilibrium distribution of the ensemble of conformations that has not made contact. Fast interconversion between individual chain conformations is in agreement with results on conformational relaxation processes in strained peptides, which were shown to occur in the picoseconds time scale [69, 70]. Secondly, the contact radius is small compared to the chain length, which leads to a small probability of contact formation in agreement with the observation that triplet–triplet transfer can only occur when the two labels are in van der Waals contact [7, 68]. A small fraction of chain conformations in equilibrium are predicted to have very short donor–acceptor distances [63] which might allow contact formation on the subnanosecond time scale. From the nanosecond TTET experiments it can be ruled out, however, that a significant fraction (> 5–10%) of chain molecules form donor–acceptor contacts on the subnanosecond time scale, even in the shortest peptides [54]. However, the dynamics of linear peptides in the subnanoseconds time region has not been investigated yet. The fast photochemistry of TTET between xanthone and naphthalene should allow the study of peptide dynamics on the picosecond time scale to detect small fraction of fast transfer processes.

22.4.2.2 Effect of Loop Size on the Dynamics in Flexible Polypeptide Chains

The scaling of the end-to-end diffusion with loop size was measured in TTET experiments by varying the number of amino acids between xanthone and naphthylalanine in two series of homopolypeptides. One series represented flexible polypeptide chains of Xan-$(\text{Gly-Ser})_x$-NAla-Ser-Gly peptides with x varying from 1 to 28. These peptides allowed measurements of contact formation kinetics between two points on the chain separated by between 3 and 57 peptide bonds, which covers the range of side-chain contacts in small proteins. Figure 22.7 displays three repre-

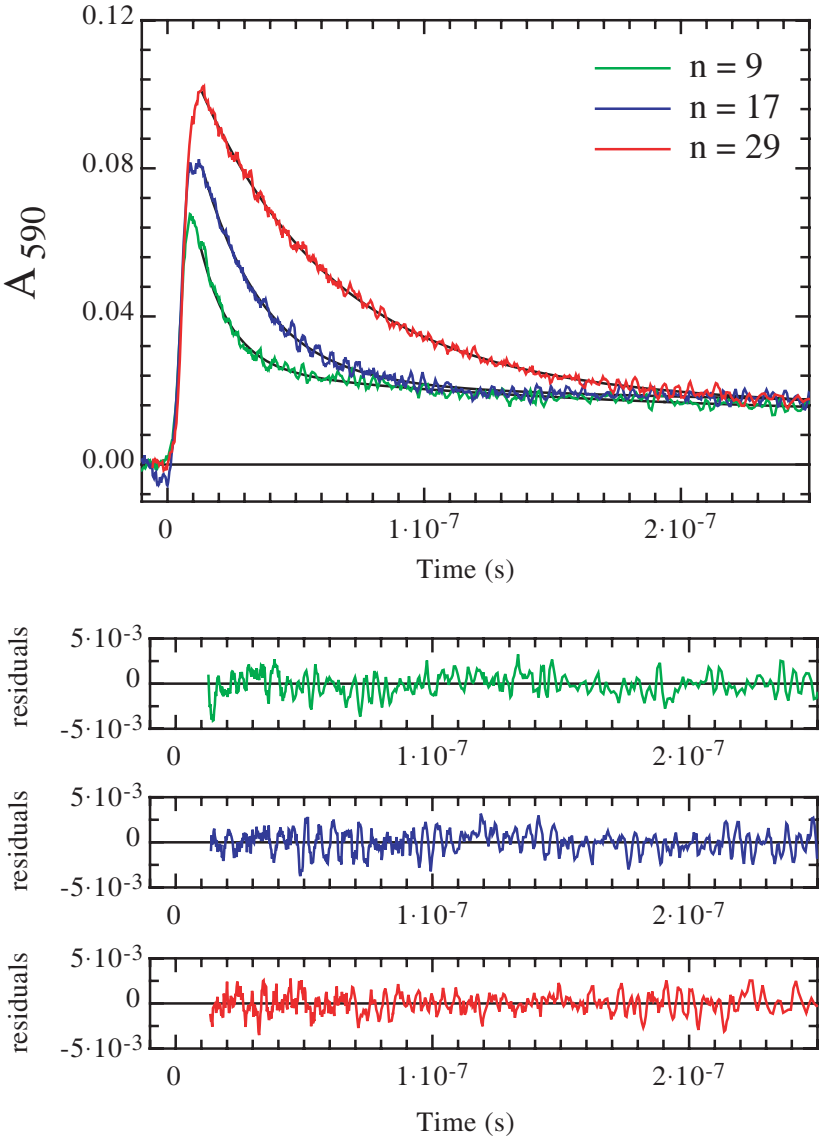

Fig. 22.7. Time course of formation and decay of xanthone triplets in peptides of the form Xan-(Gly-Ser)$_x$-NAla-Ser-Gly after a 4 ns laser flash at $t = 0$ measured by the change in absorbance of the xanthone triplets at 590 nm. Data for different numbers of peptide bonds (n) between donor and acceptor are displayed. Additionally, single exponential fits of the data and the corresponding residuals are shown. The fits gave time constants shown in Figure 22.8. Adapted from Ref. [54].

sentative TTET kinetics for peptides from this series. As mentioned above, single exponential kinetics for contact formation were observed for all peptides.

Figure 22.8 shows the effect of increasing loop size on the rate constant for contact formation. For long loops ($n > 20$) the rate of contact formation decreases with $n^{-1.7\pm0.1}$ (n is the number of peptide bonds between donor and acceptor). This indicates a stronger effect of loop size on the rate of contact formation than expected for purely entropy-controlled intrachain diffusion in ideal freely jointed Gaussian

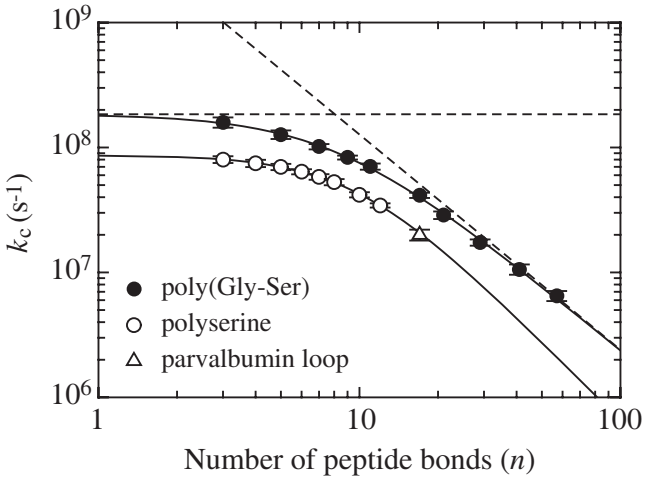

Fig. 22.8. Comparison of the rate constants (k_c) for end-to-end diffusion in poly(glycine-serine) (filled circles), polyserine (open circles) and a parvalbumin loop fragment 85–102 (triangles) measured by TTET between xanthone and naphthylalanine. The data were fitted to Eq. (16) and gave results of $k_a = (1.8 \pm 0.2) \cdot 10^8$ s^{-1}, $k_b = (6.7 \pm 1.6) \cdot 10^9$ s^{-1} and $m = 1.72 \pm 0.08$ for the poly(glycine-serine) series and of $k_a = (8.7 \pm 0.8) \cdot 10^7$ s^{-1}, $k_b = (1.0 \pm 0.8) \cdot 10^{10}$ s^{-1} and $m = 2.1 \pm 0.3$ for polyserine. The dashed lines indicate the limiting cases for dynamics for short chains ($k_c = k_a$) and long chains $k_c = k_b \cdot n^{-m}$). Data were taken from Refs [54, 55].

chains, which should scale with $k \sim n^{-1.5}$ (see above) [4, 7]. However, Flory already pointed out that excluded volume effects should significantly influence the chain dimensions [11]. Accounting for excluded volume effects in the end-to-end diffusion model of Szabo, Schulten, and Schulten [7] gives $k \sim n^{-1.8}$, which is nearly identical to the value found for the long poly(Gly-Ser) chains [54]. This indicates that the dimensions and the dynamics of unfolded polypeptide chains in water are significantly influenced by excluded volume effects, which is in agreement with recent results on conformational properties of polypeptides derived from simplified Ramachandran maps [25]. Additionally, hydrodynamic interactions and the presence of small enthalpic barriers, which were observed in the temperature dependence of intrachain diffusion might contribute to the length dependence (F. Krieger and T. Kiefhaber, unpublished).

The observed simple scaling law breaks down for $n < 20$ and contact formation becomes virtually independent of loop size for very short loops with a limiting value of $k_a = 1.8 \cdot 10^8$ s^{-1}. As pointed out above, the limiting rate constant for contact formation in short loops is not due to limits of TTET (k_{TT} in Figure 22.6), since this process is faster than 2 ps. Obviously, the intrinsic dynamics of polypeptide chains are limited by different processes for motions over short and over long segments. This is in agreement with polymer theory, which suggests that the properties of short chains are strongly influenced by chain stiffness. This leads to a breakdown of theoretically derived scaling laws for ideal chains [12]. To compare the experimental results with predictions from polymer theory the effect of loop size on the rate constants for contact formation (Figure 22.8) can be compared to

the length dependence of the characteristic ratio (C_n; Figure 22.2). By comparison with polymer theory the limiting value for k_c for formation of short loops might be related to intrinsic chain stiffness, which causes the increase in C_n with chain length for short chains (see Section 22.2).

The 1:1 mixture of glycine and serine used in these experiments is expected to have a C_∞-value of about 3 and C_∞ should be reached for $n > 10$ (Figure 22.2) [21]. Figure 22.8 shows, however, that the poly(glycine-serine) chains behave like random chains only over distances longer than 20–30 amino acids, where $k_c \sim n^{-1.7}$. This indicates increased chain stiffness compared to the predicted value, which could be due to specific intrachain hydrogen bonds or van der Waals interactions and to excluded volume effects that restrict the number of chain conformations. This model is supported by the measurements of activation energies for the peptides of different length. Formation of long loops shows very low activation enthalpies whereas formation of short loops encounter significant energy barriers (F. Krieger and T. Kiefhaber, unpublished).

The complete effect of loop size on intrachain contact formation can be described by a model where length-dependent diffusional processes, which scale with $k = k_b \cdot n^{-m}$, limit the kinetics of formation of long loops. Contact formation reaches a limiting rate constant (k_a) when these diffusional motions become slower than length-independent short-range motions, which are probably governed by chain stiffness and steric effects. Accordingly, the effect of loop size on contact formation can be described by

$$k_c = \frac{1}{1/k_a + 1/(k_b \cdot n^{-m})} \tag{16}$$

The fit of the experimental results to Eq. (16) is shown in Figure 22.8 and gives a value of $k_a = (1.8 \pm 0.2) \cdot 10^8$ s^{-1}, $k_b = (6.7 \pm 1.6) \cdot 10^9$ s^{-1}, and $m = 1.72 \pm 0.08$ for poly(glycineserine), as discussed above.

22.4.2.3 Effect of Amino Acid Sequence on Chain Dynamics

Both theoretical considerations [18, 19, 21] (see Section 22.2) and experimental results from NMR measurements [71] show that polypeptide chains are especially flexible around glycyl residues. All amino acids except proline ($C_\infty > 100$) and glycine ($C_\infty = 2.2$) are predicted to have C_∞-values around 8.5–9.5 and C_∞ should be reached for intrachain distances longer than about 40–50 amino acids [18, 19, 21] (Figure 22.2). This indicates increased chain stiffness and longer root mean square end-to-end distances ($\sqrt{\langle r^2 \rangle_0}$) compared to the poly(glycine-serine) series (Figure 22.2). The effect of chain stiffness on peptide dynamics was tested in TTET experiments in polyserine chains [54]. Figure 22.8 compares the effect of loop size on intrachain diffusion in a series of Xan-(Ser)$_x$-NAla-Ser-Gly peptides with $x = 2$–11 ($n = 3$–12) to the behavior of poly(Gly-Ser) chains. Single exponential kinetics for contact formation were observed in all polyserine peptides. For short loops ($n < 5$) contact formation is virtually independent of loop size with a limiting value of $k_a = 8.7 \cdot 10^7$ s^{-1} (see Eq. (18)). This indicates that the local dynamics in polyser-

ine are about two- to threefold slower than in the poly(glycine-serine) peptides, which seems to be a small effect compared to the largely different properties expected for the stiffer polyserine chains (see Figure 22.2).

The decreased flexibility and the longer donor-acceptor distances in the polyserine chains are probably compensated by the decreased conformational space available for polyserine compared to poly(glycine-serine) peptides. [54] For longer polyserine chains contact formation slows down with increasing loop size. The effect of increasing loop size on the rates of contact formation seems to be slightly larger in polyserine compared to the poly(glycine-serine) series ($m = 2.1 \pm 0.3$; $k_b = (1.0 \pm 0.8) \cdot 10^{10}$ s^{-1}; see Eq. (16)). However, due to limitations in peptide synthesis it was not possible to obtain longer peptides, which would be required to get a more accurate scaling law for the polyserine peptides.

The kinetics of formation of short loops differ only by a factor of 2 for polyserine compared with poly(glycine-serine), arguing for only little effect of amino acid sequence on local chain dynamics (Figure 22.8). The effect of other amino acids on local chain dynamics was measured by performing TTET experiments on short host–guest peptides of the canonical sequence Xan-Ser-Xaa-Ser-NAla-Ser-Gly using the guest amino acids Xaa = Gly, Ser, Ala, Ile, His, Glu, Arg, and Pro [54]. Figure 22.9 shows that the amino acid side chain indeed has only little effect on the rates of contact formation. All amino acids except proline and glycine show very similar dynamics. Interestingly, there is a small but significant difference in rate between short side chains (Ala, Ser) and amino acids with longer side chains (Ile, Glu, Arg, His). Obviously, chains that extend beyond the C_β-atom slightly decrease the rates

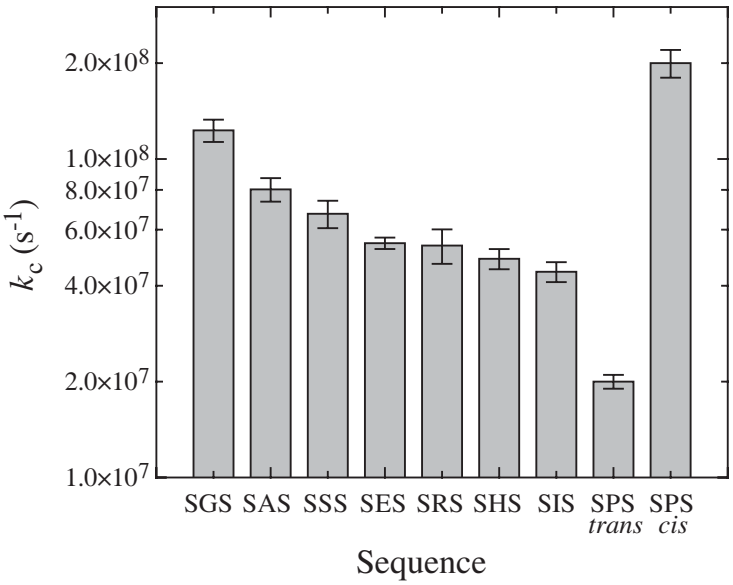

Fig. 22.9. Effect of amino acid sequence on local chain dynamics measured in host–guest peptides with the canonical sequence Xan-Ser-Xaa-Ser-NAla-Ser-Gly. The guest amino acid Xaa was varied and the rate constants for the different guest amino acids are displayed. Data taken from Ref. [54].

of local chain dynamics, whereas charges do not influence the dynamics. Glycyl and prolyl residues show significantly different dynamics compared with all other amino acids, as expected from their largely different conformational properties [19].

As shown before (Figure 22.8) glycine accelerates contact formation about two- to threefold compared with serine. Proline shows slower and more complex kinetics of contact formation with two rate constants of $k_1 = 2.5 \cdot 10^8$ s^{-1} and $k_2 = 2 \cdot 10^7$ s^{-1} and respective amplitudes of $A_1 = 20 \pm 5\%$ and $A_2 = 80 \pm 5\%$. This essentially reflects the *cis–trans* ratio at the Ser-Pro peptide bond in our host–guest peptide, which has a *cis* content of $16 \pm 2\%$ as determined by 1D ^{1}H-NMR spectroscopy using the method described by Reimer et al. [72]. Since the rate of *cis–trans* isomerization is slow ($\tau \sim 20$ s at 22 °C) there is no equilibration between the two isomers on the time scale of the TTET experiments. This allows the measurement of the dynamics of both the *trans* and the *cis* form. The results show that the two isomers significantly differ in their dynamic properties of $i, i + 4$ contact formation and that the *cis*-prolyl isomer actually shows the fastest rate of local contact formation of all peptides (Figure 22.9).

22.4.2.4 Effect of the Solvent on Intrachain Diffusion

The dynamics of short poly(glycine-serine) peptides measured with the xanthone–naphthalene TTET pair in water [54] were about 3 times faster than the previously measured rates in the same peptides using the thioxanthone–naphthalene pair in EtOH [50], although both systems were shown to be diffusion-controlled. Figure 22.10 shows that this difference can be attributed to solvent effects [54]. $\ln k_c$ linearly decreases with increasing EtOH concentration in a Xan-(Gly-Ser)$_4$-NAla-Ser-Gly peptide (Figure 22.10A). EtOH is a better solvent for polypeptide chains than water and should thus lead to a more extended ensemble of unfolded states. This model was supported by measuring the effect of GdmCl and urea on the contact rates in aqueous solutions. Both denaturants show similar effects on intrachain diffusion as EtOH, with a linear decrease in $\ln k_c$ with increasing denaturant concentration. Interestingly, the change in $\ln k_c$ with denaturant concentration ($m_c = \partial \ln k_c / \partial$ [Denaturant]) is twofold higher for GdmCl compared with urea, which essentially corresponds to their relative strength in unfolding proteins [73] (see below). Similar m_c-values for EtOH, urea and GdmCl were observed in a Xan-(Ser)$_9$-NAla-Ser-Gly peptides. [54] The observed effect is significantly stronger than expected from the increased solvent viscosity in concentrated GdmCl and urea solutions [50, 74].

The effect of GdmCl and urea on the chain dynamics suggested that these cosolvents may significantly change the chain properties. This was supported by measurements of the effect of GdmCl on the distance dependence of intrachain contact formation. Figure 22.10B compares the effect of loop size on the kinetics of contact formation in the Xan-(Gly-Ser)$_n$-NAla-Ser-Gly series in 8 M GdmCl and water. At high denaturant concentrations the switch from the length-independent dynamics to the length-dependent regime occurs already for formation of shorter loops. This indicates decreased chain stiffness in 8 M GdmCl compared with

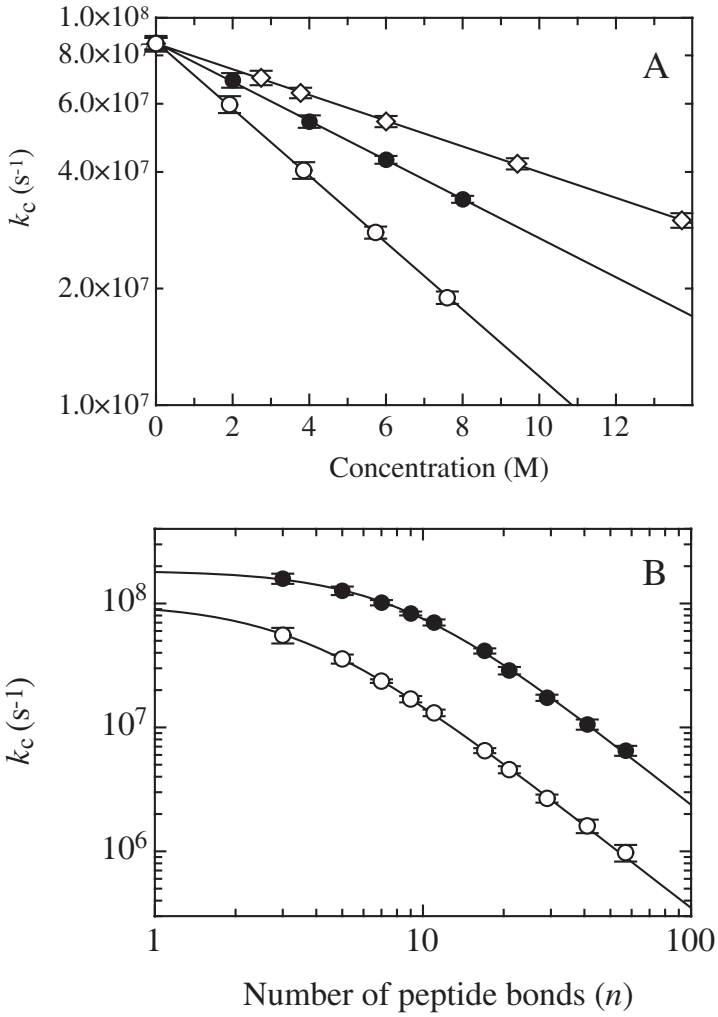

Fig. 22.10. A) Effect of various co-solvents on the dynamics of intrachain contact formation in a Xan-(Gly-Ser)$_4$-NAla-Ser-Gly peptide measured by TTET. Measurements were performed in aqueous solutions in the presence of ethanol (diamonds), urea (filled circles) and GdmCl (open circles). B) Effect of donor–acceptor distance (n) on the rate constant of contact formation in series of poly(Gly-Ser) peptides (cf. Figure 22.8). The rate constants for contact formation in water (filled circles) are compared with the values in 8 M GdmCl (open circles). Data taken from Ref. [54].

water, although the dynamics are significantly slowed down in the presence of GdmCl both for formation of short and long loops (Figure 22.10). For long peptides the effect of chain length on the rates of contact formation is similar in 8 M GdmCl and water with $k_c \sim n^{-1.8\pm0.1}$. These results revealed that denaturants like GdmCl and urea slow down local chain dynamics but lead to more flexible chains that behave like ideal polymers already at shorter donor–acceptor distances (Figure 22.10B). These seemingly contradicting findings can be rationalized based on the effect of denaturants on the conformational properties of polypeptide chains. Unlike water, solutions with high concentrations of denaturants represent good solvents for polypeptide chains. This reduces the strength of intramolecular in-

teractions like hydrogen bonds and van der Waals interactions relative to peptide–solvent interactions, which makes unstructured polypeptide chains more flexible and leads to a behavior expected for an unperturbed chain.

In agreement with this interpretation the effect of loop size on the rates of contact formation in 8 M GdmCl is close to the behavior of an unperturbed polypeptide chain predicted by Flory and coworkers [21] (see Figure 22.2). The decreased rate of contact formation at high denaturant concentrations can only in part be explained by an increased solvent viscosity. Additional effects like increased donor–acceptor distance, which is expected in good solvents compared to water and denaturant binding might also contribute to the decreased rate constants [74].

22.4.2.5 Effect of Solvent Viscosity on Intrachain Diffusion

Intrachain contact formation was shown to be strongly viscosity dependent as expected for a diffusional reaction. Viscosity effects on contact formation rates have been measured in TTET experiments on poly(Gly-Ser) peptides [50] (F. Krieger and T. Kiefhaber, unpublished). In all peptides a linear dependency of $\log k_c$ vs. $\log \eta$ was observed and the dependencies could be fitted with the empirical relationship

$$k = \frac{k_0}{\eta^{-\beta}} \tag{17}$$

with $\beta \leq 1$ (Figure 22.11). In the limit for long chains ($n > 15$) the rate of contact formation was found to be inversely proportional to the viscosity ($\beta = 1$) independent of the co-solvent used to alter the viscosity of the solution. In the limit for

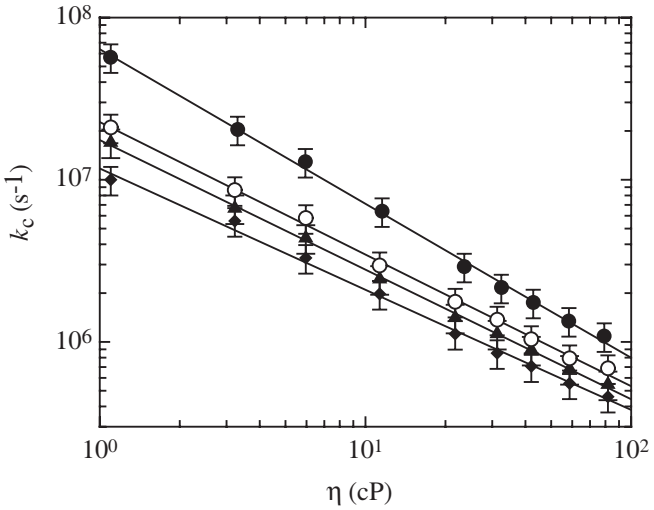

Fig. 22.11. Viscosity dependence of the rate of contact formation for poly(Gly-Ser)$_x$ peptides containing $x = 1$ (filled circles), 2 (open circles), 3 (filled triangles) and 4 (filled diamonds) glycine-serine pairs between thioxanthone and naphthylalanine (cf. Figure 22.3B). Linear fits of the double logarithmic plot of the data give slopes of -0.96 ± 0.05, -0.83 ± 0.05, -0.80 ± 0.05, and -0.81 ± 0.05, respectively. Experiments were carried out in ethanol/glycerol mixtures. Data were taken from Ref. [50].

short chains ($n < 10$), β was smaller than unity (0.8–0.9) [50]. This is not compatible with theoretical consideration which predict $\beta = 1$ as a result from Stokes law relating the solvent viscosity and the diffusion coefficient. β-values < 1 have also been observed for motions of simpler polymers in organic solvents [75–77] and for dynamics of native proteins [78–80].

Several origins have been proposed to explain such behavior like either position-dependent [81] or frequency-dependent [82, 83] friction coefficients. In addition, experiments on myoglobin [80] suggested that deviations from the Stokes law can also be caused by the structure of protein–solvent interfaces, which preferably contain water molecules and have the viscous co-solvent molecules preferentially excluded [84]. This results in a smaller microviscosity around the protein compared with bulk solvent. Additional experiments will be needed to identify the origin of fractional viscosity dependencies of dynamics in short chains.

22.4.2.6 End-to-end Diffusion vs. Intrachain Diffusion

When side-chain contacts are formed within a polypeptide chain during the folding process, the residues are commonly not located near the end of the polypeptide chain. Thus, the end-to-end contact formation experiments represent a rather specific and rare situation during the folding process. Based on the location of the contact sites, three categories of contact formation events in polymers can be distinguished (Figure 22.12). Type I corresponds to end-to-end contact formation. Type II corresponds to end-to-interior contacts and type III contacts are formed between two position remote from the chain ends. Measurements in long hydrocarbon chains yielded trends that cyclization rates are slowed down by additional groups at the ends of the chain [46] without yielding absolute magnitudes of the effects. The xanthone–NAla TTET system has proved to be suitable to perform such experiments in peptides. TTET experiments in type II and III systems have shown that k_c depends on the size of the additional tail (B. Fierz and T. Kiefhaber, unpublished). The strength of the effect is dependent on the nature of the sequence in the observed segment. In long and flexible chains between the labels (i.e., the long chain limit) the dependence on tail length is weaker than for short or stiff chains (the short chain limit).

Such behavior has been predicted by theory [85]. The observed effect should correlate with the surface of the additional amino acids on the ends, if solvent friction limits chain motions as suggested by the viscosity-dependence of the chain diffusion. However the chain movements should only be slowed down to a limiting value. In this limit, the segmental dynamics are independent on further extension of the chain. This limiting rate of innersegmental diffusion corresponds to the maximal rate at which specific side-chain contacts can be formed in the interior of a protein during folding.

22.4.2.7 Chain Diffusion in Natural Protein Sequences

Recently, contact formation rates have been measured in natural protein sequences from cytochrome *c* [64] and carp parvalbumin [55]. The results from these dynam-

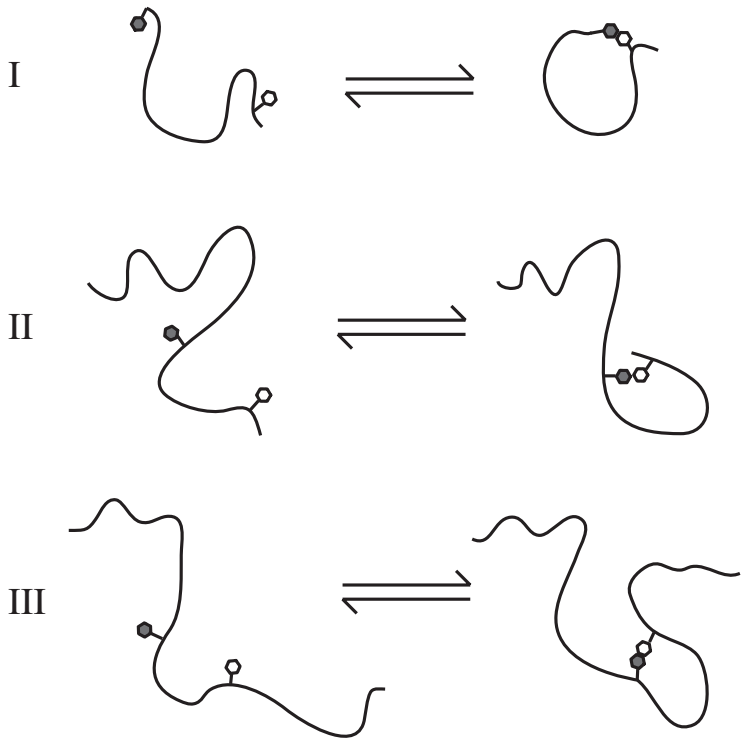

Fig. 22.12. Schematic representation of different types of contact formation in polymer chains. For details see text.

ics are in agreement with dynamics expected from the host–guest studies shown in Figure 22.9. The 18-amino-acid EF-loop of carp parvalbumin connects two α-helices and brings two phenylalanine residues into contact in the native protein, which were replaced by xanthone and naphthylalanine to measure TTET kinetics (Figure 22.13) [55]. The measured kinetics were single exponential (Figure 22.14) and the time constant for contact formation ($\tau = 50$ ns) was comparable to the dynamics for polyserine chains of the same length (Figure 22.8). The EF-loop contains several large amino acids like Ile, Val, and Leu but also four glycyl residues. Obviously, the effects of slower chain dynamics of bulkier side chains and faster dynamics around glycyl residues compensate, which leads to dynamics comparable to polyserine chains. These results indicate that polyserine is a good model to estimate the dynamics of glycine-containing loop sequences in proteins.

The Zn-porphyrine/Ru system was used to measure contact formation in cytochrome *c* unfolded in 5.4 M GdmCl [64]. The donor and quencher groups were separated by 15 amino acids (Figure 22.13) and contact formation was significantly slower ($\tau = 250$ ns) than for polyserine peptide chains of the same length. However, correcting for the effects of denaturant concentration (see Figure 22.10) and end-extensions (Section 22.4.2.6) on chain dynamics gives rate constants for the cytochrome *c* sequence which are comparable to the parvalbumin EF-loop in water.

A

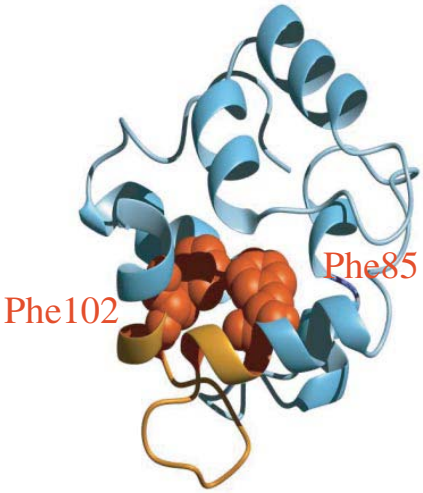

B

Residues 85-102 in carp parvalbumin:

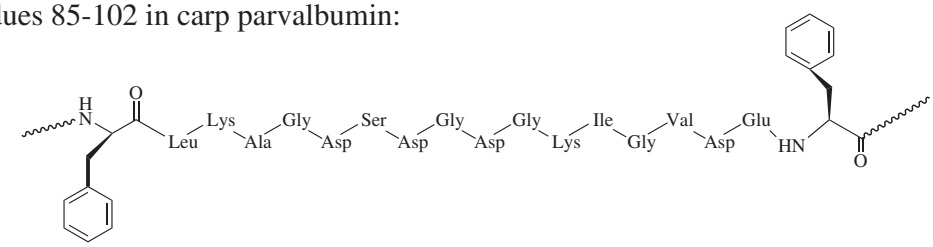

Chemically synthesized fragment with TTET labels:

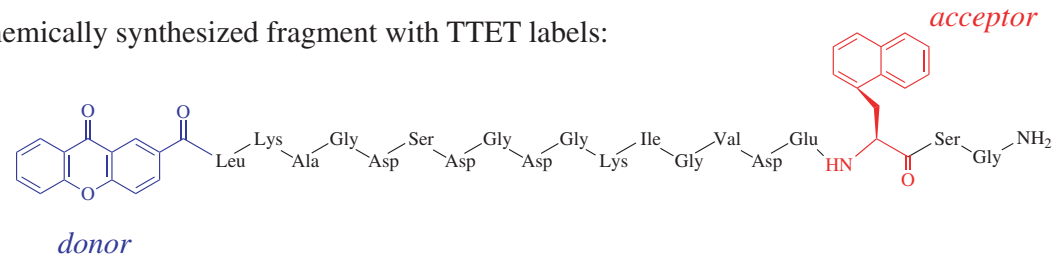

C

Residues 14-33 in horse heart cytochrome c with triplet quenching labels:

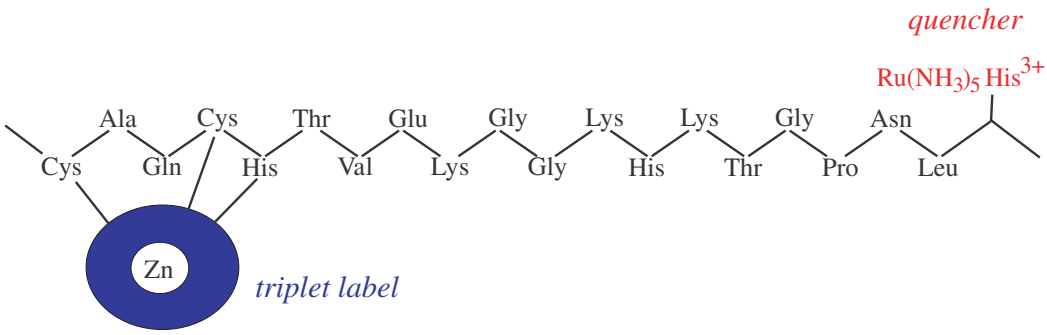

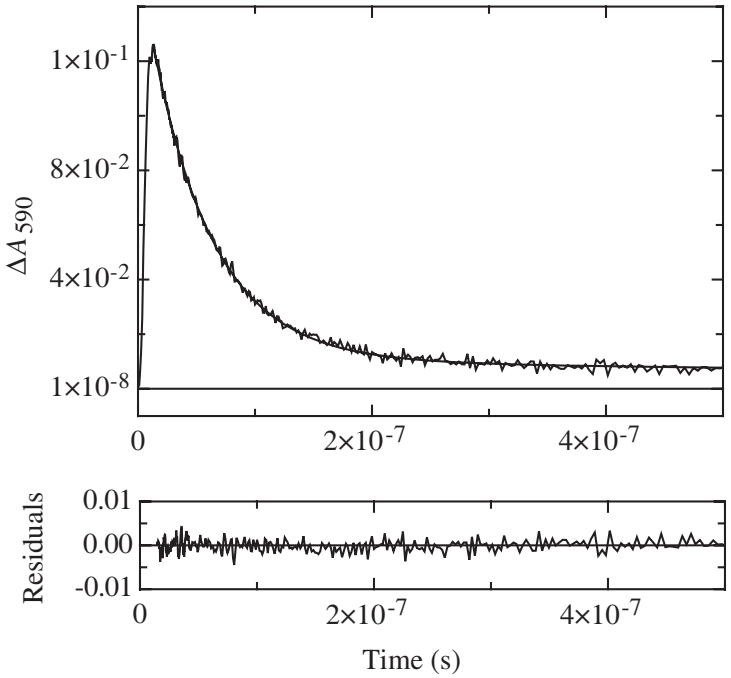

Fig. 22.14. Time course of formation and decay of xanthone triplets in parvalbumin loop fragment 85–102 after a 4 ns laser flash at $t = 0$. The change of xanthone triplet absorbance is measured at 590 nm. The dynamics of contact formation can be described by a single exponential with a time constant of 54 ± 3 ns. Data are taken from Ref. [55].

22.5
Implications for Protein Folding Kinetics

22.5.1
Rate of Contact Formation during the Earliest Steps in Protein Folding

The results on the time scales of intrachain diffusion in various unfolded polypeptide chains show that the amino acid sequence has only little effect on local dynamics of polypeptide chains. All amino acids show very similar rates of end-to-end diffusion with time constants between 12 and 20 ns for the formation of $i, i+4$

Fig. 22.13. A) Ribbon diagram of the structure of carp muscle β-parvalbumin [127]. Phe85 and Phe102 are shown as space-fill models. The phenylalanine residues have been replaced by the triplet donor and acceptor labels, xanthonic acid and naphthylalanine, respectively. The figure was prepared using the program MolMol [128] and the PDB file 4CPV [127]. B) Sequence of the carp muscle β-parvalbumin EF loop region (residues 85–102) and the synthesized fragment labeled with the two phenylalanine residues at position 85 and 102 replaced by donor (xanthone) and acceptor (naphthylalanine) groups for triplet–triplet energy transfer. C) Sequence from cytochrome *c* between the Zn-pophyrine group (excited triplet group) and the Ru-His complex used in triplet quenching experiments reported by Chang et al. [64].

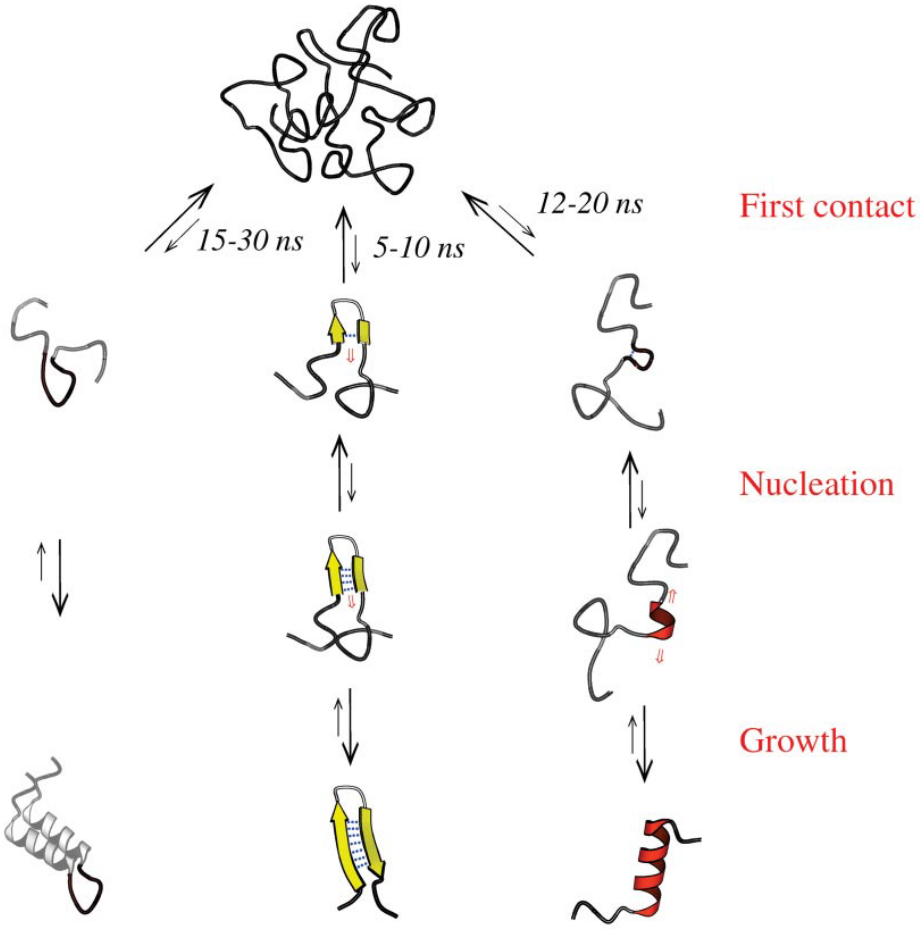

Fig. 22.15. Schematic representation of the time constants for the first steps in formation of loops, β-hairpins and α-helices during protein folding derived from the data measured by TTET in water. Adapted from Ref. [54].

contacts. Polypeptide chains are significantly more flexible around glycine ($\tau = 8$ ns) and stiffer around prolyl residues ($\tau = 50$ ns for the *trans* isomer). Presumably due to the shorter chain dimensions resulting from a *cis* peptide bond the rates of $i, i+4$ contact formation are fastest around the *cis* Ser-Pro bond ($\tau = 4$ ns). These results allow to set an upper limit for the rates of formation of the first productive local contacts during protein folding (Figure 22.15). They can directly be used to estimate the kinetics of loop formation, which are typically of the size of 6–10 amino acids [86]. The results suggest that loops can form with time constants of about 15 ns for glycine-rich loops and 30–40 ns for stiffer loops. β-hairpins, which are the most local structures in proteins, are often rich in glycine and proline [87]. Gly-Ser is actually one of the most frequent sequences found in hairpin loops. The results indicate that the time constants for the first steps in the formation of the tightest turns with $i, i+3$ contacts are around 5 ns for Gly and *cis* Xaa-Pro (Figures 22.8 and 22.9). In glycine- and proline-free turns these rates are slowed down to about 10–20 ns, depending on the amino acid sequence.

Formation of α-helices is most likely initiated by formation of a helical turn,

which involves formation of an $i, i+4$ interaction [88, 89]. Since helices are usually free of glycyl and prolyl residues the initiation cannot occur faster than in about 12–20 ns (Figures 22.8 and 22.9). It should be noted that these values do not represent time constants for nucleation of helices and hairpins (Figure 22.15), which most likely requires formation of more than one specific interaction and most likely encounters additional entropic and enthalpic barriers. The results on the rates of intrachain contact formation rather represent an upper limit for the dynamics of the earliest steps in secondary structure formation (i.e., $<$ for formation of the first contact during helix nucleation). They represent the prefactors (k_0) in the rate equation for secondary structure formation

$$k = k_0 \cdot e^{-\Delta G^{\circ\ddagger}/RT} \tag{18}$$

The measured contact rates thus allow us to calculate the height of the free energy barriers ($\Delta G^{\circ\ddagger}$) when they are compared to measured rate constants (k) for secondary structure formation. However, up to date no direct data on helix or hairpin formation in short model peptides are available. The dynamics of secondary structures were mainly studied by relaxation techniques like dielectric relaxation [90], ultrasonic absorbance [91], or temperature jump [92–94] starting from predominately folded structures (for a review see Ref. [95]). Since helix–coil and hairpin–coil transitions do not represent two-state systems, neither thermodynamically nor kinetically, the time constants for unfolding can not be directly related to rate constants of helix formation [96]. However, the observation of relaxation times around 1 μs for helix unfolding allowed the estimation of time constants for the growth steps of nucleated helices of about 1 to 10 ns, depending on the experimental system [90, 91, 93].

It may be argued that intrachain contacts in a polypeptide chain with a stronger bias towards folded structures can form faster than the observed dynamics in unstructured model polypeptide chains. However, weak interactions like van der Waals contacts between side chains and hydrogen bonds should dominate the early interactions during the folding process and the data on the dynamics of unfolded chains will provide a good model for the earliest events in folding. A stronger energy bias towards the native state will mainly increase the strength or the number of these interactions but not their dynamics of formation.

22.5.2
The Speed Limit of Protein Folding vs. the Pre-exponential Factor

Many small single domain proteins have been found to fold very fast, some of them even on the 10 to 100 μs time scale (for a review see Ref. [97]). These fast folding proteins include α-helical proteins like the monomeric λ-repressor [98, 99] or the engrailed homeodomain [100], β-proteins like cold shock protein of *Bacillus subtilis* or *B. cacodylicus* [101] or the WW-domains [102] and α,β-proteins like the single chain arc repressor [103]. There has been effort to design proteins that fold even faster [104, 105]. A folding time constant of 4.1 μs has been reported for a designed Trp-cage.

These very fast folding proteins sparked interest in finding the speed limit for protein folding, which is closely related to the speed limit of the fundamental steps of protein folding and thus also to the dynamics of the unfolded chain. The results on dynamics of contact formation in short peptides showed that no specific interactions between two points on the polypeptide chain can be formed faster than on the 5–10 ns time scale. Considering that dynamics are slowed down if the two groups are located in the interior of a long chain this time constant increases to about 50 ns. Formation of intrachain interactions represents the elementary step in the conformational search on the free energy landscape. Thus, the dynamics of this process set the absolute speed limit for the folding reaction. However, it will not necessarily represent the prefactor (k_0) for the folding process which represents the maximum rate for protein folding in the absence of free energy barriers ($\Delta G^{\circ\ddagger} = 0$, see Eq. (18)). It was shown that even fast apparent two-state folding proceeds through local minima and maxima on the free energy landscape [106, 107] and up to date it is unclear which processes contribute to the rate-limiting steps in protein folding (see Chapters 12.1, 12.2 and 14).

The transition state for folding seems to be native-like in topology but still partly solvated [108–111], Thus, both protein motions and dynamics of protein–solvent interactions in a native-like topology might contribute to the pre-exponential factor and k_0 will probably depend on the protein and on the location of the transition state along the reaction coordinate, which may change upon change in solvent conditions or mutation (see Section 5.3) [44, 106, 107].

22.5.3
Contributions of Chain Dynamics to Rate- and Equilibrium Constants for Protein Folding Reactions

As discussed above, the pre-exponential factor (k_0) for a protein folding reaction should contain major contributions from the rate of intrachain diffusion in an unfolded or partially folded polypeptide chain [112]. Thus, factors that influence intrachain diffusion, like denaturant concentration (Figure 22.10), will also affect the pre-exponential factor for folding. This will influence the observed folding rate constants and thus also the observed equilibrium constants [112]. A method that allows a quantitative description of reaction rates for processes in solution was developed by Kramers [113]. He considered a particle moving on an energy surface with two metastable states (e.g., native and unfolded protein) separated by a barrier (Figure 22.16). The motion of the particle is diffusional and can be described by the Langevin equation (Eq. (8)). The thermal motion of the solvent is modeled as the random force. Solving the diffusion equations, Kramers observed three different regimes which differ in the strength of interaction between system and environment. In the low friction limit the interactions are only weakly coupled. In this limit the rate of the barrier crossing reaction from the educt to the product state increases with increasing friction γ. In the intermediate friction limit the rate is independent on friction and the results from transition state theory and from Kramers' theory approach each other. In the high friction limit, which should cor-

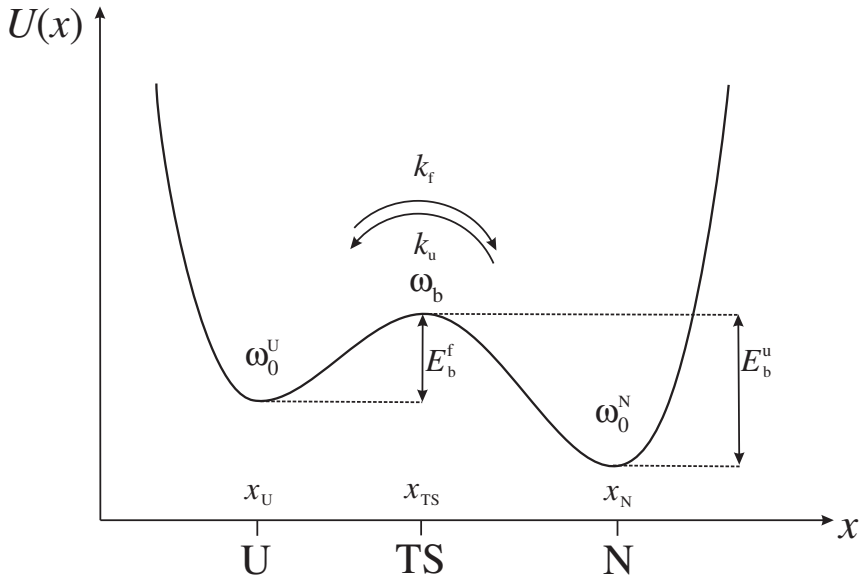

Fig. 22.16. Potential U(x) with two states N and U separated by an energy barriers. Escape from state U to N occurs via the rates k_f and k_u. E_b^f and E_b^u are the activation energies for the forward and back reaction. ω denotes the frequencies of phase point motion at the extremes of the potential. The drawing was adapted from Ref. [114].

respond to most reactions in solution and also to protein folding reactions, the rate of the reaction decreases when the friction is further increased. In this limit the equation for the rate as a function of friction, barrier height and temperature can be written as:

$$k = \frac{\omega_0 \omega_B}{2\pi\gamma} e^{(-E_b/kT)} \tag{19}$$

where ω stands for the frequency of motion of the particle in the starting well (ω_0) and on top of the barrier (ω_B). ω depends on the shape of the barrier and on the nature of the free energy surface [114]. By applying Stokes law this equation can then readily be expressed in terms of thermodynamic parameters and solvent viscosity.

$$k = \frac{C}{\eta(T)} \cdot \exp(-\Delta G^{\circ\ddagger}/RT) = k_0 \cdot \exp(-\Delta G^{\circ\ddagger}/RT) \tag{20}$$

It is not clear whether Kramers' approach in its simple form as described above is directly applicable to protein folding reactions, since it is difficult to measure the viscosity-dependence of folding and unfolding rate constants. The co-solvents used to modify solvent viscosity like glycerol, sucrose, or ethylene glycol generally stabilize the native state [84] and in part also the transition state of folding. This makes a quantification of the effect of solvent viscosity on protein folding rate constants difficult [115, 116].

The results from the viscosity dependence of end-to-end contact formation show that the rate constants in short peptides ($n < 10$) are not proportional to η^{-1} but rather to $\eta^{-0.8}$. This suggests that the presence of barriers in these peptides leads to a more complex behavior than expected from Eq. (20) and indicates that the frictional coefficient from Kramers' theory (γ, see. Eq. (19)) is not only determined by solvent viscosity for protein folding reactions.

Application of Kramers' theory to protein folding reactions shows the problems with quantitatively characterizing the barriers for protein folding. It is very difficult to determine pre-exponential factors for the folding and unfolding reaction, which are most likely different for each protein. Since the pre-exponential factors depend on the shape of the potential and on the dynamics in the individual wells (states), ω_0 will be different for the refolding reaction starting from unfolded protein (ω_0^{U}) and for the unfolding reaction starting from native protein (ω_0^{N}) and hence also the prefactors will be different for the forward and backward reactions. However, under all conditions Eq. (21) must be valid [117]:

$$K_{\mathrm{eq}} = \frac{k_{\mathrm{f}}}{k_{\mathrm{u}}} \tag{21}$$

Thus, the equilibrium constant (K_{eq}) contains contributions from the pre-exponential factors for folding (k_0^{f}) and unfolding (k_0^{u}) and from differences in $\Delta G^{\circ\ddagger}$, according to [112]

$$K_{\mathrm{eq}} = \frac{k_0^{\mathrm{f}} \cdot \mathrm{e}^{-\Delta G_{\mathrm{f}}^{\circ\ddagger}/RT}}{k_0^{\mathrm{u}} \cdot \mathrm{e}^{-\Delta G_{\mathrm{u}}^{\circ\ddagger}/RT}} \tag{22}$$

The contribution of differences in the prefactors for folding and unfolding to $\Delta G^{\circ}(= -RT \ln K_{\mathrm{eq}})$ are consequently [112]

$$\Delta G^{\circ} = \Delta G_{\mathrm{f}}^{\circ\ddagger} - \Delta G_{\mathrm{u}}^{\circ\ddagger} + \Delta G_{\mathrm{pref}}^{\circ}$$

$$\Delta G_{\mathrm{pref}}^{\circ} = RT \ln \frac{k_0^{\mathrm{u}}}{k_0^{\mathrm{f}}} \tag{23}$$

Differences in k_0 for folding and unfolding can thus significantly contribute to apparent protein folding barriers. A fivefold difference in k_0 would contribute 4 kJ mol^{-1} to the experimentally determined barrier height at 25 °C. Consequently, also changes in the dynamics of the unfolded state, which change the pre-exponential factor for the folding reaction by changing ω_0, will influence K_{eq}, even if the heights of the barriers are not changed. For many proteins significant residual structure in the unfolded state has been observed either directly by NMR [27, 28, 34, 43] or from the analysis of the denaturant dependence [44]. It was shown that this residual structure is sensitive to mutation, which can lead to significant changes in the solvent accessibility [44] and in the dynamics [39] of the unfolded state. This will lead to changes in k_0 for the folding reaction (k_0^{f}) by changing ω_0^{U} and will result in a change of the folding rate constant (k_{f}) and consequently also in the apparent free energy of activation, $\Delta G_{\mathrm{f}}^{\circ\ddagger}$(app) even if $\Delta G_{\mathrm{f}}^{\circ\ddagger}$ is

not affected by the mutations [112].

$$\Delta\Delta G_f^{\circ\ddagger}(\text{app}) = \Delta\Delta G_f^{\circ\ddagger} + RT \ln \frac{k_0^f(\text{wt})}{k_0^f(\text{mutant})} \quad (24)$$

As in the example above, a fivefold increase in k_0 of a mutant would apparently decrease $\Delta G_f^{\circ\ddagger}$ by 4 kJ mol^{-1}. This would have large effects on the interpretation of the results in terms of transition state structure (ϕ-value analysis, see Chapters 12.2 and 13), and might contribute to the large uncertainty in ϕ-value from mutants that lead to small changes in ΔG° [111].

Mutants that disrupt residual interactions in the unfolded state will most likely have only little effect on k_0 for unfolding (k_0^u), which should be determined by chain motions in the native state. Most native protein structures and transitions state structures were shown to be rather robust against mutations [44]. Thus, mutations which change the dynamics of unfolded proteins will result in an apparent change in ΔG°, in analogy to the effects discussed above (Eq. (24)).

Figure 22.10 shows that denaturants like urea and GdmCl significantly decrease the rate constants for intrachain diffusion (k_c). According to the considerations discussed above, this will also affect the denaturant dependence of the rate constants for protein folding (m_f-values with $m_f = \partial\Delta G_f^{\circ\ddagger}/\partial[\text{Denaturant}]$). Even if pre-equilibria involving unstable intermediates may dominate the early stages of folding, the observed denaturant dependence of intrachain diffusion will influence these steps by changing the forward rate constants of these equilibria. The m_c-values ($m_c = \partial(-RT \ln k_c)/\partial[\text{Denaturant}]$ for peptide dynamics vary only little with chain length and show values around 0.35 kJ mol^{-1} M^{-1} for urea and 0.50 kJ mol^{-1} M^{-1} for GdmCl [74]. Typical m_f-values for folding of the smallest fast folding proteins with chain length between 40 and 50 amino acids are around 1.0 kJ mol^{-1} M^{-1} for urea, indicating that up to 30% of the measured m_f-values may arise from contributions of chain dynamics. Larger two-state folders consisting of 70–100 amino acids typically show m_f-values around 3 kJ mol^{-1} M^{-1} for urea and 5 kJ mol^{-1} M^{-1} for GdmCl [107, 118], indicating that the denaturant dependence of chain dynamics constitutes up to 10% of the experimental m_f-values.

It is difficult to judge the effect of denaturants on the dynamics of the native state, which will influence the experimental m_u-values. However, it was observed that the effect of denaturants on chain dynamics is mainly based on increased chain dimensions (A. Möglich and T. Kiefhaber, unpublished results). This would argue for only little effects of denaturants on the internal dynamics of the native state and on the transition state structures, which were shown to be structurally robust against changes in denaturant concentration [44, 107, 111]. Thus, the m_u-values should have only little contributions from the effects of denaturants on chain dynamics.

Comparison of kinetic and equilibrium m-values ($m_{eq} = \partial\Delta G^\circ/\partial[\text{Denaturant}]$) is frequently used to characterize protein folding transition states according to the rate-equilibrium free energy relationship [44, 119, 120]:

$$\alpha_D = \frac{m_f}{m_{eq}} \quad (25)$$

α_D is interpreted as a measure for the solvent accessibility of the transition state. The contributions from chain dynamics to the m_f-values of small proteins lead to apparently higher α_D-values and thus to apparently less solvent exposed transition states. This might explain the commonly observed higher α_D-values compared to α_C-values ($\alpha_C = \frac{\Delta C_p^{\circ\ddagger}}{\Delta C_p^{\circ}}$), which are also believed to monitor the solvent accessibility of transition states [44, 120]. Temperature dependence of intrachain diffusion in unstructured peptides showed that this process is not associated with a measurable change in heat capacity (F. Krieger and T. Kiefhaber, unpublished results). This suggests that α_C-values give a more reliable picture of the solvent accessibility of the transition state than α_D-values.

This shows that changes in the dynamics of the unfolded state of a protein lead to changes in the prefactor for the folding reaction which has consequences for both the rate constant and the equilibrium constant of the folding reaction. In general, we cannot expect the pre-exponential factors to be independent of the solvent conditions such as denaturant concentration, temperature, and pressure. This will contribute to the experimentally determined *m*-values and the activation parameters ($\Delta H^{\circ\ddagger}, \Delta S^{\circ\ddagger}, \Delta V^{\circ\ddagger}$, and $\Delta C_p^{\ddagger}$) and to the equilibrium properties of the protein.

22.6
Conclusions and Outlook

Several experimental systems have been recently developed to measure rate constants for intrachain diffusion processes. Experimental studies on the dynamics of unfolded proteins have revealed single exponential kinetics for formation of specific intrachain interactions on the nanosecond time scale and have been able to elucidate scaling laws and sequence dependence of chain dynamics. It has further been shown that the results derived from homopolypeptide chains and host-guest studies are in agreement with dynamics of loop formation in short natural sequences. Further studies should aim at the investigation of the dynamics in full length unfolded proteins and in folding intermediates to obtain information on the special equilibrium and dynamic properties of free energy landscapes for protein folding reactions.

22.7
Experimental Protocols and Instrumentation

To measure absolute rate constants for contact formation several requirements have to be met by the experimental method and by the equipment for detection. The methods of choice to study contact formation are electron transfer or excited state quenching reactions. The main advantage of energy transfer systems is that they allow both the donor and the acceptor populations to be quantified during the experiment (see Figure 22.5).

22.7.1
Properties of the Electron Transfer Probes and Treatment of the Transfer Kinetics

The lifetime of excited states of the labels used in a specific system determine the time scale on which experiments can be performed. Triplet states are very long lived compared to fluorescence probes and thus allow studies in long chains and in unfolded proteins. Donor groups which undergo very fast intersystem crossing to the triplet state and which have a high quantum yield for intersystem crossing are well-suited. The xanthone derivatives used by Bieri et al. [50] and Krieger et al. [54, 55] form triplet states with a time constant of 2 ps and a quantum yield of 99% [56]. Tryptophan in contrast, which was used by Lapidus et al., has about 18% quantum yield [60] and forms triplet states with a time constant of 3 ns [62], which sets a limit to the fastest processes that can be monitored using tryptophan as a triplet donor. Triplet states usually have strong absorption bands that are easily observable. It is, however, important that the donor has an UV absorption band in a spectral region where no other part of the protein absorbs (i.e., >300 nm). This allows selective excitation of the donor. The requirements for the triplet acceptor are that the molecule should have lower triplet energy than the donor to enable exothermic TTET and it should not absorb light at the excitation wavelength of the donor. Additionally, no radicals should be formed at any time in the reaction, since they may damage the sample and their strong absorbance bands usually interfere with the measurements.

Further requirements of experimental systems which allow to measure the kinetics of contact formation on an absolute time scale are (i) that the process is very strongly distance dependent to allow transfer only at van der Waals distance between donor and acceptor and (ii) that the transfer reaction is faster than dissociation of the complex so that each van der Waals contact between the labels leads to transfer. The coupling of electron transfer to chain dynamics displayed in Figure 22.6 can be kinetically described by a three-state reaction if the excitation of the donor is fast compared to chain dynamics (k_c, k_{-c}) and electron transfer (k_{TT}).

$$\mathrm{O} \underset{k_{-c}}{\overset{k_c}{\rightleftharpoons}} \mathrm{C} \xrightarrow{k_{TT}} \mathrm{C}^* \tag{26}$$

O and C represent open chain conformations (no contact) and contact conformations of the chain, respectively. k_c and k_{-c} are apparent rate constant for contact formation and breakage, respectively. If the excited state quenching or transfer (k_{TT}) reaction is on the same time scale or slower than breaking of the contact (k_{-c}), the measured rate constants (λ_i) are functions of all microscopic rate constants.

$$\begin{aligned} \lambda_{1,2} &= \frac{B \pm \sqrt{B^2 - 4C}}{2} \\ B &= k_c + k_{-c} + k_{TT} \\ C &= k_c \cdot k_{TT} \end{aligned} \tag{27}$$

If the contact states have a much lower probability than the open conformations ($k_{-c} \gg k_c$) the kinetics will be single exponential and the observed rate constant corresponds to the smaller eigenvalue (λ_1) in Eq. (27). Since this is in agreement with experimental results we will only consider this scenario in the following. We can further simplify Eq. (27) if the time scales of electron transfer and chain dynamics are well separated. In the regime of fast electron transfer compared to chain dynamics ($k_{TT} \gg k_c, k_{-c}$) Eq. (27) can be approximated by

$$\lambda_1 = k_c \tag{28}$$

This is the desired case, since the observed kinetics directly reflect the dynamics of contact formation. In the regime of fast formation and breakage of the contact compared to electron transfer ($k_{TT} \ll k_c, k_{-c}$) Eq. (27) can be approximated by

$$\lambda_1 = \frac{k_c}{k_c + k_{-c}} \cdot k_{TT} \cong \frac{k_c}{k_{-c}} \cdot k_{TT} = K_c \cdot k_{TT} \tag{29}$$

where K_c reflects the ratio of contact conformations (C) over open chain conformations (O). In this limit the chain dynamics can not be measured but the fraction of closed conformations can be determined. It should be kept in mind that these simplifications only hold if the formation of excited states is fast compared to the following reactions. If the excitation is on the nanosecond time scale or slower, the solutions of the linear four-state model have to be used to analyze the kinetics [121, 122].

These considerations show that it is crucial to determine the rate constants for the photochemical processes in the applied system to be able to interpret the kinetic data. The photochemistry of the donor excitation and of the electron transfer process are usually characterized by investigating the isolated labels and the kinetics should be studied on the femtosecond to the nanosecond time scale to gain complete information on all photochemical processes in the system [56] (cf. Figure 22.6). To test whether each donor–acceptor contact leads to transfer it should be tested whether the reaction is diffusion controlled. This can be done by studying the bimolecular transfer process from the donor to acceptor groups and determine its rate constants, its temperature-dependence and its viscosity dependence (F. Krieger and T. Kiefhaber, in preparation). These tests will be described in detail in the following. The results showed, that both the xanthone/NAla system [54–56] and the porphyrin/Ru system [64] fulfill these requirements and thus allow measurements of absolute rate constant for contact formation. The Trp/Cys triplet quenching system, in contrast, is not diffusion controlled and gives significantly slower apparent contact rates than the diffusion-controlled systems [59, 63]. Also the DBO/Trp fluorescence quenching system does not seem to be completely diffusion controlled and might have slow electron transfer kinetics, since it gives significantly slower dynamics [65] compared to the xanthone/NAla system in the same peptides [54].

22.7.2
Test for Diffusion-controlled Reactions

22.7.2.1 **Determination of Bimolecular Quenching or Transfer Rate Constants**

To test whether an energy transfer or energy quenching pair has diffusion-controlled kinetics, the rate constant of energy transfer (k_q) should be measured using the free labels in solution under pseudo first-order conditions. In these experiments the concentration of the quencher or acceptor [Q] should be at least 10 times higher than the concentration of the donor to be in the pseudo first order regime. Since [Q] is approximately constant during the experiment, the apparent first-order rate constant (k) under pseudo first-order conditions is given by [123]

$$k = k_q \cdot [Q] \tag{30}$$

Thus, the bimolecular transfer constant (k_q) can be obtained by varying the quencher concentration [Q] and analyzing the data according to the Stern-Vollmer equation [124] (see Figure 22.17):

$$k = k_0 + k_q[Q] \tag{31}$$

Here, k_0 denotes the rate constant for triplet decay of the donor in absence of quencher (acceptor) and k the time constant in presence of the acceptor or quencher. For diffusion-controlled reactions of small molecules in water k_q is around $4–6 \cdot 10^9$ s^{-1}.

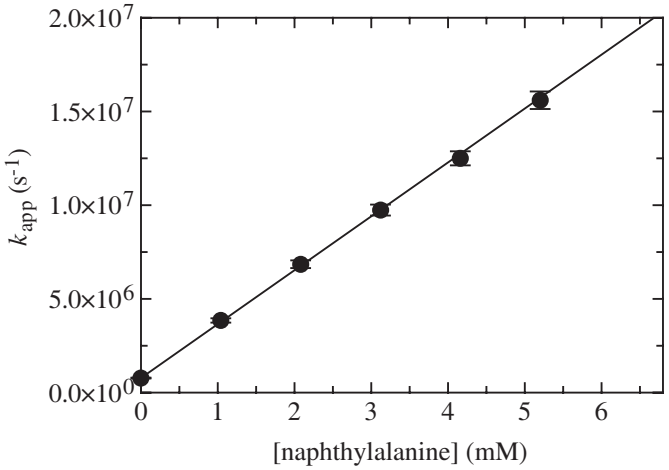

Fig. 22.17. Pseudo first-order measurements of bimolecular TTET from xanthonic acid to naphthylalanine in water. Xanthone concentration was 30 μM. The slope gives a bimolecular transfer constant (k_q) of $3 \cdot 10^9$ M^{-1} s^{-1} (see Eq. (31)). The data were discussed in Ref. [54].

22.7.2.2 Testing the Viscosity Dependence

For a diffusion-controlled reaction, k_q is inversely proportional to solvent viscosity ($k \sim 1/\eta$). The viscosity is usually varied by adding co-solvents like ethylene glycol or glycerol. To determine the final macroscopic viscosity instruments like the falling-ball viscosimeter or the Ubbelohde viscosimeter are used. The molecular size of the co-solvent used in a viscosity study is an important factor. The macroscopic viscosity of a glycerol/water mixture and a solution of polyethylene glycol might be the same, although the microscopic properties of these solutions are very different [80]. In the latter case the dissolved reactant molecules do only feel a fraction of the macroscopic viscosity. Thus it is advisable to use viscous co-solvents of small molecular weight. Glycerol/water mixtures have proven to be most useful because the viscosity can be varied from 1 cP (pure water) over three orders of magnitude by addition of glycerol. It is imperative to control the temperature when working with high concentrations of glycerol because the viscosity is strongly temperature dependent. Note that viscous co-solvents can interfere with the reaction that is studied.

In protein folding studies, the polyols used to vary the viscosity tend to stabilize the native state of proteins [84] making an analysis of the kinetic data difficult. However, for measurements of chain dynamics in unfolded polypeptide chains this effect should not interfere with the measurements as long as the co-solvents do not induce a structure. Specific effects of the polyols on chain conformations/dynamics can be tested by comparing the results from different co-solvents.

22.7.2.3 Determination of Activation Energy

Diffusion-controlled reactions typically have activation energies close to zero. The lack of an activation barrier in a diffusion controlled quenching reaction can be verified by determining the temperature dependence of k_q. The diffusion coefficients of the reactants are, however, temperature dependent, mainly through the effect of temperature on solvent viscosity according to the Stokes-Einstein equation.

$$D = \frac{k_B T}{6\pi r \eta} \tag{32}$$

After correcting for the change in viscosity of the solvent with temperature, the slope in an Arrhenius plot should not be higher than $k_B T$. As any photophysical reaction takes some time, diffusion control is only possible to a certain maximal concentration of quencher molecules. After that the photochemistry of the quenching or transfer process becomes rate limiting. This provides an upper limit of the rate constants that can be measured, even if the system is diffusion controlled at lower quencher concentrations. For the xanthone/naphthalene system TTET has been shown to occur faster than 2 ps and thus this system is suitable to obtain absolute time constants for all processes slower than 10–20 ps [56].

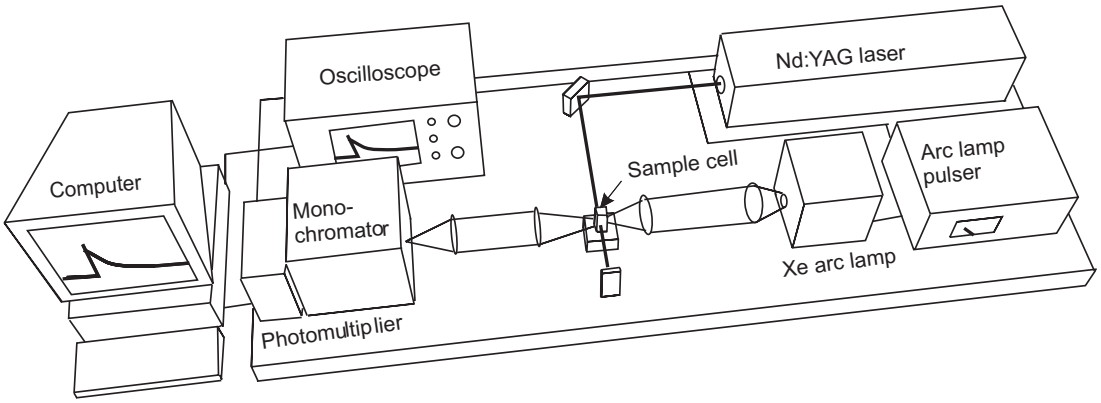

Fig. 22.18. Schematic representation of a laserflash set-up used to measure electron transfer reactions.

22.7.3
Instrumentation

The instrumentation required to perform experiments on contact formation kinetics consists of a high-energy light source to produce excited states and a detection mechanism (Figure 22.18). A pulsed laser is used to produce triplet donor states in TTET or triplet quenching experiments. The duration of the light pulse has to be very short (i.e., shorter than the time scale of the reaction of interest). Additionally, the excitation pulse has to provide enough energy to excite the major portion of the molecules in the sample to order to generate a large signal. A pulsed Nd:YAG laser with a pulse width of <5 ns and a pulse energy of $\sim$100 mJ is well-suited for these purposes. Transient UV absorption is used to detect the triplet states in TTET or triplet quenching experiments. A pulsed flash lamp generates enough light for the absorption measurements. The lamp intensity typically stays at a constant plateau value for several hundred microseconds, which is sufficient for TTET measurements. A monochromator is used to monitor single wavelengths. Transient spectra can be reconstructed from measurements at different wavelengths or by using a CCD camera.

Acknowledgments

We thank Annett Bachmann, Florian Krieger, Robert Kübler and Andreas Möglich for discussion and comments on the manuscript.

References

1 EINSTEIN, A. (1906). Eine neue Bestimmung der Molekül-dimensionen. *Ann. d. Phys.* 19, 289–306.

2 VON SMOLUCHOWSKI, M. (1906). Zur kinetischen Theorie der Brownschen Molekularbewegung und der Suspensionen. *Ann. d. Phys.* 21, 756–780.

3 VON SMOLUCHOWSKI, M. (1916). Drei Vorträge über Diffusion, Brownsche Molekularbewegung und Koagulation von Kolloidteilchen. *Phys. Z.* 17, 557–571.

4 JACOBSEN, H. & STOCKMAYER, W. H. (1950). Intramolecular reaction in polycondensations. I. The theory of linear systems. *J. Phys. Chem.* 18, 1600–1606.

5 ROUSE, P. E. (1953). A theory of the linear viscoelastic properties of dilute solutions of coiling polymers. *J. Chem. Phys.* 21, 1272–1280.

6 ZIMM, B. (1956). Dynamics of polymer molecules in dilute solutions: viscoelasticity, flow bifringence and dielectric loss. *J. Chem. Phys.* 24, 269–278.

7 SZABO, A., SCHULTEN, K. & SCHULTEN, Z. (1980). First passage time approach to diffussion controlled reactions. *J. Chem. Phys.* 72, 4350–4357.

8 DE GENNES, P. G. (1985). Kinetics of collapse for a flexible coil. *J. Phys. Lett.* 46, L639–L642.

9 FIXMAN, M. (1987). Brownian dynamics of chain polymers. *Faraday Discuss. Chem. Soc.* 83, 199–211.

10 THIRUMALAI, D. (1995). From minimal models to real protein: time scales for protein folding kinetics. *J. Phys.* 5, 1457–1467.

11 FLORY, P. J. (1953). *Principles of Polymer Chemistry.* Cornell University Press, Ithaca.

12 FLORY, P. J. (1969). *Statistical Mechanics of Chain Molecules.* Hanser Publishers, Munich.

13 YAMAKAWA, H. (1971). *Modern Theory of Polymer Solutions.* Harper & Row, New York.

14 DOI, M. (1996). *Introduction to Polymer Science.* Oxford University Press, Oxford.

15 RUBINSTEIN, M. & COLBY, R. H. (2003). *Polymer Physics.* Oxford University Press, Oxford.

16 KUHN, W. (1934). Über die Gestalt fadenförmiger Moleküle in Lösungen. *Kolloid-Z* 52, 269.

17 KUHN, W. (1936). Beziehungen zwischen Molekülgrösse, statistischer Molekülgestalt und elastischen Eigenschaften hochpolymerer Stoffe. *Kolloid-Z* 76, 258.

18 BRANT, D. A. & FLORY, P. J. (1965). The configuration of random polypeptide chains. II. Theory. *J. Am. Chem. Soc.* 87, 2791–2800.

19 SCHIMMEL, P. R. & FLORY, P. J. (1967). Conformational energy and configurational statistics of poly-L-proline. *Proc. Natl Acad. Sci. USA* 58, 52–59.

20 BRANT, D. A., MILLER, W. G. & FLORY, P. J. (1967). Conformational energy estimates for statistically coiling polypeptide chains. *J. Mol. Biol.* 23, 47–65.

21 MILLER, W. G., BRANT, D. A. & FLORY, P. J. (1967). Random coil configurations of polypeptide chains. *J. Mol. Biol.* 23, 67–80.

22 RAMACHANDRAN, G. N. & SASISEKHARAN, V. (1968). Conformation of polypeptides and proteins. *Adv. Protein Chem.* 23, 283–437.

23 DE GENNES, P. G. (1979). *Scaling Concepts in Polymer Physics.* Cornell University Press, Ithaca.

24 DOI, M. & EDWARDS, S. F. (1986). *The Theory of Polymer Dynamics.* Oxford University Press, Oxford.

25 PAPPU, R. V., SRINAVASAN, R. & ROSE, G. D. (2000). The Flory isolated-pair hypthesis is not valid for polypeptide chains: Implications for protein folding. *Proc. Natl Acad. Sci. USA* 97, 12565–12570.

26 EDWARDS, S. F. (1965). The statistical mechanics of polymers with excluded volume. *Proc. Phys. Soc.* 85, 613–624.

27 EVANS, P. A., TOPPING, K. D., WOOLFSON, D. N. & DOBSON, C. M. (1991). Hydrophobic clustering in nonnative states of a protein: interpretation of chemical shifts in NMR spectra of denatured states of lysozyme. *Proteins* 9, 248–266.

28 NERI, D., BILLETER, M., WIDER, G. & WÜTHRICH, K. (1992). NMR determination of residual structure in

a urea-denatured protein, the 434-repressor. *Science* 257, 1559–1563.

29 Logan, T. M., Theriault, Y. & Fesik, S. W. (1994). Structural characterization of the FK506 binding protein unfolded in urea and guanidine hydrochloride. *J. Mol. Biol.* 236, 637–648.

30 Smith, C. K., Bu, Z. M., Anderson, K. S., Sturtevant, J. M., Engelman, D. M. & Regan, L. (1996). Surface point mutations that significantly alter the structure and stability of a protein's denatured state. *Protein Sci.* 5, 2009–2019.

31 Sari, N., Alexander, P., Bryan, P. N. & Orban, J. (2000). Structure and dynamics of an acid-denatured protein G mutant. *Biochemistry* 39, 965–977.

32 Wong, K. B., Clarke, J., Bond, C. J. et al. (2000). Towards a complete description of the structural and dynamic properties of the denatured state of barnase and the role of residual structure in folding. *J. Mol. Biol.* 296, 1257–1282.

33 Teilum, K., Kragelund, B. B., Knudsen, J. & Poulsen, F. M. (2000). Formation of hydrogen bonds precedes the rate-limiting formation of persistent structure in the folding of ACBP. *J. Mol. Biol.* 301, 1307–1314.

34 Kortemme, T., Kelly, M. J., Kay, L. E., Forman-Kay, J. D. & Serrano, L. (2000). Similarities between the spectrin SH3 domain denatured state and its folding transition state. *J. Mol. Biol.* 297, 1217–1229.

35 Garcia, P., Serrano, L., Durand, D., Rico, M. & Bruix, M. (2001). NMR and SAXS characterization of the denatured state of the chemotactic protein CheY: implications for protein folding initiation. *Protein Sci.* 10, 1100–1112.

36 Choy, W. Y. & Forman-Kay, J. D. (2001). Calculation of ensembles of structures representing the unfolded state of an SH3 domain. *J. Mol. Biol.* 308, 1011–1032.

37 Kazmirski, S. L., Wong, K. B., Freund, S. M., Tan, Y. J., Fersht, A. R. & Daggett, V. (2001). Protein folding from a highly disordered denatured state: the folding pathway of chymotrypsin inhibitor 2 at atomic resolution. *Proc. Natl Acad. Sci. USA* 98, 4349–4354.

38 Yi, Q., Scalley-Kim, M. L., Alm, E. J. & Baker, D. (2000). NMR characterization of residual structure in the denatured state of protein L. *J. Mol. Biol.* 299, 1341–1351.

39 Klein-Seetharaman, J., Oikawa, M., Grimshaw, S. B., Wirmer, J., Duchardt, E., Ueda, T. et al. (2002). Long-range interactions within a nonnative protein. *Science* 295, 1719–1722.

40 Gardiner, C. W. (1985). *Handbook of Stochastic Methods.* Springer Verlag, Berlin, Heidelberg, New York.

41 Sakanishi, A. (1968). Dynamic viscoelastic properties of dilute polyisobutylene solutions. *J. Chem. Phys.* 48, 3850–3858.

42 Perkins, T. T., Quake, S. R., Smith, D. E. & Chu, S. (1994). Relaxation of a single DNA molecule observed by optical microscopy. *Science* 264, 822–826.

43 Dyson, H. J. & Wrigth, P. E. (2002). Insights into the structure and dynamics of unfolded proteins from nuclear magnetic resonance. *Adv. Protein Chem.* 62, 311–340.

44 Sánchez, I. E. & Kiefhaber, T. (2003). Hammond behavior versus ground state effects in protein folding: evidence for narrow free energy barriers and residual structure in unfolded states. *J. Mol. Biol.* 327, 867–884.

45 Mar, A. & Winnik, M. A. (1985). End-to-end cyclization of hydrocarbon chains: temperature effects on an intramolecular phosphorescence quenching reaction in solution. *J. Am. Chem. Soc.* 107, 5376–5382.

46 Lee, S. & Winnik, M. A. (1997). Cyclization rates for two points in the interior of a polymer chain. *Macromolecules* 30, 2633–2641.

47 Stryer, L. & Haugland, R. P. (1967). Energy transfer: a spectroscopic ruler. *Proc. Natl Acad. Sci. USA* 58, 719–726.

48 Haas, E., Katchalski-Katzir, E. & Steinberg, I. Z. (1978). Brownian

motion at the ends of oligopeptid chains as estimated by energy transfer between chain ends. *Biopolymers* 17, 11–31.

49 Beechem, J. M. & Haas, E. (1989). Simultaneous determination of intramolecular distance distributions and conformational dynamics by global analysis of energy transfer measurements. *Biophys J.* 55, 1225–1236.

50 Bieri, O., Wirz, J., Hellrung, B., Schutkowski, M., Drewello, M. & Kiefhaber, T. (1999). The speed limit for protein folding measured by triplet-triplet energy transfer. *Proc. Natl Acad. Sci. USA* 96, 9597–9601.

51 Haas, E., Wilchek, M., Katchalski-katzir, E. & Steinberg, I. Z. (1975). Distribution of end-to-end distances of oligopeptides in solution as estimated by energy-transfer. *Proc. Natl Acad. Sci. USA* 72, 1807–1811.

52 Hagen, S. J., Hofrichter, J., Szabo, A. & Eaton, W. A. (1996). Diffusion-limited contact formation in unfolded cytochrome c: Estimating the maximum rate of protein folding. *Proc. Natl Acad. Sci. USA* 93, 11615–11617.

53 Camacho, C. J. & Thirumalai, D. (1995). Theoretical predictions of folding pathways by using the proximity rule, with applications to bovine pancreatic inhibitor. *Proc. Natl Acad. Sci. USA* 92, 1277–1281.

54 Krieger, F., Fierz, B., Bieri, O., Drewello, M. & Kiefhaber, T. (2003). Dynamics of unfolded polypeptide chains as model for the earliest steps in protein folding. *J. Mol. Biol.* 332, 265–274.

55 Krieger, F., Fierz, B., Axthelm, F., Joder, K., Meyer, D. & Kiefhaber, T. (2004). Intrachain diffusion in a protein loop fragement from carp parvalbumin. *Chem. Phys.*, in press.

56 Satzger, H., Schmidt, B., Root, C. et al. (2004). Ultrafast quenching of the xanthone triplet by energy transfer: new insight into the intersystem crossing kinetics in press.

57 Closs, G. L., Johnson, M. D., Miller, J. R. & Piotrowiak, P. (1989). A connection between intramolecular long-range electron, hole and triplet energy transfer. *J. Am. Chem. Soc.* 111, 3751–3753.

58 Wagner, P. J. & Klán, P. (1999). Intramolecular triplet energy transfer in flexible molecules: electronic, dynamic, and structural aspects. *J. Am. Chem. Soc.* 121, 9626–9635.

59 Lapidus, L. J., Eaton, W. A. & Hofrichter, J. (2000). Measuring the rate of intramolecular contact formation in polypeptides. *Proc. Natl Acad. Sci. USA* 97, 7220–7225.

60 Volkert, W. A., Kuntz, R. R., Ghiron, C. A., Evans, R. F., Santus, R. & Bazin, M. (1977). Flash photolysis of tryptophan and *N*-acetyl-L-tryptophanamide; the effect of bromide on transient yields. *Photochem. Photobiol.* 26, 3–9.

61 Gonnelli, M. & Strambini, G. B. (1995). Phosphorescence lifetime of tryptophan in proteins. *Biochemistry* 34, 13847–13857.

62 Bent, D. V. & Hayon, E. (1975). Excited state chemistry of aromatic amino acids and related peptides: III. Tryptophan. *J. Am. Chem. Soc.* 97, 2612–2619.

63 Yeh, I. C. & Hummer, G. (2002). Peptide loop-closure kinetics from microsecond molecular dynamics simulations in explicit solvent. *J. Am. Chem. Soc.* 124, 6563–6568.

64 Chang, I.-J., Lee, J. C., Winkler, J. R. & Gray, H. B. (2003). The protein-folding speedlimit: Intrachain diffusion times set by electron-transfer rates in denatured $Ru(NH_3)_5$(His-33)-Zn-cytochrome c. *Proc. Natl Acad. Sci. USA* 100, 3838–3840.

65 Hudgins, R. R., Huang, F., Gramlich, G. & Nau, W. M. (2002). A fluorescence-based method for direct measurements of submicroscond intramolecular contact formation in biopolymers: an exploratory study with polypeptides. *J. Am. Chem. Soc.* 124, 556–564.

66 Huang, F. & Nau, W. M. (2003). A conformational flexibility scale for amino acids in peptides. *Angew. Chem. Int. Ed. Engl.* 42, 2269–2272.

67 NEUWEILER, H., SCHULZ, A., BÖHMER, M., ENDERLEIN, J. & SAUER, M. (2003). Measurement of submicrosecond intramolecular contact formation in peptides at the single-molecule level. *J. Am. Chem. Soc.* 125, 5324–5330.

68 ZWANZIG, R. (1997). Two-state models for protein folding. *Proc. Natl Acad. Sci. USA* 94, 148–150.

69 SPÖRLEIN, S., CARSTENS, H., SATZGER, H. et al. (2002). Ultrafast spectroscopy reveals sub-nanosecond peptide conformational dynamics and validates molecular dynamics simulation. *Proc. Natl Acad. Sci. USA* 99, 7998–8002.

70 BREDENBECK, J., HELBING, J., SIEG, A. et al. (2003). Picosecond conformational transition and equilibration of a cyclic peptide. *Proc. Natl Acad. Sci. USA* 100, 6452–6457.

71 SCHWALBE, H., FIEBIG, K. M., BUCK, M. et al. (1997). Structural and dynamical properties of a denatured protein. Heteronuclear 3D NMR experiments and theoretical simulations of lysozyme in 8 M urea. *Biochemistry* 36, 8977–8991.

72 REIMER, U., SCHERER, G., DREWELLO, M., KRUBER, S., SCHUTKOWSKI, M. & FISCHER, G. (1998). Side-chain effects on peptidyl-prolyl cis/trans isomerization. *J. Mol. Biol.* 279, 449–460.

73 PACE, C. N. (1986). Determination and analysis of urea and guanidine hydrochloride denaturation curves. *Methods Enzymol.* 131, 266–280.

74 MÖGLICH, A., KRIEGER, F. & KIEFHABER, T. (2004). Molecular basis of the effect of urea and guanidinium chloride on the dynamics of unfolded proteins. submitted.

75 ZHU, W., GISSER, D. J. & EDIGER, M. D. (1994). C-13 NMR measurements of polybutadiene local dynamics in dilute-solution – further evidence for non-Kramers behavior. *J. Polym. Sci. B Polym. Phys.* 32, 2251–2262.

76 ZHU, W. & EDIGER, M. D. (1997). Viscosity dependence of polystyrene local dynamics in dilute solutions. *Macromolecules* 30, 1205–1210.

77 TYLIANAKIS, E. I., DAIS, P. & HEATLEY, F. (1997). Non-Kramers' behavior of the chain local dynamics of pvc in dilute solution. Carbon-13 NMR relaxation study. *J. Polym. Sci. B* 35, 317–329.

78 BEECE, D., EISENSTEIN, L., FRAUENFELDER, H. et al. (1980). Solvent Viscosity and Protein Dynamics. *Biochemistry* 19, 5147–5157.

79 YEDGAR, S., TETREAU, C., GAVISH, B. & LAVALETTE, D. (1995). Viscosity dependence of O2 escape from respiratory proteins as a function of cosolvent molecular weight. *Biophys. J.* 68, 665–670.

80 KLEINERT, T., DOSTER, W., LEYSER, H., PETRY, W., SCHWARZ, V. & SETTLES, M. (1998). Solvent composition and viscosity effects on the kinetics of CO binding to horse myoglobin. *Biochemistry* 37, 717–733.

81 GAVISH, B. (1980). Position-dependent viscosity effects on rate coefficients. *Phys. Rev. Lett.* 44, 1160–1163.

82 DOSTER, W. (1983). Viscosity scaling and protein dynamics. *Biophys. Chem.* 17, 97–103.

83 SCHLITTER, J. (1988). Viscosity dependence of intramolecular activated processes. *Chem. Phys.* 120, 187–197.

84 TIMASHEFF, S. N. (2002). Protein hydration, thermodynamic binding and preferential hydration. *Biochemistry* 41, 13473–13482.

85 PERICO, A. & BEGGIATO, M. (1990). Intramolecular diffusion-controlled reactions in polymers in the optimized Rouse Zimm approach 1. The effects of chain stiffness, reactive site positions, and site numbers. *Macromolecules* 23, 797–803.

86 LESZCYNSKI, J. F. & ROSE, G. D. (1986). Loops in globular proteins: a novel category of secondary structure. *Science* 234, 849–855.

87 WILMOT, C. M. & THORNTON, J. M. (1988). Analysis and prediction of the different types of β-turns in proteins. *J. Mol. Biol.* 203, 221–232.

88 ZIMM, B. H. & BRAGG, J. K. (1959). Theory of phase transition between helix and random coil in polypeptide chains. *J. Chem. Phys.* 31, 526–535.

89 LIFSON, S. & ROIG, A. (1961). On the

theory of helix-coil transitions in polypeptides. *J. Chem. Phys.* 34, 1963–1974.

90 Schwarz, G. & Seelig, J. (1968). Kinetic properties and the electric field effect of the helix-coil transition of poly(γ-benzyl L-glutamate) determined from dielectric relaxation measurements. *Biopolymers* 6. 1263–1277.

91 Gruenewald, B., Nicola, C. U., Lustig, A. & Schwarz, G. (1979). Kinetics of the helix-coil transition of a polypeptide with non-ionic side chain groups, derived from ultrasonic relaxation measurements. *Biophys. Chem.* 9, 137–147.

92 Williams, S., Causgrove, T. P., Gilmanshin, R. et al. (1996). Fast events in protein folding: helix melting and formation in a small peptide. *Biochemistry* 35, 691–697.

93 Thompson, P., Eaton, W. & Hofrichter, J. (1997). Laser temperature jump study of the helix-coil kinetics of an alanine peptide interpreted with a ''kinetic zipper'' model. *Biochemistry* 36, 9200–9210.

94 Munoz, V., Thompson, P., Hofrichter, J. & Eaton, W. (1997). Folding dynamics and mechanism of β-hairpin formation. *Nature* 390, 196–199.

95 Bieri, O. & Kiefhaber, T. (1999). Elementary steps in protein folding. *Biol. Chem.* 380, 923–929.

96 Schwarz, G. (1965). On the kinetics of the helix-coil transition of polypeptides in solution. *J. Mol. Biol.* 11, 64–77.

97 Kubelka, J., Hofrichter, J. & Eaton, W. A. (2004). The protein folding speed limit. *Curr. Opin. Struct. Biol.* 14, 76–88.

98 Huang, G. S. & Oas, T. G. (1995). Submillisecond folding of monomeric lambda repressor. *Proc. Natl Acad. Sci. USA* 92, 6878–6882.

99 Burton, R. E., Huang, G. S., Daugherty, M. A., Fullbright, P. W. & Oas, T. G. (1996). Microsecond protein folding through a compact transition state. *J. Mol. Biol.* 263, 311–322.

100 Mayor, U., Guydosh, N. R., Johnson, C. M. et al. (2003). The complete folding pathway of a protein from nanoseconds to microseconds. *Nature* 421, 863–867.

101 Perl, D., Welker, C., Schindler, T. et al. (1998). Conservation of rapid two-state folding in mesophilic, thermophilic and hyperthermophilic proteins. *Nat. Struct. Biol.* 5, 229–235.

102 Ferguson, N., Johnson, C. M., Macias, M., Oschkinat, H. & Fersht, A. R. (2001). Ultrafast folding of WW domains without structured aromatic clusters in the denatured state. *Proc. Natl Acad. Sci. USA* 98, 13002–13007.

103 Robinson, C. R. & Sauer, R. T. (1996). Equilibrium stability and submillisecond refolding of a designed single-chain arc repressor. *Biochemistry* 35, 13878–13884.

104 Neidigh, J. W., Fesinmeyer, R. M. & Andersen, N. H. (2002). Designing a 20-residue protein. *Nat. Struct. Biol.* 9, 425–430.

105 Qiu, L., Pabit, S. A., Roitberg, A. E. & Hagen, S. J. (2002). Smaller and faster: The 20-residue Trp-cage protein folds in 4 μs. *J. Am. Chem. Soc.* 124, 12952–12953.

106 Bachmann, A. & Kiefhaber, T. (2001). Apparent two-state tendamistat folding is a sequential process along a defined route. *J. Mol. Biol.* 306, 375–386.

107 Sánchez, I. E. & Kiefhaber, T. (2003). Evidence for sequential barriers and obligatory intermediates in apparent two-state protein folding. *J. Mol. Biol.* 325, 367–376.

108 Kuwajima, K., Mitani, M. & Sugai, S. (1989). Characterization of the critical state in protein folding. Effects of guanidine hydrochloride and specific Ca^{2+} binding on the folding kinetics of alpha-lactalbumin. *J. Mol. Biol.* 206, 547–561.

109 Makarov, D. E., Keller, C. A., Plaxco, K. W. & Metiu, H. (2002). How the folding rate constant of simple single-domain proteins depends on the number of native contacts. *Proc. Natl Acad. Sci. USA* 99, 3535–3539.

110 MAKAROV, D. E. & PLAXCO, K. W. (2003). The topomer search model: A simple. quanitative theory of two-state protein folding kinetics. *Protein Sci.* 12, 17–26.

111 SÁNCHEZ, I. E. & KIEFHABER, T. (2003). Origin of unusual phi-values in protein folding: Evidence against specific nucleation sites. *J. Mol. Biol.* 334, 1077–1085.

112 BIERI, O. & KIEFHABER, T. (2000). Kinetic models in protein folding. In *Protein Folding: Frontiers in Molecular Biology*, 2nd edn (PAIN, R., ed.), pp. 34–64. Oxford University Press, Oxford.

113 KRAMERS, H. A. (1940). Brownian motion in a field of force and the diffusion model of chemical reactions. *Physica* 4, 284–304.

114 HÄNGGI, P., TALKNER, P. & BORKOVEC, M. (1990). Reaction-rate theory: fifty years after Kramers. *Rev. Mod. Phys.* 62, 251–341.

115 JACOB, M., SCHINDLER, T., BALBACH, J. & SCHMID, F. X. (1997). Diffusion control in an elementary protein folding reaction. *Proc. Natl Acad. Sci. USA* 94, 5622–5627.

116 PLAXCO, K. W. & BAKER, D. (1998). Limited internal friction in the rate-limiting step of a two-state protein folding reaction. *Proc. Natl Acad. Sci. USA* 95, 13591–13596.

117 VAN'T HOFF, J. H. (1884). *Etudes de dynamique*. Muller, Amsterdam.

118 JACKSON, S. E. (1998). How do small single-domain proteins fold? *Folding Des.* 3, R81–R91.

119 TANFORD, C. (1970). Protein denaturation. Part C. Theoretical models for the mechanism of denaturation. *Adv. Protein Chem.* 24, 1–95.

120 SÁNCHEZ, I. E. & KIEFHABER, T. (2003). Non-linear rate-equilibrium free energy relationships and Hammond behavior in protein folding. *Biophys. Chem.* 100, 397–407.

121 SZABO, Z. G. (1969). Kinetic characterization of complex reaction systems. In *Comprehensive Chemical Kinetics* (BAMFORD, C. H. & TIPPER, C. F. H., eds), Vol. 2, pp. 1–80. 7 vols. Elsevier, Amsterdam.

122 KIEFHABER, T., KOHLER, H. H. & SCHMID, F. X. (1992). Kinetic coupling between protein folding and prolyl isomerization. I. Theoretical models. *J. Mol. Biol.* 224, 217–229.

123 MOORE, J. W. & PEARSON, R. G. (1981). *Kinetics and Mechanisms*., John Wiley & Sons, New York.

124 STERN, O. & VOLMER, M. (1919). Über die Abklingungszeit der Fluoreszenz. *Phys. Z.* 20, 183–188.

125 LAPIDUS, L. J., EATON, W. A. & HOFRICHTER, J. (2001). Dynamics of intramolecular contact fromation in polypeptides: distance dependence of quenching rates in a room-temperature glass. *Phys. Rev. Lett.*, 258101-1–258101-4.

126 LAPIDUS, L. J., STEINBACH, P. J., EATON, W. A., SZABO, A. & HOFRICHTER, J. (2002). Effects of chain stiffness on the dynamics of loop formation in polypeptides. Appendix: Testing a 1-diensional diffusion model for peptide dynamics. *J. Phys. Chem. B* 106, 11628–11640.

127 KUMAR, V. D., LEE, L. & EDWARDS, B. F. (1990). Refined crystal structure of calcium-liganded carp parvalbumin 4.25 at 1.5 Å resolution. *Biochemistry* 1404–1412.

128 KORADI, R., BILLETER, M. & WÜTHRICH, K. (1996). MOLMOL: a program for display and analysis of macromolecular structures. *J. Mol. Graphics* 14, 51–55.

10

Using Triplet–Triplet Energy Transfer to Measure Conformational Dynamics in Polypeptide Chains

Beat Fierz, Karin Joder, Florian Krieger, and Thomas Kiefhaber

Summary

Intrachain diffusion processes play an important role in protein folding and function. In this chapter we discuss the application of triplet–triplet energy transfer to directly measure rate constants for intrachain contact formation in polypeptide chains. The photochemistry of triplet–triplet energy transfer is described, experimental prerequisites of the method are discussed, and a detailed description of the experimental protocols and data analysis is given.

Key Words: Triplet–triplet energy transfer; chain dynamics; protein folding; electron transfer; laserflash photolysis.

1. Introduction

Dynamics of polypeptide chains play an essential role in folding and function of proteins and peptides. They represent the underlying motions in the transitions between different protein conformations and they determine the rate at which a folding polypeptide chain can explore conformational space. Conformational search within a polypeptide chain is limited by intrachain diffusion processes, i.e., by the rate at which two points along the chain can form an interaction. The knowledge of the rates of intrachain contact formation in polypeptide chains and their dependence on amino acid sequence, chain length, and local structure formation is therefore essential for an understanding of the dynamics of protein folding and for the characterization of the free energy barriers of the folding reactions. In addition, intrachain diffusion provides an upper limit for the speed at which a protein can reach its native state just like free diffusion provides an upper limit for the rate constant of bimolecular reactions.

In the last years, several experimental systems have been developed to measure contact formation between specific sites on a polypeptide chain. The dynamics of

From: *Methods in Molecular Biology, vol. 350: Protein Folding Protocols*
Edited by: Y. Bai and R. Nussinov © Humana Press Inc., Totowa, NJ

unfolded polypeptide chains have first been studied using fluorescence resonance energy transfer (FRET) from an energy donor to an energy acceptor group ***(1)***. FRET was shown to be a powerful tool to determine donor–acceptor distances ***(2)***, but time-resolved FRET kinetics also contain major contributions from diffusion of the two FRET probes relative to each other ***(1,3)***. Determination of the diffusion constants allowed the first estimates of the time scale of chain diffusion processes in polypeptide chains, but it remained unclear whether the same diffusion constants represent the dynamics for formation of van der Waals contact between two groups. In addition, analysis of the FRET data critically depends on the shape of the donor–acceptor distribution function, which had to be introduced in the data analysis and, thus, did not allow model-free analysis of the data.

Rates of intrachain diffusion have later been estimated from the rate constant for intramolecular bond formation in guanidinium hydrochloride (GdmCl)-unfolded cytochrome c ***(4)***. The reaction of a methionine with a heme group separated by 50–60 amino acids along the chain gave time constants around 35–40 μs. Extrapolating these data to shorter distances gave an estimate of 1 μs for the time constant of contact formation at a distance of 10 peptide bonds. However, it turned out that the recombination reaction of heme with methionine is too slow to directly measure chain dynamics and the resulting rate constants did not directly reflect chain dynamics.

These early studies on intrachain diffusion did not yield absolute rate constants for contact formation, but they were important to trigger the development of more direct and model-free methods to study chain diffusion. Recently, several experimental systems using triplet states to directly monitor contact formation in model peptides and protein fragments have been introduced. In the following, we will present systems using triplet–triplet energy transfer (TTET) and triplet quenching to directly measure chain dynamics. We will briefly introduce the photochemistry of the processes involved and will discuss the experimental requirements for direct model-free measurements of chain dynamics in detail.

2. Using TTET to Measure Peptide Dynamics

Figure 1 illustrates the concept of TTET experiments applied to measurements of protein dynamics. A triplet donor and a triplet acceptor group are introduced at specific points in polypeptide chains. The donor is selectively excited by a laserflash and typically undergoes fast intersystem crossing into the triplet state (*see* **Fig. 2**). Upon intrachain diffusion the triplet donor and triplet acceptor groups meet and the triplet state is transferred to the acceptor. Because TTET is a two-electron exchange process (Dexter mechanism), it has a very strong distance dependence and usually requires van der Waals contact to allow for electron transfer ***(5)***. This should be contrasted to FRET, which occurs through dipole–dipole interactions and, thus, allows energy transfer over larger distances.

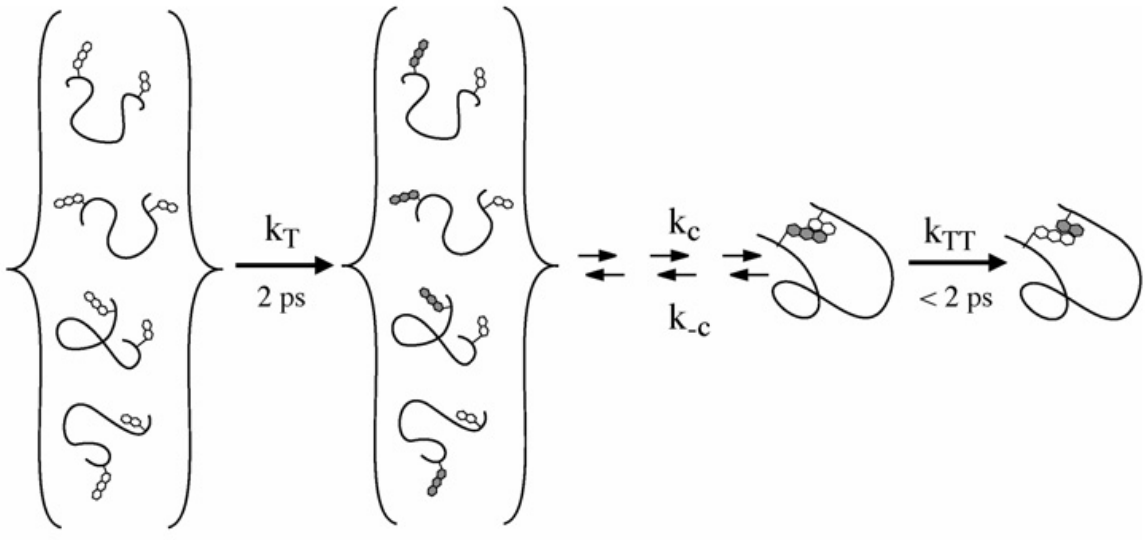

Fig. 1. Schematic representation of the triplet–triplet energy transfer experiments. The experiments allow determination of the absolute rate constant for contact formation (k_c) in the ensemble of unfolded conformation, if formation of the triplet state (k_T) and the transfer process (k_{TT}) are much faster than chain dynamics (k_{TT}, $k_t >> k_c$, k_{-c}; *see* **Subheading 2.1.**). The rate constants given for k_T and k_{TT} were taken from **ref. *6***.

A prerequisite for efficient and rapid transfer is that the acceptor group has a significantly lower triplet energy than the donor group (**Fig. 2**). A well-suited pair for TTET measurements are xanthone derivates as a triplet donor and naphthalene as a triplet acceptor group (**Fig. 3**) The triplet states of these molecules have specific absorbance bands, which can easily be monitored to measure the decay of the donor triplet states and the concomitant increase of acceptor triplet states (**Fig. 4**). The time constant for formation of xanthone triplet states is around 2 ps ***(6)***. TTET between xanthone and naphthalene is faster than 2 ps and has a bimolecular transfer rate constant of 4×10^9 $M^{-1}s^{-1}$ ***(6,7)***, which is the value expected for a diffusion-controlled reaction between small molecules in water (*see* **Subheading 2.2.**). Owing to this fast photochemistry, TTET between xanthone and naphthalene allows measurements of absolute rate constants for diffusion processes slower than 10–20 ps (*see* **Subheading 2.1.**). The upper limit of the experimental time window accessible by TTET is set by the intrinsic lifetime of the donor, which is around 20–30 µs for the xanthone triplet state in water. Xanthone has a high quantum yield for intersystem crossing ($\phi_{ISC} = 0.99$, $\varepsilon \approx 4000$ $M^{-1}cm^{-1}$) and the triplet state has a strong absorbance band with a maximum around 590 nm in water ($\varepsilon^T_{590} \approx 10{,}000$ $M^{-1}cm^{-1}$). This allows single pulse measurements at rather low peptide concentrations (10–50 µ*M*). The low concentrations applied in the experiments also rule out contributions from intermolecular transfer reactions, which would have half times higher than 50 µs in this concentration range ***(7,8)***. Also contributions from through-bond transfer

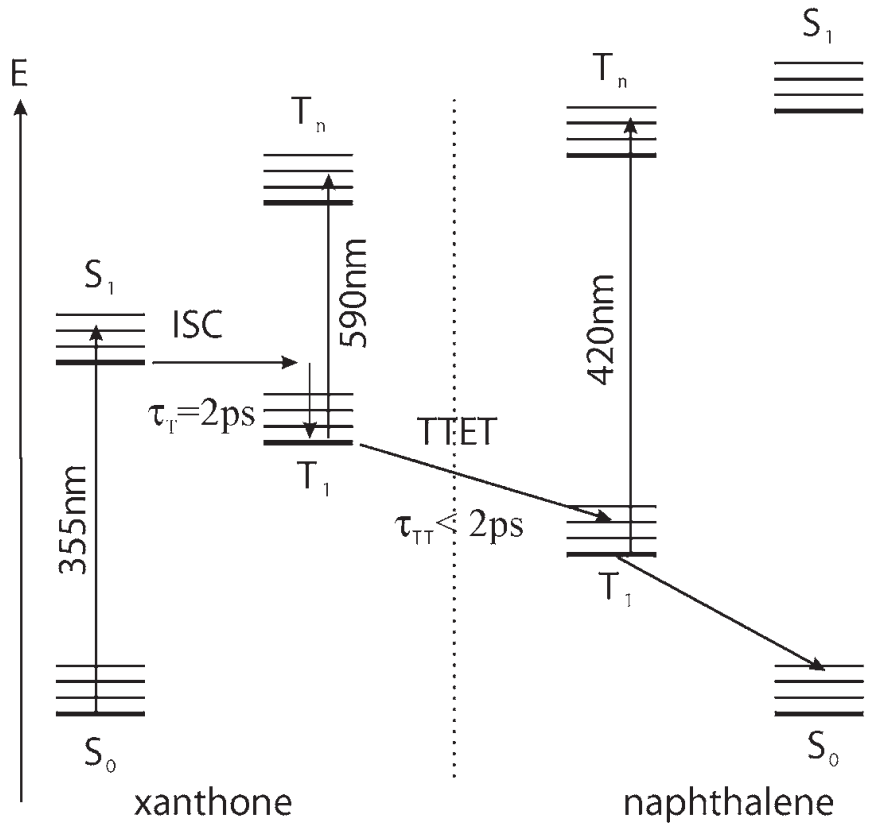

Fig. 2. Jablonski diagram for triplet–triplet energy transfer (TTET) from xanthone to naphthalene. Rate constants for triplet formation (k_T) and TTET (k_{TT}) were measured by laserflash photolysis using fs pulses ***(6)***.

processes can be neglected, because this can not occur over distances beyond eight bonds ***(9,10)*** and even the shortest peptides used in TTET studies had donor and acceptor separated by 11 bonds.

2.1. Kinetics of TTET Coupled to Polypeptide Chain Dynamics

The coupling of electron transfer to chain dynamics displayed in **Fig. 1** can be kinetically described by a three-state reaction if the excitation of the donor is fast compared with chain dynamics (k_c, k_{-c}) and electron transfer (k_{TT}).

$$O \underset{k_{-c}}{\overset{k_c}{\rightleftharpoons}} C \xrightarrow{k_{TT}} C^* \qquad (1)$$

O and *C* represent open chain conformations (no contact) and contact conformations of the chain, respectively. k_c and k_{-c} are apparent rate constant for contact formation and breakage, respectively. If the excited state quenching or transfer (k_{TT}) reaction is on the same time scale or slower than breaking of the contact (k_{-c}), the measured rate constants (λ_i) are functions of all microscopic rate constants.

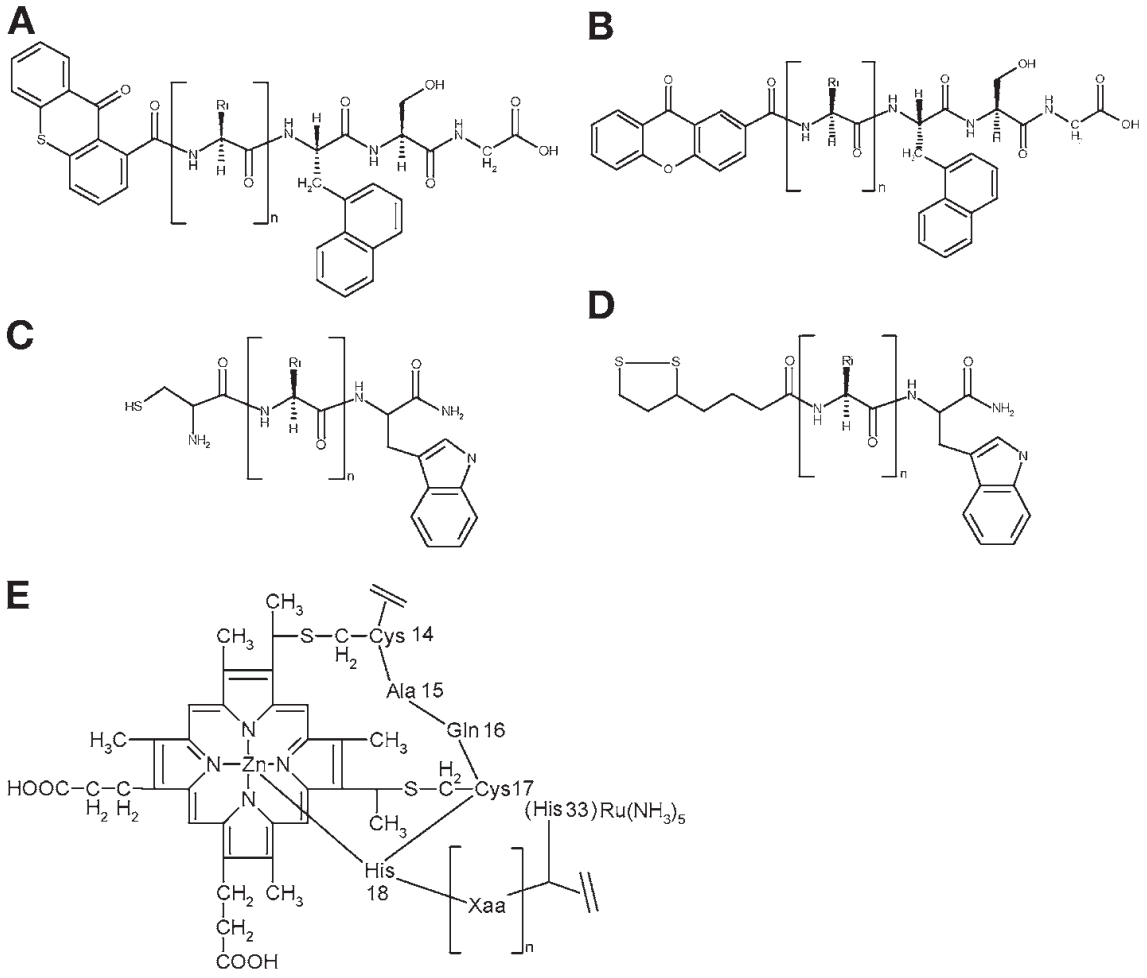

Fig. 3. Structures of different experimental systems used to measure intrachain contact formation. Results from these systems are summarized in **Table 1**. **(A)** Thioxanthone- and naphthylalanine-labeled poly(Gly-Ser) peptides to measure contact formation by triplet–triplet energy transfer (TTET) ***(8)***. **(B)** Xanthone- and naphthylalanine-labeled peptides to measure contact formation by TTET in various homopolymer chains and natural sequences with up to 57 amino acids between donor and acceptor ***(7,20,21,23)***. **(C,D)** Tryptophan and cysteine or lipoate-labeled peptides to measure contact formation by Trp triplet quenching in various short peptide chains ***(19,28,29)***. **(E)** Quenching of Zn-porphyrin triplets by Ru-His complexes in unfolded cytochrome c ***(27)***.

$$\lambda_{1,2} = \frac{B \pm \sqrt{B^2 - 4C}}{2}$$
$$B = k_c + k_{-c} + k_{TT} \qquad (2)$$
$$C = k_c \cdot k_{TT}$$

If the population of contact conformations is low ($k_{-c} >> k_c$) the kinetics will be single exponential and the observed rate constant corresponds to the smaller

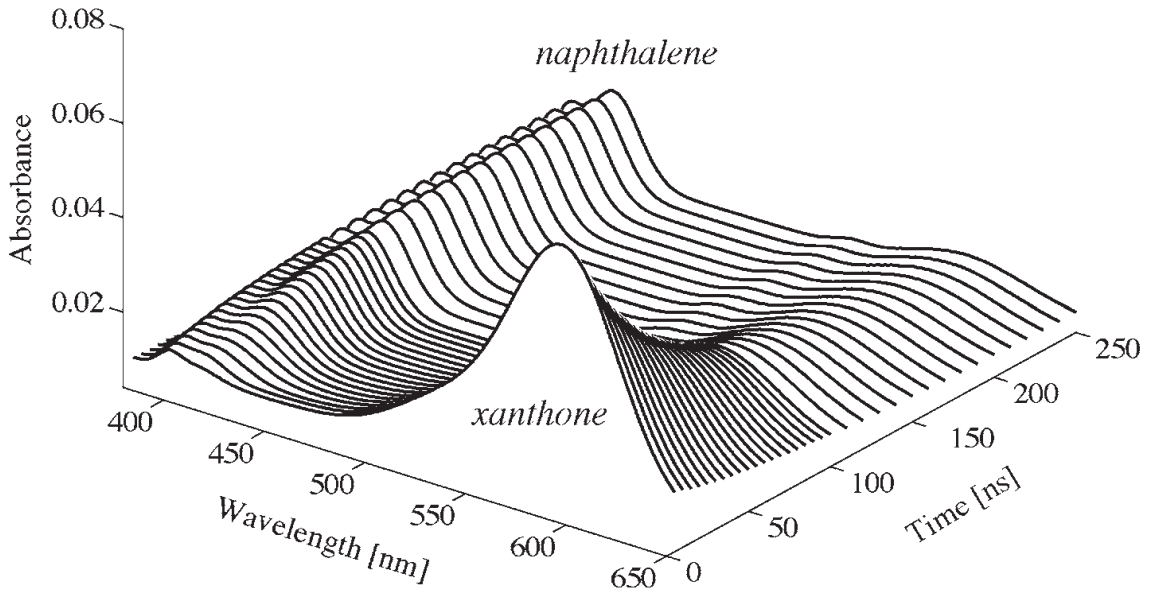

Fig. 4. Time-dependent change in the absorbance spectrum of a Xan-(Gly-Ser)$_{14}$-NAla-Ser-Gly peptide after a 4-ns laser flash at 355 nm. The decay in the intensity of the xanthone triplet absorbance band around 590 nm is accompanied by a corresponding increase in the naphthalene triplet absorbance band around 420 nm (adapted from **ref.** *7*).

eigenvalue (λ_1) in **Eq. 2**. Because this is in agreement with experimental results, we will only consider this scenario in the following. We can further simplify **Eq. 2** if the time scales of electron transfer and chain dynamics are well separated. In the regime of fast electron transfer compared with chain dynamics ($k_{TT} >> k_c, k_{-c}$) **Eq. 2** can be approximated by:

$$\lambda_1 = k_c \tag{3}$$

This is the desired case, because the observed kinetics directly reflect the dynamics of contact formation. In the regime of fast formation and breakage of the contact compared to electron transfer ($k_{TT} << k_c, k_{-c}$) **Eq. 2** can be approximated by:

$$\lambda_1 = \frac{k_c}{k_c + k_{-c}} \cdot k_{TT} \cong \frac{k_c}{k_{-c}} \cdot k_{TT} = K_c \cdot k_{TT} \tag{4}$$

where K_c reflects the ratio of contact conformations (C) over open chain conformations (O). In this limit the chain dynamics cannot be measured but the fraction of closed conformations can be determined. It should be kept in mind that these simplifications only hold if the formation of excited states is fast compared with the following reactions. If the excitation is on the nanosecond time scale or slower, the solutions of a linear four-state model have to be used to analyze the kinetics ***(11,12)***.

2.2. Test for Suitability of a Donor–Acceptor Pair to Directly Measure Chain Dynamics

2.2.1. Characterization of the Photochemistry

The considerations previously discussed show that it is crucial to characterize the rate constants for the photochemical processes in the applied system to be able to interpret the kinetic data. The photochemistry of the donor excitation and of the electron transfer process are usually characterized by investigating the isolated labels. Because the photochemical processes involved in TTET are often fast, the kinetics should be studied on the fs to the nanosecond time scale to gain complete information on all photochemical processes in the system ***(6)*** (**Fig. 2**).

2.2.2. Test for Diffusion Controlled Reactions

To test whether each donor–acceptor contact leads to transfer, it should be examined whether the reaction is diffusion-controlled. This can be done by studying the bimolecular transfer process from the donor to acceptor groups and determine its rate constants, its temperature-dependence, and its viscosity-dependence.

2.2.2.1. Determination of the Bimolecular Transfer Rate Constant

The bimolecular rate constant for energy transfer (k_q) can be measured using the free labels in solution under pseudo first-order conditions. In these experiments the concentration of the quencher or acceptor (Q) should be at least 10 times higher than the concentration of the donor to be in the pseudo first-order regime. Because (Q) is approximately constant during the experiment, the apparent first-order rate constant (k) under pseudo first-order conditions is given in **ref. *13***.

$$k = k_q \cdot [Q] \tag{5}$$

Thus, the bimolecular transfer constant (k_q) can be obtained by varying the quencher concentration (Q) and analyzing the data according to the Stern–Volmer equation ***(14)*** (*see* **Fig. 5**).

$$k = k_0 + k_q[Q] \tag{6}$$

Here, k_0 denotes the rate constant for triplet decay of the donor in absence of quencher (acceptor) and k the rate constant in presence of the acceptor or quencher. For diffusion-controlled reactions of small molecules in water, k_q is around 4–6 $\times$ 10^9 s^{-1}.

2.2.2.2. Viscosity-Dependence of the Transfer Reaction

For a diffusion-controlled reaction, the viscosity dependence of k_q is inversely proportional to solvent viscosity ($k \sim 1/\eta$). The viscosity is usually varied by

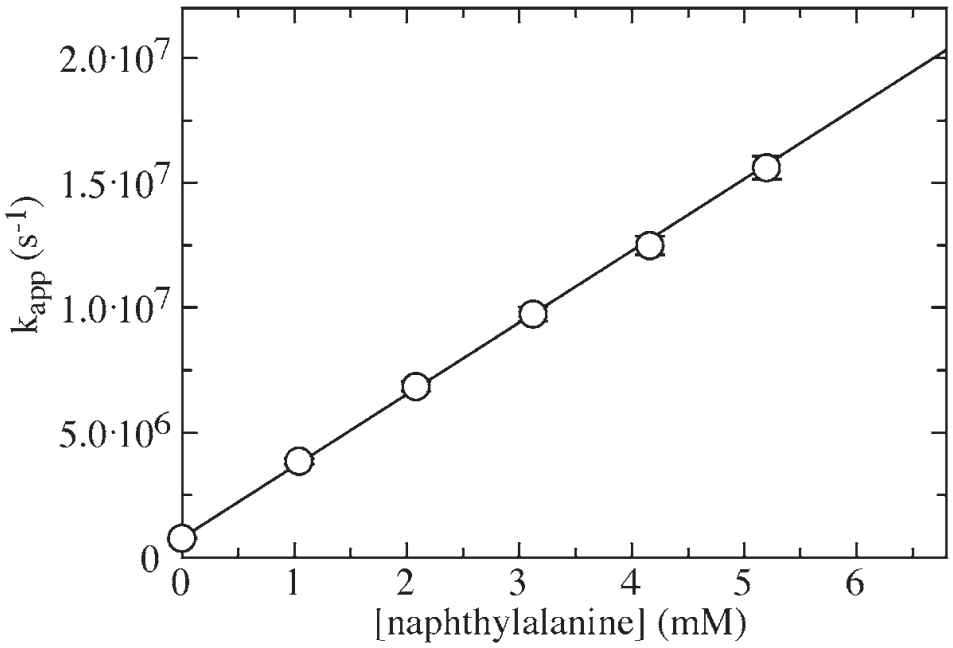

Fig. 5. Pseudo first-order measurements of bimolecular triplet–triplet energy transfer from xanthonic acid to naphthylalanine in water. Xanthone concentration was 30 μ*M*. The slope gives a bimolecular transfer constant (k_q) of 3×10^9 $M^{-1}s^{-1}$. The data were discussed in **ref.** ***7*** (adapted from **ref.** ***22***).

adding cosolvents like ethylene glycol or glycerol. To determine the final macroscopic viscosity, instruments like the falling-ball viscosimeter or the Ubbelohde viscosimeter are used. The molecular size of the cosolvent used in a viscosity study is an important factor. The macroscopic viscosity of a glycerol/water mixture and a solution of polyethlyleneglycol might be the same, although the microscopic properties of these solutions are very different ***(15)***. In the latter case, the dissolved reactant molecules only feel a fraction of the macroscopic viscosity. Thus, it is advisable to use viscous cosolvents of small molecular weight. Glycerol/water mixtures have proven to be most useful because the viscosity can be varied from 1 cP (pure water) over three orders of magnitude by addition of glycerol. It is imperative to control the temperature when working with high concentrations of glycerol because the viscosity is strongly temperature dependent. Note that viscous cosolvents can interfere with the reaction that is studied. In protein folding studies, the polyols used to vary the viscosity tend to stabilize the native state of proteins ***(16)*** making an analysis of the kinetic data difficult. However, for measurements of chain dynamics in unfolded polypeptide chains, this effect should not interfere with the measurements as long as the cosolvents do not induce a structure. Specific effects of the polyols on chain conformations/dynamics can be tested by comparing the results from different cosolvents.

2.2.2.3. DETERMINATION OF THE ACTIVATION ENERGY

Diffusion-controlled reactions typically have activation energies close to zero. The lack of an activation barrier in a diffusion-controlled quenching reaction can be verified by determining the temperature dependence of k_q. The diffusion coefficients of the reactants are, however, temperature dependent, mainly through the effect of temperature on solvent viscosity according to the Stokes–Einstein equation.

$$D = \frac{k_B T}{6\pi r \eta} \tag{7}$$

After correcting for the change in viscosity of the solvent with temperature, the slope in an Arrhenius plot should not be higher than $k_B T$. As any photophysical reaction takes some time, diffusion control is only possible to a certain maximal concentration of quencher molecules. After that the photochemistry of the quenching or transfer process becomes rate limiting. This provides an upper limit of the rate constants that can be measured, even if the system is diffusion-controlled at lower quencher concentrations. For the xanthone/naphthalene system TTET has been shown to occur faster than 2 ps and thus this system is suitable to obtain absolute time constants for all processes slower than 10–20 ps ***(6)***.

2.2.3. Testing Interference From Other Amino Acids

To test for possible interference from amino acid side chains with the TTET reaction, the effect of various amino acids on the donor triplet lifetimes must be tested. **Table 1** shows bimolecular quenching and TTET rate constants for the interaction of various amino acids with xanthone measured under pseudo first-order conditions. The thioether group of methionine ($k_q = [2.0 \pm 0.1] \times 10^9\ M^{-1}\ s^{-1}$) and the deprononated imidazole ring of histidine ($k_q = [1.8 \pm 0.1] \times 10^9\ M^{-1}\ s^{-1}$) quench xanthone triplets very efficiently with a rate constant close to the diffusion limit. The other amino acid side chains quench xanthone triplets either very inefficiently (Cys, His^+, N-terminus) or not at all (Ala, Arg, Asn, Asp, Gly, Lys, Ser, Phe). The aromatic amino acids tryptophan, tyrosine and phenylalanine are possible acceptors for xanthone triplets in TTET reactions. **Table 1** shows that TTET between xanthone and tryptophan ($k_{TTET} = (3.0 \pm 0.1] \times 10^9\ M^{-1}\ s^{-1}$) and tyrosine ($k_{TTET} = [2.5 \pm 0.1] \times 10^9\ M^{-1}\ s^{-1}$) occur in diffusion-controlled reactions with virtually the same bimolecular rate constants as observed for TTET from xanthone to naphthylalanine ($k_{TTET} = [2.8 \pm 0.1] \times 10^9\ M^{-1}\ s^{-1}$). However, TTET from xanthone to tryptophan and tyrosine are complex reactions with at least two observable rate constants. For both amino acids, TTET is accompanied by radical formation ***(17,18)***, which explains the complex kinetics and makes them not suitable for the use as TTET

Table 1
Interaction of Different Amino AcidsWith the Triplet State of Xanthone[a]

Amino acid	$k_q(M^{-1}s^{-1})$[b]	Conditions
Naphthyl acetic acid[c]	$(4.0 \pm 0.1) \times 10^9$	water, pH 7.0
Trp[c]	$(3.0 \pm 0.1) \times 10^{9e}$	water, pH 7.0
NAla[c]	$(2.8 \pm 0.1) \times 10^9$	water, pH 7.0
Tyr[c]	$(2.5 \pm 0.1) \times 10^{9e}$	water, pH 7.0
Met[d]	$(2.0 \pm 0.1) \times 10^9$	water, pH 7.0
His[d]	$(1.8 \pm 0.1) \times 10^{9e}$	0.1 *M* KKP, pH 8.0
His^{+d}	$(2.8 \pm 0.2) \times 10^7$	0.1 *M* NaOAc, pH 4.0
Cys[d]	$(5.1 \pm 0.2) \times 10^7$	water, pH 7.0
N-Terminal NH^{3+d}	$(2.0 \pm 0.5) \times 10^6$	water, pH 7.0

[a]No effect on the xanthone triplet lifetime was observed for Ala, Arg^+, Asn, Gly, Lys^+, Phe, Ser, Asp, Asp^-.

[b]Bimolecular quenching constants were measured under pseudo first-order conditions as described in **Subheading 2.2.2.1.**

[c]Triplet–triplet energy transfer.

[d]Triplet quenching.

[e]Radical formation as side reaction.

acceptors in polypeptide chains. These results show that mainly methionine, tryptophan, and tyrosine interfere with TTET from xanthone to naphthalene in intrachain diffusion experiments. Histidine containing sequences can be measured with this donor/acceptor pair if the pH of the solution is below 5.5.

2.3. Experimental Procedure to Measure TTET

2.3.1. Instrumentation

The instrumentation required to perform experiments on contact formation kinetics consists of a high-energy light source to produce excited states and of a detection mechanism (**Fig. 6**). A pulsed laser is used to produce triplet donor states in TTET or triplet quenching experiments. The duration of the light pulse has to be very short, i.e., shorter than the timescale of the reaction of interest. Additionally, the excitation pulse has to provide enough energy to excite the major portion of the molecules in the sample in order to generate a large signal. A pulsed Nd:YAG laser with a pulse width of <5 ns and a pulse energy of approx 100 mJ is well suited for these purposes. Transient ultraviolet absorption is used to detect the triplet states in TTET or triplet quenching experiments. A pulsed flash lamp generates enough light for the absorption measurements. The lamp intensity typically stays at a constant plateau value for several hundred microseconds, which is sufficient for TTET measurements. Using a monochromator allows the monitoring

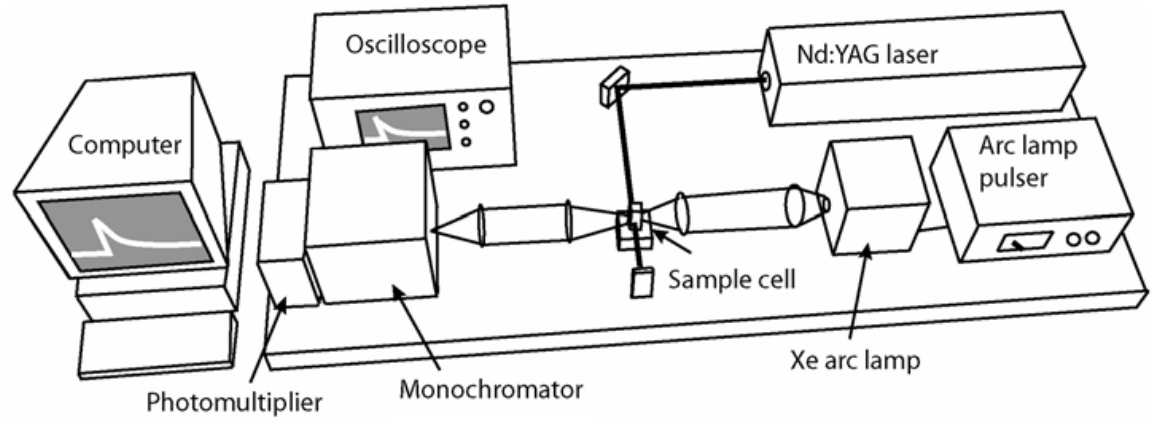

Fig. 6. Schematic representation of a laserflash setup used to measure electron transfer reactions. (Adapted from **ref. *22***.)

of single wavelengths. Transient spectra can be reconstructed from measurements at different wavelengths or by using a CCD camera.

2.3.2. Data Analysis

For data analysis transient spectra may be analyzed and fitted globally to different mechanisms (*see* **Fig. 4**). This allows testing for side reactions, such as radical formation, which occurs in some triplet systems and interferes with the actual transfer process ***(19)***. If a system has been photochemically characterized, the kinetics are typically measured at the wavelengths of maximum signal change of donor and acceptor groups. In the case of the xanthone/naphthalene pair, kinetics are measured at 590 and 420 nm (**Fig. 3**). Typical peptide concentrations required for this donor/acceptor pair are 30–50 μ*M* in a 1 cm cuvet. To test for possible contributions from bimolecular processes, TTET should be measured in a mixture of peptides containing either donor or acceptor ***(7,8)***.

For all unstructured peptides investigated up-to-date single exponential kinetics of intrachain contact formation on the nanosecond time scale were observed (**Fig. 7**) ***(7,20–22)***. The only exception was proline-containing peptides. In this case, the dynamics of peptides containing a *cis* or a *trans* Xaa–Pro peptide bond could be distinguished, which gave rise to double exponential kinetics ***(21)***.

In addition to the determination of the rate constants, the amplitude of the observed reaction should be analyzed to test for possible fast processes occurring in the dead time of the laserflash experiments. These may be caused by conformations, which have donor and acceptor in close proximity at the time point of the laserflash.

3. Comparison of Results From Different Experimental Systems

Recently, several experimental systems using TTET of triplet quenching to monitor contact formation in model peptides and protein fragments have been

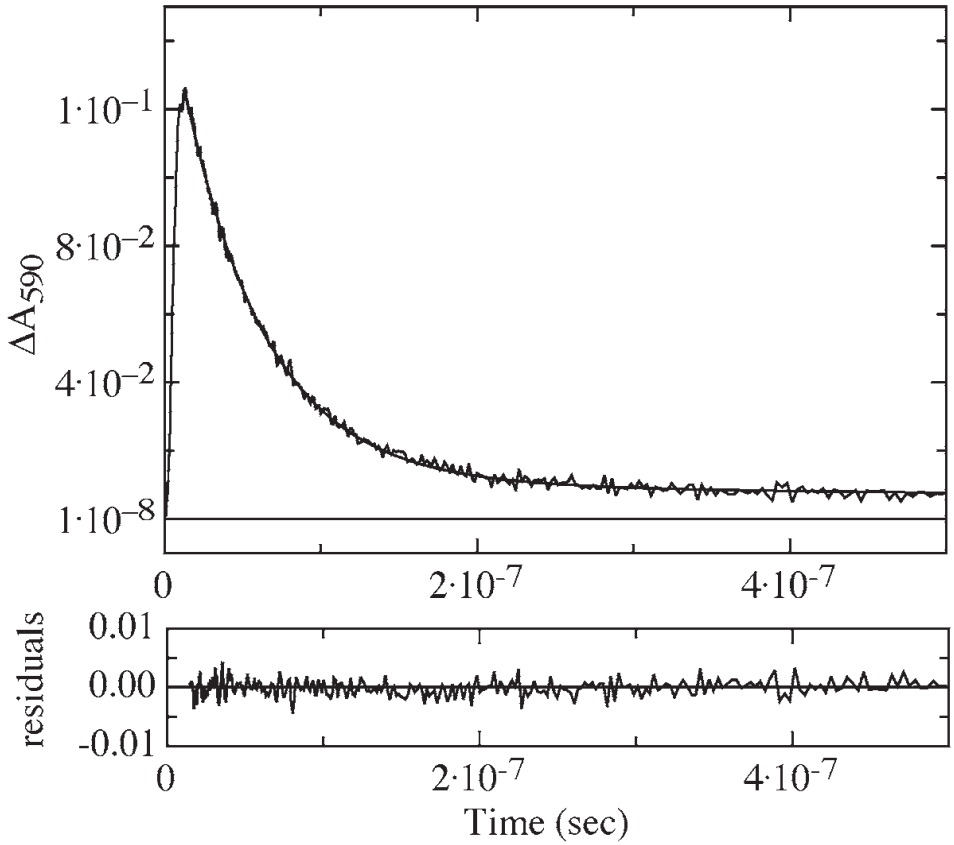

Fig. 7. Time course of formation and decay of xanthone triplets in parvalbumin loop fragment 85–102 after a 4-ns laser flash at t = 0. The change of xanthone triplet absorbance is measured at 590 nm. The dynamics of contact formation can be described by a single exponential with a time constant of 54 ± 3 ns. (Data are taken from **ref. *20***.)

introduced (*see* **Table 2**). The main advantage of energy transfer systems is the ability to monitor the population of both the donor and the acceptor populations during the experiment (*see* **Fig. 4**). Bieri et al. ***(8)*** and Krieger et al. ***(7,20)*** used TTET between thioxanthone or xanthone derivatives and naphthalene as discussed in **Subheadings 2.1.–2.4.** (*see* **Fig. 3A**,**B**) to directly measure rate constants for intrachain contact formation in synthetic polypeptide chains. In the initial studies a derivate of thioxanthone was used as triplet donor and the nonnatural amino acid naphthylalanine (NAla) as triplet acceptor ***(8)***. Because of the sensitivity of the triplet energy of the donor on solvent polarity, the measurements had to be carried out in ethanol. TTET detected single exponential kinetics in all peptides with time constants of 20 ns for the shortest loops in poly(glycine-serine)-based polypeptide chains ***(8)***. Based on these experiments, the minimum time constant for intrachain contact formation was shown to be around 20 ns for formation of short and flexible loops. The thioxanthone used in the initial experiments as triplet donor was later replaced by xanthone ***(7)***, which has higher triplet energy than thioxanthone and thus allowed measurements in water (*see* **Fig. 3B**).

Table 2
Comparison of End-to-End Contact Formation Rate Constants Observed in Different Systems

k_{app} (s^{-1})	Loop size (n)[a]	Method	Labels[b]	Sequence	Conditions	Reference
$5 \times 10^7 - 1.2 \times 10^7$	3–9	TTET	thioxanthone/NAla	$(Gly\text{-}Ser)_x$	EtOH	***(8)***
9.1×10^6	10	triplet quenching	Trp/Cys	$(Ala\text{-}Gly\text{-}Gln)_3$	H_2O, phosphate	***(19)***
1.1×10^7	10	triplet quenching	Trp/cystine	$(Ala\text{-}Gly\text{-}Gln)_3$	H_2O, phosphate	***(19)***
1.7×10^7	10	triplet quenching	Trp/lipoate	$(Ala\text{-}Gly\text{-}Gln)_3$	H_2O, phosphate	***(19)***
6.2×10^4	10	triplet quenching	Trp/lipoate	Pro_9	H_2O, phosphate	***(19)***
2.4×10^7	10	triplet quenching	Trp/lipoate	$(Ala)_2Arg(Ala)_4ArgAla$	H_2O, phosphate	***(19)***
$1.8 \times 10^8 - 6.5 \times 10^6$	3–57	TTET	xanthone/NAla	$(Gly\text{-}Ser)_x$	H_2O, 22.5°C	***(7)***
$8 \times 10^7 - 3.4 \times 10^7$	3–12	TTET	xanthone/NAla	$(Ser)_x$	H_2O, 22.5°C	***(7)***
$2.5 \times 10^8 - 2.0 \times 10^7$	4	TTET	xanthone/NAla	Ser-Xaa-Ser[c]	H_2O, 22.5°C	***(7)***
4.0×10^6	15	triplet quenching	Zn-porphyrin/Ru	unfolded cytochrome c	5.4 *M* GmdCl, 22°C	***(27)***
2.0×10^7	17	TTET	xanthone/NAla	carp parvalbumin	H_2O, 22.5°C	***(20)***

[a] *n* is the number of peptide bonds between the reacting groups.
[b] The structures of the labels are shown in **Fig. 3**.
[c] Xaa = Gly, Ala, Ser, Gly, Arg, His, Ile, Pro. The highest (*cis* Pro) and lowest values (*trans* Pro) for the observed rate constants are given.
TTET, triplet–triplet energy transfer experiments.

These results showed two- to threefold faster rate constants for contact formation compared with the same peptides in ethanol ***(7)***, setting the time constant for intrachain diffusion in short flexible chains in water of 5–10 ns. The faster kinetics compared to the thioxanthone/NAla system could be attributed to the effect of ethanol ***(7)***, which slows down chain dynamics. The xanthone/naphthalene system was further used to test the effect of chain length, amino acid sequence, and denaturants on chain dynamics in model peptides and in peptides derived from natural proteins ***(7,20–23)***. These results allowed setting an upper limit for the rate of formation of local structures early in the folding process (**Fig. 8**). A disadvantage of TTET from xanthone to NAla in its application to natural proteins is that Tyr, Trp, and Met interact with the xanthone triplet state either by TTET or by triplet quenching (*see* **Subheading 2.2.3.**) and, thus, should not be present in the studied polypeptide chains ***(20)***.

Lapidus et al. ***(19)*** used a related system to measure chain dynamics in short peptides. In this approach contact formation was measured by quenching of tryptophan triplet states by cysteine (*see* **Fig. 3C**). Tryptophan can be selectively excited by a laserflash ($\phi_{ISC} = 0.18$, $\varepsilon_{266} \approx 3500\ M^{-1}cm^{-1}$, $\varepsilon^{T}_{460} \approx 5000\ M^{-1}cm^{-1}$) and its triplet decay can be monitored by absorbance spectroscopy ***(24)***. The use of naturally occurring amino acids is an advantage of this system. Thus, the groups can be introduced at any position in peptides and proteins. As in the case of TTET from xanthone to naphthalene, some amino acids interfere with the measurements (e.g., Tyr, Met) because they interact with tryptophan triplets and, thus, should not be present in the studied polypeptide chains ***(25)***. Major disadvantages of the Trp/Cys system are, (1) that the formation of tryptophan triplets is slow ($\tau = 3$ ns) ***(17)***. (2) That triplet quenching is accompanied by the formation of S· radicals ***(19)*** and (3) that the quenching process is not diffusion controlled ***(26)***. These properties reduce the time window available for the kinetic measurements and do not allow direct and model-free analysis of the quenching time traces. In addition, its low quantum yield makes the detection of the triplet states and the data analysis difficult, especially because the kinetics are obscured by radical absorbance bands. In addition to cysteine quenching, two other systems were presented by the same group ***(19)*** with cystine or the cyclic disulfide lipoate serving as quencher (**Fig. 3D**). The advantage of using lipoate is that the quenching kinetics are much closer to the diffusion limit. Thus, the rates measured with this system are generally faster. Still, all systems used for quenching of tryptophan triplets gave significantly slower kinetics of intrachain contact formation compared to TTET from xanthone to NAla in the same or in similar sequences (**Table 3**). This indicates that tryptophan triplet quenching does not allow measurements of chain dynamics on the absolute time scale ***(26)***.

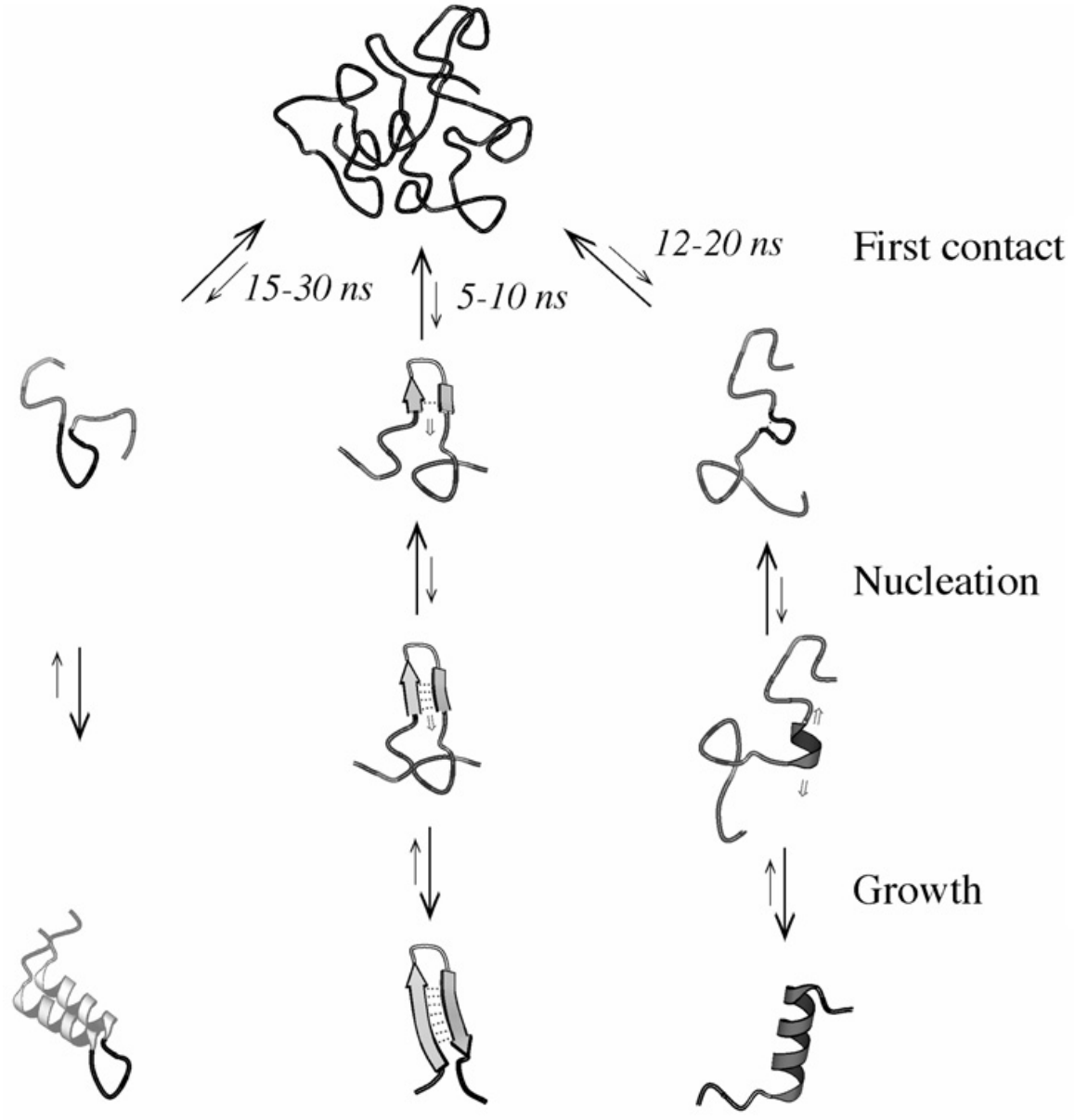

Fig. 8. Schematic representation of the time constants for the first steps in formation of loops, β-hairpins, and α-helices during protein folding derived from the data measured by triplet–triplet energy transfer in water. (Adapted from **ref. *7***.)

Another recent experimental approach investigated intrachain contact formation in unfolded cytochrome c using electron transfer from a triplet excited Zn-porphyrine group to a Ru complex, which was bound to a specific histidine residue (His 33; **Fig. 3E**). Because electron transfer is fast and close to the diffusion limit, these experiments should also yield absolute rate constants for chain diffusion. Contact formation in the 15 amino acid loop from cytochrome c was observed with a time constant of 250 ns ***(27)*** in the presence of 5.4 *M*

Table 3
Comparison of End-to-End Contact Formation Rates Observed in Different Systems Measured or Extrapolated to $n \approx 10$

k_{app} (s^{-1})	Loop size (n)	Method	Labels	Sequence	Conditions[a]	Reference
1.2×10^7	9	TTET	thioxanthone/NAla	$(GS)_4$	EtOH	***(8)***
9.1×10^6	10	triplet quenching	Trp/Cys	$(AGQ)_3$	H_2O, phosphate buffer	***(19)***
1.1×10^7	10	triplet quenching	Trp/cystine	$(AGQ)_3$	H_2O, phosphate buffer	***(19)***
1.7×10^7	10	triplet quenching	Trp/lipoate	$(AGQ)_3$	H_2O, phosphate buffer	***(19)***
8.3×10^7	9	TTET	xanthone/NAla	$(GS)_4$	H_2O, 22.5°C	***(7)***
4.1×10^7	10	TTET	xanthone/NAla	$(Ser)_9$	H_2O, 22.5°C	***(7)***
1×10^7	10	triplet quenching	Zn-porphyrin/Ru	unfolded cytochrome c	5.4 *M* GmdCl, 22°C	***(27)***

[a]Solvent was H_2O unless indicated. The data measured in concentrated GdmCl solutions or EtOH were not corrected for solvent effects. This would lead to a significant increase in k_c.

TTET, triplet–triplet energy transfer experiments.

GdmCl. This is significantly faster than the dynamics in unfolded cytochrome c reported by Hagen et al. ***(4)*** under similar conditions. However, the dynamics measured by Chang et al. agree well with TTET measurements ***(7,8,20)***, when the kinetics are extrapolated from 5.4 *M* GdmCl to water ***(22)*** (**Table 2**).

A more detailed comparison of the results obtained from the different experimental systems and a discussion of other methods applied to measure chain dynamics is given in **ref. *22.***

4. Conclusions

Several experimental systems have recently been developed to measure rate constants for intrachain diffusion processes. An essential prerequisite of methods applied to measure absolute rate constants for intrachain diffusion is that photochemistry is faster than the formation and breakage of the intramolecular contact between donor and acceptor or between donor and quencher. Presently the xanthone/naphthalene and the Zn-porphyrine/Ru system fulfill these requirements and allow model-free measurements of intrachain diffusion reactions.

References

1. Haas, E., Katchalski-Katzir, E., and Steinberg, I. Z. (1978) Brownian motion at the ends of oligopeptid chains as estimated by energy transfer between chain ends. *Biopolymers* **17,** 11–31.
2. Stryer, L. and Haugland, R. P. (1967) Energy transfer: a spectroscopic ruler. *Proc. Natl. Acad. Sci. USA* **58,** 719–726.
3. Beechem, J. M. and Haas, E. (1989) Simultaneous determination of intramolecular distance distributions and conformational dynamics by global analysis of energy transfer measurements. *Biophys. J.* **55,** 1225–1236.
4. Hagen, S. J., Hofrichter, J., Szabo, A., and Eaton, W. A. (1996) Diffusion-limited contact formation in unfolded cytochrome c: estimating the maximum rate of protein folding. *Proc. Natl. Acad. Sci. USA* **93,** 11,615–11,617.
5. Klessinger, M. and Michl, J. (1995) *Excited States and Photochemistry of Organic Molecules,* VCH, Weinheim.
6. Satzger, H., Schmidt, B., Root, C., et al. (2004) Ultrafast quenching of the xanthone triplet by energy transfer: new insight into the intersystem crossing kinetics. *J. Phys. Chem. A* **108,** 10,072–10,079.
7. Krieger, F., Fierz, B., Bieri, O., Drewello, M., and Kiefhaber, T. (2003) Dynamics of unfolded polypeptide chains as model for the earliest steps in protein folding. *J. Mol. Biol.* **332,** 265–274.
8. Bieri, O., Wirz, J., Hellrung, B., Schutkowski, M., Drewello, M., and Kiefhaber, T. (1999) The speed limit for protein folding measured by triplet-triplet energy transfer. *Proc. Natl. Acad. Sci. USA* **96,** 9597–9601.
9. Closs, G. L., Johnson, M. D., Miller, J. R., and Piotrowiak, P. (1989) A connection between intramolecular long-range electron, hole and triplet energy transfer. *J. Am. Chem. Soc.* **111,** 3751–3753.

10. Wagner, P. J. and Klán, P. (1999) Intramolecular triplet energy transfer in flexible molecules: electronic, dynamic, and structural aspects. *J. Am. Chem. Soc.* **121,** 9626–9635.
11. Szabo, Z. G. (1969) Kinetic characterization of complex reaction systems. In: *Comprehensive Chemical Kinetics*, (Bamford, C. H. and Tipper, C. F. H., eds.) Elsevier Publishing Company, Amsterdam, the Netherlands, pp. 1–80.
12. Kiefhaber, T., Kohler, H. H., and Schmid, F. X. (1992) Kinetic coupling between protein folding and prolyl isomerization. I. Theoretical models. *J. Mol. Biol.* **224,** 217–229.
13. Moore, J. W. and Pearson, R. G. (1981) *Kinetics and Mechanisms,* John Wiley and Sons, NY.
14. Stern, O. and Volmer, M. (1919) Über die Abklingungszeit der Fluoreszenz. *Physik. Z.* **20,** 183–188.
15. Kleinert, T., Doster, W., Leyser, H., Petry, W., Schwarz, V., and Settles, M. (1998) Solvent composition and viscosity effects on the kinetics of CO binding to horse myoglobin. *Biochemistry* **37,** 717–733.
16. Timasheff, S. N. (2002) Protein hydration, thermodynamic binding and prefential hydration. *Biochemistry* **41,** 13,473–13,482.
17. Bent, D. V. and Hayon, E. (1975) Excited state chemistry of aromatic amino acids and related peptides: III. Tryptophan. *J. Am. Chem. Soc.* **97,** 2612–2619.
18. Bent, D. V. and Hayano, T. (1975) Excited state chemistry of aromatic amino acids and related peptides: I. Tyrosine. *J. Am. Chem. Soc.* **97,** 2599–2606.
19. Lapidus, L. J., Eaton, W. A., and Hofrichter, J. (2000) Measuring the rate of intramolecular contact formation in polypeptides. *Proc. Natl. Acad. Sci. USA* **97,** 7220–7225.
20. Krieger, F., Fierz, B., Axthelm, F., Joder, K., Meyer, D., and Kiefhaber, T. (2004) Intrachain diffusion in a protein loop fragement from carp parvalbumin. *Chemical Physics* **307,** 209–215.
21. Krieger, F., Möglich, A., and Kiefhaber, T. (2005) Effect of proline and glycine residues on the dynamics and barriers of loop formation in polypeptide chains. *J. Am. Chem. Soc.* **127,** 3346–3352.
22. Fierz, B. and Kiefhaber, T. (2004) Dynamics of unfolded polypeptide chains. In: *Protein Folding Handbook* (Buchner, J. and Kiefhaber, T., eds.) Wiley-VCH Verlag GmbH and Co. KGaA, Weinheim, Germany, pp. 805–851.
23. Möglich, A., Krieger, F., and Kiefhaber, T. (2004) Molecular basis of the effect of urea and guanidinium chloride on the dynamics of unfolded proteins. *J. Mol. Biol.* **345,** 153–162.
24. Volkert, W. A., Kuntz, R. R., Ghiron, C. A., Evans, R. F., Santus, R., and Bazin, M. (1977) Flash photolysis of tryptophan and N-acetyl-L-tryptophanamide; the effect of bromide on transient yields. *Photochem. Photobiol.* **26,** 3–9.
25. Gonnelli, M. and Strambini, G. B. (1995) Phosphorescence lifetime of tryptophan in proteins. *Biochemistry* **34,** 13,847–13,857.
26. Yeh, I. C. and Hummer, G. (2002) Peptide loop-closure kinetics from microsecond molecular dynamics simulations in explicit solvent. *J. Am. Chem. Soc.* **124,** 6563–6568.

27. Chang, I. -J., Lee, J. C., Winkler, J. R., and Gray, H. B. (2003) The protein-folding speed limit: intrachain diffusion times set by electron-transfer rates in denatured Ru(NH3)5(His-33)-Zn-cytochrome c. *Proc. Natl. Acad. Sci. USA* **100,** 3838–3840.
28. Lapidus, L. J., Eaton, W. A., and Hofrichter, J. (2001) Dynamics of intramolecular contact fromation in polypeptides: distance dependence of quenching rates in a room-temperature glass. *Phys. Rev. Lett.* 258101-1–258101-4.
29. Lapidus, L. J., Steinbach, P. J., Eaton, W. A., Szabo, A., and Hofrichter, J. (2002) Effects of chain stiffness on the dynamics of loop formation in polypeptides. Appendix: Testing a 1-diensional diffusion model for peptide dynamics. *J. Phys. Chem. B* **106,** 11,628–11,640.

9. Curriculum Vitae

Name and address: Beat Fierz
Biozentrum der Universität Basel
Abteilung Biophysikalische Chemie
Klingelbergstrasse 70
CH-4056 Basel
Tel.: ++41 (0)61 267 22 07
Fax: ++41 (0)61 267 21 89
Email: beat.fierz@unibas.ch

Date of birth: Basel
Place of birth: 25. August, 1978
Nationality: Swiss
Marital status: unmarried

Education

11/2002 – 06/2006 Biozentrum der Universität Basel
Graduate (Ph.D.) studies in Biophysics
Thesis supervisor: Prof. Dr. Thomas Kiefhaber
Thesis title: "Dynamics of Unfolded and α-Helical Polypeptide Chains"

07/2001 – 07/2002 Biozentrum der Universität Basel
Diploma Thesis in Biophysics
Thesis supervisor: Prof. Dr. Thomas Kiefhaber
Thesis title: "Dynamics of Intramolecular Contact Formation in Model Peptides"

10/1998 – 10/2002	Biozentrum der Universität Basel Diploma studies in Biology II (Molecular Biology)
08/1995 – 1998/06	Realgymnasium Basel Matur Typus B (Latein) 1998